Laboratory and Balloon Flight Performance of the Liquid Xenon Gamma Ray Imaging Telescope (LXeGRIT)

Alessandro Curioni

Submitted in partial fulfillment of the
requirements for the degree
of Doctor of Philosophy
in the Graduate School of Arts and Sciences

COLUMBIA UNIVERSITY
2004

Laboratory and Balloon Flight Performance of the Liquid Xenon Gamma Ray Imaging Telescope (LXeGRIT)

Alessandro Curioni

Advisor: Professor Elena Aprile

Submitted in partial fulfillment of the
requirements for the degree
of Doctor of Philosophy
in the Graduate School of Arts and Sciences

COLUMBIA UNIVERSITY
2004

ABSTRACT

Laboratory and Balloon Flight Performance of the Liquid Xenon Gamma Ray Imaging Telescope (LXeGRIT)

Alessandro Curioni

This thesis presents the laboratory calibration and in-flight performance of the liquid xenon γ-ray imaging telescope (LXeGRIT). LXeGRIT is the prototype of a novel concept of Compton telescope, based on a liquid xenon time projection chamber (LXeTPC), developed through several years by Prof. Aprile and collaborators at Columbia. When I joined the collaboration in Spring 1999, LXeGRIT was getting ready for a balloon borne experiment with the goal of performing the key measurement of the background at balloon altitude. After the 1999 balloon flight, a good deal of work was devoted to a thorough calibration of LXeGRIT, both through several tests in the laboratory and through improving the analysis software and developing Monte Carlo simulations. After substantial advancements in our understanding of the detector performance, LXeGRIT was improved and calibrated before a long duration balloon campaign in the Fall of 2000. Data gathered in this flight have allowed a detailed study of the background at balloon altitude and of the sensitivity to celestial γ-ray sources, the focus of the second part of my thesis. As this dissertation is intended to show, "the LXeGRIT phase" - defined as the prototype work, the experimental demonstration of the LXeTPC concept as a Compton telescope, the measurement of the background and of the detection sensitivity - has been now successfully completed. We are now ready for future implementations of the LXeTPC technology for astrophysics observations. The detailed calibration of LXeGRIT, both as an imaging calorimeter and as a Compton telescope is described in Chapters 2, 3 and 4. In Chapter 5 more details are given of LXeGRIT as a balloon borne instrument and its flight performance in year 2000. The measurement of the background at balloon altitude, based on the data collected in year 2000, is presented in Chapter 6 and the sensitivity of the instrument is derived in

Chapter 7. An overview of future developments for the LXeTPC technology in the field of γ-ray astronomy is given in Chapter 8. The main results from the 1999 balloon flight are summarized in Appendix A.

Contents

List of Figures

List of Tables

ACKNOWLEDGMENTS

I would like to thank all the people I have collaborated with while working toward my dissertation; among them, Prof. Elena Aprile, Doctor K.-L. Giboni, Prof. Ed Chupp, Prof. Uwe Oberlack and the long time friend Sandro Ventura. And no acknowledgments would be complete without mentioning Tommaso Tabarelli de Fatis. On a more private tone, I would like to thank the many friends with whom I shared my New York years: Nestor Mirabal, Sera Cremonini, Michel Sorel, Yashar Teherani, Chad Finley, Maurice Leutenegger, Chun Zhang and the many more whom I do not mention here but sure I do not forget. Soccer-wise, I will not forget the Pupin Strikers. Brother and father, sister and mother deserve more than the concise thanks I can give them here. But more than anybody else, I am thanking my lovely wife Silvia.

a Silvia,
per amore infinito

Chapter 1

Introduction

1.1 MeV γ-ray astronomy

The energy range covered by MeV γ-ray astronomy is conventionally defined to lay between 0.511 MeV, i.e. the rest mass of the electron, and 70 MeV, i.e. the energy of each of the two photons from the decay at rest of the π^0 [1] MeV γ-rays are rarely thermal radiation, since it would require temperatures of about 10^9 K [2]. More often they are emitted by charged particles accelerated in strong electric fields, by up-scattering of low energy photons through collisions with energetic particles (inverse Compton scattering), nuclear transitions and annihilation of e^+-e^- pairs which gives two 0.511 MeV photons. The next two sections outline some of the more common astrophysical sources of γ-ray photons (Sec. 1.1.1) and how they are possibly observed (Sec. 1.1.2).

1.1.1 Phenomenology

A fair idea of the objects observed so far in the MeV sky is given in Table 1.1, which has been adapted from the first COMPTEL catalogue (Ref. (84)). As can be seen, the possible sources of MeV γ-rays are classified as:

i. Spin-Down Pulsars

---

[1] A thorough and updated introduction to the field of MeV γ-ray astronomy can be found, for example, in the book V. Schönfelder (ed.) “The Universe in Gamma Rays” (86), to which I largely refer throughout the present chapter.

[2] The core of the Sun is at a temperature of $\sim 10^7$ K, i.e. keV thermal energy.

ii. Stellar Black Hole Candidates

iii. Supernova Remnants

iv. Active Galactic Nuclei (AGN)

v. Unidentified Sources

vi. Gamma-Ray Line Sources

vii. Gamma-Ray Burst Sources

To this list, one should add the study of solar flares, classical novae (still undetected in the MeV), continuum interstellar and cosmic γ-radiation and all-sky maps of specific γ-ray lines (the most significant completed so far being for the 1.809 MeV ^{26}Al line. See Fig. 1.1). Some of the γ-ray line measurements have been supplemented with more spectroscopy-oriented observations which combine good energy resolution and a generally poor imaging capability. Gamma ray bursts (GRBs) are easily the topic which has drawn the most attention and excitement in the scientific community, but GRBs have so far been somewhat peripheral to our definition of MeV γ-ray astronomy.

Arguably the most striking features in Table 1.1 is the small number of sources: only 32 steady sources and 31 γ-ray bursters were detected after about 5 years of observation. Given the meager number of objects detected in each category, it is very likely that we are seeing only the most favorable objects - i.e. objects uncommonly bright in the MeV - instead of the "typical" ones.

Neutron stars and spin-down pulsars

Historically, the first pulsar was discovered by Jocelyn Bell in 1967 using radio telescope observations and the result was published in Ref. (52) in 1968. It was soon interpreted (Refs. (75) and (48)) as generated by a rotating magnetized neutron star. Now the Princeton catalogue of radio pulsars [3] contains 706 pulsars.

Neutron stars are believed to be the final stable configuration reached by massive stars, with stellar mass ranging between 1.44 $M_\odot$, the Chandrasekhar

---

[3] http://pulsar.princeton.edu/pulsar/catalog.shtml

Type of Source	**Number of Sources**	**Comments**
Spin-Down Pulsars:	3	Crab, Vela, PSR B1509-58.
Stellar Black Hole Candidates:	2	Cyg X-1, Nova Persei 1992 (GRO J0422+32).
Supernova Remnants: (Continuum Emission)	1	Crab nebula.
Active Galactic Nuclei:	10	CTA 102, 3C 454.3, PKS 0528+134, GRO J 0516-609, PKS 0208-512, 3C 273, PKS 1222+216, 3C 279, Cen A, PKS 1622-297.
Unidentified Sources:		
• $\|b\| < 10°$	4	GRO J1823-12, GROJ2228+61 (2CG 106+1.5), GRO J0241+6119 (2CG 135+01), Carina/Vela region (extended).
• $\|b\| > 10°$	5	GRO J1753+57(extended), GRO J1040+48, GRO J1214+06, HVC complexes M and Aarea (extended), HVC complex C (extended).
Gamma-Ray Line Sources:		
• 1.809 MeV (^{26}Al)	3	Cygnus region(extended), Vela region (extended, may include RX J0852-4621), Carina region.
• 1.157 MeV (^{44}Ti)	2	Cas A, RX J0852-4621 (GRO J0852-4642).
• 0847 and 1.238 MeV (^{56}Co)	1	SN 1991T.
• 2.223 MeV (n-capture)	1	GRO J0317-853.
Gamma-Ray Burst Sources: (within COMPTEL field-of- up to Phase IV/Cycle-5)	31	Location error radii vary from 0.34° to 2.79° (mean error radius: view 1.13°).

Table 1.1: Summary of the most significant COMPTEL source detections (adapted from Ref. (84)).

limit, and 3.6 $M_\odot$, which exerts the maximum gravitational pressure which can be balanced by a degenerate Fermi gas of neutrons. From the study of X-ray binaries (XRBs), most neutron stars have masses of about 2 $M_\odot$.

Some general characteristics of a newly formed neutron star can be derived from basic conservation laws. Angular momentum conservation implies $r^2\omega$ conservation, where r is the radius of the star and ω its angular frequency. In a stellar core collapse, the r shrinks from 10^{11} cm to 10^6 cm, thus increasing ω by $\sim 10^{10}$, and reducing the period of rotation from days to milliseconds. The interior of a star is a conductive medium and the magnetic flux ($\propto\ Br^2$) is therefore conserved. In a core collapse, the typical field of a star ($\sim 10^2$ G) is expected to increase to $\sim 10^{12}$ G.

Relativistic charged particles in intense magnetic fields lead to emission of high-energy photons. A theoretical treatment of pulsar high-energy emission is highly non-trivial and has to include magnetic bremsstrahlung, curvature radiation, pair production and photonsplitting (see for example Ref. (43)).

A prime example of the importance of pulsar high-energy emission is the Geminga pulsar, i.e. an object which emits an overwhelming fraction of its power in X- and γ-rays. Such an object was not identified outside the γ-ray band until 1992, when it was identified by ROSAT in X-rays.

The phase-resolved continuum spectra from radio pulsars indicates that most of the departing energy is in high energy photons. One of the goals of MeV γ-ray astronomy, combined with higher energy observations, is to unravel the particle acceleration and photon production mechanisms in the outer reaches of the pulsar's magnetosphere.

Neutron stars in binary systems are luminous in X-rays and are part of the broader class of XRBs. The X-ray luminosity is powered by accretion of matter from the companion star onto the neutron star. Assuming that all the gravitational energy is converted to radiation, the luminosity L will be

$$L \sim \frac{GM_c}{R_c}\dot{M}$$

where G is the gravitational constant, M_c and R_c mass and radius of the neutron star and $\dot{M}$ the mass accretion rate. Assuming M_c=1.4 $M_\odot$ and R_c=10 km, which are typical values for a neutron star, and a luminosity of 10^{37} erg s^{-1}, as typically measured in X-rays, an accretion rate $\dot{M}$ of about $10^{-9}M_\odot$ per year is required. Accreting neutron stars usually have not been detected as γ-ray emitters and their energy spectra show a cut off at few tens of keV; only two of the known XRBs, Cygnus X-3 and Centaurus X-3, have been detected in γ-rays at energies above 100 MeV. This high-energy component cannot be explained as a continuation of the detected hard X-rays

[4] tails and the emission scenario is modeled separately for X-ray and γ-rays. More sensitive observations in the MeV region (sensitivity to a flux of about 10^{-7} ph cm^{-2} s^{-1}) could close the gap.

The discovery of gravitationally red-shifted γ-ray line emission from neutron stars in a binary system would possibly be a fundamental discovery. Any line originating from the radially thin atmosphere would immediately yield the gravitational redshift, thereby constraining the nuclear equation of state at matter densities currently unavailable in the terrestrial laboratory. The first gravitationally redshifted atomic spectral line was just recently reported in Ref. (32) from a summed spectra of many Type I burst events, yielding a neutron star radius $R \sim 4.4\ GM/c^2$. A promising γ-ray line emission mechanism was first discussed in Ref. (88), where it was noted that matter accreting onto a neutron star has large enough kinetic energies to excite or destroy nuclei. The subsequent γ-ray line emission from nuclear de-excitation or neutron recombination (i.e. H(n,γ)D giving a 2.2 MeV photon) might just provide the needed probe of the gravitational redshift. The problem was later studied in detail in Ref. (21) and it was found that the flux of red-shifted, rotationally broadened 2.2 MeV photons from Sco X-1 could be nearly 10^{-6} ph cm^{-2} s^{-1}. This estimate assumed that the accreting material has just a solar abundance of He, which is the main neutron source. Just like during solar flares, neutrons liberated during the deceleration of the incident He nuclei either recombine with atmospheric protons and emit 2.2 MeV γ-rays or suffer charge exchange on atmospheric ^{3}He, i.e. ^{3}He(n,p)T. Only a fraction of the liberated neutrons produce an unscattered 2.2 MeV γ-ray since the emission occurs at Compton scattering optical depths of order unity. This reduces the expected line emission so that only the brightest persistent X-ray sources will be detectable. Other possibly detectable sources would be bright accreting pulsars in outburst and any of the newly discovered ultracompact binaries in outburst, as these systems are accreting pure He or a C/O mix that is neutron-rich and a likely source of emission lines.

Stellar black-hole candidates and AGN

The compact object in a XRB may be a black hole as well; it is considered a black hole if its mass is in excess of 3.6 $M_\odot$, the theoretical upper limit

---

[4] By convention, photon energy below 200 keV constitutes the X-ray band, 0.2-0.5 MeV the soft γ-ray band and the γ-ray band starts above 0.5 MeV.

on the mass of a stable neutron star. To date 11 black hole binary systems have been identified. Active galaxies are broadly identified through their large luminosity concentrated in a small core region. Based on light-travel arguments and the time variability, the size of the core region should be $\sim 10^{10}$ km, roughly the size of our solar system [5]. AGN are thought to be powered by mass accretion onto a supermassive ($> 10^6 M_\odot$) black hole, and radiate close to their Eddington limit. The Eddington limit is derived from the balance of gravitational force and radiation pressure, and is reached when the radiation pressure would stop the accretion process.

Results from CGRO [6] show that galactic black hole candidate sources and AGN are bright at soft γ-ray energies, and display a wide range of spectral states both individually and among classes. Black hole XRBs such as GRO J0422+32 and Cygnus X-1 undergo a series of transitions from the bright soft X-ray state to a dimmer, hard γ-ray state where the photon energy E_{pk} of peak power output is at hundreds of keV. GRO J0422+32 and Cygnus X-1 are also the only two black hole XRBs detected in MeV photons. No significant emission has been detected above 100 MeV. Cygnus X-1 reaches a flux of 10^{-2} ph cm^{-2}s^{-1} MeV^{-1} at 0.5 MeV, which may allow a sensitive future instrument to search for broadened annihilation line features.

AGN constitute the larger class of identified MeV sources in the COMPTEL catalogue. All the AGN in the COMPTEL catalogue are “blazars”, i.e. BL Lac objects or radio loud quasars. Blazars show highly variable flux on a time scale of one day or less. Such short term variability and the large luminosity in γ-rays have led to model the γ emission scenario as inverse Compton emission from a relativistic jet pointing toward the observer within 10°, enhanced in intensity due to Doppler boosting. γ-emission from radio galaxies such as Centaurus A, and from blazars like 3C 273, PKS 0528+134, and Mrk 421, are as bright as 10^{-3} ph cm^{-2} s^{-1} MeV^{-1} between 0.5 MeV

---

[5] The emission radius r is estimated from

$$r < \frac{c\Delta t}{1+z}$$

where Δt is the observed time variability, z the redshift of the source and c the speed of light. Δt can be of the order of one day.

[6] The Compton Gamma Ray Observatory (CGRO) includes four detectors with different capabilities: *i.* BATSE, the Burst And Transient Source Experiment; *ii.* OSSE, the Oriented Scintillation Spectrometer Experiment; *iii.* COMPTEL, COMPton TELescope, in the 1-30 MeV energy range; *iv.* EGRET, the Energetic Gamma Ray Experiment Telescope, above 100 MeV.

isotope	lifetime	decay chain	energy [MeV]
^{7}Be [a]	77 days	^{7}Be→^{7}Li*	0.478
^{56}Ni [b]	111 days	^{56}Ni→^{56}Co*→^{56}Fe*	0.847, 1.238
^{57}Ni [b]	390 days	^{57}Ni→^{57}Co*→^{57}Fe*	0.122
^{22}Na [a]	3.8 yrs	^{22}Na→^{57}Ne* + e^{+}	1.275, 0.511
^{44}Ti [b]	89 yrs	^{44}Ti→^{44}Sc*→^{44}Ca*	1.156, 0.068, 0.078
^{26}Al [a,b,c]	1.04 10^{6} yrs	^{26}Al→^{26}Mg* + e^{+}	1.809, 0.511
^{60}Fe [b]	2.0 10^{6} yrs	^{60}Fe→^{60}Co*	1.173, 1.332, 0.059

Table 1.2: Isotopes of interest in MeV γ-ray astronomy. Production sites: [a]: classical novae, [b]: supernovae, [c]: stellar nucleosynthesis.

and 1 MeV.

Seyfert galaxies are radio quiet and have been detected in hard X-rays and soft γ-rays, but are undetected in the MeV (apart maybe for the peculiar Cen A object). Seyfert AGN such as NGC 4151 reach flux levels of 10^{-4} ph cm^{-2} s^{-1} MeV^{-1} at 0.5 MeV, which should allow for high quality energy spectra at higher energies with a future instrument. Searches for highly obscured black-hole sources surrounded by Thomson-thick material are also possible in the MeV range, extending searches by black-hole finder probes sensitive at hard X-ray energies.

Supernovae and supernova remnants (SNR)

Both core collapse (Type II) and thermonuclear (Type Ia) supernovae are sites of nucleosynthesis, and produce large amounts of radioactive isotopes (^{56}Ni, ^{57}Ni, ^{44}Ti, ^{60}Fe, ^{56}Co and ^{26}Al: see Table 1.2) which, through the supernova explosion, are instantaneously released in the interstellar medium. The observation of γ-ray lines probes the nucleosynthesis and dynamics of a supernova explosion and - potentially - is helpful in understanding the explosion mechanism and expansion dynamics of supernovae. If the current models of supernova explosion hold true, a wide-field sky survey with a 10^{-6} ph cm^{-2} s^{-1} sensitivity could detect ^{56}Ni and ^{56}Co lines from type Ia supernovae to a distance of about 85 Mpc. Based on current estimates of the rate of type Ia supernovae, that would translate to about 50 supernovae per year.

The only Type Ia supernova which has possibly been seen in γ-rays is SN 1991T in the galaxy NGC 4527, $\sim$17 Mpc away in the direction of the Virgo cluster. It was classified as a "peculiar" Type Ia supernova. ^{56}Co γ-rays were detected by COMPTEL at 3-4 σ significance (Ref. (68)) with the COMPTEL flux translated into a very large ^{56}Ni mass of $\sim$2 $M_{\odot}$, at odds with current models.

The 1.157 MeV ^{44}Ti γ-ray line (89 years lifetime) has been detected from two SNR: Cas A (Ref. (54)) and RX J0852-4621 (GRO J0852-4642) (Refs. (55) and (85)). The detected ^{44}Ti flux from Cas A implies $\sim$$10^{-4}$ $M_{\odot}$ of ^{44}Ti, while supernova models (Ref. (92)) predicted only $\sim$$10^{-5}$ $M_{\odot}$ of ^{44}Ti. Together with an estimated rate of galactic core-collapse supernovae of one every 30 yr (Ref. (40)), the fact that only two SNR have been actually detected may suggest that ^{44}Ti-producing supernovae are exceptional events.

With the current sensitivity only a handful of sources and lines have been detected so far (as in Table 1.1), too few to produce a breakthrough in supernova science. A much improved experimental sensitivity is required to detect a significant sample of galactic and Local Group SNR emitting γ-ray line from longer-lived radionuclides. This would eventually permit a detailed study of the production of ^{44}Ti, ^{26}Al and ^{60}Fe in the various sub-types of supernovae. For the brighter remnants, the ability to spatially resolve the remnant will permit the study of the dynamics of the remnant's expansion.

Unidentified sources

A large fraction of high-energy ($>$ 100 MeV) γ-ray sources - about two thirds of the EGRET catalogue - are still unidentified, i.e. they have not yet been detected at other wavelengths. As shown in Table 1.1, about one third of the already much smaller COMPTEL catalogue are classified as unidentified sources. A good example of a previously unidentified source is the Geminga high-energy pulsar. If it is a prototype for a larger class of unidentified sources, their nature could be determined in the future following a strategy similar to the one successful in the Geminga case. Most of the interest is at high-energy, and the GLAST instrument [7] (but also the AGILE mission [8]) is expected to shed new light on this interesting topic.

---

[7] http://glast.gsfc.nasa.gov/

[8] http://agile.mi.iasf.cnr.it/

Diffuse galactic emission [9]

Diffuse line emission from interstellar radionuclides, e^+-e^- annihilation and nuclear excitation by accelerated particles afford us the opportunity of a kind of galactic tomography that allows us to study stellar evolution, the origin of the elements, and the most energetic processes throughout the Milky Way Galaxy.

The decay of ^{26}Al, with its 1.04 Myr decay time, shows directly (Fig. 1.1) a million years worth of massive star and supernova activity. It shows clearly that star formation and massive star nucleosynthesis is an ongoing, galaxy-wide process and, within instrumental limitations, where it is occurring. The imaging capability and improved sensitivity of the COMPTEL instrument have provided this information at a glance in its sky maps. Individual massive star associations, spiral arm tangents, and perhaps even individual supernova remnants and massive stars reveal themselves and can be studied quantitatively. Still a great deal remains to be learned from this emission. COMPTEL's large background and extended point spread function leave systematic uncertainties in fluxes and questions of the reality of small scale structures.

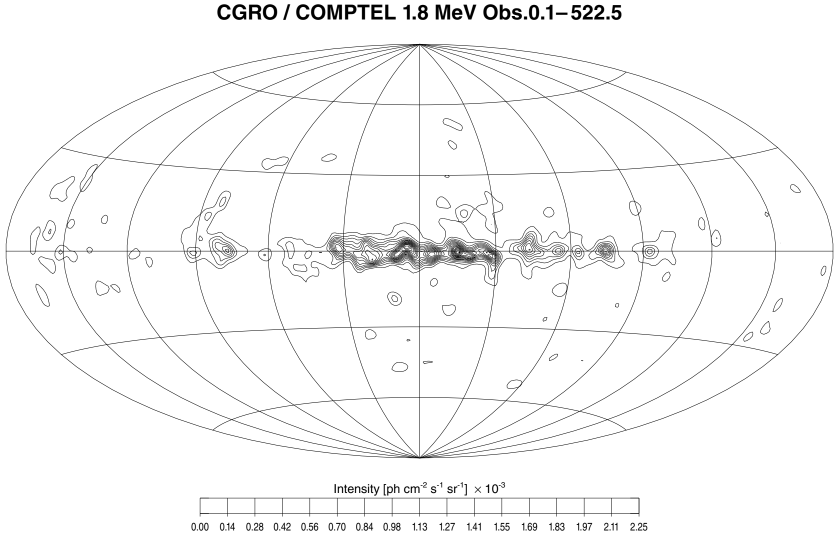

Figure 1.1: COMPTEL maximum entropy map at 1.809 MeV (from Ref. (84)).

---

[9] Part of this section has been adapted from Ref. (7).

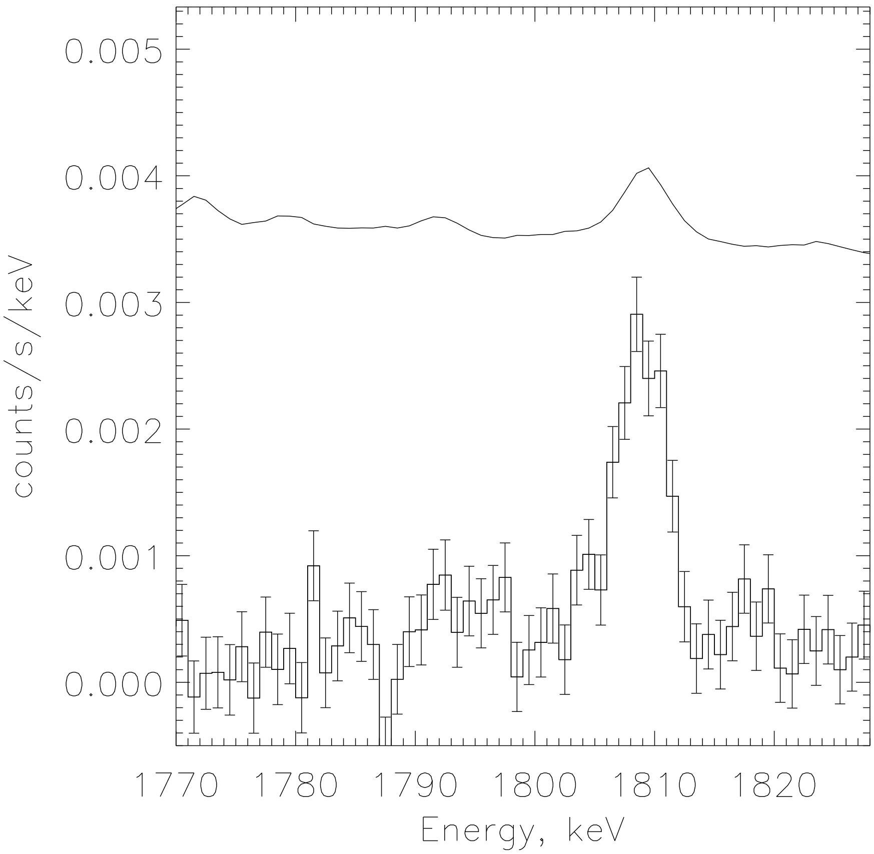

Figure 1.2: Inner-Galaxy spectra in the vicinity of the 1.809 MeV line. The lower curve is the *RHESSI* background-subtracted count rate spectrum and the upper curve is 3% of the average background spectrum during this period. The bins shown are 1 keV wide and the instrumental resolution at 1809 keV is (4.10 ± 0.07) keV (adapted from Ref. (89)).

With greatly improved sensitivity and angular resolution, we expect these apparently diffuse emissions to be resolved, at least in part, into hundreds of distinct regions, which can be understood in terms of objects and regions visible at other wavelengths. ^{26}Al 1.809 MeV emission is expected from OB associations and individual supernova remnants, as well as from the stellar ejecta already merged into the interstellar medium.

An earlier claim of a broad line profile (Ref. (69)) generated a lively debate. The GRIS Ge detector instrument reported a ΔE of 5.4±1.4 keV, exceeding the nominal energy resolution of 3 keV. Galactic rotation is expected to result in $\sim$1 keV Doppler broadening of the line and it is very hard to devise a mechanism to maintain a high velocity motion of the million year time scale of ^{26}Al. Recently (Ref (89); see Fig. 1.2) the RHESSI instrument measured a line width compatible with the 4.1 keV instrumental resolution and inconsistent with the GRIS result. More recent but still not conclusive results from SPI on the INTEGRAL mission (41; 56) support the RHESSI results and tend to rule out the GRIS claim.

One of the primary scientific goals of MeV γ-ray astronomy is the discovery and mapping of ^{60}Fe radioactivity from the Galaxy. With a mean lifetime of 2.2 Myr, ^{60}Fe provides, through its daughter ^{60}Co, lines at 1.17 MeV and at 1.33 MeV, a snapshot of supernova activity similar, but complementary, to that of ^{26}Al. The core-collapse supernova ^{60}Fe yield is thought to be about 1/3 that of ^{26}Al and is made in the same explosive Ne-burning zones (97; 91), which implies a γ-ray line flux ratio of $\sim$1/7, so the total fluxes in each ^{60}Fe line from the inner Galaxy could be as large as $5 \times 10^{-5}\,\gamma\,\mathrm{cm}^{-2}\,\mathrm{s}^{-1}$, but could be less if ^{26}Al has other sources contributing significantly. We would of course like to turn this argument around with a measurement of the ^{60}Fe flux and then ^{60}Fe will lead us to the source of the ^{26}Al. There might be an additional bulge component to the ^{60}Fe emission, arising from Type Ia (thermonuclear) supernovae, in particular those which undergo some initial nuclear burning with a flame moving slowly enough to allow significant electron capture. No comparable constraints on SN Ia physics are currently available from any other observable. A total bulge flux of $10^{-5}\,\gamma\,\mathrm{cm}^{-2}\,\mathrm{s}^{-1}$ is possible, if Chandrasekhar mass SN Ia populate the bulge. So far, only upper limits on ^{60}Fe γ-ray line emission have been derived (Refs. (65; 62; 70)), the most recent one just starts to put limits on theoretical expectations (14% of 1.81 MeV flux, 2 σ limit).

Galactic e^+-e^- annihilation radiation has not been mapped by any imaging instrument. OSSE has been able to make crude maps of the emission by combining many observations with its small field of view in a mosaic of the inner Galaxy. The dominant components are a disk and a compact bulge, with perhaps an additional component above the Galactic center (77), which suggests to some a recent starburst at the galactic center (39). It would be important to confirm this feature with improved angular resolution and sensitivity. Other unexpected features may lie where OSSE has not yet looked with sufficient exposure (which is everywhere but very close to the Galactic center). Many sources from multiple populations might contribute to this emission, which, with a total flux of $\gtrsim 10^{-3}\ \gamma\,\mathrm{cm}^{-2}\,\mathrm{s}^{-1}\mathrm{sr}^{-1}$, can in principle be disentangled into many separate regions and several distinct components. In addition to contributions from positrons due to ^{26}Al and ^{44}Ti, a significant number of positrons from shorter-lived ^{56}Co in Type Ia supernovae probably contribute as well. Additional positrons from pulsar pair winds and pair-dominated transient episodes of accretion disks may be sorted out from the radioactive sources. The contributions from longer-lived progenitors, AGB stars and classical novae, might be identifiable from their smoother spatial distributions. Interstellar positrons entrained in galactic magnetic fields will provide part of the complex 0.511 MeV map, which will also feature individual supernova remnants and stellar and compact object wind nebulae, and possibly the galactic center.

Cosmic rays with energies of 10-100 MeV/nucleon, which are an important ingredient in the interstellar energy budget, are still undetected. The cross sections for most of the processes producing γ-ray lines - spallation and direct nuclear excitation at diffuse levels - have a maximum at several tens MeV / nucleon, rapidly declining above 100 MeV. Some of the most important signature lines are expected to be 4.44 MeV from ^{12}C* and 6.13 MeV, 6.92 MeV and 7.12 MeV form ^{16}O*. More lines can be produced from heavier nuclei such as ^{20}Ne (1.63 MeV), ^{22}Ne (1.28 MeV), ^{24}Mg (1.37 MeV), and ^{28}Si (1.78 MeV) (e.g. Ref. (78)). Observation of nuclear γ-ray lines is likely to be the only means to study such low energy particles in the interstellar space. Enhancements could be significant where young supernova remnants are accelerating nuclei near cloud targets; an earlier claim of detection from the Orion complex was later discarded as an instrumental effect (see Fig. 1.3 for the Orion complex and Ref. (23)).

Diffuse gamma-ray background

The extragalactic background radiation (EBR) provides a unique window on a variety of fundamental topics in cosmology, astrophysics, and particle physics. These topics include the origin of the universe, the formation of structure and the evolution of galaxies, the formation of stars and the production of metals, gas, and dust, and the properties of exotic elementary particles. There are two distinct possibilities for the origin of the EBR: it may result from the superposition of unresolved point sources or originate from

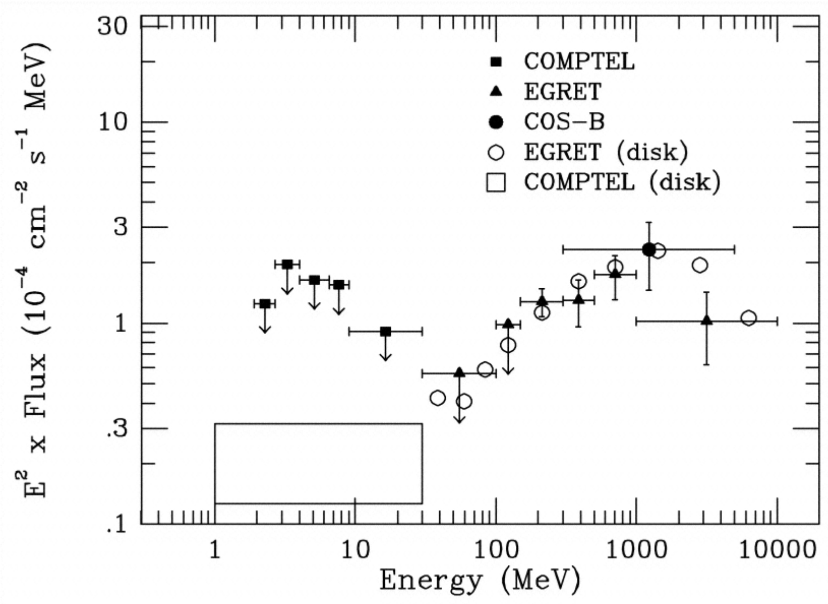

Figure 1.3: Flux spectrum of the Orion complex (from Ref. (23)).

truly diffuse mechanisms. Arguably, the least explored portion of the EBR, often referred to as diffuse γ-ray background, is in the 100 keV to 10 MeV region. This waveband is of particular interest since at these energies a transition seems to occur in the physical processes governing the emission of the various source populations. Below about 100 keV thermal emission processes seem to dominate, as in the accretion disks of Seyfert galaxies, above about 10 MeV non-thermal processes seem to dominate, as in the jets of blazars. In addition, the radioactivity of supernovae could contribute significantly around 1 MeV. Other source populations, among them normal galaxies, may contribute as well, and a truly diffuse emission component can not yet be ruled out conclusively.

Gamma-ray bursts

Gamma-ray bursts (GRBs) [10] are the most luminous objects known in the Universe. Assuming isotropic emission [11] an amount of energy as large as 10^{54} erg is emitted in a timescale of few seconds. Energy flux spectra of GRBs typically peak at several hundreds keV, but from BATSE observations, many of them are observed to peak at energies > 0.5 MeV. For many additional GRBs, a significant fraction of the total GRB energy is emitted above $\sim$0.4 MeV, an energy at which the BATSE detectors were relatively insensitive. Thus a sufficiently sensitive "MeV γ-ray telescope" is needed in order to obtain the total bolometric luminosity of GRBs. A Compton telescope (see Sec. 1.1.2) might promptly localize GRBs to accuracies which are sufficient to allow sensitive ground-based multiwavelength counterpart searches.

More interestingly, a direct measurement of the properties of the prompt γ-emission is one of the few means available for probing the central engine in the electromagnetic regime, since all other emissions originate either after the burst or far from the site of the explosion. Recently (Ref. (30); see Fig. 1.4), the discovery of linear polarization in the prompt γ-ray emission from GRB021206 has been reported, and has been interpreted as a signature of synchrotron emission from relativistic electrons in a strong magnetic field. This result may be difficult to explain within the current GRB standard model.

1.1.2 Experimental matters

Broadly speaking, instrumentation for "modern" MeV γ-ray astrophysics should image γ-ray sources and measure their energy spectra; this is part a trivial definition and part a still-to-be-achieved goal. Pioneering γ-ray astrophysics in the sixties and early seventies was limited to the mere *detection* of celestial γ-rays and only after the launch of the Compton Observatory - CGRO (1991) the COMPTEL instrument provided the first good quality images of the sky in the MeV band.

MeV γ-ray spectroscopy is a time honored field and a very classic and ex-

---

[10] For a recent review of this fascinating and still largely mysterious phenomena, see Ref. (66).

[11] In the case of beamed emission the total energy released would be three orders of magnitude lower, $\sim 10^{51}$ erg.

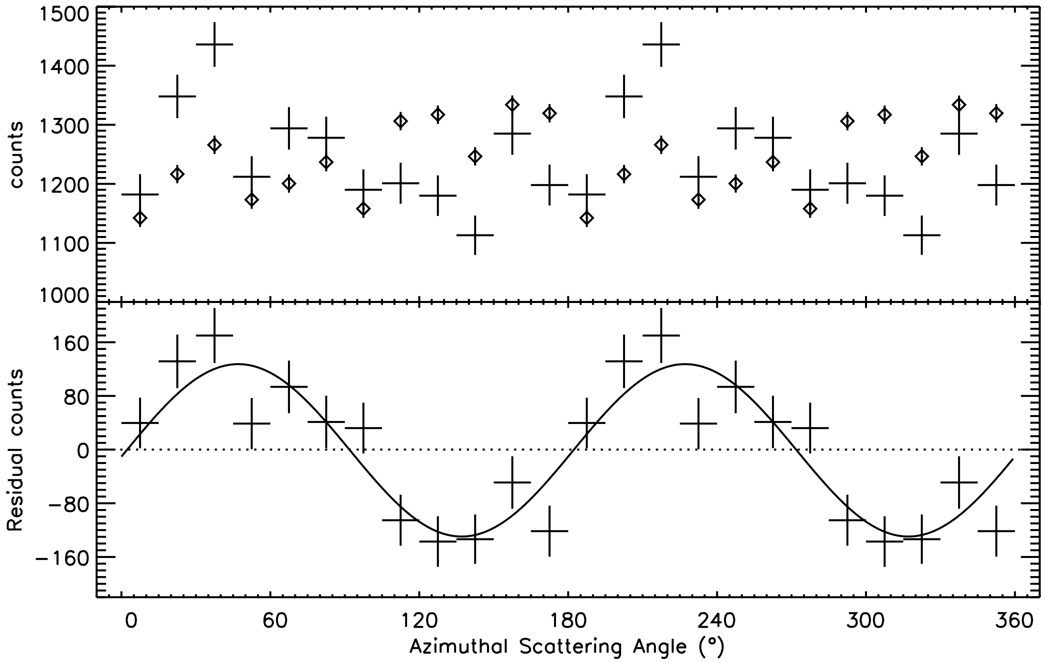

Figure 1.4: The azimuthal scatter distribution for the RHESSI data, corrected for spacecraft rotation. Counts were binned in 15° angular bins between 0°-180°, and plotted here twice for clarity. The top plot shows the raw measured distribution (crosses), as well as the simulated distribution for an unpolarized source (diamonds) as modelled with a Monte Carlo code, given the time-dependent incident flux. The bottom plot shows the RHESSI data with the simulated distribution subtracted. This residual is inconsistent with an unpolarized source (dashed line) at a confidence level $> 5.7\sigma$. The solid line is the best-fit modulation curve, corresponding to a linear polarization of $(80 \pm 20)\%$ (from Ref. (30)).

cellent reference textbook is Knoll (59). Ge detectors are still unchallenged in providing the highest energy resolution. When large volume ($\gtrsim$1000 cm^3) are needed, inorganic scintillators are often used. NaI has found the most widespread application, but newer materials (e.g. BGO) are rapidly gaining ground, with LaBr$_3$ (cerium doped) showing an energy resolution of 3% FWHM at 662 keV [12].

Imaging γ-ray sources is still an evolving experimental field. The main

---

[12] See for example http://wwwiso.iri.tudelft.nl/ISO_info/research/iso_006/info.htm

challenge is that no focusing optics exists so far [13] and MeV γ-rays have to be looked at as *particles*. With different levels of refinement, source imaging is pursued through passive or active collimators, rotating modulation collimators (RMC), coded apertures (with a signal modulation in the space domain), and Compton telescopes. The most advanced instruments are RHESSI, with time modulation of the signal and dedicated to solar physics, and INTEGRAL, using a coded aperture. The only example of a Compton telescope which produced valuable scientific results is the late COMPTEL. While it is commonly believed that collimators and coded apertures have been brought close to their optimum performance in the MeV range, and therefore substantial progresses will be extremely hard to achieve, Compton telescopes can still largely improve over COMPTEL.

Indipendently of the specific detection technique, the question is: What makes MeV γ-ray astronomy so peculiar [14] (and bad, considering the tiny number of sources detected so far)? There are at least four culprits:

1. low fluxes $\sim 10^{-3}\gamma\,\mathrm{cm}^{-2}\,\mathrm{s}^{-1}$for bright sources;
2. the atmosphere is opaque to γ-rays, so that observations must be performed on the top of the atmosphere and scientific balloons or satellites are required;
3. high background level: this will be discussed in detail in the present dissertation. It is clear that source imaging is powerful in separating background and foreground, and the difficulties in imaging MeV γ-rays are part of the background problem;
4. so far, a rather low detection efficiency. The interaction cross section of γ-rays in matter has a minimum in the MeV, but usually the detection efficiency is dramatically reduced by too stringent event selections.

Since nothing can be done to correct the low fluxes and the opacity of the atmosphere, experimentalists in MeV γ-ray astronomy work on instrumentation which can deliver the lowest possible background and the highest

---

[13] But see http://www.cesr.fr/~pvb/Claire/C_ho_e.html for recent developments.

[14] GRBs have different peculiarities: an extremely *intense* flux concentrated in a very short time, which makes the problem related to the high background level much less severe. This may suggest a different approach to the observation of the prompt γ-emission from a GRB.

possible efficiency. This dissertation is an example of such an activity. At this point it is fair to say that MeV γ-ray astronomy is *not* as advanced as most other fields in astronomy, and it is essentially due to the lack of reliable experimental observations. In the next session I am focusing on Compton telescopes, adhering to the paradigm that Compton telescopes are going to advance MeV γ-ray astronomy.

1.2 Compton telescopes

Sketchily, a Compton telescope (CT from now on) works in the following way: Starting from the Compton formula,

$$E'_\gamma \; = \; \frac{E_\gamma \cdot m_e c^2}{E_\gamma \cdot (1 - cos\bar{\varphi}) + m_e c^2} \tag{1.1}$$

(where E'_γ is the energy of the scattered γ-ray, E_γ the initial energy of the γ-ray, $\bar{\varphi}$ the scattering angle, m_e is the rest mass of the electron, c the speed of light) one obtains

$$\bar{\varphi} \; = \; arcos\left[1 - m_e c^2 \cdot \left(\frac{1}{E_\gamma - E_1} - \frac{1}{E_\gamma}\right)\right] \tag{1.2}$$

where E_1 is the energy loss in the Compton scatter, and $E'_\gamma \; = \; E_\gamma - E_1$. The initial direction of the γ-ray is then obtained combining the scatter angle, $\bar{\varphi}$, and the direction of the scattered γ-ray given by the spatial coordinates $(x_1,\ y_1,\ z_1)$ and $(x_2,\ y_2,\ z_2)$, the subscripts 1 and 2 indicating the first and second interaction of the γ-ray.

From the *detector* point of view only, and oversimplifying the complex problem of Compton imaging, a CT is a position sensitive spectrometer able to measure $(x_1,\ y_1,\ z_1,\ E_1)$ and $(x_2,\ y_2,\ z_2,\ E_\gamma - E_1)$ for each γ-ray. It is worthwhile stressing that the correct sequence of the two interactions must be known.

COMPTEL is the father of all Compton telescopes (and its scions are still in their infancy; more about this fatherly figure throughout this work) and deserves a presentation one bit more thorough.

COMPTEL is a double-scatter γ-ray telescope which uses liquid scintillator in the upper part and NaI crystals in the lower one; the two parts are separated by a distance of 1.5 m. γ-rays are detected with a first interaction in the upper detector (Compton scatter) followed by total absorption

Table 1.3: Specifications of the COMPTEL instrument (adapted from http://wwwgro.unh.edu/comptel/comptel_table.html). [a] event selections eventually reduce the the effective area to $\sim$5 cm^2; [b] the 3σ line sensitivity at 1.8 MeV was $\sim$1.6 10^{-5} γ cm^{-2} s with an effective observing time of 0.5 yr, as in Table 1.4.

1. Detectors:	
a. Detector type:	
1) upper detector D1	liquid scintillator NE 213A
2) lower detector D2	NaI(Tl)
b. Geometric arrangement:	
1) D1:	7 cylindrical modules 27.6 cm in diameter and 8.5 cm deep; total geometric area 4188 cm^2
2) D2:	14 cylindrical modules 28 cm in diameter and 7.5 cm deep; total geometric area 8620 cm^2
c. Effective area for γ-rays[a]:	20 - 50 cm^2 (no event selections applied to the data)
d. Energy range	0.8 - 30 MeV
e. Energy resolution	5% - 8% (FWHM)
f. Angular resolution	1.7°- 4.4°(FWHM)
g. Field-of-view	1 sr
h. Accuracy on Source Position	5 - 30 arcmin
2. Experimental Sensitivity[b]:	
a. Telescope Observations of a Point Source	
1) Minimum source detectability (3 σ) 1-30 MeV and 2-week observation	1.6 10^{-4} $\gamma\,$cm$^{-2}\,$s^{-1}
2) Line sensitivity (3 σ) 2-week observation	6 10^{-5} $\gamma\,$cm$^{-2}\,$s^{-1} at 1 MeV 1.5 10^{-5} $\gamma\,$cm$^{-2}\,$s^{-1} at 7 MeV
b. Burst Observations	
1) Telescope mode	lower limit: (>1 MeV) = 2 10^{-6} erg cm^{-2} upper limit: (>1 MeV) = 1 10^{-4} erg cm^{-2} (45 s duration)
2) Single detector burst mode variable, depending on duration	
3. Miscellaneous Instrument Specifications:	
a. Weight	1460 kg
b. Dimensions	2.61 m × 1.76 m diameter
c. Power	206 W
d. Telemetry Rate	6125 bit/s (equivalent time-average)
e. Timing accuracy	±1/8 msec with respect to UTC

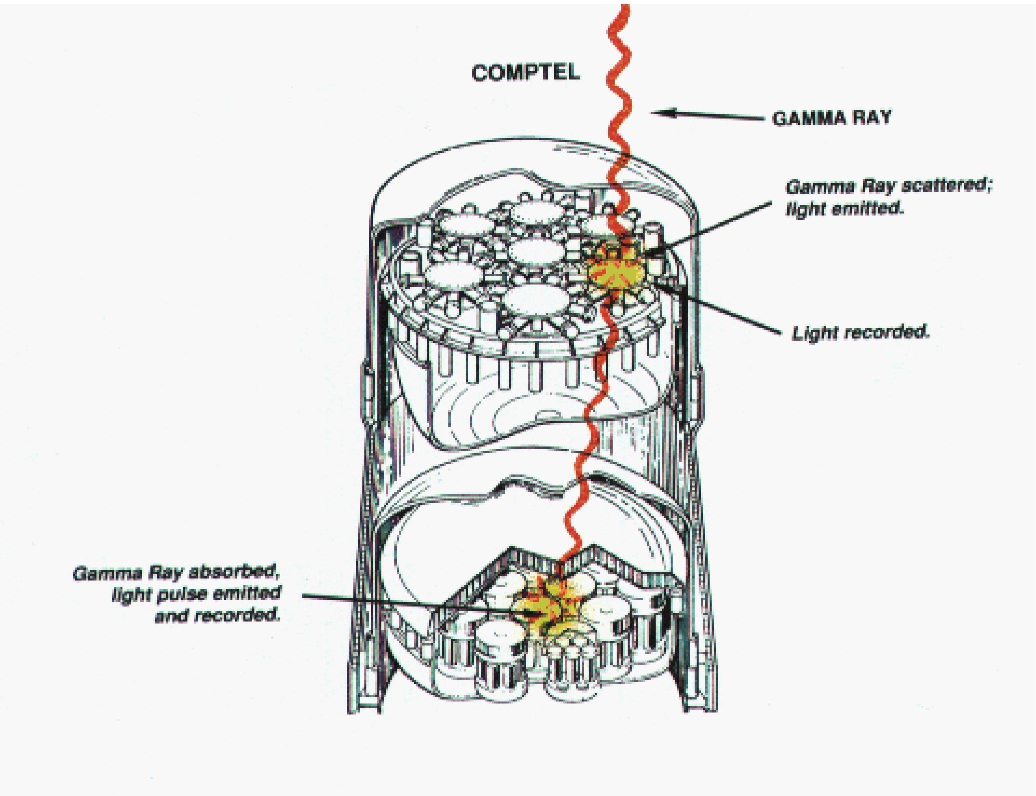

Figure 1.5: Schematic of the COMPTEL instrument.

in the lower detector. The total geometrical area of the upper detector exceeds 4000 cm^2. COMPTEL obtained, during laboratory calibration, an energy resolution of about 10% FWHM at 1 MeV, an effective area between 5-15 cm^2 in the energy range 1-10 MeV, which implies an efficiency well below 1%. The sequencing of Compton interactions was based on a *time of flight* measurement for the photon between the upper and the lower detector, which has been a widespread technique applied to various balloon borne CT's (see for example Refs. (51) and (82)). In flight the lower energy threshold for Compton imaging was 0.75 MeV, out of rate considerations. These figures give a broad idea of the state-of-the-art in MeV γ-ray astronomy. The double-scatter γ-ray telescope has been the one and only incarnation of a CT for many years.

An approach to CT rather different than COMPTEL has been proposed

	3σ Flux Limits [10^{-5} ph cm^{-2} s^{-1}]		
E_γ[MeV]	2 weeks in Phase 1	Phase 1+2+3	Phase 1+2+3+4 (Cycle-5)
0.75 – 1	20.1	7.4	3.7
1 – 3	16.8	5.5	3.8
3 – 10	7.3	2.8	1.7
10 – 30	2.8	1.0	0.8
1.157	6.2	2.0	1.6
1.809	6.6	2.2	1.6

Table 1.4: COMPTEL 3σ point source sensitivity limits (adapted from Ref. (84)).

some time ago (5), using a more compact homogeneous detector, specifically a liquid Xe time projection chamber (LXeTPC), in order to increase the efficiency and improve the background rejection capability well beyond the COMPTEL achievement. Part of this concept is not limited to the specific LXe technology, and several detector concepts for CT with compact structures and fine granularity have been proposed to date and are currently under development (e.g. Ref. (24)).

1.3 Liquid xenon detectors

Liquid xenon detectors (LXeDs) are part of the larger class of devices using liquefied rare gases, which includes liquid argon and liquid krypton detectors as well. The relevant properties of LAr, LXe and LKr are listed in Table 1.5.

Why is making radiation and particle detectors out of liquefied rare gases an attractive option? First of all, because they are dielectrics, which makes it possible to drift free charge (i.e. electrons) under the influence of a proper electric field, generating a detectable electronic signal. This property is trivial and is common to all the conceivable ionization detectors. More interestingly, free electrons can drift over large distances ($\gtrsim$1 m!) in properly purified noble liquids, without recombining. It is therefore possible to build big, massive and homogeneous detectors. Large masses (and volumes) are among the main requirements to study rare phenomena (from proton decay searches to neutrino detection to dark matter searches) and to efficiently stop high energy particles (calorimeters).

Table 1.5: Physical properties of noble liquids (adapted from Ref. (98)).

	LAr	LKr	LXe
Atomic Number Z	18	36	54
Atomic Weight A	39.95	83.8	131.3
Density (g/cc)	1.39	2.45	3.06
Melting Point T_m (K)	83.8	115.8	161.4
Boiling Point T_b (K)	87.3	119.8	165.1
Critical Temperature T_c (K)	150.7	209.5	289.7
Critical Pressure P_c (atm)	48.3	54.3	57.64
Critical Density (g/cc)	0.54	0.91	1.10
Volume Ratio (ρ_l/ρ_g)	784	641	519
Fano Factor	0.107	0.057	0.041
Drift Velocity (mm/μsec) @ 1(5) kV/cm	1.8(3.0)	2.4(4.0)	2.2(2.7)
Mobility (cm $V^{-1}s^{-1}$)	525	1800	2000
Radiation Length (cm)	14.3	4.76	2.77
(dE/dx) (MeV/cm)	2.11	3.45	3.89
Liquid Heat Capacity (cal/g-mole/K)	10.05	10.7	10.65
W-value (eV) (ionization)	23.3	18.6	15.6
W-value (eV) (scintillation)	19.5	15.5	14.7
Wavelength of Scintillation Light (nm)	130	150	175
Decay const.			
fast (ns)	6.5	2	2
slow (ns)	1100	85	30
Refractive index @ 170 nm	–	1.41	1.60
Dielectric constant	1.51	1.66	1.95

LAr is well established in calorimetry for high energy physics; the ATLAS ((18)) and D0 ((1)) sampling calorimeters are based on LAr technology. Arguably the most impressive technological achievement is the 600 tonnes LAr time projection chamber (TPC) built by the ICARUS [15] collaboration (but no science results yet, alas). An example of the spectacular 3D imaging capability provided by the ICARUS-LArTPC technology is shown in Fig. 1.6. LKr has been used for the electromagnetic calorimeter of the NA48 experiment ((44)).

LXe - all the most relevant here - has gained preeminence in diverse fields, despite being difficult to handle and expensive too. LXe is both a good scintillator and a good material for ionization detectors. Being a dense, high Z material, it also provides and excellent stopping power. It has been used and/or its future use is the focus of intense R&D in dark matter searches (20; 28; 11), neutrinoless double-β decay (36; 95) and MeV γ-ray astrophysics, which is the theme of this thesis.

1.4 Overview of the dissertation

The subject of the present dissertation is the liquid xenon γ-ray imaging telescope (LXeGRIT). LXeGRIT is the prototype of a novel concept of CT, based on a liquid xenon time projection chamber, developed through several years by Prof. Aprile and collaborators at Columbia. When I joined the collaboration in Spring 1999, LXeGRIT was getting ready for its third experiment at balloon altitude. While the first two experiments (1997) allowed one to address many issues related to changing a laboratory prototype into a working balloon borne instrument, the third experiment was designed to be the first focusing on the key measurement of the background at balloon altitude. After the 1999 balloon flight, a good deal of work was devoted to a thorough calibration of LXeGRIT, both through several tests in the laboratory and improving the analysis software and a dedicated Monte Carlo simulation. After substantial advancements in our understanding of the detector performance and after having fixed the problems encountered in 1999, LXeGRIT had its fourth (and last) balloon flight in Oct. 2000, which eventually allowed a detailed study of the background at balloon altitude and of the sensitivity to celestial γ-ray sources.

---

[15] http://pcnometh4.cern.ch/

As this dissertation is intended to show, “the LXeGRIT phase” - defined as the prototyping work, the experimental demonstration of the soundness of the entire concept, the measurement of the background and of the detection sensitivity - has been now successfully completed. And we are getting ready for the future.

The dissertation is subdivided in seven chapters plus an appendix:

1. Chapter 2 gives a detailed description of the LXeTPC, which is the core of the LXeGRIT instrument, and its performance.
2. Chapter 3 describes the complete calculation of the response of LXeGRIT to MeV γ-rays, combining experimental data and an extensive Monte Carlo simulation of the instrument.
3. In Chapter 4, the performance of LXeGRIT as a CT and its source imaging capability are presented.
4. The performance of LXeGRIT as a balloon borne instrument (year 2000) is described in Chapter 5.
5. The results from the crucial measurement of the background at balloon altitude are given in Chapter 6 .
6. Having measured the background and with a solid understanding of the detector response function, its *sensitivity* to celestial γ-ray sources is derived in Chapter 7.
7. In Chapter 8, I stack some possible future developments and more scattered considerations.
8. The main results from the 1999 balloon experiment are presented in the Appendix.

I have tried to make each chapter as stand-alone as possible, at the cost of some redundancy and repetition.

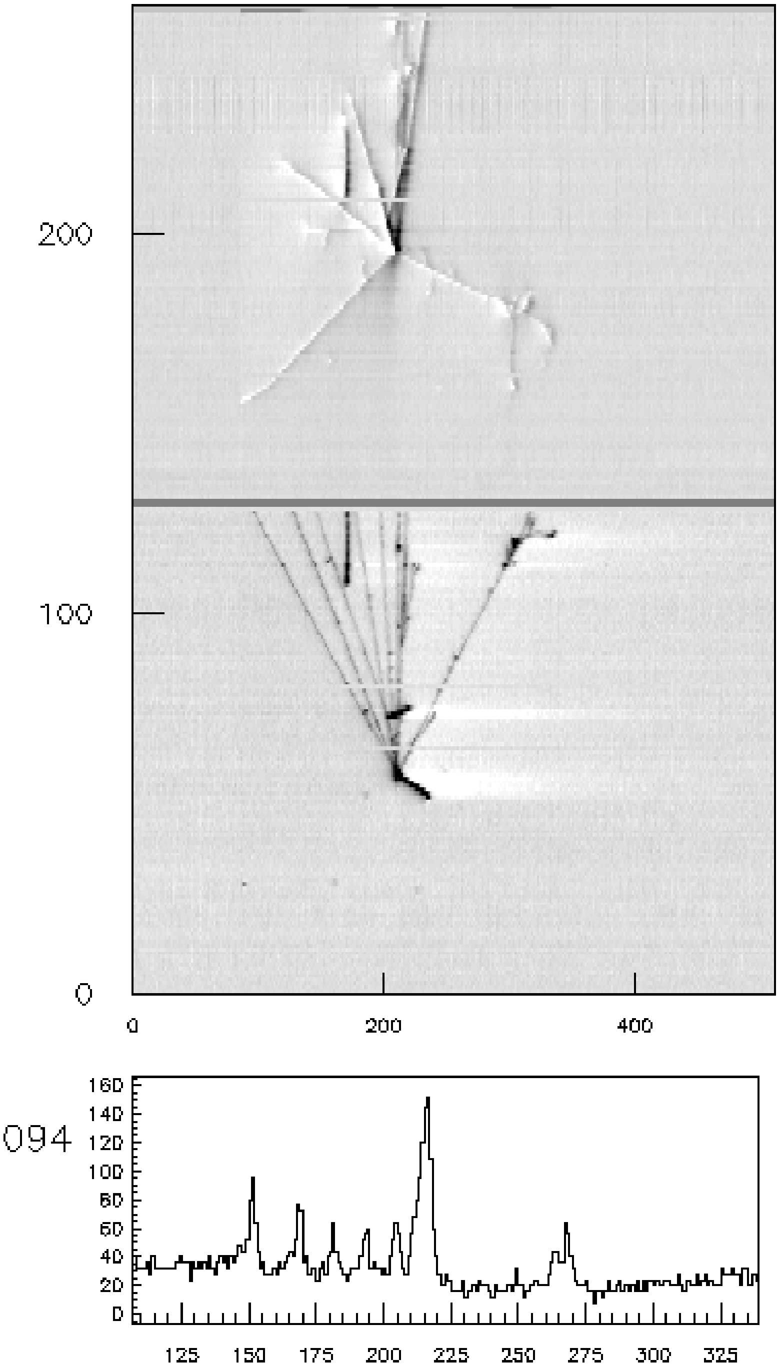

Figure 1.6: Deep-inelastic neutrino (ν_μ) interaction visualized with an ICARUS-like LArTPC (from Ref. (33)).

Chapter 2

LXeGRIT: description and performance

Introduction

LXeGRIT (Liquid Xenon Gamma-Ray Imaging Telescope) is the first working prototype of a Compton telescope (CT) markedly different from the standard "scatterer + absorber" CT, which had its most successful realization in the late COMPTEL on the CGRO satellite.

Working prototype means: *i.* with enough geometric area (>100 cm^2) and stopping power to detect celestial γ-ray sources; *ii.* fully tested as a γ-ray detector and imager; *iii.* fully integrated as a balloon borne instrument.

Markedly different means: based on a single detector, which acts as scatterer and absorber at the same time.

The idea that a fine grained imaging calorimeter could work as well as a CT was first proposed in Ref. (5), specifically discussing the case of a liquid Xe time projection chamber (LXeTPC). In making the case for this radically different CT concept, it was pointed out that a more compact homogeneous detector might increase the efficiency and improve the background rejection capability well beyond the COMPTEL achievement. Part of this concept is not limited to the specific LXe technology, and several detector concepts for CT with compact structures and fine granularity have been proposed to date (e.g. Ref. (24)).

LXe was proposed as active medium because: *i.* being a high density, high Z material, it guaranteed an excellent stopping power; *ii.* LXe is both an excellent scintillator and an excellent active medium for a ionization detector; *iii.* back then, due to its small *calculated* Fano factor, it was believed that LXe could provide high energy resolution (comparable to the resolution in Ge detectors). The promise of high energy resolution has not been fulfilled, and it is now well established that there are fundamental reasons which bar the energy resolution from reaching even the Poisson limit.

Developing the LXeTPC technology up to the point described here took several years - once a large volume LXeTPC had been developed and successfully tested in the “mild” laboratory environment, it was turned into a balloon borne instrument (LXeGRIT) able to work in the much more demanding and radiation harsh environment encountered at balloon altitude (40 km). The LXeGRIT instrument has been tested at balloon altitude four times (cfr. Ch. 5, Ch. 6 and Appendix A) - twice in 1997, mainly engineering balloon flights, in 1999 and in 2000 - the year 2000 flight, in particular, lasted 27 hours and provided a data sample large enough to address all the main technical issues, to give a thorough in-flight calibration and to study the background in the near space environment.

Being born as a laboratory prototype, the LXeGRIT instrument suffered from several shortcomings which would have been easily avoided in an instrument specifically designed for balloon applications, among them the relatively large amount of passive materials surrounding the active volume of the LXeTPC.

This chapter describes in a detailed manner the LXeTPC (Sec. 2.1) [1] and its laboratory performance (Sec. 2.2).

2.1 Description of the instrument

2.1.1 Mechanical structure

The core of the LXeGRIT instrument is a 18.6×18.6×7 cm^3 (2.4 l) volume, filled with ultra-pure LXe, which defines the *active volume* of the TPC. The LXeTPC mechanical design is shown in Fig. 2.1. It is delimited on top by the cathode, which is made out of alumina-998, a ceramic which combines good mechanical properties and dielectric strength. The cathode is coated on both sides with a 1 μm layer of a Ni-Mg-Al alloy. Above the cathode

---

[1] One main source for the description of the instrument has been Ref. (98); for the signal formation and the signal recognition and fitting procedure, Ref. (74).

there is a layer of LXe, about 5 mm thick (the precise thickness of it can vary slightly in different experiments and is difficult to monitor). 7 cm below the cathode, at the bottom of the fiducial volume, there is a shielding grid and below the shielding grid the non-destructive readout structure, i.e. two orthogonal wire planes (62 wires each, with a 3 mm pitch) and four separate anodes. The separation between the readout planes is 3 mm. The top view of the readout structure is shown in Fig. 2.2. On the sides, the fiducial volume is defined by the shaping rings, one per cm in the direction of the electric field, which guarantee a good uniformity of the electric field in the sensitive volume (Figs. 2.3 and 2.4). A description of the readout structure and signal formation is given in Secs. 2.1.4, 2.1.5. The TPC is mounted in a stainless steel cylindrical vessel, with a diameter of 35 cm and 11.5 cm high, with an internal volume of about 10 l. The walls of the vessel are 3 mm thick, and the top flange is 10 mm thick, thinned to 5 mm in the area covering the TPC. Between the anodes and the bottom flange there is a gap of 3 cm, thus we have we have 3.9 cm of passive LXe in between the bottom of the active volume and the bottom flange. To reduce the amount of LXe outside the active region, spacers made out of stainless steel were used on three sides, the fourth one housing the HV feedthrough (as visible in Fig. 2.4). The amount of LXe needed to fill the chamber is thus reduced by about 2 l. Four quartz windows are braced on the bottom flange to couple four UV photo-multiplier tubes (PMTs), visible in Fig. 2.2. Hermetic feedthroughs for signals and HV lines are also welded on this flange. Thermal insulation of the cold vessel is provided by a vacuum cryostat. The lower section of the cryostat encloses the four PMTs and HV circuitry. The cryostat is made out of stainless steel, has cylindrical shape, the walls are 3 mm thick while the top flange is 7 mm thick, thinned to 5 mm above the sensitive area. The diameter of the vacuum cryostat is 47.6 cm and the height is 36.1 cm. The total mass, including LXe, is about 190 kg.

2.1.2 Cryogenic system

High purity Xe is liquefied into the vessel by a controlled flow of liquid nitrogen (LN_2) through the copper coil of the condenser on top of the detector (the “cooling tower”, shown in Fig. 2.1). The filling procedure takes about 5 hours, which corresponds to a flow rate (gas phase) of about 15 l/min. The temperature of LXe is about -95°C at 1.5 atm. Once the LXe is inside the vessel, the temperature is maintained by controlling the pressure above the

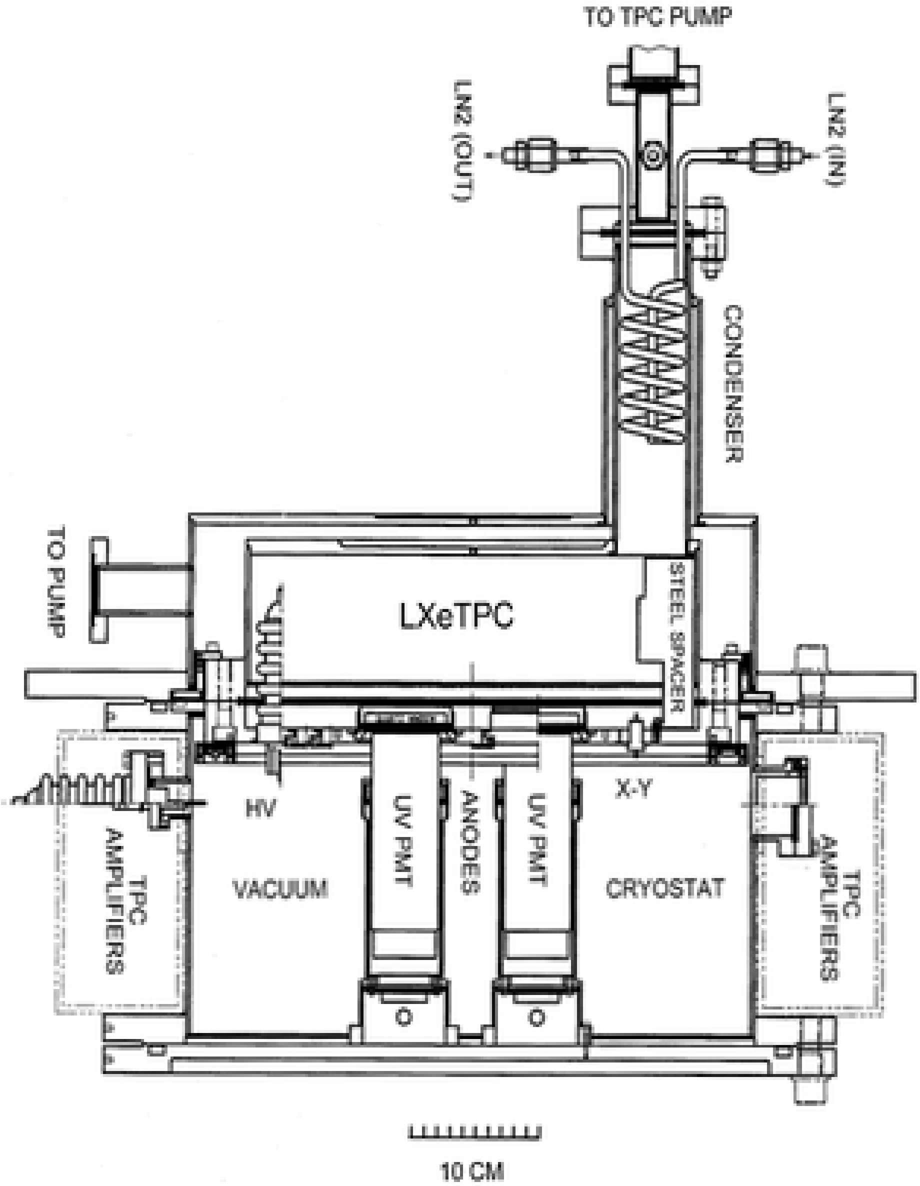

Figure 2.1: The LXeTPC mechanical design.

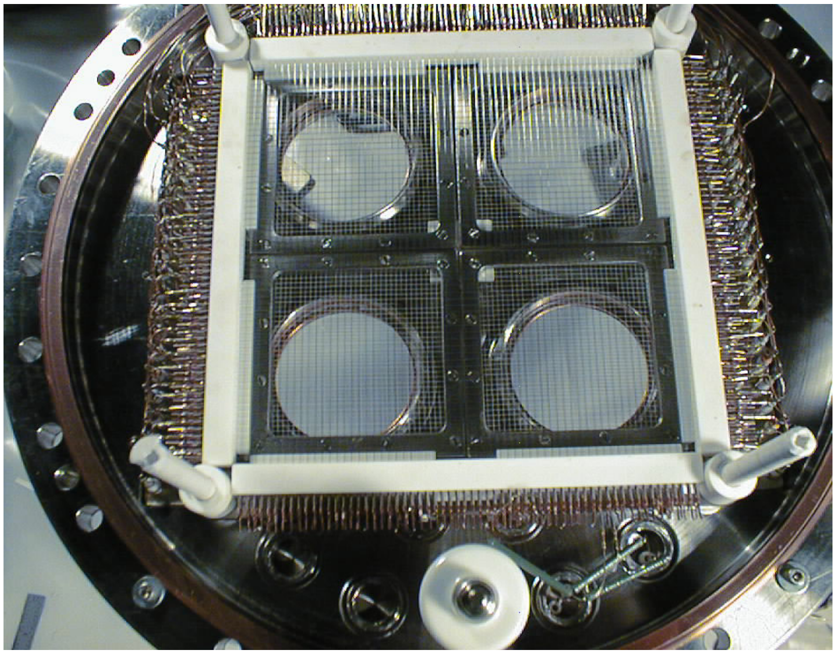

Figure 2.2: Top view of the LXeTPC readout structure. Four windows in the bottom flange, for light transmission to four PMTs, are visible below the readout structure.

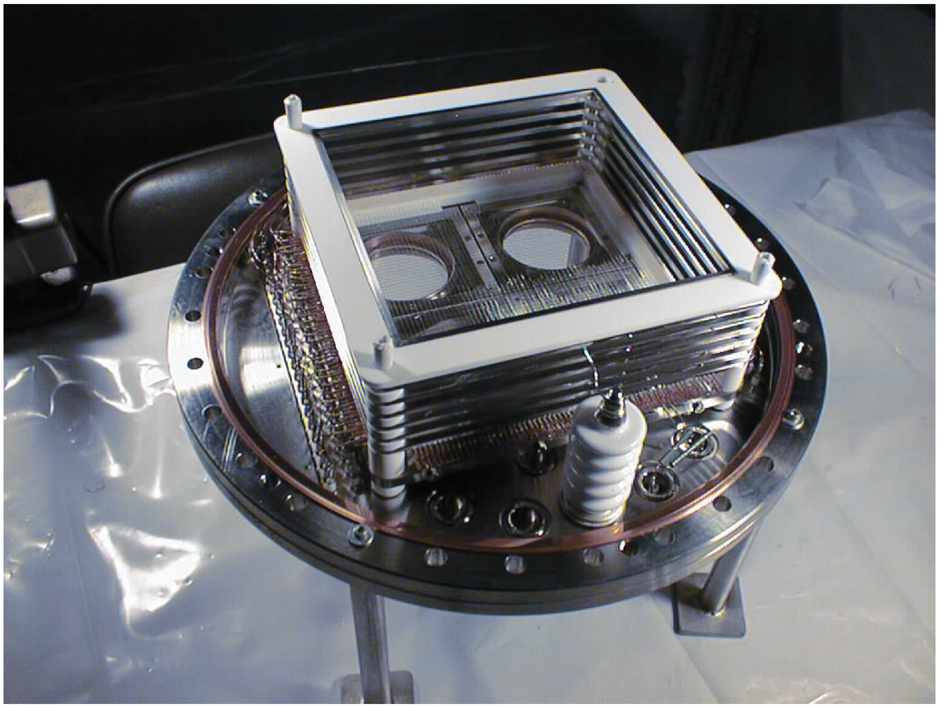

Figure 2.3: Top view of the LXeTPC with the field-shaping rings. The ceramic HV feedthrough is visible in the lower part of the picture.

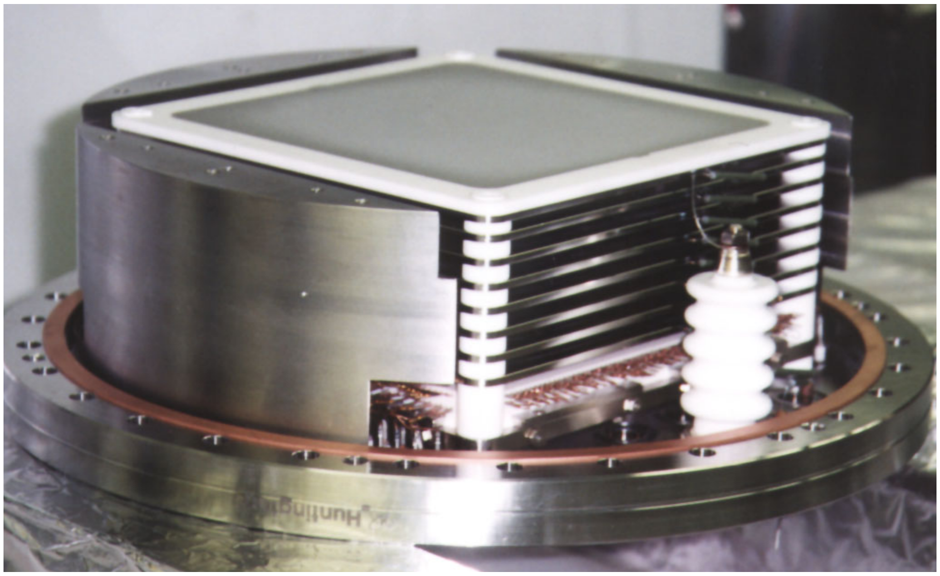

Figure 2.4: The LXeTPC completely assembled; on top, the cathode. On three sides, stainless steel spacers; on the side, the HV feedthrough.

liquid with a flow of LN_2 gas through the condenser. Since the LN_2 cooling produces microphonic noise, the vapor pressure is allowed to build up from (typically) 1.4 and 2.4 atm; at this point a solenoid valve opens to start the flow of LN_2 and it closes once the pressure reaches again 1.4 atm. An example of such a cycle is shown in Fig. 2.5, as pressure of Xe vapor vs. time.

2.1.3 LXe purification

It is well known that for detectors with a large drift region, like LXeGRIT, the Xe purity plays a major role in determining the charge yield and thus the spectral response. The most common electro-negative impurities dissolved in LXe which affect the drift of free electron are O_2, H_2O, CO, CO_2 and N_2O. The level of contamination must be kept lower than 1 ppb O_2 equivalent. To do so, an efficient purification system capable of purifying several liters of LXe was developed. The Xe gas purification and handling system for the LXeTPC was built based on the system used for a 3.5 liter gridded ionization chamber, fully discussed in Refs. (12) and (98). Two gas storage cylinders, each with a volume of four gallons, are used to store LXe up to ∼30 liters.

LXe is purified through two purifiers: *i.* an Oxisorb, which removes impu-

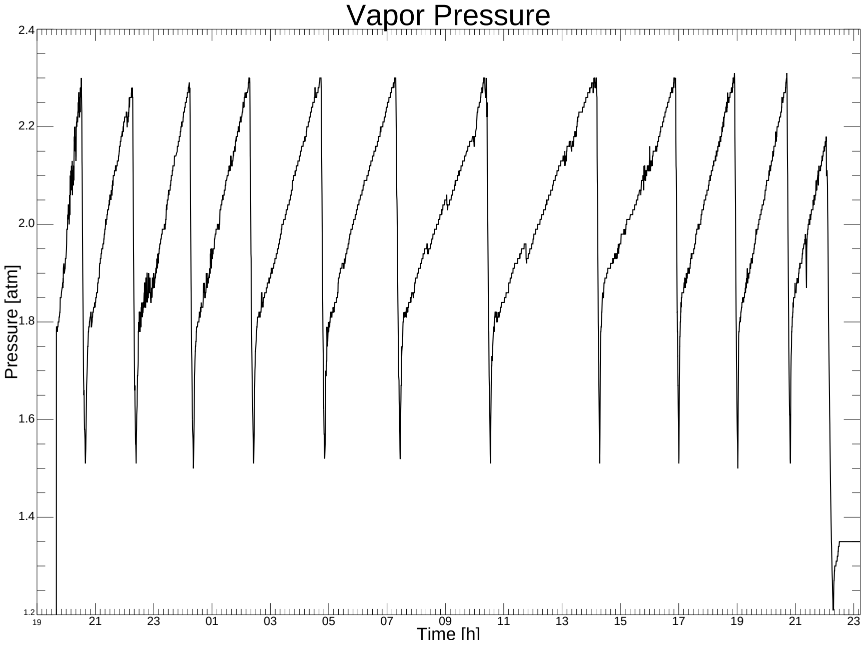

Figure 2.5: Pressure of Xe vapor vs. time in the LXeTPC during a 27 hr balloon flight. The pressure was allowed to build up from 1.5 to 2.3 atm. The duration of each cycle varies between less than 2 hr to more than 3 hr, depending on the external temperature.

rities by chemioabsorption and is effective in reducing O_2 to less than 0.1 ppb and H_2O to less than 0.5 ppb (as can be derived from the measurement presented in Sec. 2.2.1); *ii.* a high temperature getter [2], which consists of an alloy of Zr-V-Fe as active material and removes impurities (H_2O, H_2, O_2, N_2, NH_3, CO, CO_2 and hydrocarbons) by forming complex compounds at temperatures of several hundreds Celsius. The system has a self-enclosed gas flow cycle, thereby allowing purification of Xe gas between the storage cylinders without passing through the detector.

2.1.4 Drift field and readout structure

The drift region is 7 cm in the field direction, bounded by the cathode on top and the shielding grid below. The cathode is placed on top of a metal ring, with the aluminum coating touching the ring, thus forming a "cusp-shaped" cathode. The high voltage is applied to the cathode through the metal ring; soldering is avoided because it can be troublesome for the LXe purity. The high voltage is distributed to seven field-shaping rings mounted around the sensitive volume through a resistive divider chain, with 2 GΩ resistors between two consecutive rings. The field-shaping rings guarantee the uniformity of the field in the drift region. The TPC was typically operated with a field of 1 kV/cm.

A γ-ray interaction deposits an initial charge of $Q_0 = \Delta E / W_{\mathrm{LXe}}$ in the liquid, which is 6400 e^-/100 keV for $W_{\mathrm{LXe}} = 15.6$ eV (67). Typically, 83% of this charge escapes immediate recombination at the operating field of 1 kV/cm (60). The charge cloud generated by ~1 MeV energy deposits can be considered point-like, given its small extent of ~ 0.5 mm and negligible diffusion in the liquid (87). In a uniform field of 1 kV/cm the drift speed is ~2 mm/μs (99).

The electric field is doubled in the region below the grid, to focus the drifting electrons through the mesh and a structure of 2×62 x- and y-wires. The wire pitch is 3 mm and grid, wire layers, and anodes are all separated by 3 mm from each other. The grid and $x - y$ wire planes are assembled with stainless steel wires of 100 μm diameter, stretched on four MACOR bars fixed on a stainless steel frame. The four anodes are made of nickel meshes [3] sandwiched between stainless steel rings, are mounted to the same holder

---

[2] SAES MonoTorr Phase II.

[3] Solid anodes are not an option because they must be transparent to the LXe scintil-

as the wires and are kept isolated by a MACOR spacer.

No signal is seen before the charge cloud passes the grid at time 'a'. The drifting electrons subsequently induce a linearly increasing charge on the x-wire until they reach the x-plane at time 'b'. The x-signal decreases at the same rate back to zero, as the charge moves toward the y-wire plane, which it reaches at time 'c'. The rise and fall times of the triangular wire signals are therefore given by the drift time between the grid, wire, and anode planes, respectively. The anode signal starts to rise only at time 'c', until the charge is collected at time 'd'. The pulse height of this "step" is proportional to the energy deposit.

2.1.5 Signal readout

Wire and anode signal shapes in the LXeTPC were simulated to optimize the electronics design and electric potential settings. The simulation uses the GARFIELD package (45) to compute the signal shapes, including rise and decay times of the preamplifier circuit. Fig. 2.7 shows the induced signals on x- and y-wires for various lateral distances of the charge cloud with respect to the sensing wire. The charge is always seen on at least the two neighboring wires, with a relative weighting depending on its location in between. Wires farther away see a much reduced signal, which is usually not measured for signals of $\lesssim$ 1 MeV, but becomes apparent at higher energies. In Fig. 2.8a, the corresponding anode signals are overlaid with the wire signals. Electronic shaping on the anodes was modeled with 2.0 μs rise time and 50 μs decay time. Fig. 2.8b shows *measured* anode and wire signals as a function of drift time for a γ-ray energy deposit of 1.8 MeV, with a fit to the anode signal superimposed. The amplitudes of anode and wire signals are gain-corrected and normalized to the fitted amplitude of the anode. Three wires show signals on each view. The signal of the middle wire is plotted in black, the others in gray. The maximum amplitudes of the wire signals are at a level of 20% - 30% of the fitted anode amplitude (which is somewhat larger than the maximum of the anode waveform, due to signal shaping).

The electronic noise for each wire was measured to be $\sim$ 450 e^- equivalent noise charge (ENC), with a charge signal of $\sim$ 940 $e^-/100$ keV, corresponding to a signal/noise ratio of 3σ at 150 keV. The charge signal on the anodes is $\sim$ 5000 $e^-/100$ keV. Under measured noise conditions of $\sim$1000 e^- rms, the

---

lation light.

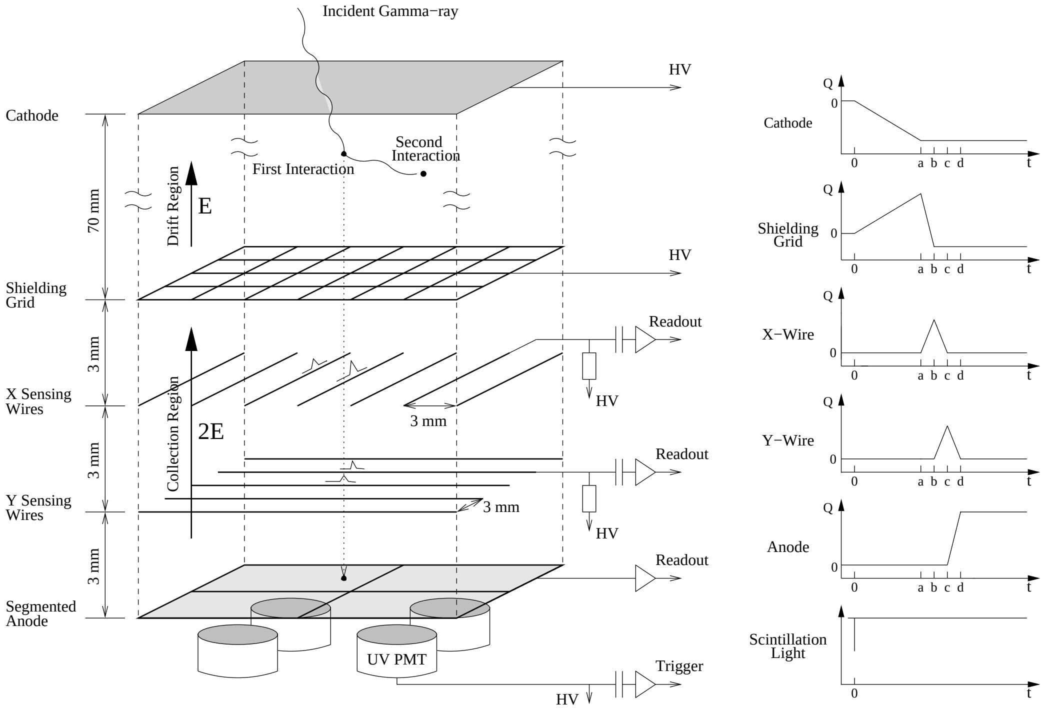

Figure 2.6: Schematic of the LXeTPC read-out structure with corresponding light trigger and charge signals (from (98) and (74)).

detection efficiency for energy deposits of $\sim$ 100 keVis near 100%.

The display of a *raw event* is shown in Fig. 2.9. It consists of the FADC pulse height signals of 62 x-wires, 62 y-wires and 2 anodes, out of 4, where a signal has been detected, all of them plotted vs. drift time, which constitutes the z-axis. The size of such an event is $\sim$30 kB. The more usual data-taking mode transfers only wire waveforms which crossed preset thresholds together with the four anode waveforms. For typical settings, the average event-size is $\sim$5 kB.

2.1.6 Data acquisition

This section is adapted from Ref. (10).

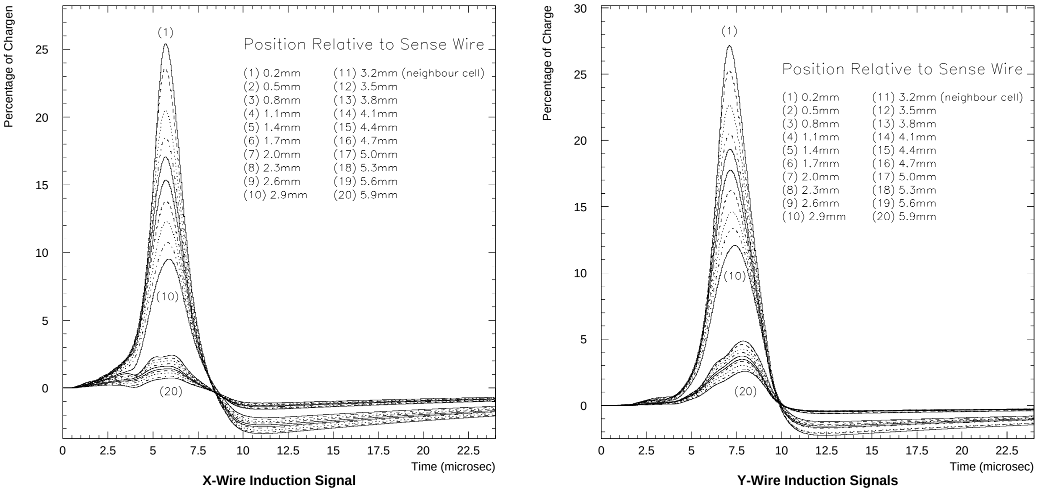

Figure 2.7: Simulated induction signals on x- and y-wires for different distances from the sensing wire. Graphs 1-10 are for positions between one wire and its neighboring wire, while graphs 11-20 are for positions beyond the neighboring wire (from Ref. (98)).

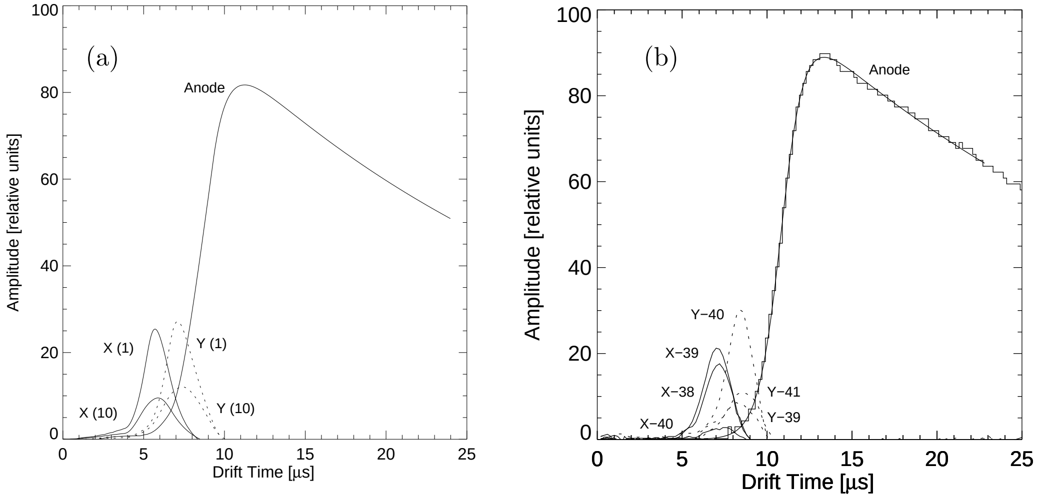

Figure 2.8: (a) Simulated collection signal on an anode compared to induction signals at a perpendicular distance of 0.2 mm (1) and 2.9 mm (10) (from Ref. (98)). (b) Measured anode and wire signals as a function of drift time for a γ-ray energy deposit of 1.8 MeV. A fit to the anode signal is over plotted. The amplitudes of anode and wire signals are gain-corrected and normalized to the fitted amplitude of the anode (from Ref. (74)).

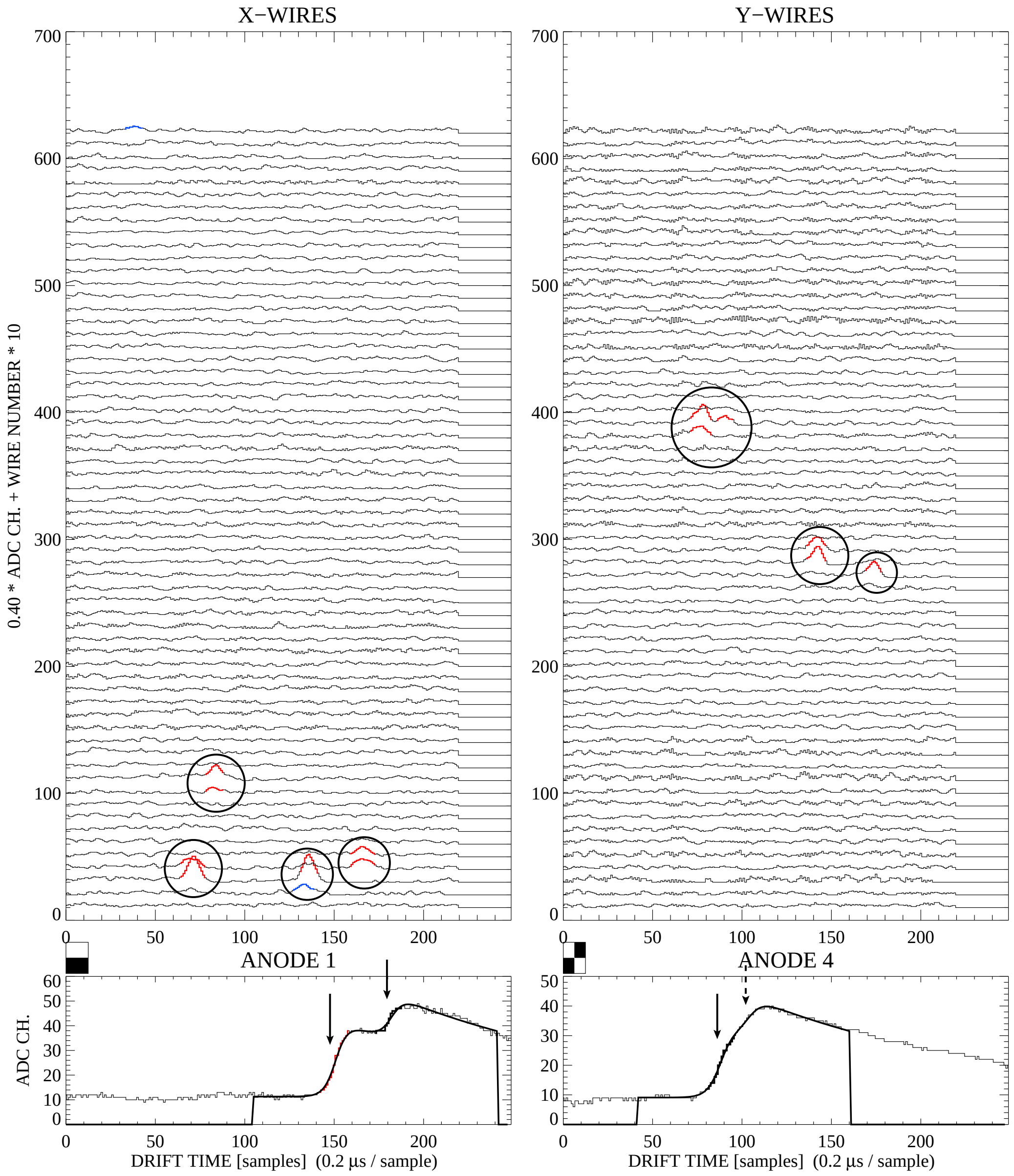

Figure 2.9: Digitized waveforms on wires and active anodes as a function of drift time in FADC samples, for an ^{88}Y 1836 keV γ-ray event with 4 interactions. The upper panels show all wire waveforms, in scaled units of ADC channels, each separated by an offset. Matched wire signals are indicated by circles, and only their corresponding anodes are shown. The wire-anode correspondence is indicated by the dark fields at the top left corner of each anode display. The solid arrows mark three steps found by the anode signal algorithm, and the dashed arrow marks an additional step, included in the fit (smooth solid line) after signal recognition on the wires (from Ref. (74)).

System Hardware

The front-end electronics [4] converts the charge signals from the 124 induction wires (62 x- and 62 y-wires) and the 4 anodes into voltage pulses. Each channel has a charge sensitive preamplifier, which drives the twisted pair line to the digitizer system. The digitizers convert the analog signals into a digital history of the ionizing event. The FADC system consists of 17 printed circuit boards housed in a standard VME-crate: 16 Gamma-Ray (x-y) Induction Signal Processor (GRISP) boards with 8 channels each to handle the 124 wire signals, and one Gamma-Ray Anode Signal Processor (GRASP) board to handle the 4 anode signals.

The x-y wire signals are digitized with 8 bit precision at a rate of 5 MHz. The information is stored in a dual port random access memory (DRAM). The depth of this buffer is 256 samples, corresponding to 51.2 μs, which covers the maximum drift time in the TPC of about 40 μs for a drift velocity of $\sim$ 2 mm/μs. The charge collection signals from the 4 anode channels are digitized at the same rate with 10 bit precision, for better energy determination with a large dynamic range.

For each channel, the digital signal is passed through a comparator to record the sample number when a software-set threshold is exceeded. The recording of the threshold crossing point facilitates locating useful information and can be used to reduce the data amount and to accelerate the data read-out process. Each GRISP board with at least one channel above threshold issues a signal that sets a flag in a 16 bit register, which was located on the microprocessor board in the original design, and is now located on a separate board ("latch card") within the crate.

The GRASP board can send 3 different interrupt requests to the processor: STARTADC and SAVEDATA signal the start and the completion of event digitizing, while FLUSHDATA signals that the process was interrupted by a second trigger, the system aborted the data recording, and is ready to accept a new event. In the new design, these interrupts are registered on the "latch card" mentioned above and read out by the external processor. The GRASP board can also start an event digitizing process on command from the read-out processor, independent of an external trigger. These test triggers are used to determine baselines and noise conditions on anodes and wires.

The front-end and FADC system of the LXeGRIT instrument has re-

---

[4] More details about the front-end and FADC system of the LXeGRIT instrument can be found in Ref. (6)

mained unchanged from the original design, with the exception of the trigger electronics. The circuitry amplifying and discriminating the signals from the 4 UV-sensitive photomultiplier tubes, originally on the GRASP board, has been replaced by new electronics. Event recording is now triggered by a fast TTL pulse signaling the start of the event. The recording is pre-triggered, but will be stopped if a second trigger pulse signals the occurrence of a second event within 40 μs, while the charges of the first event are still drifting in the sensitive volume of the TPC. In this case, both events are rejected.

Read-out processor

Since the connections to the GRISP/GRASP boards followed the VME standard to a large extent, it was natural to choose a VME processor board. The final choice was a Motorola MVME 2700 coupled to a communication interface MVME761 Transition Module. Not all connections in a standard VME bus are used by the GRISP/GRASP FADC system, and some bus lines were assigned a different meaning. The processor could therefore not be housed in the same crate. It is located instead in a separate box, together with the communication board.

An interface board was developed to buffer the data and address lines, and also to emulate the correct timing of the handshake signals for data transfer. This is necessary to adapt the synchronous read and write cycles of the FADC memories to the inherent asynchronous operation of a standard VME bus. During data acquisition most of the operations on the bus are read cycles from the FADC memories. These cycles were therefore kept as short as possible (250 ns) to obtain the required data transmission rate.

Most of the data words to be read from the GRISP/GRASP boards are digitized waveforms, which are stored in consecutive locations in memory. Block transfers are thus a natural choice to increase data throughput compared to single reads. Initial tests with block transfers, however, revealed that the processor board does not keep the address lines stable during the full transfer, as this is not required by the VME standard. The address lines had therefore to be latched with each address strobe to achieve the higher transfer rate.

The FADC system interface board is connected to the VME port of the processor via the VME Junction. This circuit buffers the lines and allows for the connection of additional instruments to the VME bus. Presently there is one such instrument, the trigger logic system.

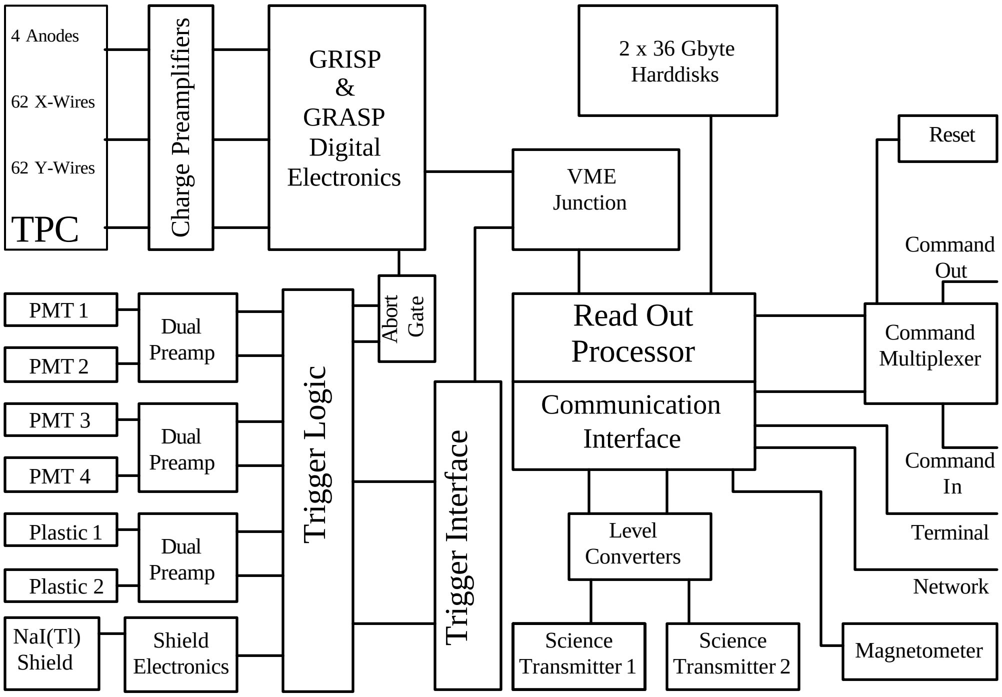

Figure 2.10: Diagram of the interconnections of the LXeGRIT read-out electronics. From Ref. (10).

After processing the data, the processor can either send the events via two fast serial ports to the science data transmitters, or via the SCSI port to two 36 GB hard disks for storage on board (two 9 GB disks in the 1999 flight). Although the data can be stored on disk much faster than transmitted to ground via telemetry, the data might be lost in case of a bad landing. To guarantee a good sample of science data even in this case and to allow online control of the data acquisition and thus the tuning of data taking parameters, a subset of the acquired events is transferred to the two fast serial ports. After level conversion, the data are sent by two transmitters to ground, with a throughput of 2×500 kbits/s. The rate could be increased by about a factor of two, but the analog tape drives of the National Scientific Balloon Facility (NSBF), providing a backup copy of the science data, are not designed for such high rates.

Other connections to the processors are: the magnetometer and tiltmeter which provide directional information of the LXeGRIT instrument via a slow serial port; a terminal and an Ethernet connection used for operation support while the payload is in the laboratory. During the flight, the processor is controlled by 16 bit command words received via the Consolidated Instrumentation Package (CIP), the standard NSBF package to control instruments during balloon flights. The commands are provided to the parallel port of the processor via the command multiplexer, which formats the 16 bit word into 2 bytes to be read consecutively. The interconnections of the LXeGRIT read-out electronics are shown schematically in Fig. 2.10.

System performance

The upgraded DAQ system has proven reliable during two flights in 1999 and 2000. For the 2000 flight, the development of an interface that allows block transfers using the on-board DMA (direct memory access) controller for reading of event data from the digitizer electronics, as well as optimization of event selection criteria, has accelerated the DAQ by a factor of about 2.5 with respect to the 1999 flight read-out. The data flow is now mainly limited by the digitizer, which requires ~ 1 μs per single byte access or ~ 600 ns using block transfers. This sets a limit on the total throughput of about 1.6 MB/s, restricting the event building rate to 40 - 50 events/s in “full-image” mode, in which the complete digitized waveforms from all channels are to be read out, amounting to about 30 kB per event. Standard data taking mode transfers only waveforms that crossed preset thresholds, plus the four anode waveforms, and only for those events that fulfill a potential Compton scattering topology, i.e., where the number of wire hits and therefore the number of γ-ray interactions is within a preset range. In this mode, the event build rate increases to 200-400 Hz. The actual value strongly depends on the selection parameters and on the light trigger configuration, which also determine the average event size. For typical settings, the average event size is 4.5-6.5 kB.

The throughput is sufficient to fill the two 500 kbps serial down-links, corresponding to about 2 full-image events/s per down-link, or about 10-15 events/s in standard mode. The large bandwidth of disk writing, however, is frequently not filled in standard mode, as event selections discard many unwanted events in order to maximize the total number of triggers that can be served by the system. During the October 2000 flight (see Ch. 5 and Ch. 6), the system was able to handle about 300-350 triggers/s out of a trigger rate of about 650 Hz, which included charged particles since no plastic veto counters were used. About 20% of the handled triggers were typically accepted as valid events, resulting in a data throughput in the range of 0.4-0.5 MB/s sent via the transmitters and written to disk. In laboratory conditions with calibration sources, where the ratio of accepted events is higher, this rate can become up to three times as large.

The data acquisition system is now optimized to the point where the main bottleneck, the read-out of the digital electronics by the DAQ processor, cannot be further improved very significantly.

2.1.7 Event trigger

Trigger logic

As a pre-triggered digitizer system, the GRISP/GRASP boards requires a fast signal to start recording an event. This signal is derived from the fast xenon scintillation light detected by four UV-sensitive PMTs, which view the sensitive volume of the TPC through quartz windows. Originally, the system was triggered on a logical OR of the four PMT signals, above a given threshold. The trigger was then vetoed with the signal from plastic counter(s) above and from the NaI(Tl) shield sections around and below the LXeTPC (see Appendix A). Timed gates removed double triggers. This system was insufficient, mainly because no record was kept of the various signal rates, only the four single PMT rates were stored together with other housekeeping information. Since events can produce a signal on more than one PMT, and triggers can be vetoed or rejected as double events, the information was not sufficient for a rate calculation. Separate trigger electronics were therefore custom built, providing the FADC system with a TTL pulse to start the read-out.

After amplification, the signals from the 4 PMTs are passed through 4 window discriminators. The lower threshold of the window rejects noise pulses and can also be used to introduce an energy bias by requiring a minimum energy deposited in the TPC. The reason for the upper threshold, which is optional, was to discriminate against charged particle tracks. A charged particle deposits about 3.9 MeV/cm in liquid xenon, i.e., a total energy well in excess of the typical gamma-ray energies of interest for observations of cosmic sources during the flights. The OR of the PMT signals still generates the trigger for the FADC system, unless it is vetoed or it is preceded by a PMT signal above the lower discriminator threshold in the previous 40 μs (double or multiple events). A veto signal is generated by the OR of plastic and NaI(Tl) scintillators, used to reject cosmic rays, and γ-rays entering the TPC from the side or from below. For the 2000 flight, all shields were removed, thus no PMT signals were vetoed. In case of multiple events, an ABORT signal is issued to stop the FADC recording of the first trigger. Since the FADC system does not have a separate input for the ABORT signal, event recording can only be stopped by a second trigger-like signal. If, however, a first PMT-OR signal did not result in a trigger signal, either because it was vetoed or because the signal surpassed the upper discriminator threshold, the occurrence of a subsequent ABORT signal would in fact trigger the digitizer system. An ABORT gate was therefore introduced to filter out all ABORT signals not preceded by a trigger.

A set of 16 counters, automatically reset once every second, register all signals at various locations of the trigger logic, providing the means to calculate the flux of events and the rejection rates. The rates from the counters are also a very good monitor of the trigger system. The trigger electronics unit is connected to the VME bus of the read-out processor via an interface. Thus, the processor can read the 16 counters, set the window discriminator thresholds, and set the operation mode. Different operation modes can be enabled: the veto signals can be switched on and off, the upper level of the window discriminators can be turned off, and the veto can be replaced by a coincidence, effectively triggering on charged particle tracks for debugging purposes, or to study the spatial resolution of the detector in the laboratory.

First Level Trigger - FLT

The FLT is provided by a light signal from the TPC. LXe is well known as an excellent scintillator, emitting in the UV (175 nm) with a light yield similar to NaI scintillators but a faster response ($\sim$5 ns). Four PMTs (2 inch Electron Tubes 9813QA), with quantum efficiency about 15% at 175 nm, detect the scintillation light produced by particles interacting in the fiducial volume. Each PMT sees the LXe volume through a 2.4 inch diameter quartz window with good transparency in the UV. A few millimeter gap separates the quartz window from the corresponding PMT. This gap was envisaged in order to prevent mechanical stress from damaging the system in case of brusque taking off and landing, which happen all but too often for balloon flights. It is anyway clear that this arrangement allows only a far from optimal optical coupling and reduces the final light yield.

The bottom of the fiducial volume and the quartz windows are separated by a 3 cm thick layer of LXe plus the collection region, about 1 cm thick (Fig 2.11). This relatively large (almost 60% of the fiducial region thickness) separation induces a twofold negative effect in the performance of the light trigger system. On one side it reduces the solid angle for events in the active region, and consequently the light yield; on the other side, interactions in the insensitive LXe layer can trigger the detector without any corresponding charge signal. Such events are then rejected at the second level of trigger, yet keeping the DAQ busy. The importance of this category of "false triggers" heavily depends on the source rate and position and, most likely, is rather small in the usual laboratory conditions.

Rather detailed calculations of the light yield have been performed and for that the reader is referred to Ref. (13). To make a long story short, several photo-electrons (p.e.) are expected for every MeV of energy deposited in the fiducial volume [5]. The average energy required to produce a UV scintillation photon in LXe (W_{light}) is 23.7 eV, which implies that about 4×10^4 UV scintillation photons per MeV of deposited energy are expected in LXe. Since only a small number of p.e. is then detected, the efficiency of the conversion of UV photons into p.e. is at the level of $\sim10^{-4}$ p.e./UV-photon. Even with this low efficiency, which does not allow any energy resolution, the light trigger efficiency can be saturated, at least for energies above 1 MeV, as shown in Ref. (73) and Sec. 3.3.3.

---

[5] Because of solid angle effect and other inhomogeneities in the light yield over the fiducial volume, the expected number of p.e./MeV is better described by a broad distribution.

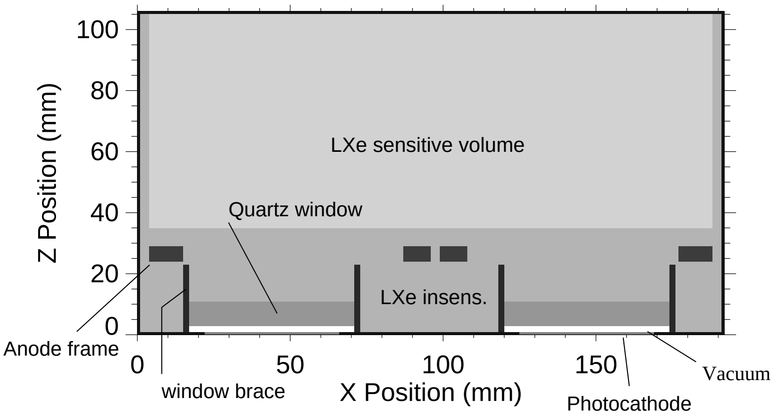

Figure 2.11: Schematics of the light readout as seen in the x-z plane. From Ref. (13).

We will see in Ch. 3 that other considerations may suggest that a lower trigger efficiency is more appropriate.

Once signals from the PMTs have been amplified, they are passed through four window discriminators. At this point the OR of the PMT signals generates the trigger for the FADC system, unless vetoed.

Second Level Trigger - SLT [6]

Wire and anode signals are also exploited to perform on-line checks. We call these checks second level trigger and they fall into two main categories:

1. A requirement of a minimum and a maximum number of wire hits on each view (x and y separately), i.e., wire signals above thresholds recognized in hardware is imposed;
2. a minimum signal amplitude above initial baseline for at least one anode is required.

The importance of 1 and 2 is rather different. Imposing a threshold on the anode waveform is very effective in rejecting low energy events which are useless for a CT, but it requires to previously readout the digitized waveforms

---

[6] Results are presented in Sec. 3.3.3

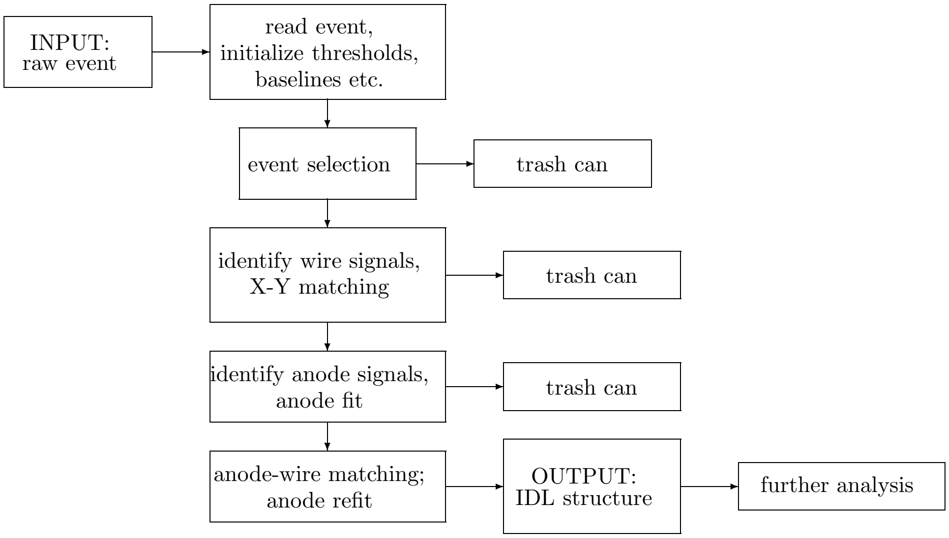

Figure 2.12: Block diagram of the signal recognition algorithm described in Sec. 2.1.8; see text for a thorough explanation.

and the slowness of this process greatly reduces the usefulness of such an on-line selection. It has been mainly used during laboratory calibrations, when efficiency is not a real concern, in order to save disk space. Checking the number of wire hits is, on the other side, relatively fast and is sensitive to specific event multiplicities. This option is relevant for a CT, since Compton imaging requires at least two, but preferably three, interactions (Compton scatter followed by photoabsorption). In practice this criterion is not as sharp as one could imagine (hope), because of electronic noise on the wires.

2.1.8 The signal recognition and fitting procedure

The analysis package is based on the Interactive Data Language (IDL) from Research Systems Inc. (53), which is a high level language well suited for building complex analysis packages. The analysis procedure is sketched in the block diagram shown in Fig. 2.12.

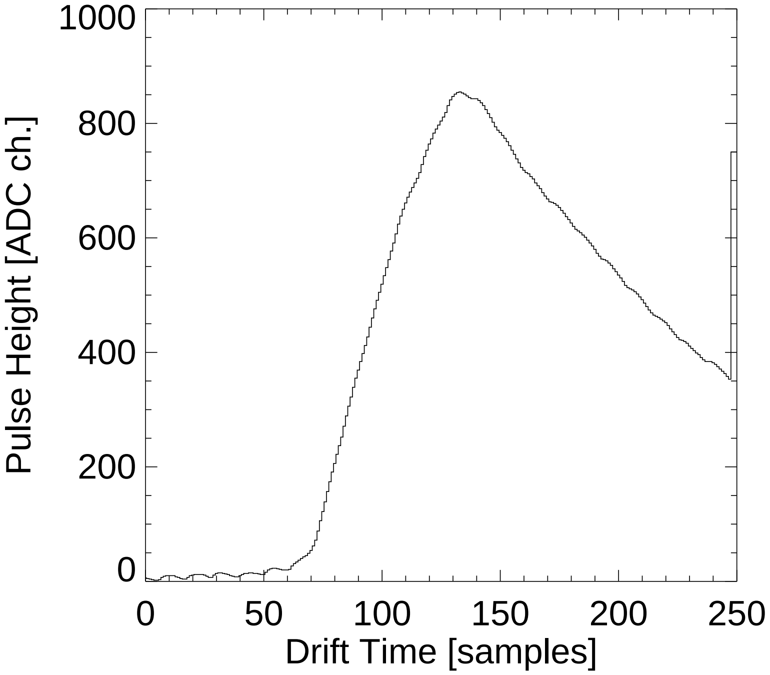

Figure 2.13: Cosmic ray track as seen on an anode (from Ref. (74)).

Event selections

The identification of good γ-ray events is achieved through several steps throughout the analysis procedure. Initial selections are as follows:

1. Events for which the anode baseline, measured in the first 20 samples, is outside a specified range around a nominal baseline value are rejected. Also rejected are events for which the baseline value of the first 10 samples differs by more than the same preset value from the baseline value of the subsequent 10 samples. Such events are due to a signal in the collection region, to pile-up with a previous signal that did not trigger the detector, or to noise. Moreover, events with a digitized anode baseline of zero are rejected, since the full signal amplitude cannot be determined in such cases. This can happen if a preceding event deposited a large amount of energy in the chamber, resulting in an undershoot of the signal waveform before the nominal baseline is restored [7] . Some events have signals at unphysically high drift time, e.g., due to the coincidence of a γ-ray that did not trigger the DAQ itself with a preceding γ-ray (pile-up) or noise trigger. These events are easily rejected.

2. Charged particles are rejected by amplitude, if any of the anodes is saturated, or by signal rise time. If the slope of the waveform remains positive for more than a specified number of samples, the event is considered a charged-particle track. Empirically, this number has been optimized to 42 samples, while a γ-ray signal usually rises over no more than $\sim$ 25 samples. Fig. 2.13 shows an example of a cosmic-ray track on an anode.

Wire signals

Wire signals are found above preset or continuously updated thresholds. Their drift time (t_d) values are determined by an amplitude-weighted average within ±5 samples around the position of the signal maximum. The signal amplitude is taken as the maximum value above baseline and corrected for gain differences in the preamplifiers. The signal width is defined as the width in which the signal is above half its maximum value. Fig. 2.14 shows a histogram of wire signal widths. The distribution is bimodal, with the true

---

[7] Negative amplitudes are digitized as zero.

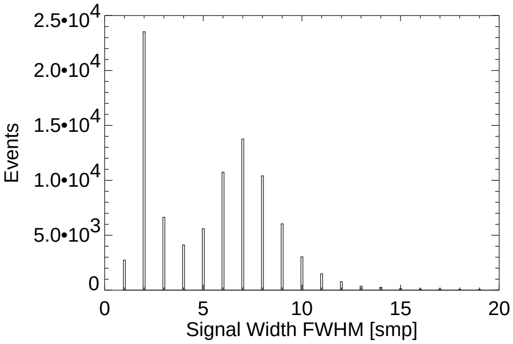

Figure 2.14: Width of wire signals recognized above threshold (from Ref. (74)).

signals centered around a width of about 7 samples with a spread of 4.2 samples FWHM. The expected signal width is about the same as the drift time between x- and y-wires (6.3 samples). The second population of wire signals clusters around 2 samples, with a spread of 1.4 samples FWHM, and consists mainly of noise hits. To reduce the number of noise hits, we require valid wire signals to have a width of at least 3 samples and less than of 16 samples. Visual inspection shows that broad signals are often due to charge collection on the wires, which occurs preferentially near the edge of the sensitive volume where the electric field becomes less uniform. Other effects resulting in wide wire signals are the occurrence of two unresolved close interactions, high-energy events that saturate dynamic range or low-frequency noise. The analysis procedure provides a user-selectable scale factor α_w, by which the noise value on each wire is multiplied to determine individual thresholds, which are typically set at 3σ above the noise. Once all wire signals are found, signals from up to three neighboring wires are combined to one signal if their time coincides to within ± 2.5 samples (0.5 μs). This signal "collection" is necessary because even an ideal point charge distributes its signal over at least two wires. The algorithm starts with the largest signals, searching for signals on the two neighboring wires, and continues through all remaining wire signals on both views. The amplitudes of the signals in x- and y-clusters are added and the interaction locations in x or y, and in t_d, are weighted by amplitude. The number of collected signals increases slowly with energy, from typically a single wire near the lower energy threshold to up to three wire signals at higher energies, as the weaker signals on adjacent wires emerge from the

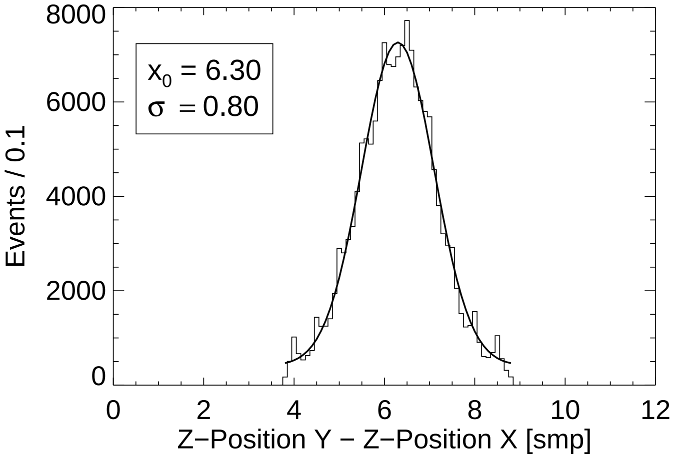

Figure 2.15: Distribution of drift time differences between matched wire signals in y and x. The width of 0.8 samples (1σ) corresponds to a measurement accuracy of 160 ns in drift time or 0.32 mm in z (from Ref. (74)).

noise. In the next step, the combined induction signals on the x- and y-view are matched in drift time (marked with circles in Fig. 2.9) within a window of ±2.5 samples, after subtraction of the drift time offset between the x- and y-wire planes. Fig. 2.15 shows the distribution in drift time difference between y- and x-signals. It has a width of typically $\sigma = 0.8$ samples, or 160 ns [8] . The acceptance window for x/y-matching corresponds therefore to about $\pm 3\sigma$. In addition, the signal amplitudes are required to be similar within a user-selectable factor, usually set to a value of 4. At large amplitudes, the correspondence between matching wire signals is in fact significantly better than this. At small charge signals ($\lesssim$ 6000 e$^-$, corresponding to $\lesssim$ 300 keV), however, one of two wire signals can be missed and the energy resolution of the wire signals degrades, such that x- and y-amplitudes of matching signals can differ significantly. If the match by drift time is not unique, the better match by amplitude is chosen. The requirement on the drift time match within a 5 sample window reduces the noise from chance coincidences by a factor of $\sim 220/5 = 44$, where 220 is the number of samples in which a wire signal is searched. Unless the wire threshold parameter α_w is set very low, the drift time selection is mostly sufficient to find a unique match. Fig. 2.16 illustrates to which extent the LXeTPC wire structure can separate individ-

---

[8] The theoretical limit for the sampling time of 200 ns is ∼140 ns.

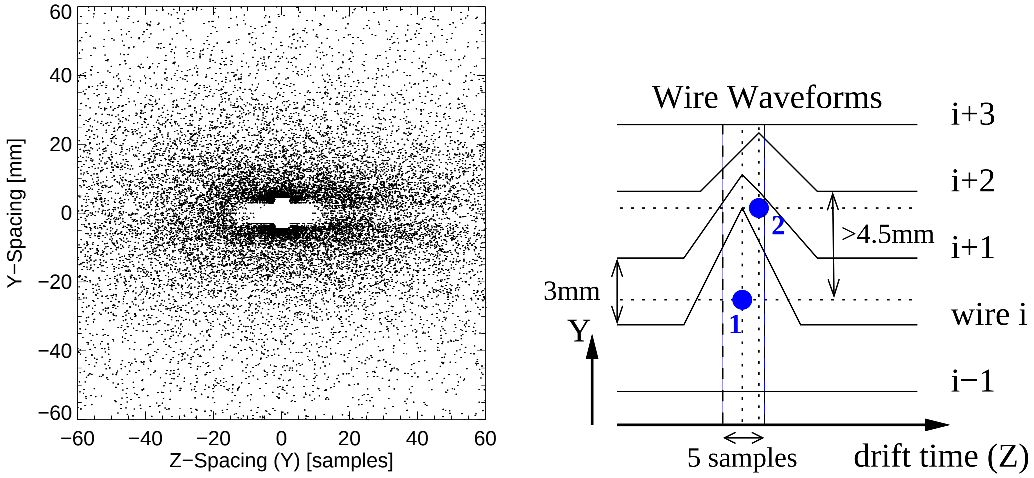

Figure 2.16: Left panel: y- and z-separation of events with two x/y-matching wire signals, without consideration of anode signals, for ^{88}Y data. Right panel: Schematic of wire signal waveforms vs. y and z. Two interactions, with charge clouds indicated by filled circles, within ±2.5 samples drift time can only be separated if they occur in separate ‘cells’ of wire pairs on each view. From Ref. (74).

ual interactions. Noting that x and y spatial resolution are identical, the left panel shows the y- vs. z-separation between the interactions in events where two matched x/y wire signals were recognized, independent of the anode signal. The physical distribution of separations falls off exponentially, with a peak at zero. Two interactions that fall within the same drift time window of ±2.5 samples, i.e., $|\Delta z| \lesssim 1$ mm, are only separated if they occur in separate 'cells' of wire pairs in both x and y views. If they are identified as separate interactions, their assigned coordinates will have a separation of at least 4.5 mm, i.e. 1.5 times the pitch. The reason is illustrated in the right panel, for two minimum separable interactions: Wire $i+1$ sees signals from both charge clouds. If both signals are sufficiently close in drift time, and/or the charge clouds are sufficiently close to this wire, it will have the largest amplitude of the three wires, and would be combined into one signal. If wire i has the largest amplitude, wire $i+2$ is recognized as a separate interaction, and the coordinates will result from the weighted average of i and $i+1$ for interaction 1 and the coordinate of wire $i+2$ for interaction 2. Hence, the minimum reconstructed y separation is 1.5 times the wire pitch. If both interactions occur within the same cell (on either view), a minimum separation in z of about the signal width is required (~ 8 samples or 3.2 mm).

Anode signals

Recognition of anode signals, shown in Fig. 2.17, uses a filter 'A' which computes for each FADC sample i a smoothed first derivative, by subtracting the samples $[i-5, i-1]$ from the samples $[i+1, i+5]$. A step is found if the filtered waveform crosses a preset threshold and remains above for at least 5 samples. Filter 'B' subtracts the samples $[i-16, i-9]$ from the samples $[i+9, i+16]$, and is usually used for an initial estimate of the step height only. Strong *negative* slopes that follow within 6 samples of a positive threshold crossing, are associated with digital noise, and the affected anode samples are excluded from fitting. The mean time difference between x-wire signal and anode signal is about 17 samples, due to the drift time difference and signal shaping on the anodes, thus for anodes signals in the first 17 samples the corresponding x signals will be missed. These events, which correspond to interactions below the drift region, are therefore rejected.

The energy deposits in individual interactions derived from a fit of the anode signal, plotted as smooth line on top of the anode waveforms in Fig. 2.8b and 2.9. The fit function consists of one or multiple steps described by Fermi-

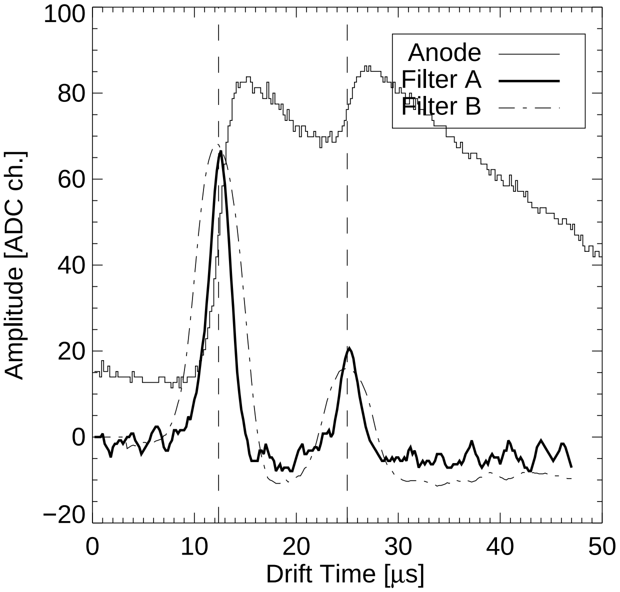

Figure 2.17: Anode signal recognition, here for a 2-step event, applying two filters. Filter A determines the step position precisely, while filter B measures the signal amplitude. Both values become start parameters for subsequent waveform fitting. From Ref. (74).

Dirac thresholds, an exponential decline, and a flat baseline. For a one-step anode signal, the function is defined as follows:

$$f_1(t) = a_0 \cdot \left(1 - \frac{1}{1 + \exp\{a_2\,(t - a_1)\}}\right) \cdot \exp\{-a_3\,(t - a_1)\} + a_4 \qquad (2.1)$$

where a_0 is the signal amplitude, a_1 is the step position measured at about half height of the signal, a_2^{-1} describes the signal rise time, a_3^{-1} is the exponential decay time resulting from RC shaping in the preamplifier, and a_4 is the baseline value. For n steps, the formula expands to a function with $2\,n + 3$ parameters, since rise time, decay time, and baseline are the same for all steps. The rise time is kept fixed at predetermined values, which vary for the four anodes due to differences in signal shaping. The exponential decay time is also fixed, at 135 samples. The baseline parameter a_4 is determined for each event in a separate step before the waveform fit, to increase fit stability and to prohibit undesired trade-offs between signal and baseline determination for noisy signals. a_4 is set to the average over a 30 samples wide window at $[-45, -15]$ samples before the initial estimate of the step position. If the step position is less than 45 samples, the baseline is determined in the window $[-(\textit{step position}), -15]$; the requirement of a reliable baseline estimate led us to discard all events with anode signals within the first 20 samples.

Since the ultimate goal of the anode fitting procedure is an accurate determination of the signal amplitude a_0 (the z coordinate is more accurately determined from the wires), the fit range is restricted to $[-45, +60]$ samples around the initial position estimate, a region which entirely contains the amplitude information. If the step position is less than 45 samples, the fit window is reduced to $[-(\textit{step position}), +60]$ samples. The highest possible step position inside the drift region is 195 samples, while the anode waveform is sampled up to 248 samples; for step positions above 188 samples the fit window is reduced to $[-45, 248 - (\textit{step position})]$ samples. In case of multiple steps, the fit range is extended to the first step position -45 samples and the last step position $+60$ samples. The ultimate figure of merit for the goodness-of-fit is the accuracy in extracting the signal amplitude and is evaluate in Sec. 2.1.8.

Matching of wire and anode signals

In the next step, the identified and matched x- and y-signals are matched with the recognized anode signals, based on drift time and a correspondence of (x, y)-position and anode location. If all n signals match, the event is stored as $n/3$-interaction event. If more anode signals are found, all anode signals and all matching wire signals are stored, and the event is labeled correspondingly. If more wire signals are found, we attempt to refit the corresponding anodes with the additional steps, unless they are separated from other signals on the same anode by less than 10 samples in drift time. The anode step positions are restricted to a range of ±4.5 samples around the y-wire position, plus an empirical drift time offset of 11–13 samples, depending on the anode. If the anode fit is sufficiently improved and the newly fitted anode steps exceed a minimum amplitude, the refit is accepted, and the event is correspondingly flagged. Additional wire signals, for which no anode signal above a preset threshold can be fitted, are considered noise and removed. If there are signals that are too close in drift time to be fitted on the same anode, the event is stored with all wire signals and the matched anode signals, and labeled accordingly. Finally, if the number of matching signals is smaller than both the number of wire signals and the number of anode signals, the event is rejected, as it is assumed that the event reconstruction failed. The refit of the anodes, using the wire signature, enhances the detection efficiency (∼40% at 2 MeV).

Fig. 2.18 shows the absolute value of z-separation of steps after matching of wire and anode signals. The requirement of a minimum separation of 10 samples for signals on the same anode results in a sharp edge in the distribution. Comparison with Fig. 2.16 shows that the matching of anode and wire signals has a more severe impact on resolving signals close in drift time than the x/y-wire matching.

Output

The fraction of rejected/selected events, together with the specific reason for rejection, is given in a `log` file at the end of the run, of which an example is shown in Fig. 2.19. Those figures are very standard and usually reproducible within ±10%. Selected events are sorted in different files according to their anode and wire multiplicities, i.e. number of detected interactions on anodes

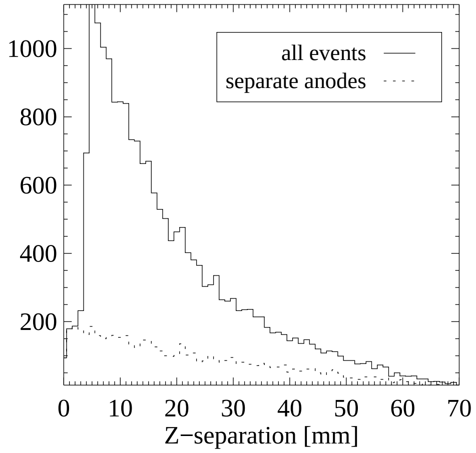

Figure 2.18: z-separation of recognized signals with matching wire and anode signals (^{88}Y source).

and wires [9], and their fraction is written in the same `log` file and shown in Fig. 2.20 for a ^{88}Y source. It should be noticed that those figures are extremely sensitive to specific experimental conditions, as source spectrum, rate and on-line selections. The data files are IDL structures which contain n entries for each event, where n is the maximum between anode and wire multiplicity. The IDL structure contains 25 *tags* for each entry in the most recent version. The 25 *tags* accommodate in a redundant way the $x - y$wire and anode amplitude, position, timing etc.. This redundancy is usually very welcome when data are further analyzed.

Performance evaluation

Speaking in general terms, the ideal analysis procedure for the LXeGRIT TPC should extract all the essential information, i.e. energy and position for each interaction, from raw data with the lowest possible energy threshold and the finest position resolution, *lowest* and *finest* being the limits imposed by the intrinsic energy resolution in LXe, electronic noise and granularity

---

[9] Anode and wire multiplicities are not required to be the same.

```
Events read ..............:     9328 =  100.000%
Rej. cosmic rays ..........:     275 =    2.948%
Rej. pile-up evts (bad BL).:     789 =    8.458%
Rej. collect. region evts .:    1065 =   11.417%
Rej. # of sig. out of range:       2 =    0.021%
Rej. a/w matches < min(a/w):     286 =    3.066%
Rej. - fit failure ........:      13 =    0.139%
Rej. wide wire signal evts.:    1156 =   12.393%
Rej. - other errors .......:       0 =    0.000%
Selected - all ...........:     5742 =   61.557%
```

Figure 2.19: Fraction of rejected/selected events, together with the specific reason for rejection, as in the *log* file at the end of the run.

```
Selected [%], relative to all selected events:
         0 Wsig  1 Wsig  2 Wsig  3 Wsig  4 Wsig
0 Asig    1.498   0.017   0.017   0.000   0.000
1 Asig    2.264  45.367   8.168   2.786   0.366
2 Asig    0.157   3.448  22.431   4.545   0.784
3 Asig    0.035   0.174   1.324   3.884   0.923
4 Asig    0.000   0.035   0.035   0.244   0.540
```

Figure 2.20: Fraction of selected events according to their anode ($Asig$) and wire ($Wsig$) multiplicities.

of the readout electrodes. The ideal algorithm should also be stable against different experimental conditions (input energy spectra, electronic noise) and fast. The analysis procedure described has been tested over the period 1999-2002 on a variety of data sets, including data from two different balloon flights, always giving an excellent performance. The time to analyze one event is ∼0.05 s, which is fast enough to perform data analysis in real time, thus meeting our requirements.

Here I define three figures of merit to evaluate the performance of the analysis procedure:

1. its impact on energy resolution and calibration;
2. its impact on position resolution;
3. lowest energy threshold.

Energy resolution

Spectroscopy with LXeGRIT is described in a detailed manner in Sec. 2.2.3; the energy is derived from the amplitude of the anode signal through the fitting procedure described in Sec. 2.1.8. To study the impact of the off-line analysis procedure on it, I break down the energy resolution in three pieces

$$\sigma_{tot} = \sigma_{LXe} \oplus \sigma_{el} \oplus \sigma_{other}$$

where $\oplus$ means sum in quadrature. σ_{LXe} is the intrinsic energy resolution in LXe for a drift field of 1 kV/cm; it is known to be $\sim 3.5/\sqrt{E}$ % (4). σ_{el} comes from electronic noise on the anodes, which is independently measured (Sec. 2.1.5) and does not depend on energy. σ_{other} accounts for everything else than σ_{LXe} and σ_{el}, therefore including inaccuracies introduced by the fitting procedure.

As shown in Sec. 2.2.3, the energy dependence of the energy resolution over the energy range 0.5-4.2 MeV is very well described by

$$\Delta E[\mathrm{MeV}]\ (FWHM) \ = \ \sqrt{6.7 \cdot 10^{-3} \cdot E[MeV] + 3.6 \cdot 10^{-3}}$$

where the term $6.7 \cdot 10^{-3} \cdot E$ accounts for $\sigma_{LXe} = 3.5\%$ and the energy independent term accounts for the electronic noise, ∼60 keV FWHM. Therefore, σ_{tot} is satisfactorily described setting $\sigma_{other} \equiv 0$ without too much room for any significant contribution. Moreover, the energy calibration over the same energy range is perfectly linear, ruling out any undesired dependence on amplitude. □

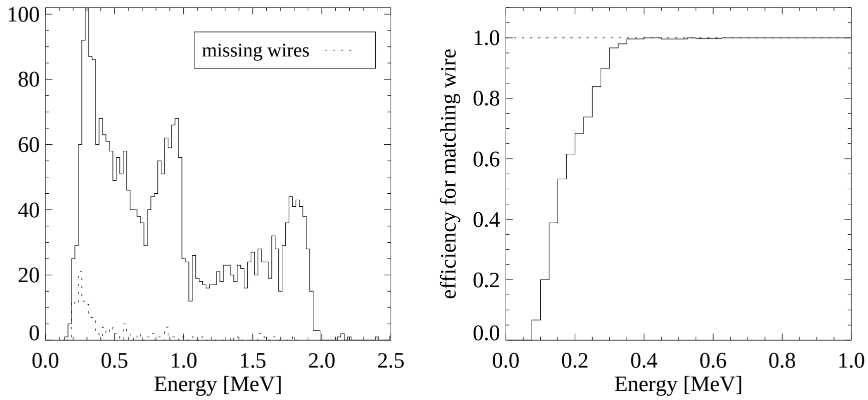

Figure 2.21: *Left:* energy spectrum for a ^{88}Y source for events with one anode signal and one or no matching wire signal; superimposed *dashed line* the energy spectrum for events with no matching wire signal. Quite clearly, wire signals are missed only below 0.5 MeV. *Right:* ratio of events with one matching anode and (x/y-matched) wire signal over the sum of all events with one anode signal and one or no matching wire signal.

Position resolution

The wire structure allows a ∼mm position resolution; naively, $3/\sqrt{12} = 0.85$ mm considering the wire pitch and an interaction seen on one wire only. Since even a pointlike interaction may induce detectable signal over two or more wires, the actual response is slightly modified. It will be shown in Sec. 2.2.2 that such resolution is well achieved in LXeGRIT. □

Energy threshold

The energy threshold for each interaction is eventually determined by the wires, which have a worse signal-to-noise ratio than the anodes. Given the higher sensitivity of the anodes for single charge signals, the efficiency for finding/matching wire signals can be estimated as the relative probability of finding a matched wire signal for all events with a single-step anode signal. As shown in Fig. 2.21, the efficiency is 55% at ∼150 keV, 90% at ∼250 keV and rapidly saturates above that energy. In Sec. 2.1.5 it was shown that the signal/noise ratio is 3σ at 150 keV. This holds true if the interaction happens exactly at the wire location; for an interaction between two wires (see Fig. 2.7) the 3σ level will be higher, ~220 keV. At this point we still have to match the x- and y-signals, which again would reduce the expected efficiency. The measured efficiency at 150 keV for wire thresholds $\sim 3\sigma$ above the noise level is therefore compatible with expectations. □

2.2 Results and performance

2.2.1 Measurement of the electron lifetime

A measurement of the lifetime of free electrons before recombination is the customary choice for determining the purity of a LXe sample, or its contamination due to electro-negative impurities.
The simple relation

$$Q_{det} \ = \ Q_0 \cdot exp(-\frac{z}{\lambda_{att}}) \tag{2.2}$$

describes the detected charge Q_{det}, given an initial charge Q_0 at a distance z from the collection point. The parameter λ_{att} is the attenuation length for electrons drifting in LXe, i.e. the electron lifetime τ_{el} times the drift velocity in LXe (typically $v_{drift} \sim 2$ mm/μs).

Given a γ-ray line, the procedure consists in measuring the amplitude corresponding to the photo-peak for different z (i.e. drift time) slices, as shown in Fig. 2.22 for six z slices, about 1 cm each. A collimated ^{137}Cs source, which gives 0.662 MeV γ-rays, has been used for this measurement, but the procedure is very general and can be extended to virtually any calibration source. The photo-peak amplitude decreases of about 8% over the full 7 cm drift length. The dependence of the photo-peak amplitude on z is then fitted with Eq. 2.2 to yield λ_{att}, i.e. the electron lifetime. This constitutes a very direct measurement, more sensitive and more "visual" than the one using muons crossing the chamber (for a description of this procedure see Refs. (26; 27)), which can not reliably measure λ_{att} when it is much larger (ten times in the present case) than the maximum drift length.
The scatter plot of the amplitude of the ^{137}Cs events vs. drift time at 1 kV/cm is also shown in Fig. 2.22, for single-site events. The enhancement seen in correspondence to the 662 keV full energy peak (FEP) moves to lower pulse heights for longer drift time. Superimposed, the photo-peak amplitude for the six z-slices and the fit with Eq. 2.2. The measured drifting electron

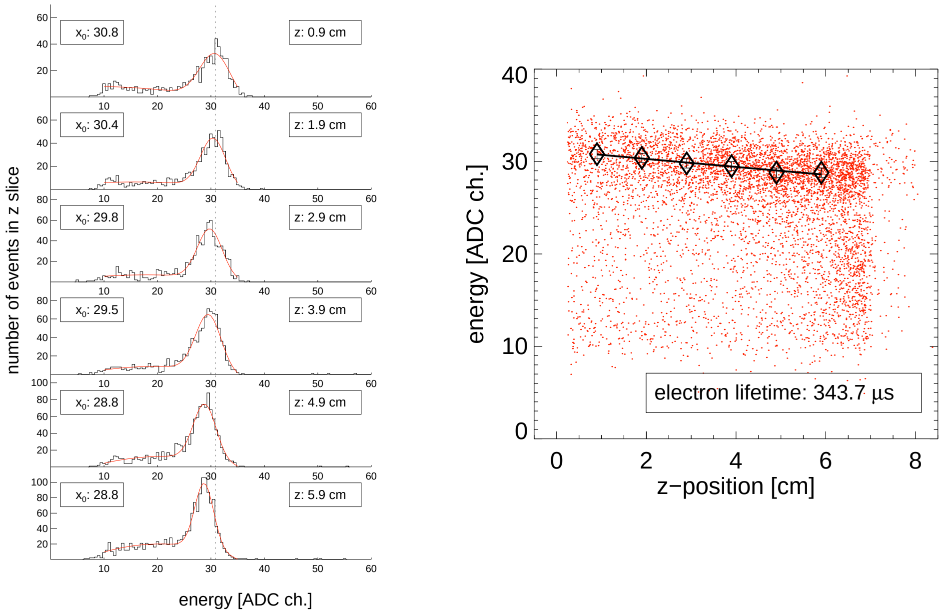

Figure 2.22: LXe purity measurement. *Left:* energy spectrum for a collimated ^{137}Cs source (0.662 MeV) for six different z-slices of the fiducial volume, each of them 1 cm thick. The z-center of the slice is written in the upper-right corner, the fitted amplitude of the photo-peak in in the upper-left corner. As expected, smaller amplitudes correspond to larger z. *Right:* scatter plot of the amplitude vs. drift time for the same source. Superimposed, the photo-peak amplitude for the six z-slices (open diamonds) and the fit with Eq. 2.2; error bars are smaller than the plot markers.

lifetime is about 340 μs; given a drift velocity of 2 mm/s for electrons in LXe at 1 kV/cm, this lifetime corresponds to an attenuation length of ∼70 cm, to be compared with the 7 cm maximum drift length in our detector.

Even having obtained an extremely pure medium, the loss of drifting charge due to electro-negative impurities still introduces a variation of few percent in the amount of collected charge, thus undermining the final energy resolution. In the present case, a variation of 8% over the drift region would completely spoil the energy resolution of ∼12% FWHM at 0.662 MeV. A correction for attachment to impurities is then applied during the event reconstruction on an event-by-event basis, removing the dependence of the signal amplitude on the distance from the anode and so significantly improving the spectral performance. Such a correction is assumed everywhere in the following.

2.2.2 Position resolution and 3-D imaging capability

The interaction location in the LXeTPC is obtained from the wire signature. Since the wire pitch is 3 mm, a spatial resolution of about 1 mm (i.e. $3/\sqrt{12}$) in the $x-y$ directions can be safely assumed, and it is experimentally confirmed. See for example Fig. 2.23 which shows the image of the γ-beam from a collimated ^{137}Cs source on top of the TPC, both in $x-y$ and in the $x-z$ views. A lead collimator 15 cm thick, composed by three separated lead bricks each of them 5 cm thick, with a conical hole such to give a 2 mm diameter beam was used to collimate the γ-rays. The z-coordinate offers a finer resolution, of about 0.35 mm, as shown in Fig. 2.24. The spatial resolution on the z-coordinate is measured as the difference between the z-position from the x and y wires for the same interaction. The z-distribution of photoabsorbed events from the same collimated ^{137}Cs source is shown in Fig. 2.25, well reproducing the exponential attenuation for 0.662 MeV photons. This spatial resolution fulfills the requirement of a fine grained CT, where a typical separation between interactions is in the cm range and the linear extension of the charge cloud due to MeV energy deposits is typically less than 1 mm.

2.2.3 Spectroscopic performance of the LXeTPC

The spectroscopic response has been tested for γ-rays in the energy range from 0.5 to 4.4 MeV for various event multiplicities, irradiating the LXeTPC in different detector configurations and for a broad variety of source rates and positions. In this section we show energy spectra for ^{22}Na and ^{88}Y γ-ray sources and for an Am-Be γ-ray/neutron source; energy spectra for a ^{137}Cs source has been shown in Sec. 2.2.1. The large amount of information available for each γ-ray event allows a detailed spectral analysis. The precise knowledge of the event topology suggests a separate analysis for events with different interaction multiplicity, namely 1-, 2-, 3-, 4-site events. Higher multiplicities are largely suppressed, as shown in Sec. 3.3.1. 1-site events, albeit being of no use for Compton imaging, are useful in characterizing the spectral performance of the LXeTPC, especially for γ-ray energies below

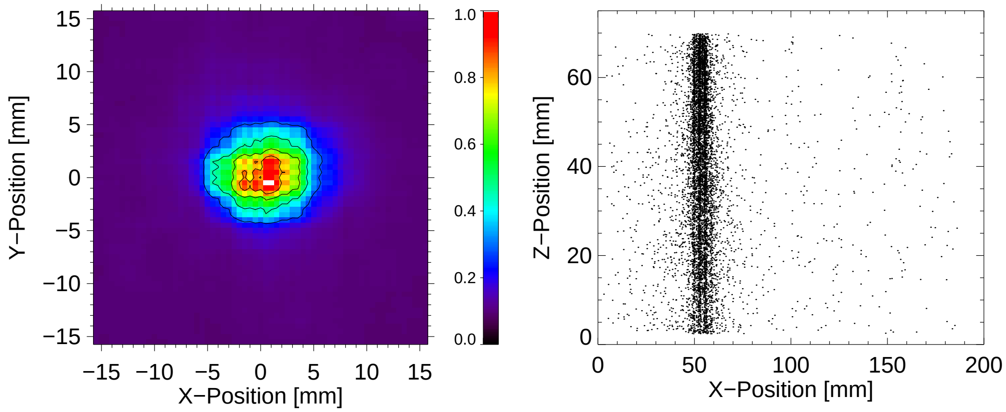

Figure 2.23: Image of the γ-beam from a collimated ^{137}Cs source on top of the TPC.*Left:* projection in the $x - y$ plane. The coordinates have been re-defined in order to have the source image centered at $x = 0$, $y = 0$. *Right:* side view ($x - z$ plane) of the same γ-beam.

1 MeV where they constitute the largest fraction of the fully absorbed events. They proved very useful in assessing the γ background rate in the LXeGRIT detector at balloon altitude (see Ch. 6 and Ref. (34)). A good performance for multi-site events is of the utmost importance for a Compton telescope. Even leaving aside the topic of Compton imaging, these event categories offer interesting properties for spectral analysis. In fact, summing up the amplitudes of separate interactions occurring at the same time, a greatly enhanced *peak-to-Compton* ratio can be obtained (somewhat resembling the so called "sum-coincidence mode" (see for example Refs. (59; 29)).

- Fig. 2.26-*left* shows the 1-site energy spectrum for a tagged ^{22}Na source (see Sec. 3.3.3). Since an external trigger is used in this configuration, the resulting energy spectrum does not depend on the light trigger efficiency. In this tagging scheme the 1.275 MeV γ-rays are reduced to a negligible level.
  Fig. 2.26-*right* shows the 2-site energy spectrum for the same ^{22}Na source, this time triggering on the LXe scintillation light, without external tagging. The two lines at 0.511 MeV and 1.275 MeV are now clearly detected, and the ratio of events in the two full energy peaks

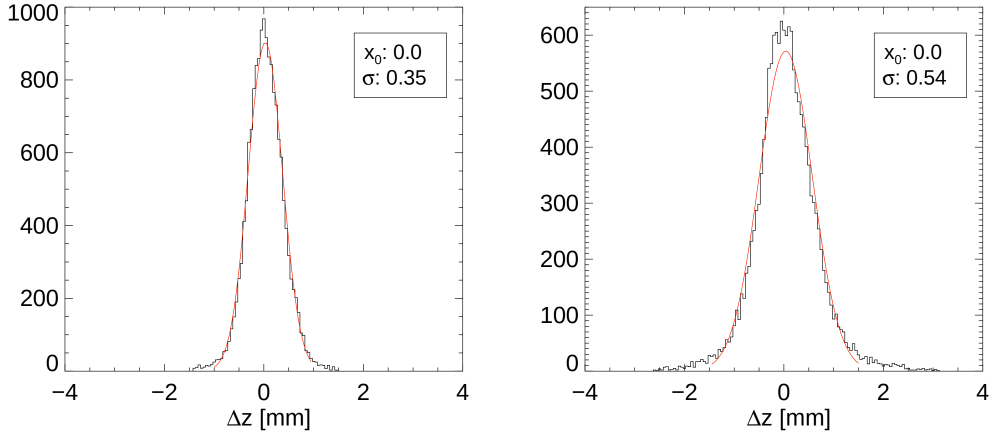

Figure 2.24: *Left:* difference between the z-position as determined from the x and y wires; the distribution has been arbitrarily centered at zero. This constitutes a direct measurement of the spatial resolution in the z-direction. *Right:* difference between the z-position from the x-wires and the anode. The distribution is broader since the determination of z on the anode (through a fit of the waveform) is less precise.

agrees with expectation (see Ch. 3) [10] . The "tail" on the right side of the 1.275 MeV line is due to pile-up events, where one 0.511 MeV and one 1.275 MeV photon, simultaneously emitted, interact in the active volume at the same time.
In both cases data were taken in 1999 flight configuration (Appendix A).

- Fig. 2.27 and 2.28 show ^{88}Y energy spectra for 1- and 2-site events. In the case of Fig. 2.27, the γ-source was placed at 3 m from the detector, on axis, in 1999 flight configuration. In the case of Fig. 2.28, the γ-source was placed at 1.5 m from the detector, 30° off-axis, and data were taken in 2000 flight configuration and the light trigger efficiency has a larger impact on the spectral shape, greatly depleting the low energy part.

---

[10] One has to remember that the ^{22}Na source simultaneously emits two 511 keV and one 1275 keV photon, so that a similar number of events is expected in the two lines.

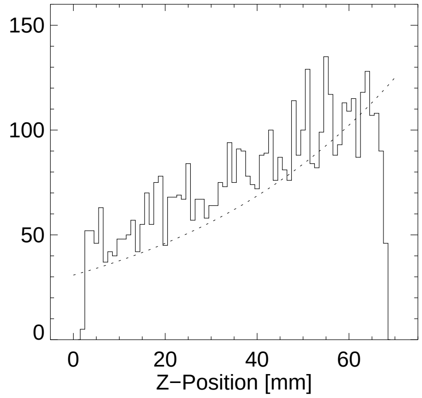

Figure 2.25: z-distribution for a collimated ^{137}Cs source sitting on top of the LXeTPC. Events in the full energy peak has been selected; superimposed (*dashed line*) the exponential attenuation for 0.662 MeV photons. The slight discrepancy at $z \sim 60$ mm is mainly due to the z dependent light trigger efficiency, which is not corrected for.

In this case we selected (off-line) one fourth of the detector, corresponding to one anode out of four. The efficiency in detecting the 0.898 MeV line is essentially the same in the two datasets, while the efficiency for the 1.836 MeV line is twice as large in the 2-site sample. This is, again, quite consistent with expectations. To explain the ratio between the two lines a more detailed detector model has to be used, accounting for the energy dependence in the detection efficiency described in Ch. 3 .

- Fig. 2.29-*left* shows an Am-Be energy spectrum, combining multiplicities up to 3: since the cross-section for pair-production is large at 4.4 MeV, the single and double escape peaks (3.92 MeV and 3.41 MeV) are the dominant features; the full energy peak is also well identified. These three features enter in the energy calibration, usefully extending the energy range. At energies above 4 MeV bremsstrahlung plays a non negligible role in LXe [11] and it accounts for extended low energy tails

---

[11] The *critical energy* E_c, above which bremsstrahlung dominates ionization as an energy loss mechanism for electrons, is 11 MeV in LXe, but the energy spectrum is significantly modified for energies as low as 4 MeV.

in the energy peaks. Fig. 3.19-*right* separately shows the 1-site and the multi-site energy spectra. The double-escape peak is very prominent in the 1-site spectrum, while the full energy peak goes almost undetected. The efficiency for containment is much enhanced in multi-site spectrum.

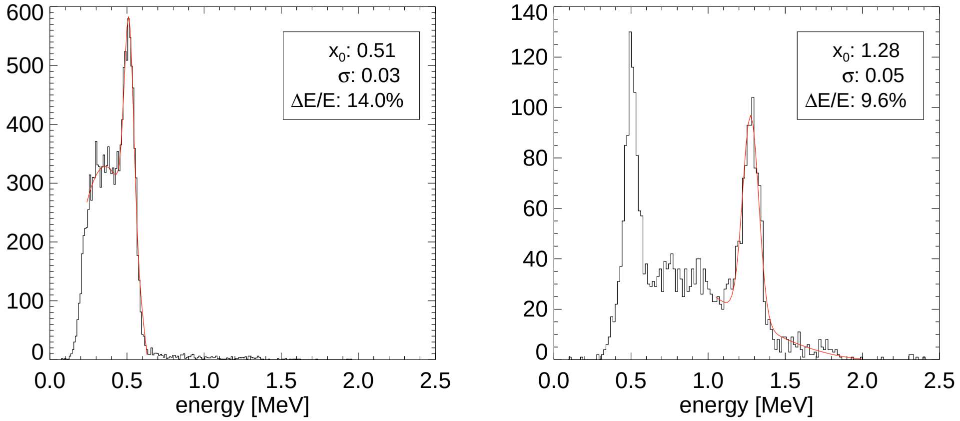

Figure 2.26: *Left:* 0.511 MeV line from a ^{22}Na source tagged source, 1-site events. The spectrum has been fitted fitted with a gaussian plus a second order polynomial to account for the underlying background; the mean and r.m.s. of the gaussian are shown in the inlet, together with the ΔE/E (FWHM). *Right:* 0.511 MeV and 1.275 MeV lines from a ^{22}Na source source, 2-site events.

Energy resolution and calibration

The starting point for the energy calibration are the energy spectra for 1-site events and the lines used for calibration are given in Table 2.1. In 1999 2-site events from ^{88}Y (single escape peak) and Am-Be 2-site and 3-site events have been used too. Each of the four anodes is independently calibrated. Each line is fitted with a gaussian plus a second order polynomial to account for the underlying background and the line position and spread come from the mean and variance of the gaussian. Several examples of such a procedure are shown in Figs. 2.26 - 2.28. This procedure could not be applied in the cases of ^{88}Y single escape peak, Am-Be single escape peak and Am-Be Compton edge,

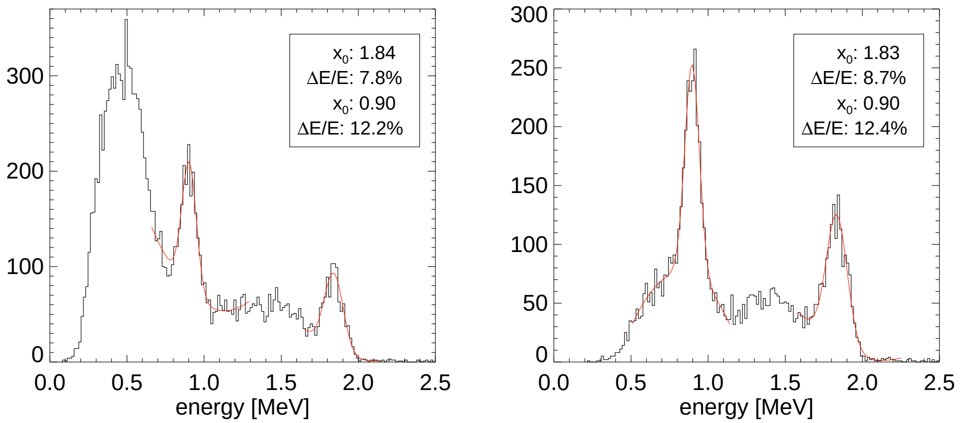

Figure 2.27: ^{88}Y (0.898 and 1.836 MeV) 1-site (*left*) and 2-site (*right*) energy spectra.

because the "line profile" was not well reproduced by a gaussian. In these cases the maximum was used instead of the mean of the gaussian, bypassing the fitting procedure.

The energy calibration, i.e. finding the conversion factors from ADC ch. to MeV, is readily obtained, showing a very good linearity in the 0.5-4.5 MeV energy range. For multi-site events, the amplitude associated with each interaction is transformed from ADC ch. to MeV according to the 1-site calibration, and the total energy is then found summing up the various interactions. This is important for LXeGRIT, because not only the total energy is needed but also the energy for each interaction. This procedure works well and line energies for 1-site and multi-site events coincide within uncertainties, i.e. better than 1%.

The energy resolution is then obtained using the same lines, but excluding the ones not reproducible through the gaussian fit; the ^{60}Co doublet has also been excluded, because of limited statistics.

The energy dependence of the energy resolution was then fitted using

$$\Delta E/E(FWHM) \;=\; \sqrt{\frac{P_1^2}{E} + \frac{P_2}{E^2}}$$

where P_1 accounts for the intrinsic energy resolution which should come from the statistics of charge carriers in LXe and should account for the $1/\sqrt{E}$

energy [MeV]	source	1999	2000
0.511	^{22}Na	yes	yes
0.662	^{137}Cs	yes	no
0.898	^{88}Y	yes	yes
1.173^{*}	^{60}Co	no	yes
1.275	^{22}Na	yes	yes
$1.325^{a,*}$	^{88}Y	yes	no
1.332^{*}	^{60}Co	no	yes
1.465	^{40}K	no	yes
1.836	^{88}Y	yes	yes
$3.41^{a,*}$	Am-Be	yes	no
3.92^{b}	Am-Be	yes	no
$4.18^{c,*}$	Am-Be	yes	no
4.43	Am-Be	yes	no

Table 2.1: Energy lines used for calibration of the LXeTPC in 1999 and 2000. All the lines are measured as FEP with the exception of: (^{a}) single escape peak; (^{b}) double escape peak; (^{c}) Compton edge. Lines marked as (*) have not been used to determine the energy resolution because of limited statistics (^{60}Co doublet) or because the line profile was not well reproduced by a gaussian (^{88}Y and Am-Be single escape peaks, Am-Be Compton edge).

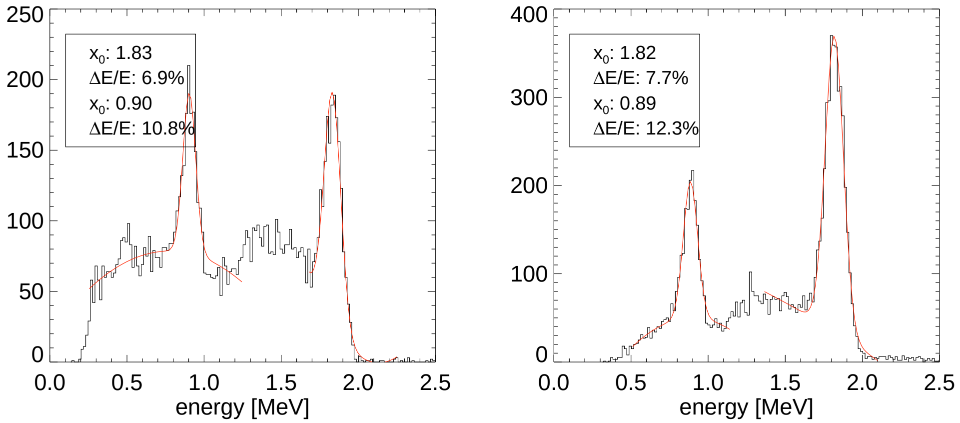

Figure 2.28: ^{88}Y (0.898 and 1.836 MeV) 1-site (*left*) and 2-site (*right*) energy spectra.

dependence expected from Poisson statistic; the second term, P_2, should account for contributions which are independent of energy, i.e. it is a *noise term*. In principle it should parameterize different contributions: electronic noise, errors in fitting the anode wave function (which can be energy dependent, in principle), shielding inefficiencies of the electrode structure etc. In practice it is well accounted for considering the electronic noise only (60 keV FWHM corresponds to about 1000 ENC, as in Ref. (6).
This value of the energy resolution is in good agreement with previous measurements in LXe at the same drift field (1 kV/cm), usually performed with gridded ionization chambers of lesser fiducial volume

Higher interaction multiplicities

The energy spectrum from 3-site events is shown in Fig. 2.31, from the same data-take as Fig. 2.28. The requirement of at least 3 interactions greatly reduces the efficiency below 1 MeV, as expected for an energy threshold of ∼150 keV on each interaction. On the other hand, requiring 3 interactions enhances the fraction of independent γ-rays interacting in the fiducial volume within the same 50 μs time window, i.e. the *pile-up events*. For this specific data-take, a rough estimate of the pile-up rate ($r_{pile-up}$) is given as

$$r_{pile-up} \;=\; r^2_{source} \cdot t_{window} \;=\; (3\text{ kHz})^2 \cdot 50\mu\text{s} \;=\; 450\text{ Hz}$$

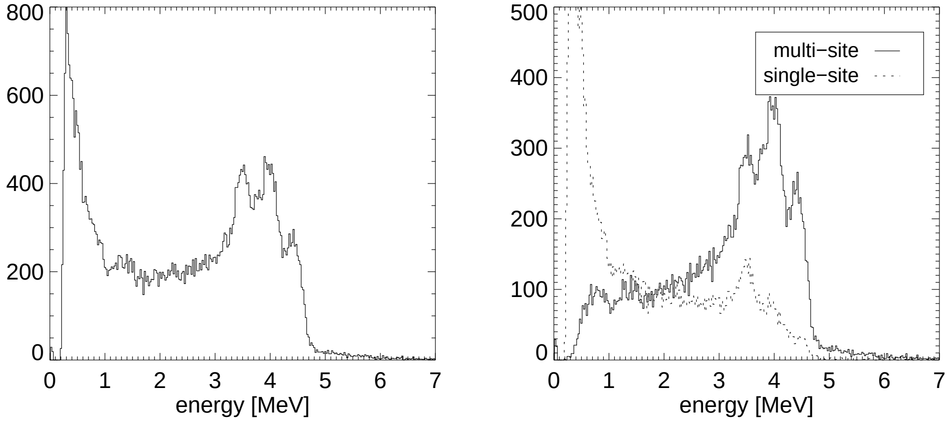

Figure 2.29: Am-Be (4.42 MeV γ-ray source) energy spectrum for 1-, 2-, 3-site events combined. The most prominent feature is the single-escape peak (3.92 MeV). The full energy peak and the double escape peak are clearly detected, too.

where r_{source} is the rate of γ-rays impinging on the detector from the source and t_{window} the time-window within which two events are piled-up. This rough estimate of the pile-up fraction ($\sim$15%), which does not account for trigger efficiency and multiplicity effects, makes clear that a sizeable number of pile-up events is actually expected. One should notice that the situation is different in the ^{22}Na data discussed previously, where photons are actually emitted at the same time; in the present case the pile-up fraction is mainly due to the modest efficiency of the light trigger system, which misses one of the two photons and does not send any ABORT signal.
Since the attenuation length in LXe for 1 MeV photon is $\sim$5 cm, interactions from a single photon are usually clustered in a relatively small region of the fiducial volume and we can exploit the 3D imaging capability of the TPC to identify events spread over a larger region and reject them as due to pile-up of independent γ-rays.

A further step in exploiting the imaging capability of the LXeTPC consists in selecting, out of a multi-site event, those interactions which come from one single γ-ray and which come from different γ-rays. In the specific case of LXeGRIT, we have four quasi-decoupled sub-detector, each one corresponding to a single anode and a single PMT delimiting a $x-y$ quadrant, about

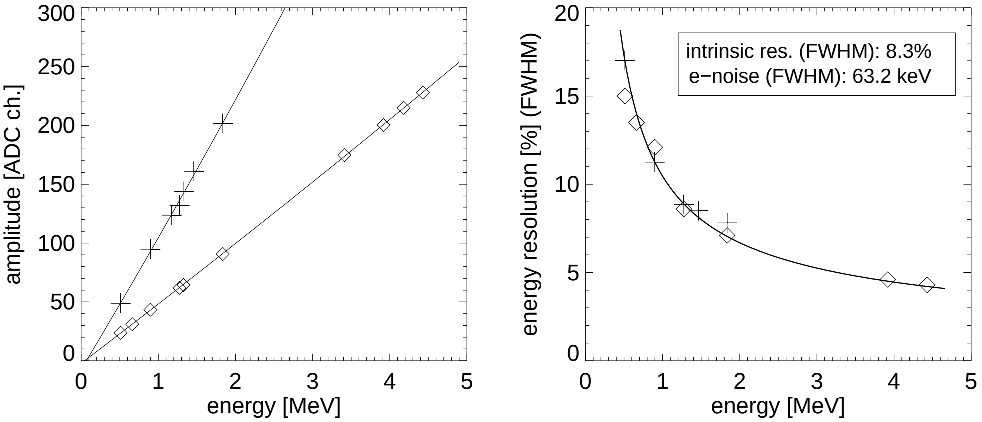

Figure 2.30: *Left:* the linearity plot for ADC ch. vs. MeV for both the 1999 (*open diamonds*) and the 2000 (*crosses*) setting. The gain in year 2000 was about twice the gain in 1999. *Right:* energy resolution versus energy, showing the $1/\sqrt{E}$ dependence expected from Poisson statistic corrected by a constant term.

10×10×7 cm^3 in volume, i.e. still sizeable to fully contain the multiple interactions of a single γ-ray but scaled down enough to largely reduce the pile-up rate. An example of such a procedure, applied to 4-site events from an ^{88}Y source, is given in Fig. 2.32. In this sample three interactions (a, b, c) are detected on a single anode while the fourth one (d) is detected on a different anode. When the four amplitudes are summed up (dotted line) no energy line is clearly detected; discarding now interaction d and summing up the amplitudes for a, b and c, a more typical ^{88}Y spectrum is recovered, with the two lines (0.898 and 1.836 MeV) clearly visible (continuous line).

Wires

The spectroscopic response from the x and y wire planes is shown in Figs. 2.33 and 2.34 for the same ^{88}Y and Am-Be data takes already used in Figs. 2.28 and 2.29. The better energy resolution achieved using the anode amplitudes is all but too apparent. The energy resolution is degraded by a factor of ~3, due to the worse signal-to-noise ratio, to the combination of several wire signals to obtain the energy deposit in a single interaction, to the less

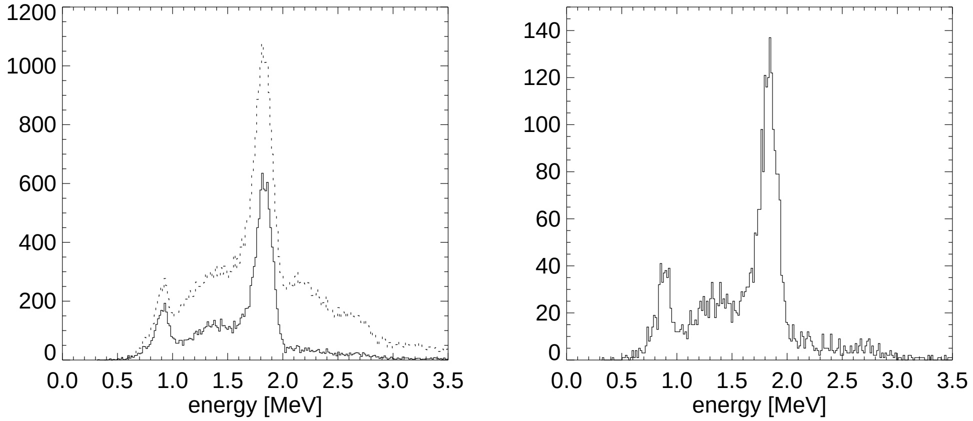

Figure 2.31: ^{88}Y (0.898 and 1.836 MeV) multi-site energy spectrum. *Right:* All events (*dotted line*) and after selections described in the text (*full line*). *Left:* One anode only, to be compared to Fig. 2.28.

than perfect wire-by-wire calibration and to the still not completely optimized off-line analysis. A better off-line analysis would doubtlessly improve the spectroscopic performance, but combining several signals, together with their electronic noise, unavoidably degrades the energy resolution. In fact, the wires are not used for spectroscopy but only to precisely locate the interaction, and there is no stringent requirement on their performance. It is anyway clear that spectroscopy with four anodes only instead of 62+62 wires is easier and more effective, both in principle and in practice.

Conclusions

In this chapter, the LXeTPC of the LXeGRIT instrument have been described, together with results about its efficiency, energy resolution and spatial resolution which completely characterize its performance:

- the LXeTPC gave a reliable performance through several experiments;
- the energy resolution is better than 10% FWHM at 1 MeV, including electronic noise, which is perfectly consistent with the best results obtained with LXe ionization detectors;

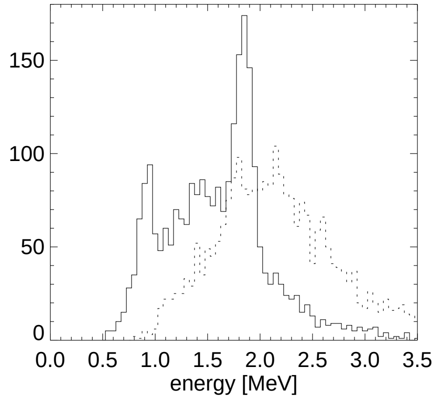

Figure 2.32: Energy spectrum for 4-site events for an ^{88}Y source. The dotted line shows the original energy spectrum when all the four amplitudes have been summed up. No energy line is clearly detected. The continuous line shows the energy spectrum for the same set of events, in which only three amplitudes have been summed up. The two lines (0.898 and 1.836 MeV) are now clearly visible. The fourth interaction has been rejected because of a large spatial separation from the other three.

- each interaction is visualized in three dimensions with a spatial resolution of 1 mm or better.

This set of results constitutes a world record for the LXeTPC technology.

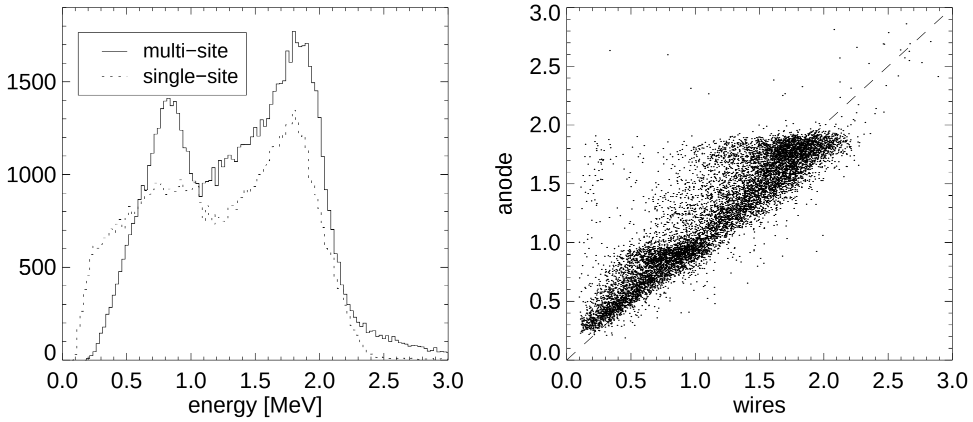

Figure 2.33: *Left:* Energy spectra for 1-site and 2-site events from a ^{88}Y source, as derived from wire amplitudes (averaged x- and y-signal). *Right:* Scatter plot of wire amplitudes (averaged x- and y-signal) vs. anode amplitudes, after energy calibration.

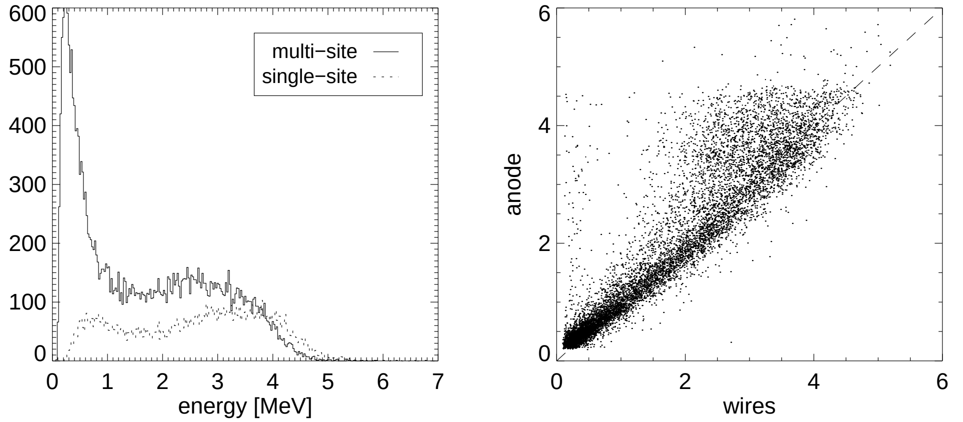

Figure 2.34: *Left:* Energy spectra for 1-site and 2-site events from an Am-Be source, as derived from wire amplitudes. *Right:* Scatter plot of wire amplitudes (averaged x- and y-signal) vs. anode amplitudes.

Chapter 3

LXeGRIT: response to MeV γ-ray

Introduction

The present chapter offers a detailed study of the response of the LXeGRIT instrument to MeV γ-rays, based both on experimental data and an extensive use of Monte Carlo (MC) simulations. I will focus on a set of data taken during the preparation of the flight in Oct. 2000.

The chapter is organized as follows:

a. Sec. 3.1: here I introduce a precise and hopefully clear definition of *response* for LXeGRIT.

b. Sec. 3.2: the MC simulation of LXeGRIT is described, as it is a necessary tool.

c. Sec. 3.3: the detection efficiency in its various parts is described; as it will be clear, the detection efficiency constitutes the crucial part in modeling the response of the instrument.

d. Sec. 3.4: a specific example of efficiency's calculation is worked out step-by-step.

3.1 Definition of the problem

Throughout this chapter, LXeGRIT will be dealt with as an imaging calorimeter but I will stop short of discussing the key issue of imaging MeV γ-ray sources, which is dealt with in Ch. 4. Experimentally, the problem we are facing is described by

$$f(E,n) = \int R(E,n \mid E_\gamma,\vec{r}) f_{source}(E_\gamma,\vec{r}) dE_\gamma d\vec{r} \tag{3.1}$$

where:

1. $f(E,n)$ is the energy (E) spectrum we measure for a given multiplicity (n).
2. $f_{source}(E_\gamma,\vec{r})$ describes the γ-ray flux; it varies from a δ-function both in energy (E_γ) and position ($\vec{r}$), if it describes a mono-energetic point-like source at infinite distance, to any function of $\vec{r}$, accounting for the geometry of the source and the angular dependece of the flux, and E_γ, for continuous emission.
3. $R(E_\gamma,\vec{r} \mid E,n)$ is the *response function*, at this point just a definition.

A little digression is useful here, to define the interaction multiplicity.

Interaction Multiplicity

The concept of *interaction multiplicity* will be ubiquitous throughout this thesis and it already poked its head out in the previous chapter. It can be naively thought about as the number of interactions a γ-ray undergoes in the detector, the ideal interaction chain being: Compton scatter - Compton scatter - ... - photoabsorption. In practice the operative definition of *interaction multiplicity* is the number of interactions that are detected above some energy threshold and spatially resolved, and events are classified accordingly as 1-site, 2-site, ..., n-site events. The concept of *multiplicity* is obviously important for a CT, for at least two interactions are required to perform any Compton imaging, but it should be clear that it is almost meaningless without specifying the actual detection device. E.g., a 2-site event in LXeGRIT has almost nothing to do with a 2-site event in COMPTEL.

It should be equally clear that the ideal interaction chain is highly unlikely at high energies (above few MeV), where the dominant interaction process is pair production and secondary bremsstrahlung photons are not negligible. □

Now back to the response function. Given a point-like, mono-energetic source at a known location, $R(E_\gamma, \vec{r}; E, n)$ is by definition the measured energy spectrum for a given multiplicity. Quite obviously the inverse problem, i.e. to find $f_{source}(E_\gamma, \vec{x})$ once $f(E, n)$ is given, is more often the interesting one (see for example Ch. 6 and Ref. (34)). To tackle Eq. 3.1 in its entirety is not advisable; in fact, written as $R(E_\gamma, \vec{r}; E, n)$, the response function hides several intermediate steps.
A more fruitful approach is to follow *each* γ-ray through the detection process, subdivided into five independent steps:

1. the γ-ray is tracked through the detector mass model; this step accounts for the solid angle, for possible interactions in the passive materials surrounding the LXeTPC and for interactions in the active volume. This first step requires a MC simulation; at the end of it, the γ-ray with initial energy E_γ and direction $\vec{r}$ is changed into an array containing energy loss and 3D location for each interaction: $(E'_1, \vec{x}'_1; ...; E'_m, \vec{x}'_m)$, where m is the interaction multiplicity. (Sec. 3.2)

2. interactions in the active volume are extracted from $(E'_1, \vec{x}'_1; ...; E'_m, \vec{x}'_m)$, a minimum energy is required in each interaction, each energy deposit is smeared according to the measured energy resolution, interactions too close in space to be resolved are clustered as a single interaction and their energies summed up. Eventually a new array $(E_1, \vec{x}_1; ...; E_n, \vec{x}_n)$ is produced, with the detected multiplicity $n \leq m$ by definition. (Sec. 3.2 and Sec. 3.3.1)

3. the probability P_1 to trigger the TPC, i.e. to give a PMT signal above threshold, is calculated for each event, as a function of energy and position for each interaction. (Sec. 3.3.3)

4. the probability P_2 to pass the second level trigger is calculated for each event, as a function of the total energy $E = \sum_1^n E_i$ and the multiplicity n. (Sec. 3.3.3)

5. additional contributions which come from the detector dead time (mainly ascribable to the DAQ system) and more off-line data analysis behave

like an overall normalization factor and do not need to be applied event-by-event. (Sec. 3.3.2 and Sec. 3.3.4)

Following these five steps, Eq. 3.1 can be re-written as

$$\begin{aligned}
(E'_1, \vec{x}'_1; ...; E'_m, \vec{x}'_m) &= R_1(E'_1, \vec{x}'_1; ...; E'_m, \vec{x}'_m \mid \\
&\quad E_\gamma, \vec{r}) \otimes (E_\gamma, \vec{r}) && (3.2)\\
(E_1, \vec{x}_1; ...; E_n, \vec{x}_n) &= R_2(E_1, \vec{x}_1; ...; E_n, \vec{x}_n \mid \\
&\quad E'_1, \vec{x}'_1; ...; E'_m, \vec{x}'_m) \otimes (E'_1, \vec{x}'_1; ...; E'_m, \vec{x}'_m) && (3.3)\\
(E_1, \vec{x}_1; ...; E_n, \vec{x}_n; P_1) &= R_3(P_1 \mid E_1, \vec{x}_1; ...; E_n, \vec{x}_n) \otimes \\
&\quad (E_1, \vec{x}_1; ...; E_n, \vec{x}_n) && (3.4)\\
(E_1, \vec{x}_1; ...; E_n, \vec{x}_n; P_1; P_2) &= R_4(P_2 \mid \sum_1^n E_i, n) \otimes \\
&\quad (E_1, \vec{x}_1; ...; E_n, \vec{x}_n) && (3.5)
\end{aligned}$$

and eventually Eq. 3 is recovered combining a proper number t of events, as

$$f(E, n) = R_5 \left[(E_1, \vec{x}_1; ...; E_n, \vec{x}_n; P_1; P_2)_i \right]_{i=1,\ldots,t} \tag{3.6}$$

The rest of the chapter will explain how this procedure is practically implemented and how it is validated.

3.2 Monte Carlo simulation of the LXeGRIT detector

A careful description of the LXeGRIT instrument cannot be given setting aside the valuable insight obtained through a detailed MC simulation of the detector. It provides valuable knowledge of the different interactions γ-rays in the 0.5-10 MeV energy band undergo in the detector, and gives a clear picture of the impact of passive materials and full energy containment. It can be used to reliably cover energies and flux configurations (e.g. extended sources with specific angular dependences) which are not directly available from radioactive sources in the laboratory. MC studies of the performance of the LXeGRIT instrument have been based on the GEANT 3.21 detector simulation package (46). Each γ-ray is tracked through a detailed mass model of the detector, describing all the constituent parts.

3.2.1 Mass Model

The mass model implemented in the MC simulation is essentially a slavish codification of the LXeTPC, its cryostat and vacuum vessel as described in Sec. 2.1; the readout electrodes, the PMTs and the boxes housing the front-end electronics have not been introduced in the simulation since they are peripheral with respect to the LXeTPC fiducial volume and their mass is rather negligible. The mass model, as encoded in the MC simulation, is shown in Fig. 3.2. Notice, in the lower panel, some of the support structure; in particular the chamber plate, made out of aluminum with a thickness of 2 cm.

Up to this point the gondola has been neglected. This is very much acceptable while dealing with sources which irradiate the LXeTPC from above, as it is always the case in laboratory experiments, since the LXeTPC sits on top of the gondola. This is most likely a bad assumption when a large fraction of the γ-ray flux comes from below the LXeTPC, as it is case for the atmospheric γ-ray flux (see Ch. 6 and Ref. (34)). For a description of the gondola as in the 1999 balloon flight, see Ch. 5 and Ref. (9). The gondola itself underwent only minor changes in view of the 2000 flight. The most relevant change was the removal of the massive NaI shields which surrounded the LXeTPC in 1999. A picture of the LXeGRIT payload, ready for the 2000 balloon flight, is shown in Fig. 3.1.

The model described in the following refers to the configuration in year 2000. The exact encoding of the gondola structure and of various pieces of equipment was not pursued, since it would have been overly intricate and unnecessary. In fact what is ultimately relevant is the amount of passive materials γ-rays have to cross *on average* before hitting the active volume. The gondola may be thought of as a truncated cone, 102 cm high with a diameter of 183 cm at the bottom and a diameter of 122 cm at the top, while the top is 38 cm from the chamber plate. The various components of the equipment are rather evenly distributed and the most abundant material is by far aluminum. A simplified model has been implemented, using parallel "disks and donuts" at three different locations in z:

1. an aluminum disk of 183 cm diameter and 3.5 cm thickness, at a distance of 140 cm from the chamber plate along z;
2. an aluminum disk of 152 cm diameter and 1.7 cm thickness, at a distance of 89 cm from the chamber plate along z;

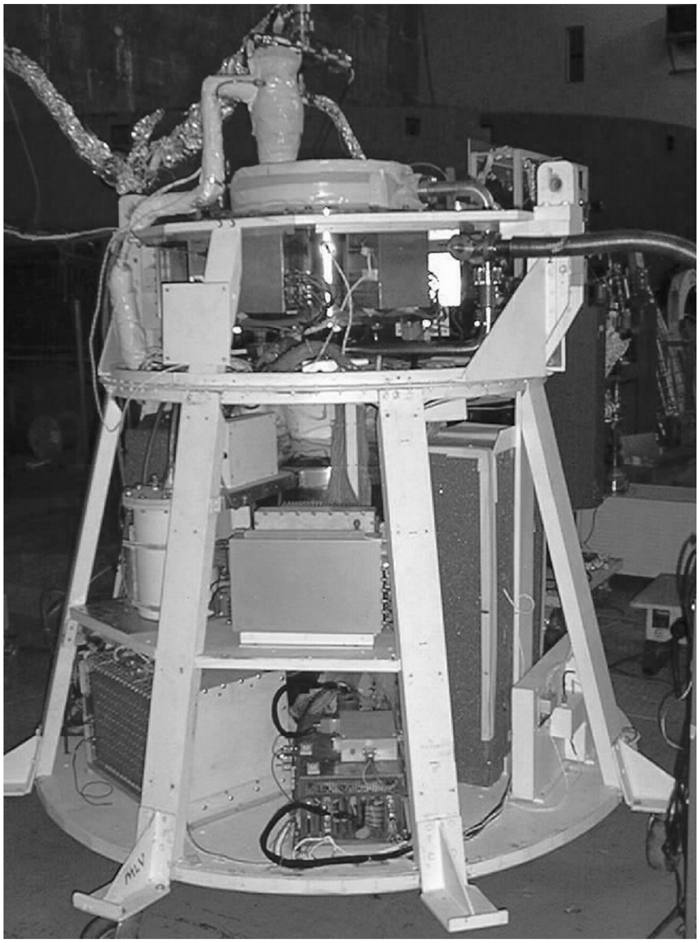

Figure 3.1: The LXeGRIT detector in flight configuration. The cryostat enclosing the LXeTPC is only partially visible in the upper part of the picture, hidden behind the boxes of the front-end electronics. On the right, the battery stack is visible; on the left (bottom) the rack of the LXeTPC digital electronics; on top of it, 2×36 GB data disks and more electronics.

3. an aluminum donut of 122 cm external diameter, 61 cm internal diameter and 1.4 cm thickness, at a distance of 38 cm from the chamber plate along z;
4. a steel disk of 61 cm diameter and 1 cm thickness, at a distance of 38 cm from the chamber plate along z.

Its main features are shown in Fig. 3.3. The accuracy of this model of the gondola is expected to be completely adequate when the γ-ray flux is azimuthally symmetric, or the spinning of the instrument around the z-axis washes out any azimuthal dependence. Unfortunately this expectation could not be tested experimentally. In practice, the gondola is needed in the MC simulation only for the atmospheric γ-ray flux, and in that case the dominant uncertainty is on the flux itself.

By way of an example, in this mass model:

- a γ-ray coming from *above* along the z-axis will cross the following passive materials: 5 mm of stainless steel (vacuum vessel thinned window), 2 mm of stainless steel (cryostat thinned window), 5 mm of passive LXe above the cathode, 5 mm of ceramic (cathode);
- a γ-ray coming from *below* along the z-axis will cross the following passive materials: 52 mm of aluminum (gondola), 10 mm of stainless steel (gondola), 10 mm of stainless steel (vacuum vessel), 20 mm of stainless steel (cryostat), 36 mm of passive LXe below the grid.

The radiation length is 2.6 cm in LXe, 7.5 cm in the ceramic of the cathode, 8.9 cm in Al and 1.8 cm in stainless steel. Passive materials amount to less than 1 radiation length for γ-rays from above, and amount to several radiation lengths for γ-rays from below. Obviously this is not a coincidence, since interesting astrophysical objects shine on top of the TPC. $\square$

For each interaction of a γ-ray tracked through the mass model, x-y-z location, energy deposit and interaction type are recorded. Up to this point, only the mass model of the detector and the physics of γ-ray interaction are accounted for.

Other main effects are then introduced in this order:

1. treatment of the *charge signal*;
2. treatment of the *light signal*.

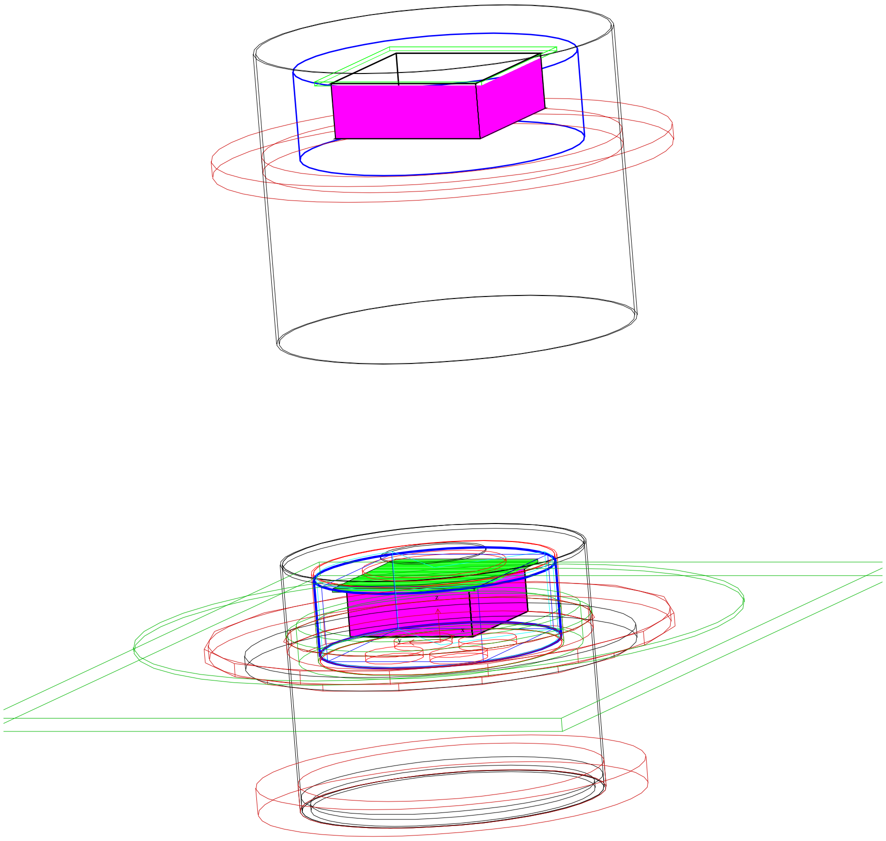

Figure 3.2: 3D schematic of the mass model of the LXeTPC, as implemented in the MC simulation. *Top:* the vacuum vessel, the cryostat and LXeTPC fiducial volume (shaded area) with the cathode on top. *Bottom:* a more intricate and detailed view. Notice the extended chamber plate and the four "holes" for the PMTs at the bottom of the LXeTPC fiducial volume.

In some way, MC events are dealt with following the inverse path respect to the real data.

The response of the TPC to a *charge signal* is parameterized in terms of minimum energy threshold and minimum spatial separation required to consider two close-by interactions mutually resolved, as derived from calibration

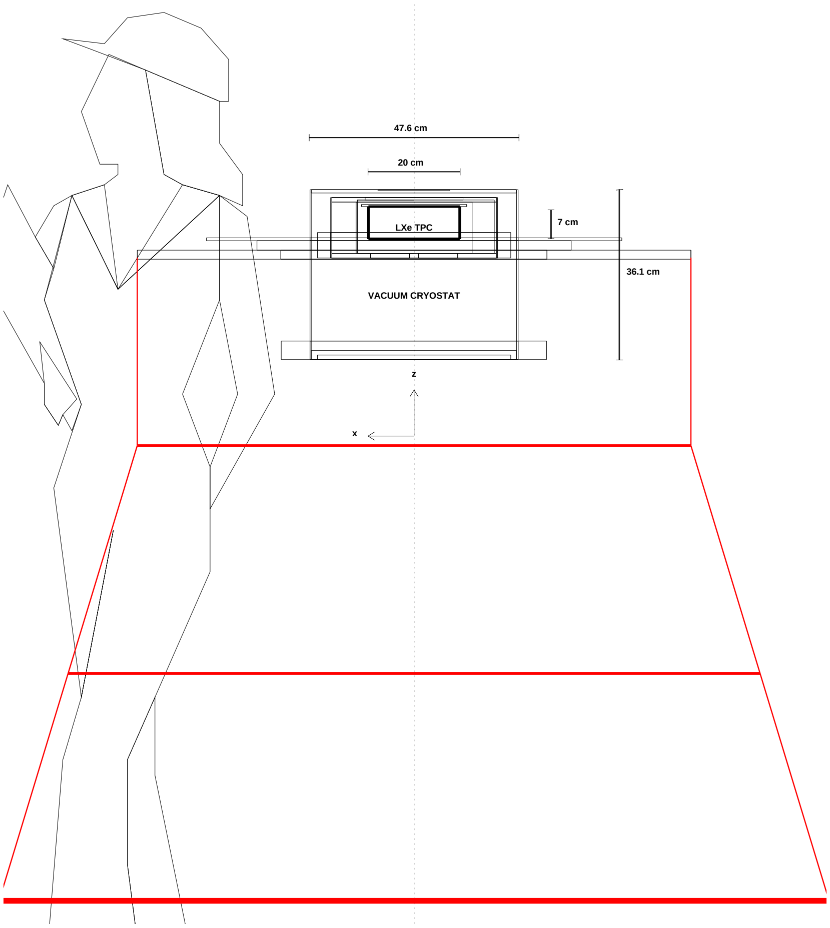

Figure 3.3: Schematic of the mass model of LXeGRIT instrument, in the x-z plane. The gondola has been modeled as if the mass was concentrated in three planes. See text for explanations.

data (cfr. Sec. 2.1). I do not use MC events to generated digitized waveforms, which would be more accurate but is deemed to bring only a modest advantage to be compared to a cumbersome implementation.

The best choice of the minimum separation in the $x - y$ coordinates is a normal distribution with mean value 5 mm, 3 mm RMS and a sharp minimum of 4 mm, while on the z coordinate a normal distribution with mean value 4 mm, 1 mm RMS and a sharp minimum of 3 mm. A pair of interaction must be resolved in $x - z$ *and* $y - z$ but can be confused in z *or* x *or* y. If this condition is not fulfilled the two interactions are clustered and considered as one single interaction, with energy equal to the summed up energies. The minimum energy threshold follows again a normal distribution with mean value 150 keV, 40 keV RMS and a sharp minimum of 40 keV. This energy threshold is applied to each single interaction (after clustering) and not to the total energy loss in the fiducial volume. The minimum energy threshold and minimum separation are given from the wire signals.

The deposited energy is then smeared according to the measured energy resolution (Sec. 2.2.3) for anode signals

$$\Delta E[\mathrm{MeV}]\ (FWHM) \ = \ \sqrt{6.7 \cdot 10^{-3} \cdot E[MeV] + 3.6 \cdot 10^{-3}}$$

We can say that we mainly describe the *wire* response (which sets an energy threshold higher than the anode one, together with providing a finer spatial resolution) but for the energy resolution, given from the fitted *anode* signal.

The LXeGRIT trigger is described in Sec. 3.3.3 and here I anticipate its implementation in the MC simulation. The efficiency of the light trigger is mapped into a 4D - E, x, y, z - data space, as described in Sec. 3.3.3, and the response of the light trigger system has to be applied to the MC data, where we have, for each event we have E_1, x_1, y_1, z_1; ...; E_n, x_n, y_n, z_n where n is the event multiplicity. For each E_i, x_i, y_i, z_i we have some “probability” to trigger the detector. For 1-site events this is exactly what is needed, but for multi-site events we have to figure out the trigger probability for the entire event, i.e. n interactions combined. First of all, the 6 lookup tables (6 z-slices) described in Sec. 3.3.3 are interpolated to give a 31×31 grid in the $x-y$ plane (∼6 mm granularity), so that the fiducial volume is now subdivided in 31×31×6 cells. Together with the energy dependence, which is described analytically, this map can be related to number of photoelectrons (p.e.) given from each point in this 4-D data space, i.e. we obtain a position-weighted energy which has a one-to-one correspondence to the number of p.e. for each interaction. The actual procedure, while starting from this basic assumption, is actually simpler. We know from the actual data that a PMT sees very little of what is happening above a neighboring quadrant and for this reason we can sum up the position-weighted energies in the same quadrant and combine trigger probabilities as uncorrelated for events in different quadrants. At this point we have, for each PMT, only one position-weighted energy and we are back to the 1-site case. It is now straightforward to relate the position-weighed energy to a proper statistical weight, named P_1 in Sec. 3.1.

The part of the detector response due to the SLT is introduced at this point of the data analysis, parameterized vs. energy for each multiplicity, as shown in Sec. 3.3.3.

This approach has been validated through detailed comparison with the actual TPC data. The good accuracy in reproducing experimental data is exemplified by the examples discussed in Sec. 3.4.

3.3 Detection efficiency

The overall efficiency of the LXeTPC to MeV γ-rays is the combination of several diverse contributions:

1. passive materials and containment
2. DAQ deadtime
3. light trigger
4. on-line selections
5. off-line selections

3.3.1 Multiplicity, passive materials and containment

It is very practical to rely on MC techniques when dealing with this piece of efficiency, for several reasons. All the other inefficiencies can be switched off, i.e. efficiencies set to one; energies not accessible with γ-rays from calibration sources and different source positions, not easily reproduced in laboratory measurements, can be studied; ways to reduce efficiency losses due to passive materials, lack of stopping power or other detector parameters can be studied in great detail.

Results presented here are for a parallel flux of monochromatic photons at normal incidence, impinging on the detector from above and covering the whole sensitive area. The detector response is carefully described, but I explicitly avoid including the response of the light trigger, of the second level trigger, of the DAQ and of the off-line data analysis.

The interaction multiplicity for 0.5, 1, 2, 3, 5 and 10 MeV photons *after* the detector response described above is shown in Fig. 3.4. The same curves for fully contained events are superimposed. It is already interesting to stress

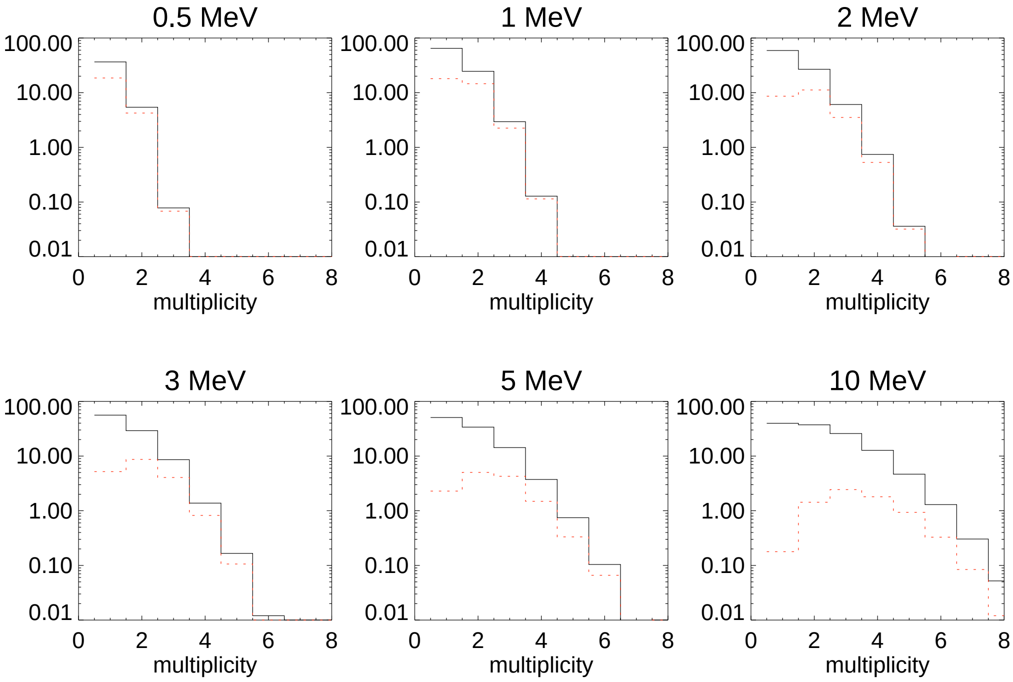

Figure 3.4: Interaction multiplicity for different energies (0.5, 1, 2, 3, 5, 10 MeV). The superimposed *dashed histogram* shows the interaction multiplicity for fully contained events.

that, while the single site events are the most numerous at all energies, the fully contained ones are more easily found in the multi site sample for energies exceeding 1 MeV. The interaction multiplicity is reduced compared to the number of interaction a γ-ray undergoes “on average” before escaping the detector or being photoabsorbed. This reduction is due both to the relatively high (150 keV) energy threshold and to the spatial confusion of close-by interactions. While the energy threshold implies a neat loss of detection efficiency, the effect of spatial confusion is a degradation of interaction multiplicity, even if the total energy is still correctly measured (e.g. a photon interacting twice can be detected as a single site event the total energy still being the correct one). At energies above 5 MeV the detected multiplicity may exceed dramatically the number of interactions of the original photon, due to the presence of secondary bremsstrahlung photons.
The ratio *contained / total* is shown as a function of multiplicity in Fig. 3.5. It is telling us that the multi-site sample, even when less efficient, is always

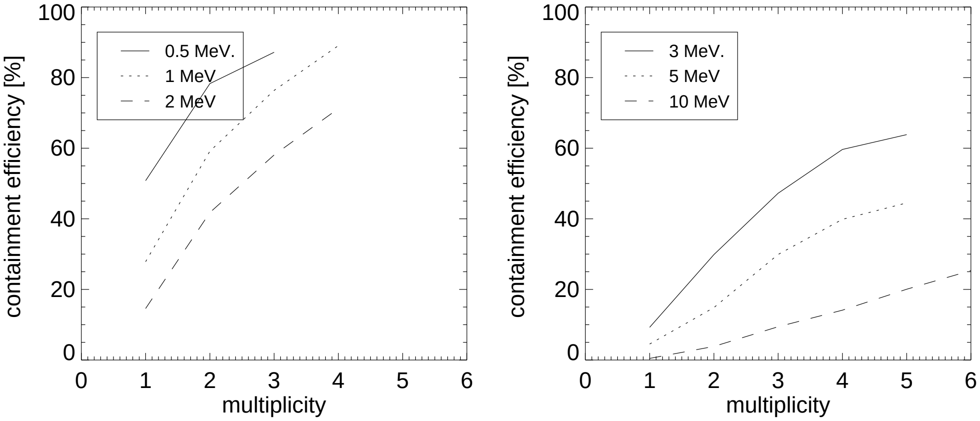

Figure 3.5: Containment efficiency as a function of interaction multiplicity for different energies (0.5, 1, 2, 3, 5, 10 MeV); as a general trend, for higher energies the containment efficiency is lower and the containment efficiency is improved for higher multiplicities.

providing a reduction of the Compton continuum and non-contained events, i.e. a cleaner signal in terms of spectroscopy. As expected, the overall efficiency for containment is decreasing as the initial energy increases.

The detection efficiency (here defined as full containment) for different event topologies, as a function of energy, is shown in Fig. 3.6. On the left, efficiency when all the events are considered; on the right, after rejecting bremsstrahlung and pair production events, which is relevant only for double and multiple site events.

For, at this point, the detector model does not account for the light trigger and other efficiencies, the estimated efficiency is obviously too optimistic, and especially for γ-rays energies below 1 MeV it would be lowered by a factor as large as (or larger than) 10 - see next. Nevertheless, this simplified model still offers a useful guideline to interpret the results shown in the next section and it provides us with a robust upper limit on the efficiency of the detector, both for mere spectroscopy (Fig. 3.6 - left) and Compton imaging (Fig. 3.6 - right). As a spectrometer, efficiencies for different multiplicities can be summed up, while as a CT only efficiencies for double and multi site events can be combined. These combined efficiencies are shown in Fig. 3.7 - efficiency as a calorimeter is robust, once inefficiencies in Secs. 3.3.3-3.3.4 do

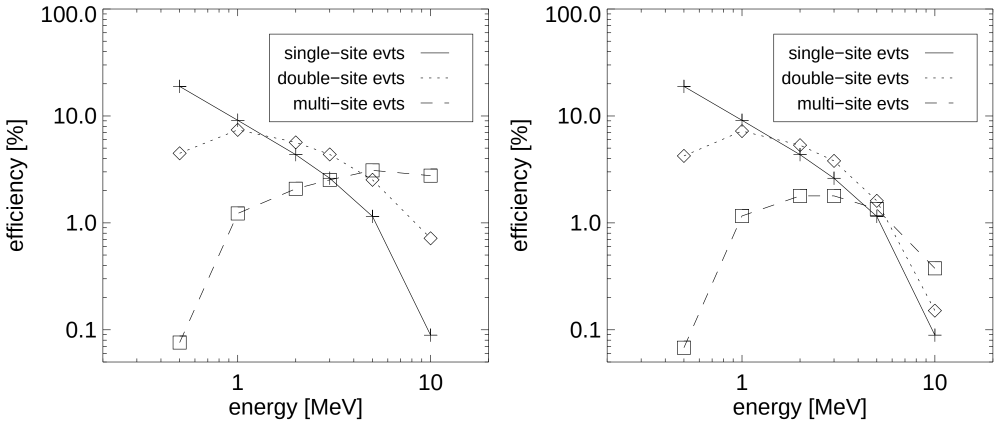

Figure 3.6: Detection efficiency as a function of energy for different multiplicities: +, 1-site events; ◊, 2-site events; □, 3-site events or higher multiplicities. *Left:* all γ-ray interactions considered. *Right:* pair-production and bremsstrahlung events excluded.

not need to be considered. As a CT, the efficiency is grossly overestimated even in that case, for multiple interactions have to be time-sequenced before proceeding to Compton imaging (but see Ch. 4).

When a more quantitative comparison to the LXeGRIT data is required and well defined experimental conditions have to be matched, more detailed models of the detector response, fully rendering the efficiency losses described in Secs. 3.3.2-3.3.4, are applied.

In Fig. 3.8 the efficiency for sources at different angles from the vertical (z-axis, in this case) is shown. It defines the *field of view* (FoV) of the instrument, which is an important parameter for a CT. In some arbitrary way we can define the FoV as the angular aperture in which the detection efficiency is larger than 50% of the efficiency on-axis. In the present case the FoV is about 50° or 0.4 2π sterad. Two main parameters determine the FoV: the geometrical area and the amount of passive materials in front of it, which varies with the angle. Results shown in Fig. 3.8 are for a source with a power law spectrum with spectral index -2, as is actually the case for the Crab Nebula. It is very apparent that the main contribution comes from the reduction of the geometrical area, from a maximum of 18.6×18.6 cm^2 for sources on-axis to a minimum of 7×18.6 cm^2 for sources at 90°. This trend is indeed mostly

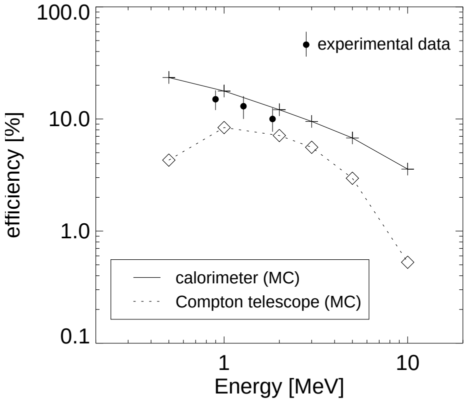

Figure 3.7: Detection efficiency of the LXeTPC as a function of γ-ray energy. Two cases are considered, the *spectrometer mode* and the *Compton telescope mode*, which requires multiplicity 2 or larger and no pair-production or bremsstrahlung interactions. The correct time sequence of interactions is assumed to be known. Experimental data are in *calorimeter or spectrometer mode* for 0.898 and 1.836 MeV (^{88}Y) and 1.275 MeV (^{22}Na); the details of the efficiency measurement are given in Sec. 3.4. (+, calorimeter; ◇, Compton telescope.)

energy independent. The impact of passive materials is on the other hand quite energy dependent, because of the dependence on energy of the attenuation length for photons - i.e. the effect is more pronounced for low energy γ-rays. It is seen both in the left panel, where the requirement for containment enhances the dependence on the angle, telling the story of a larger (on average) energy loss in passive materials before entering the fiducial volume, and in the right panel, where the energy dependence (for contained events) is shown for the energy bands 0.85-1 MeV, 1-3 MeV and 3-10 MeV.

3.3.2 Data acquisition

A detailed description of the DAQ for the LXeGRIT instrument has been given in Sec. 2.1.6 and in Ref. (10). The total throughput of the DAQ is limited to about 1.6 MB/s, restricting the event building rate to 40-50 events/s when data are taken in a mode that reads all information from anodes and wires, providing a full image of the chamber (in this case the

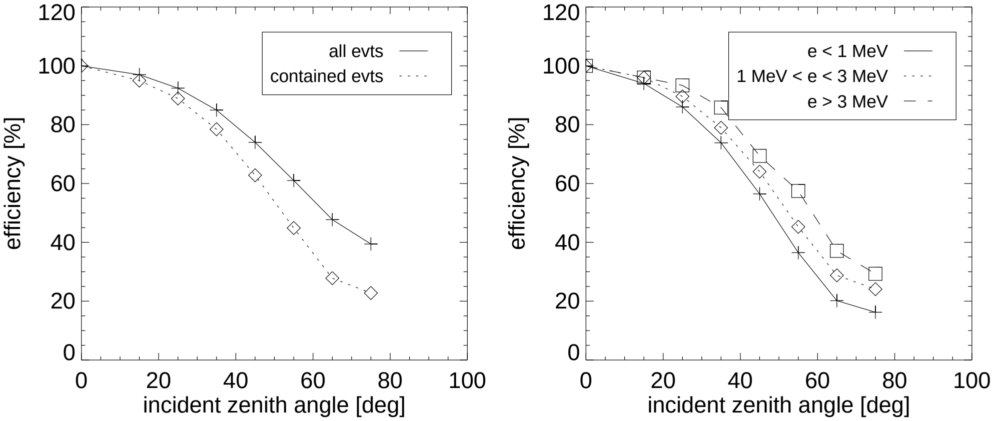

Figure 3.8: Detection efficiency as a function of the angular distance from the zenith (detector coordinates), normalized for a source on-axis. The FoV of LXeGRIT is defined by the maximum angular distance after which the detection efficiency drops below 50%. The decrease in efficiency is mainly due to the decrease in geometrical area as it is seen from the source at larger angles. Because of passive materials within the FoV and the relatively complicated interaction sequence γ-rays undergo in the detector, a MC simulation has been used. Photons have been generated following a power law spectrum with index 2. *Left:* Considering all events interacting in the fiducial volume (+ and continuous line) and fully contained events (◊ and dotted line). *Right:* Dividing the fully contained events in energy bands: 0.85-1 MeV (+ and continuous line), 1-3 MeV (◊ and dotted line) and 3-10 MeV(□ and dashed line).

event size is about 30 kB). The more usual data-taking mode transfers only wire waveforms which crossed preset thresholds together with the four anode waveforms and the maximum rate of built events increases to 200-400 Hz, the actual value heavily depending on the selection parameters and the specific source. The event size also depends on the selection parameters. For typical settings, the average event-size is ~5 kB.

In flight conditions the system was able to build about 300-350 events/s out of a trigger rate of about 650 Hz, including a large fraction of non-γ events (mainly charged particles). About 20% of the handled triggers were typically accepted as valid events, resulting in a data throughput in the range of 0.4-0.5 MB/s sent via the transmitter or written on the on-board disks. In laboratory conditions, where strong calibration sources are available together with a very small rate of non-γ background, the final throughput data rate can be three times as large. The large bandwidth of disk writing is usually not filled up and therefore there is no further efficiency loss once an event has been built.

The performance of the DAQ can be - and usually is - the main limiting factor to the efficiency of LXeGRIT for many practical applications and dictates selections at the trigger level, illustrated in Secs. 3.3.3, 3.3.3 and 3.4. The TPC itself, given a maximum time of about 40 μs needed to drift and collect the ionization charge, is hardly dead-time limited in any realistic situation.

A set of 16 counters registers all signals at various locations of the trigger logic, providing a direct measurement of the DAQ livetime fraction, of the various trigger and rejection rates.

3.3.3 Event trigger

Decisions at the trigger level are made necessary by the limited DAQ speed which ultimately imposes an upper limit to the maximum rate of useful events, i.e. events written to disk and made available for further analysis. Once this upper limit is saturated, the final CT-efficiency can be improved only being more selective and enhancing the fraction of multi-site events in the final data sample.

The LXeGRIT event trigger works on two different levels: a *first level trigger* (FLT) which requires a signal from the PMTs and a *second level trigger* (SLT) which performs further selections based on the anode/wire signature. Both the FLT and the SLT are described in greater detail in Sec. 2.1.7.

The FLT allows a fast (∼ns) decision without keeping the DAQ busy, which is very useful when dealing with high rates. For the light trigger system provides an extremely poor energy resolution and is blind to multiplicity, it is very difficult to tune in order to select specific event categories. The experience gained during the 1999 balloon flight clearly demonstrated that, when the energy spectrum is soft (as it is for the cosmic diffuse and atmospheric γ-ray background, being a power law with index 2), a high trigger efficiency at this level is equivalent to accept a dominant fraction of events at low energies (∼150 keV being the anode energy threshold) which are of little if any use for a Compton telescope.

For this reason, preparing for the 2000 flight we opted for a low efficiency of the FLT, largely gaining in efficiency for Compton imaging events. As shown in Fig. 3.9, the FLT efficiency saturates only above 4 MeV, where the flux is at any rate low, thus the instrument is optimized for the 1-3 MeV energy band. This is obviously a compromise. It is all but apparent from Fig. 3.9 that the overall performance of LXeGRIT would greatly benefit by an improved energy resolution (in practice, light yield) of the light trigger system, so as to obtain a much sharper response function vs. energy, able to reject with efficiency close to 100% events below a fixed energy threshold, and to trigger with high efficiency above that threshold. Studies in this direction have been started and are described in Ref. (13).

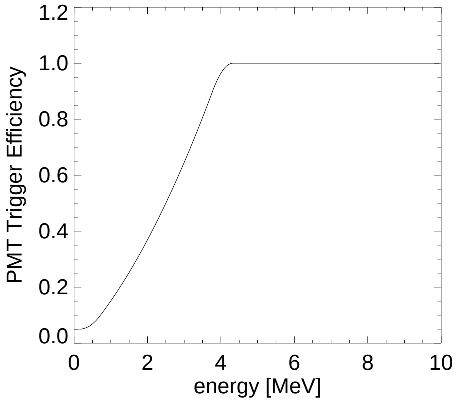

Figure 3.9: Efficiency of the light trigger system vs. energy as derived in Sec. 3.3.3, parameterized and extended up to 10 MeV.

Wire and anode signals are also exploited to perform on-line checks; these checks are called second level trigger and they fall into two main categories:

1. the event is built (see Sec. 3.3.2) and the number of threshold-crossings on the $x-$ and $y-$ wires (*wire hits*) is checked to be greater than a predefined minimum and less than a predefined maximum. This step requires little readout time, since each channel is 1 byte only (SLT);
2. the amplitude of the anode waveform is checked against a given threshold. This step requires the readout of the digitized waveforms and is relatively slow (it is considered as part of the SLT).

The importance of 1 and 2 is rather different. Imposing a threshold on the anode waveform is very effective in rejecting low energy events which are useless for a CT, but it requires to previously readout the digitized waveforms and the slowness of this process greatly reduces the usefulness of such an online selection. It has been mainly used during laboratory calibrations, when efficiency is not a real concern, in order to save disk space.

Checking the number of wire hits is, on the other hand, relatively fast and is sensitive to specific event multiplicities; this option is relevant for a CT, since Compton imaging requires at least two, but preferably three, interactions. The SLT has proven to be a powerful tool, but at the same time somewhat fragile and critically dependent on the noise level of the wires, and needed to be carefully monitored. Matching the $x-$ and $y-$signals would be an - ideally - obvious improvement. Unfortunately it requires radical - and expensive - changes to the DAQ system.

First Level Trigger: efficiency

The efficiency of the light trigger system, at least for the most recent settings, is far from saturated for energies below 4 MeV and it has to be described as a function of interaction location in the fiducial volume and energy deposit.

The efficiency of each PMT, integrated over the fiducial volume, can be measured comparing the count rate of the triggering events relative to the total count rate. Fig. 3.10 [1] shows the Multi Channel Analyzer (MCA) spectra of the charge signals from the anode directly above the PMT, gated by the PMT light trigger and ungated. The ratio of events with a trigger and of all events, under the full energy peak, was taken as the trigger efficiency for the particular γ-ray energy line. The MCA spectra were taken with 10 μs shaping time for the anode shaping amplifier. Given the 35 μs maximum drift time, γ-rays interacting two or more times in locations more than 10 μs apart in drift time contribute to the background below the line. From a fit of the lines, the trigger efficiency at 0.662 MeV (^{137}Cs) is 90% for the discriminator window of 10-255. By lowering the upper threshold from 255 to 128, the efficiency drops to 63%.

This efficiency can be directly measured and resolved vs. energy and position in greater detail. The basic procedure has been described in Ref. (73), applied to the 1999 configuration.

---

[1] The detector was in the 1999 balloon flight configuration.

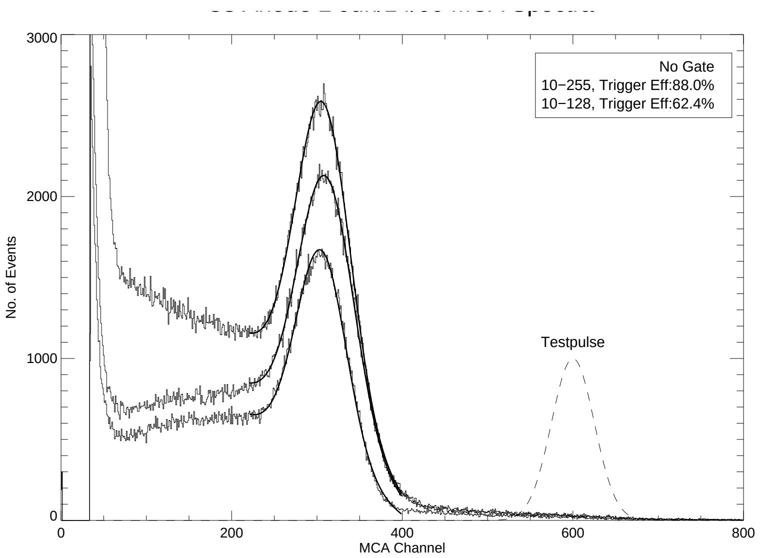

Figure 3.10: ^{137}Cs 0.662 MeV energy spectra for all anode signals (*upper curve*) and for anode signals with a light trigger (*lower curves*) for two discriminator windows.

Briefly summarizing it: an external trigger is needed, to work as FLT and start the DAQ independently of the light trigger system. This is obtained tagging a γ-ray source, which is typically done using a source coincidentally emitting two or more γ-rays and detecting one of them with an external counter. A signal from the light trigger system is then independently recorded. The collected data fall into three classes:

A. events with an interaction detected in the fiducial volume (charge signal) and a light trigger which matches the external trigger - this class is obviously the one contributing to the efficiency;

B. events with an interaction detected in the fiducial volume and a light trigger which does not match the external trigger (just a chance coincidence count) - this class introduces a background in the measurement, that has to be accounted for;

C. events with an interaction detected in the fiducial and without a light trigger - this class gives the inefficiency fraction.

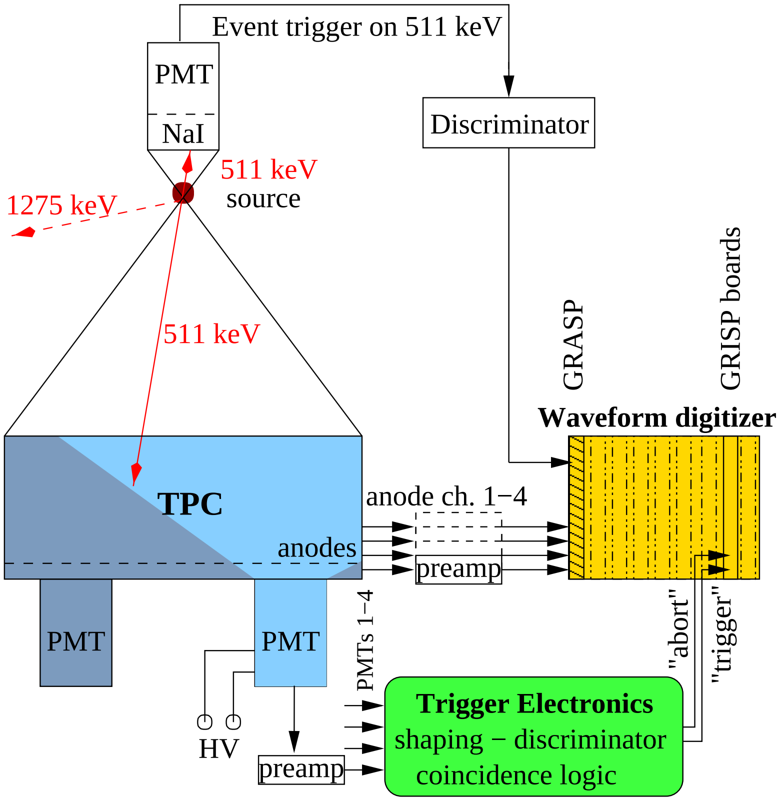

Figure 3.11: Set-up of the spatially resolved trigger efficiency measurement using the LXeGRIT flight electronics and a tagged ^{22}Na source. From Ref. (73).

The efficiency is thus given by the number of events in *class A* divided by the total number of events in which *class B* has been subtracted.

The measurement described in Ref. (73) used a ^{22}Na source, which emits three photons at the same time, one at 1.275 MeV and two at 0.511 MeV which are emitted back-to-back, so that one of the two 0.511 MeV photons could be used to tag the source; the spatial correlation of the two photons allowed a very clean measurement, keeping very low the contamination due to coincidence counts. A sketch of the experimental set-up is shown in Fig. 3.11. The energy range of this measurement was limited up to 0.511 MeV, which is far from ideal for a detector supposed to work up to 10 MeV.

A similar measurement was repeated for the 2000 settings following a different strategy. An ^{88}Y source was used, which emits simultaneously two photons at 0.898 and 1.836 MeV without any spatial correlation, and, separately, a ^{22}Na source. Because of the lack of spatial correlation between the emitted photons, the sources were tagged with low efficiency detecting one of the photons from the decay with a NaI(Tl) counter. Given the source rate and low efficiency in tagging the source, the level of contamination due to chance coincidence counts was high, and, combined with the low efficiency in the 2000 settings, more events ended up in *class B* rather than in *class A*. Nonetheless, the fraction of events in *class B* is independently determined and the final result is then corrected with good accuracy. The procedure is actually rather simple. The z-distribution for events triggered by random coincidence has no physical meaning and extends above the cathode position (7 cm), which delimits the TPC active volume. This is clearly visible in Fig. 3.12 where the z-distribution drops sharply at $z = 7$ cm. The shape of the z-distribution for events in *class B* was determined through data where a “true” random trigger was fed in as FLT; it came out flat (i.e. very little or no dependence on z), so that the fraction can be easily read out from the z-distribution itself. The efficiency of the light trigger system is in this way measured for energies up to about 2 MeV.

The efficiency was then resolved in a four dimensional data space - energy, x, y, z - as made possible by the imaging capability of the TPC. Since we want to resolve spatially each event and, at the same time, the four PMTs see the total energy deposited in the fiducial volume, we restrict ourselves to 1-site events only, for which a univocal association between total energy loss and position is given. Once analyzed the data, it was clear that the efficiency in the (energy, x, y, z) space could be described with good accuracy factoring out the energy dependence, i.e.

$$\epsilon(E, x, y, z) \;=\; \epsilon_1(E) \times \epsilon_2(x, y, z).$$

In practical terms this is very helpful, because of the low efficiency we are measuring and the fine granularity for which we are aiming, which would otherwise require a disproportionately large dataset.

The dependence of the efficiency on the deposited energy is shown in Fig. 3.13 for all the four PMTs combined, combining data from a ^{22}Na and an ^{88}Y source after the fact. A PMT is usually able to detect only interactions happening within its own quadrant and very few events are detected by more than one PMT at the same time, because of the strong solid angle effect on light collection. The response of each PMT is measured and parameterized individually and the energy dependence is easily described analytically.

The x, y, z dependence has been determined by sampling the data with a few mm granularity on each coordinate. It was then parameterized in a lookup table with a granularity of about 1 cm in z and 2 cm in x and y (6 z-slices times 11×11 bins in the $x-y$ plane), fine enough to describe well the light trigger inhomogeneities.

The dependence on z is shown in Fig. 3.12 for one PMT; as expected, the efficiency is reduced moving away from the PMT location (z = -4 cm). The energy spectrum is the one in Fig. 3.13; if energy deposits larger than 1 MeV are selected, the overall efficiency is greatly increased.

An example of efficiency map for the light trigger is shown in Fig. 3.14, as measured using a tagged ^{88}Y source. The efficiency is resolved in the $x-y$ plane of the detector with a few millimeter granularity. At locations corresponding to the four PMTs below the wire structure an enhanced efficiency is clearly visible. The four panels correspond to four different z-slices, going from the bottom of the fiducial volume (*upper-left*) to the top (*bottom-right*), i.e. moving farther away from the PMTs. The impact of solid angle is all but apparent; closer to the PMTs the overall efficiency is higher and less uniform.

Second Level Trigger: efficiency

The impact of the filter at the second level trigger can be known with good accuracy for each specific experiment, provided a sample of data in full imaging mode in which no selection based on the number of wire hits has been applied and the digitized waveform of all the 62 x- and 62 y-wires is recorded, together with the number of wire hits which is known for each event. The procedure is straightforward and one just has to apply off-line the selection usually applied on-line.

The outcome of one of these routine checks is shown in Figs. 3.15, 3.16; data were taken for an ^{88}Y source placed few meters away from the TPC. The minimum number of wire hits required both in the x and in the y plane was 6, the maximum 16; each interaction usually gives 1 or 2 hits, depending on the energy deposit and the threshold of the specific wire. Such a maximum has no impact on γ-events and mainly filters out relativistic charged particles crossing the chamber and giving many hits at the same time. If the electronic noise was negligible, a minimum of 6 would select only events with 3 or more interactions; but since it is not negligible, a certain fraction of 1-site events is accepted (see Fig. 3.16). Moreover, the fraction of accepted events depends

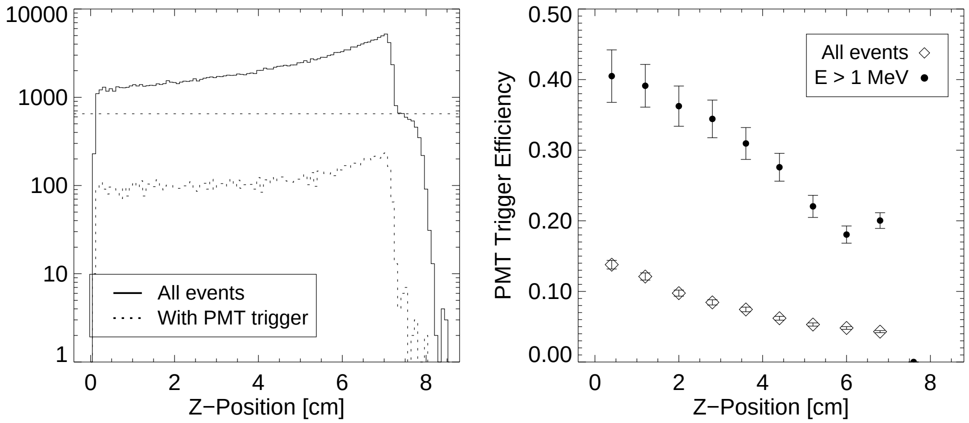

Figure 3.12: z-dependence of the light trigger efficiency; the experimental setup is described in Sec. 3.3.3. *Left:* z-distribution for all events (continuous line) and events with a PMT trigger (dotted line). A sharp drop is visible at $z = 7$ cm, corresponding to maximum "physical" z. Events with z larger than 7 cm are due to a random coincidence between the external trigger and a γ-ray interacting in the fiducial volume, in which case the absolute z position has no physical meaning. Note the logarithmic scale. *Right:* Ratio of the two z-distribution shown on the left, after correction for the fraction of random coincidence events - *open diamonds.* The same ratio after selecting energy deposits larger than 1 MeV- *full circles.*

on energy, since a large interaction is more likely to be detected over noise. For events with multiplicity 3 or higher the efficiency is $\sim 80\%$ above 1 MeV, where most of these events are.

We can say that the main goal of this filter is to reject low energy (below 0.5 MeV) 1-site events; this is especially important when the γ-ray flux has a soft spectrum, as it is case for the atmospheric γ-ray background encountered at balloon altitudes.

This simple procedure just counts the number of wire hits and does not exploit the 3D imaging capability of the TPC. When data are analyzed off-line (see next) the x, y and z coordinates are matched and the contamination due to noisy events is reduced to a truly negligible level.

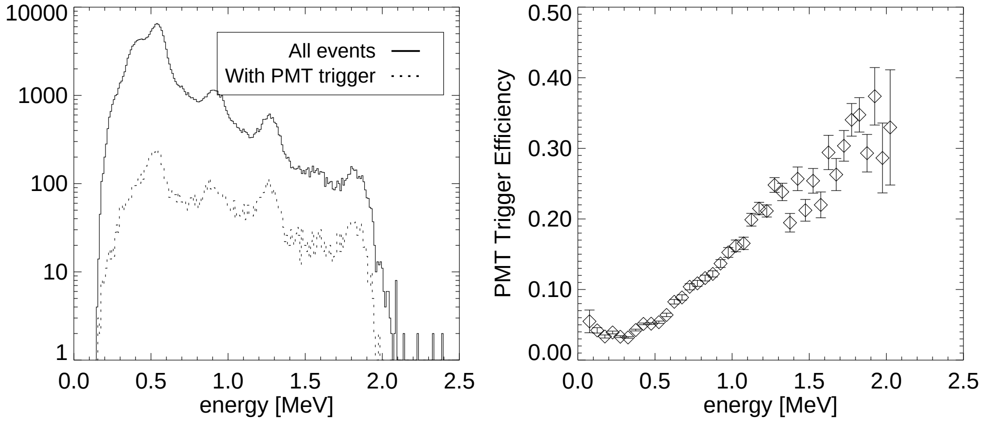

Figure 3.13: Energy dependence of the light trigger efficiency. *Left:* Energy spectrum for ^{88}Y and ^{22}Na source combined, for all events (continuous line) and events with a PMT trigger (dotted line). The 0.511, 0.898, 1.275 and 1.836 MeV lines are clearly visible. *Right:* ratio of the two energy spectra, which gives the light trigger efficiency vs. energy.

3.3.4 Off-line analysis

The off-line analysis procedure rejects "bad" events and extracts 3D position and energy for each interaction from the raw data (wire and anode digitized signals), matching in time the x and y wire signals and fitting the digitized anode waveform. For a thorough description, see Sec. 2.1.8.

In practice the efficiency of extracting the energy and position information from a raw event is extremely high, close to 100%, once a "good" event is provided. For a non negligible fraction of events - about 30% - the off-line analysis sorts out "bad" events, where "bad" means a genuine γ-ray spoiled by a shaky baseline, noisy wires or any other anomalous behavior which compromises the event reconstruction.

This kind of inefficiency obviously does not come from the off-line analysis itself, which on the contrary rejects flawed events - only, since it is recognized at the off-line analysis level, it is classified as "off-line inefficiency".

More than that, the off-line analysis removes improper events like cosmic rays, events happening in the collection region below the grid etc. - these are not considered as inefficiency.

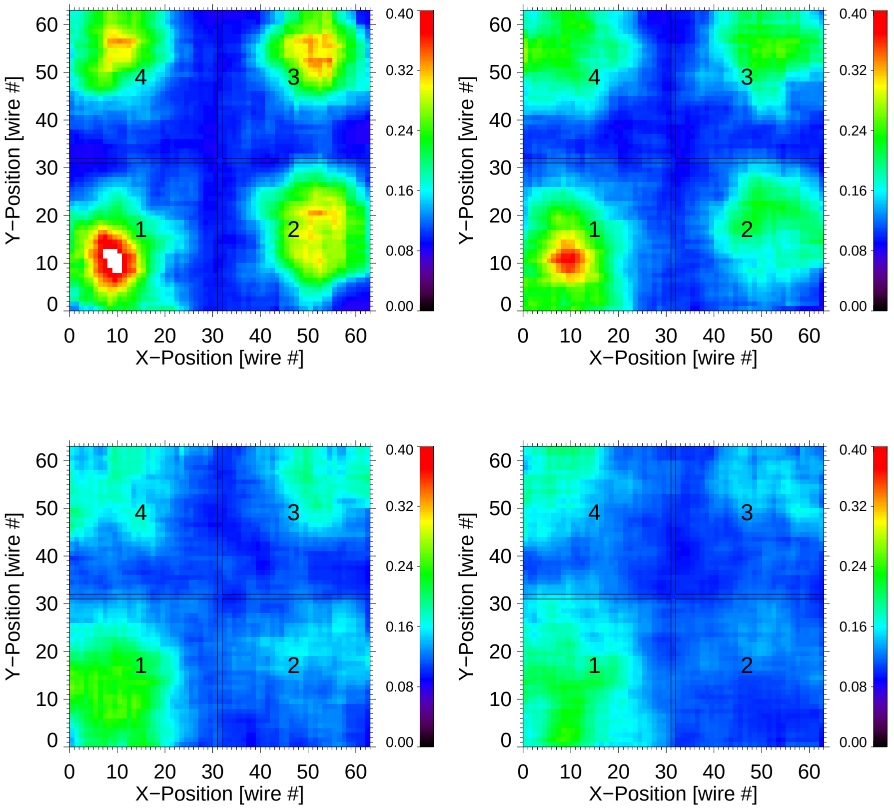

Figure 3.14: Maps of light trigger efficiency in the $x - y$ plane, for four different z-slices, ∼1.7 cm thick. The four PMTs locations are clearly visible as areas of enhanced efficiency. Going from the *top-left* panel to the *bottom-right* one we move from the z-slice closest to the PMTs toward the cathode region. Doing so we see the efficiency decreasing and becoming more uniform over the $x - y$ plane, because of solid angle effect on light collection.

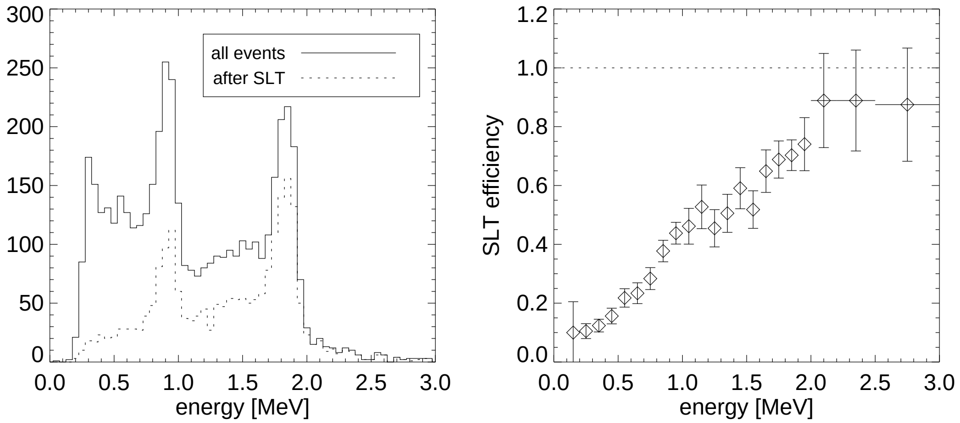

Figure 3.15: Efficiency of the second level trigger (SLT). *Left:* energy spectra for an ^{88}Y source, combining all multiplicities, before (all events, *solid line*) and after SLT (*dashed line*). *Right:* ratio of the two energy spectra, which gives the SLT efficiency vs. energy.

3.4 Model vs. experimental data

Figs. 3.17, 3.18 and 3.19 offer three examples of how well (or badly) experimental data can be reproduced and explained through the procedure described here. Fig. 3.17 shows the energy spectrum for 1-site events from an ^{88}Y source placed at a 2 m distance from the TPC, 30°off-axis. On the left, the energy spectrum for MC data before including FLT and SLT; on the right, the comparison of experimental data and MC data after including FLT and SLT. A similar comparison for 2-site events from the same exposure is shown in Fig. 3.18. Notice that the normalization is (correctly) the same for the energy spectra in Fig. 3.17 and in Fig. 3.18. The reduction of the huge Compton continuum below 0.5 MeV after FLT and SLT is very apparent in Fig. 3.17. This reduction is crucial for LXeGRIT, since its efficiency is limited by the DAQ livetime fraction. In fact: the deadtime behavior (see Ref. (59)) of the system is nonparalysable with respect to the DAQ, i.e. the recorded count rate m is given by

$$n = \frac{m}{1 - m\tau}$$

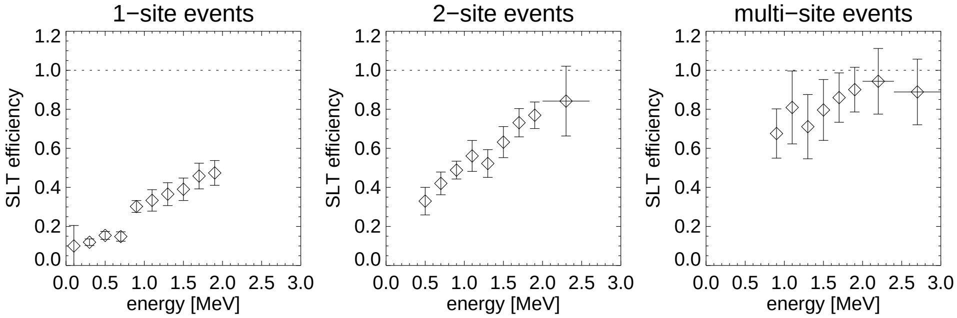

Figure 3.16: Efficiency of the second level trigger for different multiplicities. *Left:* 1-site events; *middle:* 2-site events; *right:* multi-site events.

where n is the rate at the trigger level and τ the deadtime of the system, in this case ∼2 ms. Without any filter at the trigger level, n would increase by about a factor of 30, i.e. $n \gg 1/\tau$ therefore saturating the recorded count rate m

$$m \approx \frac{1}{\tau} \approx 0.5[\mathrm{kHz}]$$

It is clear that, once the DAQ bandwidth has been saturated, the only way to increase the efficiency for contained, multi-site events is to reduce the fraction of 1-site, low energy events. This rationale would be reinforced by the presence of a non-γ background, as in flight conditions (Ch. 6). In general, it should be clear that this argument is “source-dependent”.

Fig. 3.19 shows an Am-Be energy spectrum, combining multiplicities up to 3: since the cross-section for pair-production is large at 4.4 MeV, the single escape peak (3.92 MeV) is the dominant feature. The full energy peak and the double escape peak are also well identified. At energies above 4 MeV bremsstrahlung plays a non negligible role in LXe [2] and it accounts for the lack of sharpness in the energy peaks.

MC simulated data have been superimposed and the comparison shows that the main features are well reproduced. The simulation completely neglects the neutrons from the source, which do not seem to play any major role, at

---

[2] The *critical energy* E_c, above which bremsstrahlung dominates ionization as an energy loss mechanism for electrons, is 11 MeV in LXe, but the energy spectrum is significantly modified for energies as low as 4 MeV.

least for energies above 1 MeV. We do not try to model the energy spectrum below 1 MeV where neutrons could play a more important role.

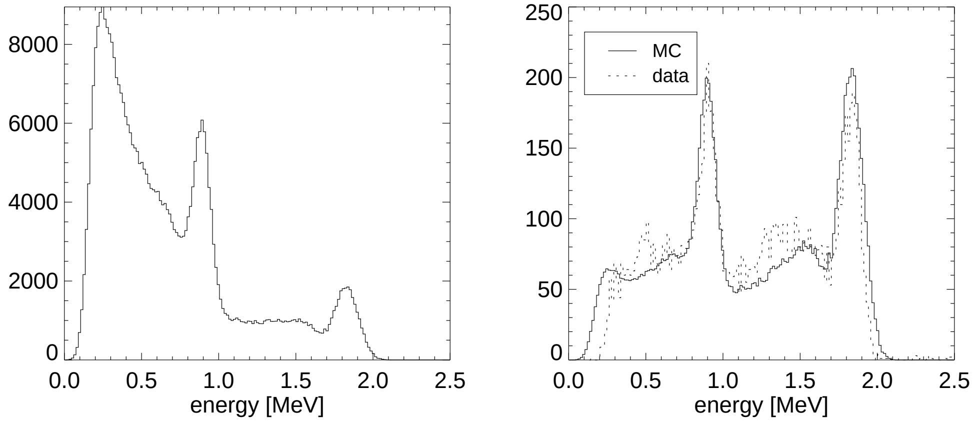

Figure 3.17: *Left:* Energy spectrum for a MC simulated ^{88}Y source at distance, selecting 1-site events; up to this point only the effects of a realistic detector geometry, passive materials, finite position resolution and an energy threshold of 150 keV have been included. *Right:* Energy spectrum for the same MC data after correcting for the efficiency at the first and second level trigger; the superimposed *dotted line* is for experimental data.

3.4.1 A detailed example of efficiency calculation

I give now a specific example of efficiency calculation for an ^{88}Y source at a distance of 2 m, on-axis. ^{88}Y emits two photons at 0.898 (branching ratio 94%) and 1.836 MeV (branching ratio 100%). The two lines provide very valuable information in the most interesting energy band for the LXeGRIT instrument (0.75-3 MeV).

The total source rate was 2738 kBq, therefore the source was emitting 1.836 MeV photons with a rate of 2738 kHz and 0.898 MeV photons with a rate of 2585 kHz. Taking into account a 5700 sec. exposure and solid angle, the 20×20 cm^2 geometrical area of the TPC was finally hit by 1.08 10^7 1.836 MeV photons and 1.01 10^7 0.898 MeV photons.

The DAQ had a 50% livetime (as expected for a PMT trigger rate of about 600 Hz) and the efficiency in writing to disk was only 18%, for only that

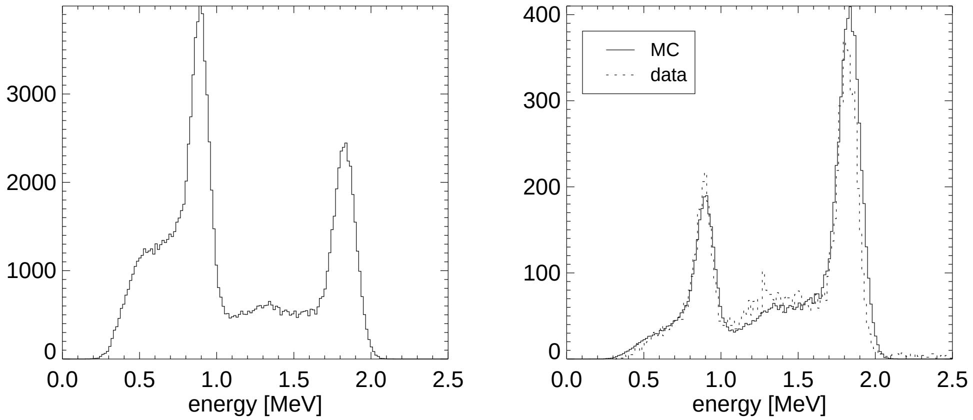

Figure 3.18: The same as Fig. 3.17, but for 2-site events. The same overall normalization factor has been used.

fraction of the bandwidth of disk writing was used. This last efficiency is usually ∼100%.
Correcting for these two inefficiencies, we are left with 9.7 10^5 1.836 MeV photons and 9.1 10^5 0.898 MeV photons.
Now we have simply to count how many events end up in the two full energy peaks (FEP) and this will give an obvious measurement of the overall detection efficiency. The procedure of counting the events in the FEP's is straightforward but introduces an uncertainty of about 5% because of the necessary background subtraction. In the end we count:

- 0.898 MeV: 0.39 10^4 events, i.e. 0.43% efficiency
- 1.836 MeV: 1.30 10^4 events, i.e. 1.34% efficiency

These small figures require some explanations. An upper limit to the detection efficiency is given in Sec. 3.3.1, Fig. 3.7, only including the efficiency for containment and the inefficiency due to passive materials. It is less than 20% at 0.898 MeV and about 11% at 1.836 MeV. The light trigger efficiency alone - as given in Sec. 3.3.3 - reduces the detection efficiency by a factor of almost 9 at 0.898 MeV and a factor of 3 at 1.836 MeV. The second level trigger again reduces the efficiency by a factor of 3 at 0.898 MeV and a factor 1.7 at 1.836 MeV (as in Fig. 3.15, which has been obtained from the same

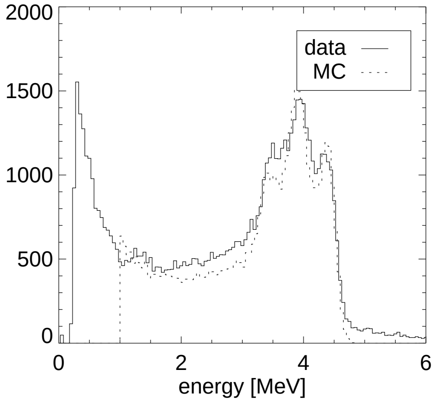

Figure 3.19: Am-Be (4.42 MeV γ-ray source) energy spectrum for 1-, 2-, 3-site events combined. The most prominent feature is the single-escape peak (3.92 MeV). The full energy peak and the double escape peak are clearly detected, too. Superimposed (*dotted line*) the Monte Carlo generated energy spectrum.

data-take). At this point I am not yet considering various reductions in efficiency coming from the off-line data analysis, and the efficiency is already down to 0.6% at 0.898 MeV and 1.9% at 1.836 MeV. Inefficiencies in the off-line analysis, about 30%, account for the missing part.

This way of presenting the detection efficiency is correct but incomplete, since an important piece of information still missing is the efficiency for different multiplicities, especially for Compton events.

Inefficiencies due to DAQ livetime and disk writing are independent of the interaction multiplicity and do not need to be considered again. It is a valid assumption that the light trigger efficiency has, on average, little dependence on the interaction multiplicity. Quite obviously, a much stronger dependence comes from the SLT, which is designed to enhance the fraction of multi-site events, as it is made clear in Sec. 3.3.3, Fig. 3.16.

Results for different multiplicities are summarized in Table 3.1. There are various sources of uncertainty on the specific efficiencies, some of them systematically lowering the final efficiency:

- the overall *measured* efficiency should be known quite precisely (5% or better), the main uncertainty coming from the subtraction of the background beneath the line;

- the FLT efficiency should be known with 5% precision for 1-site events, but assuming the same efficiency for higher multiplicities introduces a larger error [3];
- the SLT efficiency should be known with 5% precision for all the multiplicities, statistics being the limiting factor, since it is measured for each specific data-take;
- the efficiency of the off-line procedure to extract the signal is more easily evaluated for 1-site events. In this case the efficiency in finding a good signal is very close to 100% for energies larger than few hundreds keV, and the 30% inefficiency comes from the fraction of "noisy" events rejected off-line. For multi-site events the efficiency can be slightly lower since, even intuitively, is more difficult to successfully reconstruct more complex topologies (where single interactions can have energies as low as 150 keV);
- the precision of the MC expectation should be within 5% once the assumed conditions are matched. Many factors can reduce the detection efficiency: noisy or dead wires, higher energy thresholds etc. Again, these factors are more relevant for higher multiplicities.

It is clear from comparing the overall *expected* efficiencies to the *measured* ones in Table 3.1 that our expectation is too optimistic, the discrepancy ranging between 15% and 30% [4].

We can now see how the various selections (FLT and SLT) change the *ratio of multi-site or Compton events over single-site events*; since the maximum rate of events written to disk is fixed by the limited DAQ, this translates in an increased efficiency of LXeGRIT as a Compton imager. For multi-site events the final efficiency is 0.27% at 0.898 MeV and 1.0% at 1.836 MeV to be compared to an upper limit of 9% and 8%, respectively, so that the ratio of multi-site over single-site event is

---

[3] A better precision is obtained through complete MC simulation.

[4] A comparison to expectations has been previously given in Fig. 3.7; in that case, the measured overall efficiency has been corrected for FLT, SLT and off-line efficiencies, so that the result was made comparable to "MC" in Table 3.1.

energy [MeV]	overall eff. [%] (measured)^a	FLT eff. [%]	SLT eff. [%]	off-line eff. [%]	MC^b [%]	overall eff. [%] (expected)^c
0.898 - 1	0.16	12	25	70	9	0.19
1.836 - 1	0.34	30	45	70	4	0.38
0.898 - 2	0.22	12	45	70	8	0.30
1.836 - 2	0.70	30	75	70	6	0.94
0.898 - 3+	0.05	12	70	70	1	0.06
1.836 - 3+	0.30	30	90	70	2	0.38

Table 3.1: Detection efficiency for an ^{88}Y source, calculated for the two lines (0.898 MeV and 1.836 MeV) and for different multiplicities: 1-site, 2-site, 3-or-more (3+) events. Several uncertainties are involved in the determination of specific contributions - FLT, SLT, off-line and MC - to the global efficiency. A detailed discussion is given in Sec. 3.4. ^{a}:the overall efficiency has been obtained from the actual data, after correction for corrected for DAQ livetime and data transmission inefficiency. ^{b}: as shown in Fig 3.6, i.e. only passive materials and containment accounted for. It has been calculated through MC simulation. ^{c}: the *expectation* for the overall efficiency has been obtained combining FLT, SLT, off-line and MC in columns 3-6. It should come out close to the *measured* overall efficiency in column 2.

- 0.898 MeV: 0.27/0.16=1.69, to be compared to a theoretical 9.0/9.0=1 (Fig. 3.6);
- 1.836 MeV: 1.00/0.34=2.94, to be compared to 8.0/4.0=2.0.

As a conclusion, it is easy at this point to extrapolate what the efficiency would be if the DAQ could handle a 10 times larger rate. With a light trigger efficiency as high as the one obtained in 1999 for the same detector (see Ref (73)) the final efficiency could be close to the one depicted in Sec. 3.3.1.

Conclusions

In this chapter a thorough description of the response of the LXeGRIT instrument to MeV γ-rays has been presented. The detector response is well understood and reproduced through MC methods, in a way flexible enough to account for a variety of different experimental conditions. The DAQ clearly constitutes a severe bottleneck when dealing with sources which present a relatively high rate (few kHz), and this is not an uncommon situation, given the size of the LXeTPC. It has been chosen to *reduce* the efficiency at the trigger level, to specifically select multiple Compton events in the few-MeV region. The rationale of this choice is quite simple: given a maximum rate of events fixed by saturating the speed of the DAQ, one tries to maximize the fraction of good events, in our case multiple Compton events. If not limited by the current DAQ, this same prototype could achieve a detection efficiency close to 20% at 1 MeV. This efficiency can be obtained in the current configuration only for sources with a very low rate, less than 100 Hz in the LXeTPC.

Chapter 4

LXeGRIT: imaging performance

Introduction

A Compton telescope (CT) is an instrument for imaging γ-ray sources; it usually works in the few hundreds keV - 30 MeV energy band and the direction of γ-rays is reconstructed through Compton kinematics.

The scatter angle on a free electron $\bar{\varphi}$ is given by the well known Compton formula

$$\bar{\varphi} = \cos^{-1}\left[1 - m_e c^2 \left(\frac{1}{E_2} - \frac{1}{E_{tot}}\right)\right] \tag{4.1}$$

where $m_e c^2 = 0.511$ MeV, E_{tot} is the initial energy and $E_2 = E_{tot} - E_1$, all energies in MeV. Once combined with the direction of the *scattered* γ-ray - derived from x_1, y_1, z_1 and x_2, y_2, z_2 - the direction of the *incoming* γ-ray can be reconstructed; a sketch of a multiple Compton event is shown in Fig. 4.1.

Therefore, any detector able to measure E_{tot}, E_1, x_1, y_1, z_1 and x_2, y_2, z_2 is a CT. The reader should notice that the *subscripts*, i.e. the time sequence of the interactions, matter; Sec. 4.2 is dedicated to the problem of attributing the right subscripts, or "gamma ray tracking". Compton imaging of γ-sources with LXeGRIT is discussed in detail in Sec. 4.3.

The principle of Compton imaging is displayed in Fig. 4.2 [1]: A photon arriving from a source at position (χ_0, ψ_0) Compton-scatters in the plane

---

[1] The remaining of this Introduction is adapted from Ref. (72).

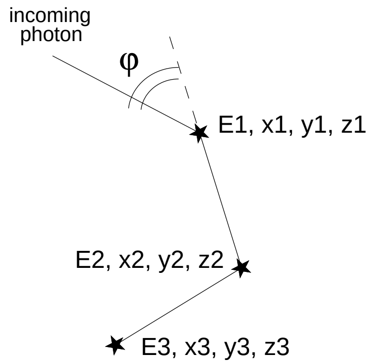

Figure 4.1: Schematic of a 3-site event with two Compton scatters followed by photoabsorption.

designated by D_1 by the true *scatter angle* $\hat{\varphi}$ and is stopped in plane D_2. Interaction positions are measured in both planes, from which the direction of the scattered photon (χ, ψ), the *scatter direction*, is determined. The direction of an individual photon can only be determined to a so-called "event circle" with radius $\bar{\varphi}$ around the direction (χ, ψ). The ambiguity is a result of the non-measurement of the direction of the scattered electron. After collection of many source events, the source position is defined by the intersection of all event circles as shown to the left in Fig. 4.3.

While back-projection of event circles on the sky is useful to visualize the basic measurement principle and was historically the most straightforward imaging method to be exploited, it is not the optimum method to actually perform Compton imaging. The reason is that the "event circle method" neglects one important piece of information, namely the probability distribution for scatter angles $d\sigma/d\bar{\varphi}$ for photons from a source at given location and energy, or, in other words, the frequency of occurrence of event circles with a given opening angle. This requires the precise knowledge of the instrument's response from calibration and Monte Carlo simulations. Fig 4.3 illustrates how this additional information can be exploited in a 3-dimensional data space consisting of $(\chi, \psi, \bar{\varphi})$, where a point source defines a cone-like structure with half opening angle of 45° centered on the source position (at

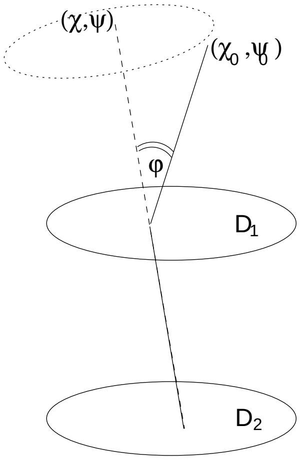

Figure 4.2: Principle of a Compton telescope

$\bar{\varphi} = 0°$) with a density along the $\bar{\varphi}$ dimension given by the Klein-Nishina cross section convolved with factors that result from the detector geometry and detector thresholds.

The simplest and very powerful imaging method for point sources is a likelihood fit of the response-cone on a grid of positions within the field of view, yielding a likelihood map that can be translated into flux levels and source significances. A complete deconvolution is required in case of diffuse emission and multiple point sources in the field of view.

In a real instrument, event circles are scattered around the true source position both by the uncertainty on interaction locations, which leads to uncertainty in the center positions of the circles, and by the uncertainty in energy measurement (and by not fully absorbed photons), which varies the radii of the circles. The angular resolution is determined by the distribution of the angular distance of the circles from the true source position, the so-called *angular resolution measure ARM*. Hence, the angular resolution of a Compton telescope is determined also by its energy resolution. In 3D imaging data space, measurement uncertainties blur the cone surface to a cone volume. Since the signal and background counts within this volume determine the sensitivity of the instrument, it seems obvious that a reduction of the width of the cone with improved energy and position resolution yields an improved sensitivity as well. However, this effect is limited if the source itself is spatially extended (diffuse emission), which results in a superposition

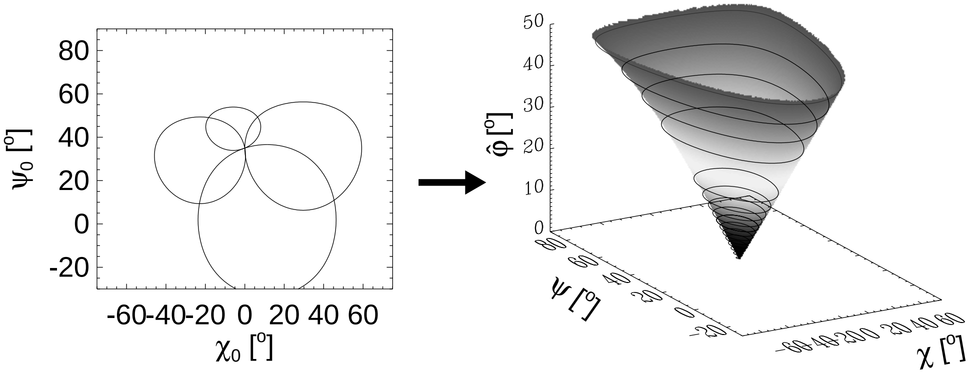

Figure 4.3: Event circles on the sky of a point source (left) and the corresponding response function in the 3D imaging data space of an ideal classical Compton telescope (right). A point source describes a cone with half-opening angle of 45° where the (spherical) coordinate system can be approximated as flat. The density along the scatter angle dimension corresponds to the Klein-Nishina cross section and describes the density of circles of radius φ in the event circle representation.

of many cone volumes and therefore in an intrinsic enlargement of the covered data space volume. Moreover, if the "Compton tail" of not fully absorbed photons is significant, the inner part of the cone is being filled up, which overlaps with response cones from close-by source positions.

4.1 The LXeGRIT Compton Telescope

Let's define the LXeGRIT output for a generic γ-ray as our starting point in the imaging process:
E_1, x_1, y_1, z_1; ...; E_n, x_n, y_n, z_n where n is the event multiplicity, i.e. the number of detected interactions once the finite spatial resolution and the minimum energy threshold have been accounted for. Throughout this chapter, $n \geq 2$ to be able to apply Eq. 4.1. Experimentally, it turns out that we can restrict our interest to $n = 2$ and $n = 3$, since events with $n \geq 4$ add very little to the final efficiency for Compton imaging. The energy range we consider for LXeGRIT as a CT is 0.5-10 MeV.

Fig. 4.4 affirms the very *raison d'etre* of LXeGRIT, i.e. the possibility of

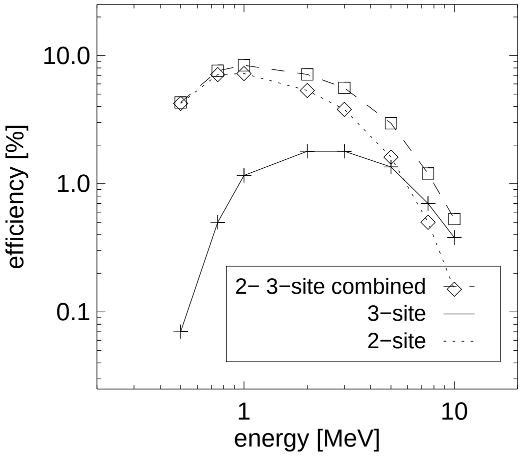

Figure 4.4: Detection efficiency for 2- and 3-site "imageable" events in the 0.5-10 MeV energy band. "Imageable" requires full containment and sequences including only Compton scatter(s) and photoabsorption. See text for a more thorough discussion. The efficiency drops below 5% above 3 MeV. 2-site events constitutes the bulk of the efficiency, while 3-site events give a comparable efficiency above 5 MeV, where the overall efficiency is steeply decreasing. Efficiencies quoted here are given before finding the correct time sequence (Sec. 4.2).

large efficiency which translates into a large effective area, the first requirement for any future instrument in MeV γ-ray astronomy. In the field of MeV γ-ray astronomy, a detection efficiency of 5-10% is a very substantial leap forward and must be compared to the eventual $\sim$0.5% efficiency [2] of COMPTEL (83). The gain in efficiency by LXeGRIT is due to its monolithic structure, compared to the double scatter (two independent, widely separated scatterer and absorber) structure of COMPTEL. In fact, in a monolithic detector more events topologies may be used for Compton imaging and the scatterer does not need to be thin (one attenuation length or less), since in this case scatterer and absorber coincides.

Fig. 4.4 deals with the following problem: given a source, its flux and energy dependence, how many imageable γ-rays will be detected in LXeGRIT? The

---

[2] The final efficiency for celestial lines around 1-2 MeV was actually as low as 0.02%, as reported in Ref. (96) .

most obvious requirement for "imageability" is full containment with at least two interactions. A less obvious but equally important requirement is that the γ-ray interact only through Compton scatter ($C.s.$) and photoabsorption ($p.a.$), excluding pair production, and that no bremsstrahlung photon radiated from secondary electrons be detected (see Sec. 4.2). The steep decline in efficiency for γ-ray energies larger than 3 MeV points to the fact that a compact CT, based on a high Z, high density material like LXe does not work well above 10 MeV, precisely because an overwhelming fraction of events will be spoiled by pair production interactions and bremsstrahlung photons and they will be of no use for Compton imaging.

4.2 Gamma ray tracking

A much needed preliminary step to Compton imaging is γ-ray tracking, or reconstruction of the proper time sequence for multi-site events. For we are interested in Compton imaging, we look for events where Eq. 4.1 applies. Therefore, the most general interaction sequence will be Compton scatter followed by full absorption of the scattered γ-ray in one or more interactions, without any other interaction in the passive materials between the source and the active LXe volume.

As shown in Fig. 4.4, a large fraction of multi-site events ends up with two interactions, i.e. Compton scatter followed by photoabsorption; the fraction of events with more than 3 interactions is irrelevant below 5 MeV and will be neglected in the following. The two cases for 2- or 3- interactions differ substantially and are treated separately in Sec. 4.2.1 and Sec. 4.2.2, where we are dealing with two classes of events:

1. $C.s.$ followed by $p.a.$ (Sec. 4.2.1);
2. $C.s.$ followed by $C.s.$ followed by $p.a.$ (Sec. 4.2.2).

Before tackling this problem, it is worthwhile considering what we are leaving behind, i.e. events which do not fall into the aforementioned classes; Fig. 4.5, based on MC data, sets the tone. It deals with the following situation: given a monochromatic γ-source, we have one sample of 2-site and one of 3-site events and we would like to know which fraction of these detected γ-rays is interesting for Compton imaging.

First of all, we quite obviously have events where the γ-ray is not fully contained in the active volume, because of a previous interaction outside the fiducial volume or because the scattered γ-ray is not contained. The fraction of fully contained events is quite high up to 2 MeV (40% for 2-site events and 60% for 3-site events), rapidly declining at higher energies (4% for 2-site events and 9% for 3-site events at 10 MeV).

Secondly, not all the fully contained events are usable for Compton imaging, the three most common cases being: *a.* *p.a.* followed by a bremsstrahlung photon which is separately photoabsorbed (2-site sample), *b.* *C.s.*, *p.a.* and a photoabsorbed bremsstrahlung photon (3-site sample) and *c.* pair production followed by photoabsorption of the two 511 keV photons from positron annihilation (3-site sample). The fraction of fully contained events where the only admissible sequences are "*C.s.* $-$ *p.a.*" and "*C.s.* $-$ *C.s.* $-$ *p.a.*" is shown in Fig. 4.5, labeled as "Compton only".

Fig. 4.5 shows separately the fraction of "Compton only" events out of the fully contained events (case A) and the fraction of "Compton only and contained" events out of the entire sample (case B) because they constitute two different cases of practical interest. If we are looking for a specific energy line and deal with a negligible background below the line, we have prior knowledge whether a γ-ray is fully contained or not, and we end up in case A. If the input energy spectrum is a continuum distribution, as it is in many relevant astrophysical problems, we do not have such prior knowledge and end up in case B. In this second case the fraction of events usable for Compton imaging is obviously lower.

The relevance of pair production and bremsstrahlung secondary photons increases with energy and becomes a major concern only above ~2 MeV. The energy threshold for pair production is in fact 1.022 MeV but the cross section saturates only at much higher energy (~GeV) and equals Compton cross section at ~6 MeV [3] . Relativistic electrons, like the ones from MeV Compton scattering, lose energy both by ionization and bremsstrahlung, i.e. radiating secondary photons which, if of sufficiently high energy (in the LXeGRIT case that means above the minimum energy threshold, 150 keV), interact at a separate location making extremely difficult if not altogether impossible the reconstruction of the interaction sequence. A very useful rule of thumb says that for electrons the radiative energy loss overcomes the one due to ionization above the *critical energy* $\mathrm{E}_c = 610$ MeV / $(Z + 1.24)$ for liquids and

---

[3] For fully contained 3-site events the fraction of pair production events over Compton events is actually *larger* than the simple ratio of the cross sections. To be accurate, any calculation where containment and/or a specific topology are imposed has to start from MC data.

solids (50); for Xe, $Z = 54$ and $E_c = 11$ MeV. Experimentally, we found that the energy spectrum is significantly modified by secondary bremsstrahlung photons for energies as low as 4 MeV.
To conclude, below 2 MeV most of the multi-site events are useful for Compton imaging, while above 2 MeV an increasingly large fraction of events cannot be used for imaging γ-sources and will eventually constitute background for the imaging process. As should be clear from Fig. 4.5, at 10 MeV the signal-to-background ratio is less than 1%, if no containment can be imposed.

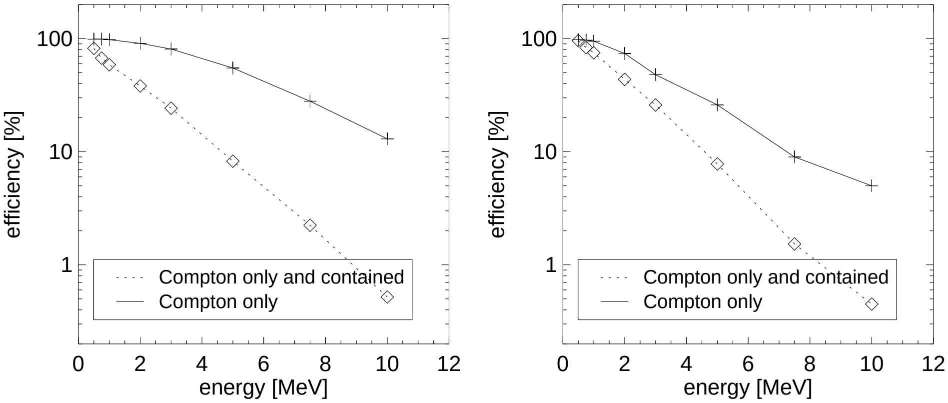

Figure 4.5: For different initial γ-ray energies, fraction of "Compton only and contained" (see text) events out of the detected 2- and 3-site samples, and fraction of "Compton only" events out of fully contained sub-samples. *Left:* 2-site events; *Right:* 3-site events.

As a final note: quite obviously the true time sequence is known for MC data and it is unknown for experimental data. When experimental data have been used, the criterion applied to determine the true sequence is described for each specific case.

4.2.1 2-site events

In the case of 2-site events, even assuming no prior knowledge we can guess the right sequence with a remarkable 50% success rate. This fraction can be substantially improved using the *energy sharing* between the two interactions

which is, in many cases, highly asymmetric [4].
For LXeGRIT, the argument goes like this:
for energies larger than ~2 MeV a γ-ray event is stopped in the fiducial volume with only two interactions if it does lose a large fraction of the initial energy in the first interaction; if the energy lost in the first interaction is small, the scattered photon will - most likely - subsequently interact more than once before being absorbed, therefore being no more a 2-site event.
Fig. 4.6 shows the energy spectra separately for E_1 and E_2 for 0.662 MeV (^{137}Cs), 0.898 and 1.835 MeV (^{88}Y) photons. The true interaction sequence is obtained in two different ways for the ^{137}Cs and ^{88}Y datasets. The ^{137}Cs source was collimated to a beam with a lateral spread of ~3 mm, which makes possible to tag the first interaction as the one within the collimator aperture. The ^{88}Y source was at a distance of 2 m above the detector, without any collimation. Since the source position is known, it is possible to use Compton imaging (Sec. 4.3) and track each γ-ray assuming the two possible sequences. The sequence which gives back the correct source position is then chosen as the true sequence.
For 1.836 MeV, the E_1 and E_2 spectra are almost mirror images of each other, and the situation $E_1 > E_2$ is clearly the most likely. At lower energies (0.662 and 0.898 MeV) the two spectra are much more similar and the $E_1 - E_2$ asymmetry is no more a good argument.
The minimum in the E_1 spectrum, clearly visible for all the three energies, corresponds to 90° scatter angle (the corresponding $E_1 = E_{tot}^2/(m_e c^2 + E_{tot})$ is marked with a vertical dashed line). It is a "geometrical artifact", due to the direction of the incident γ-rays along the detector z-axis, such that for a γ-ray scattered at 90° $z_1 \simeq z_2$, while a minimum separation of about 3 mm along the z-axis is required to ensure a good energy determination.

This argument based on the asymmetry in the energy sharing is reinforced and made quantitative over the 0.5-10 MeV energy range through a detailed MC study. In Fig. 4.7-*left* the ratio $< E_1 > /E_\gamma$ is plotted vs. E_γ, where $< E_1 >$ is the mean of the first energy deposition and E_γ is the nominal energy of the γ-ray. The trend is quite clear: $< E_1 > /E_\gamma$ increases with E_γ and $< E_1 > /E_\gamma \ \geq 75\%$ for $E_\gamma \ \geq 2$ MeV [5] . Fig. 4.7-*left* is well suggestive

---

[4] This is not a very general argument and must be tailored on the specific problem under study, in this case the LXeGRIT detector; in the case of COMPTEL, for example, 2-site events have nothing to do with the 2-site events in LXeGRIT

[5] $< E_1 > /E_\gamma$ is a sensible parameter for $E_\gamma > 2$ MeV, where the E_1 spectrum shows a narrow peak with an extended tail toward lower energies. Going to lower energies the

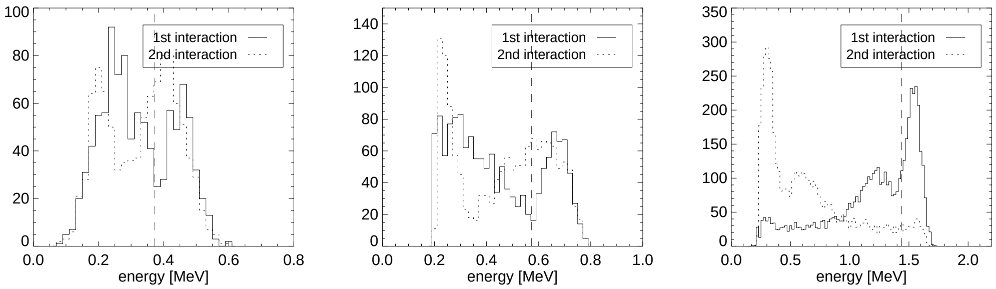

Figure 4.6: E_1, E_2 distribution for fully contained 2-site events. From left to right: 0.662 MeV (^{137}Cs), 0.898 and 1.836 MeV (^{88}Y). The minimum in the E_1 spectrum corresponds to 90° scatter angle and the corresponding $E_1 = E_{tot}^2/(m_e c^2 + E_{tot})$ is marked with a vertical dashed line.

of an optimized selection on the energy sharing, requiring the ratio E_1/E_{tot} to be larger than some value $f(E_{tot})$. $f(E_{tot})$, optimized on MC data, is defined as

$$f(E_{tot}) = 0.85 \left(1 - \frac{2}{E_{tot}^2}\right) \quad ; \; E_{tot} > 2.4 \text{ MeV} \tag{4.2}$$

$$f(E_{tot}) = 0.5 \;\; ; \; 1 \text{ MeV} \leq E_{tot} \leq 2.4 \text{ MeV} \tag{4.3}$$

and is shown in Fig. 4.7-$left$ with $E_{tot} = E_\gamma$.

Fig. 4.7-$right$ shows efficiency and contamination for this sequencing procedure in the energy range 1-10 MeV; the efficiency is as high 86% at 2 MeV and saturates (≥98%) at 5 MeV, with very little room left for any improvement (for the simple reason that there are very few events to be recovered). Between 1 and 2 MeV this sequencing procedure has a major drawback, related to angular resolution and not yet apparent here; while it is clear that the procedure is still successful in finding the right sequence, at the same it is accepting events with a large scatter angle and, as a consequence, with a rather poor angular resolution to the detriment of a still sizeable fraction of events with better angular resolution (see Sec. 4.3.1). Below 1 MeV we

---

E_1 spectrum becomes flatter without any well identified peak. In the latter case not only $< E_1 > /E_\gamma$ is poorly sensible, but the entire argument breaks down since the E_1 and E_2 spectra become quite similar.

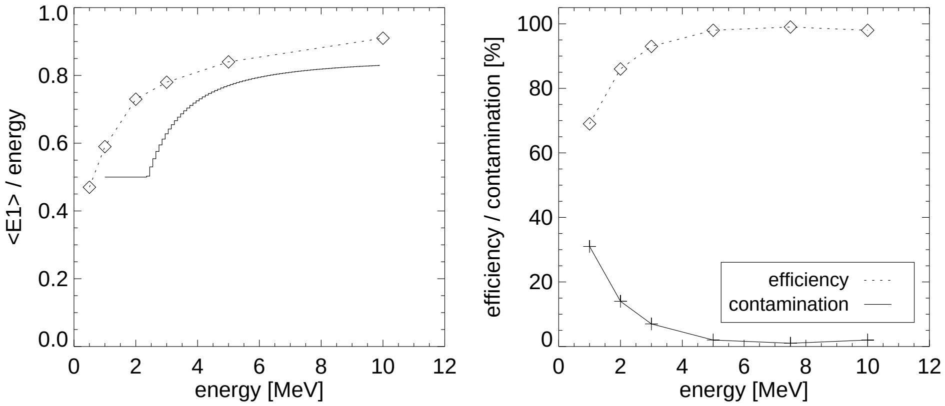

Figure 4.7: *Left:* $< E_1 > / E_\gamma$ vs. E_γ, from MC data. Superimposed $f(E_\gamma)$ as defined in Eqs. 4.2-4.3 *Right:* Efficiency and contamination in sequencing 2-site events according to the procedure described in Sec. 4.2.1.

have not found any *optimum criterion* for sequencing 2-site events. The final choice depends on the specific case under study and cannot set aside the wider problem of source imaging. Indicatively, $E_1 < E_2$ does not improve the default 50% efficiency but does improve the angular resolution (again, see Sec. 4.3.1).

4.2.2 Multi-site events

When more than two interactions are available, the time sequence is in principle univocally determined by Compton kinematics. In practice the finite resolution on energy and position poses very significant limits. In the general case of a γ-ray which undergoes $N-1$ Compton scatters and is photoabsorbed in the N^{th} interaction; symbols and indexes are defined in a slightly different way than in Eq. 4.1. Energy and momentum conservation is written as

$$
\begin{aligned}
E\,{}^{\gamma}_{i-1} &= E\,{}^{\gamma}_{i} + E\,{}^{\mathrm{e}}_{i} \qquad (4.4)\\
\vec{p}\,{}^{\gamma}_{i-1} &= \vec{p}\,{}^{\gamma}_{i} + \vec{p}\,{}^{\mathrm{e}}_{i} \qquad (i = 1, \dots, N-1) \qquad (4.5)
\end{aligned}
$$

with E^{γ}_{i} $(i = 0, \dots, N-1)$ and E^{e}_{i} $(i = 1, \dots, N)$ the energy of the γ-ray and the scattered electron after interaction i. E^{γ}_{0} is the energy of the incoming photon and $\vec{p}_i$ are the corresponding momenta. The vector equation 4.5 translates into two independent equations for the photon scatter angle φ_i and the electron scatter angle θ_i $(i = 1, \ldots, N-1)$:

$$\cos\varphi_i = 1 + \frac{1}{W_i} - \frac{1}{W_{i+1}}, \text{ with: } \quad W_i = \frac{E_i^{\gamma}}{m_0c^2} \tag{4.6}$$

$$\cot\theta_i = \left(1 + \frac{E_{i-1}^{\gamma}}{m_0c^2}\right) \tan\frac{\varphi_i}{2} \tag{4.7}$$

For LXeGRIT and for most of the existing CT the electron scatter angles are not measured and are therefore ignored in the following. The detector measures N energy deposits $E_i(\approx E_i^{\mathrm{e}})$ and N interaction locations $\vec{x}_i$. For a given interaction sequence, the locations determine geometrically $N-2$ photon scatter angles $\varphi_{\mathrm{geo}\ i}$ $(i = 2, \ldots, N-1)$:

$$\cos\varphi_{\mathrm{geo}i} = \frac{\overrightarrow{u}_i \cdot \overrightarrow{u}_{i+1}}{|\overrightarrow{u}_i||\overrightarrow{u}_{i+1}|} \tag{4.8}$$

where $\overrightarrow{u}_i = (x_i - x_{i-1},\ y_i - y_{i-1},\ z_i - z_{i-1})$.
Moreover, $N-1$ Compton scatter angles $\bar{\varphi}_i$ are measured by the energy deposits according to equation 4.6, noting that $E_i^{\gamma} = \sum_{j=i+1}^{N} E_j$ $(i = 0, \ldots, N-1)$. This redundant information allows testing of the sequence of the interaction points based solely on kinematics. A straightforward test statistic consists of summing the differences of the scatter angles quadratically, weighting the summands with the measurement errors:

$$T_{\varphi} = \sum_{i=2}^{N-1} \frac{(\cos\bar{\varphi}_i - \cos\varphi_{\mathrm{geo}\ i})^2}{\sigma_i^2} \tag{4.9}$$

$$\text{with: } \quad \sigma_i^2 = \sigma_{\cos\bar{\varphi},i}^2 + \sigma_{\cos\varphi_{\mathrm{geo}},i}^2$$

Ideally, the test statistic would be zero for the correct sequence if the photon is fully contained. With measurement errors, T'_{φ} is always greater than zero, but the correct interaction sequence is still most likely to produce the minimum value of the test statistic.
For each triplet of interactions $\sigma_{\cos\bar{\varphi}}$ and $\sigma_{\cos\varphi_{\mathrm{geo}}}$ are computed in the follow-

ing way:

$$\sigma^2_{\cos\varphi_{\mathrm{geo}},i} = \sum_{k=1}^{3}\left\{\left(\frac{u_{i+1,k}}{|\overrightarrow{u}_i|\cdot|\overrightarrow{u}_{i+1}|} - \frac{u_{i,k}\ \cos\varphi_{\mathrm{geo}}}{|\overrightarrow{u}_i|^2}\right)^2 + \left(\frac{u_{i,k}}{|\overrightarrow{u}_i|\cdot|\overrightarrow{u}_{i+1}|} - \frac{u_{i+1,k}\ \cos\varphi_{\mathrm{geo}}}{|\overrightarrow{u}_{i+1}|^2}\right)^2\right\}\cdot\sigma_k^2 \tag{4.10}$$

with: k spatial coordinate index and

σ_k position uncertainty on each coordinate

$$\sigma^2_{\cos\bar{\varphi},i} = \frac{1}{W_i^4}\cdot\sigma(W_i - W_{i+1})^2 + \left(\frac{1}{W_i^2} - \frac{1}{W_{i+1}^2}\right)^2\cdot\sigma(W_{i+1})^2 \tag{4.11}$$

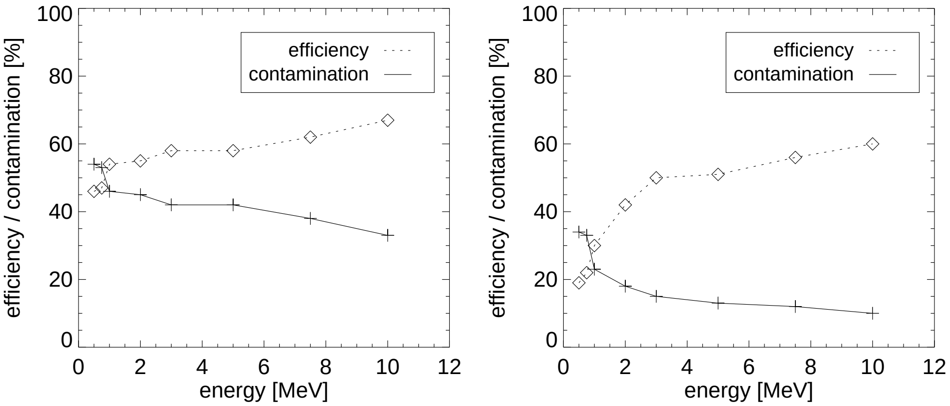

Figure 4.8: Efficiency and contamination in the reconstruction of the correct time sequence for 3-site event, as calculated using MC data and the actual algorithm used for experimental data. *Left:* without applying any further selection. In this case events can only be *correctly* or *wrongly* sequenced, since no event is rejected. *Right:* selecting $E_1/E_{tot} > 0.3$ *after the fact*, i.e. after the sequence reconstruction based on the described test statistic. The contamination fraction is here defined as the fraction of events wrongly sequenced which have $E_1/E_{tot} > 0.3$.

For LXeGRIT we will consider the case of three interactions which is by far the most likely. There are six (3!) possible sequences to start with, i.e. assuming no prior knowledge we would pick up the right sequence only 17%

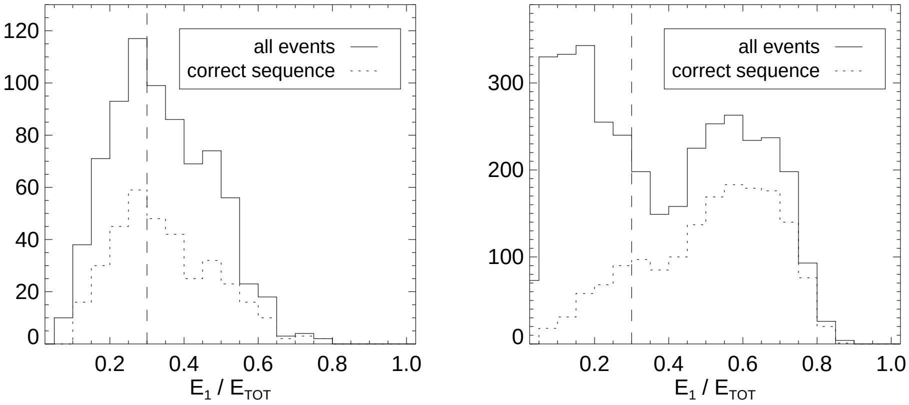

Figure 4.9: E_1/E_{tot} for 0.898 (*left*) and 1.836 (*right*) MeV γ-rays. From experimental data, imposing full energy containment.

of the times, which is a much worse starting point than the default 50% for 2-site events. The efficiency reached applying this procedure is shown in Fig. 4.8-*left*, using MC data.

The efficiency is ~55% at 2 MeV and exceeds 60% above 5 MeV; the most severe limitation to further improving the efficiency of the algorithm comes from the energy resolution in LXe. The fraction of wrongly sequenced events (contamination) is also shown in Fig. 4.8-*left*; in this case, since no event is rejected, it is just the complement to 1 of the efficiency. Assuming that the efficiency shown in Fig. 4.8-*left* is an upper limit, one can try to improve the algorithm performance applying further selections *a posteriori*, in order to remove cases identified as "problematic". Quite clearly the goal here is to keep the efficiency as close as possible to the one in Fig. 4.8-*left* while reducing the contamination.

The most powerful variable is E_1/E_{tot}, where E_1 is the energy deposited in the *first* interaction [6]. Fig. 4.9 shows E_1/E_{tot} for the 0.898 and 1.836 MeV ^{88}Y line (experimental data), when all the events are considered and selecting only events with the time sequence correctly identified [7] . At 0.898 MeV there is no clear correlation between E_1/E_{tot} and finding the right sequence. At

---

[6] *First* according to the γ-tracking algorithm, which is the only information we have up to this point.

[7] Experimentally, that means events for which the source is correctly imaged.

1.836 MeV the situation is quite different and the largest fraction of wrongly reconstructed events shows up at $E_1/E_{tot} < 0.3$. The impact of selecting $E_1/E_{tot} > 0.3$ has been studied over the energy range 0.5-10 MeV using MC data.
The efficiency of the γ-tracking procedure combined with this *a posteriori* selection is shown in Fig. 4.8-*right* together with the "contamination", here defined as the fraction of events (in the full energy peak) which are wrongly sequenced and have $E_1/E_{tot} > 0.3$. In other words, for each energy: efficiency *plus* contamination *plus* fraction of events with $E_1/E_{tot} < 0.3$ gives 100%. This technique works well above 2 MeV, while at lower energies the reduction in efficiency combined with the poor rejection power make it counterproductive, as also seen in Fig. 4.9-$left$. This kind of tighter selections are most useful in conditions of poor initial signal-to-background ratio, all but too common in MeV γ-ray astrophysics [8].

4.3 Compton imaging

The two topics of angular resolution and source imaging are separately treated in this section. The two topics are obviously intertwined, but, given the complexity of Compton imaging, they deserve a separate treatment.

4.3.1 Angular resolution

The angular resolution is maybe the most important parameter to characterize the imaging performance of a CT. One usually define the angular resolution measure (ARM) in the following way: given the source position, we have two independent measurements of the first Compton scatter angle ($\bar{\varphi}$ and φ_{geo}). The difference between the two is a measure of the angular resolution of the CT. In this section ARM and 1-σ angular resolution are interchangeable.

Three sources of error limit the angular resolution: energy resolution, which limits the precision in measuring the scatter angle; position resolution, which limits the precision in measuring the direction of the scattered γ-ray; and Doppler broadening.

---

[8] A further step would be to sequence again the rejected events, now excluding the time sequence previously selected. It would bring some advantage only in the 1-2 MeV band and it is neglected here.

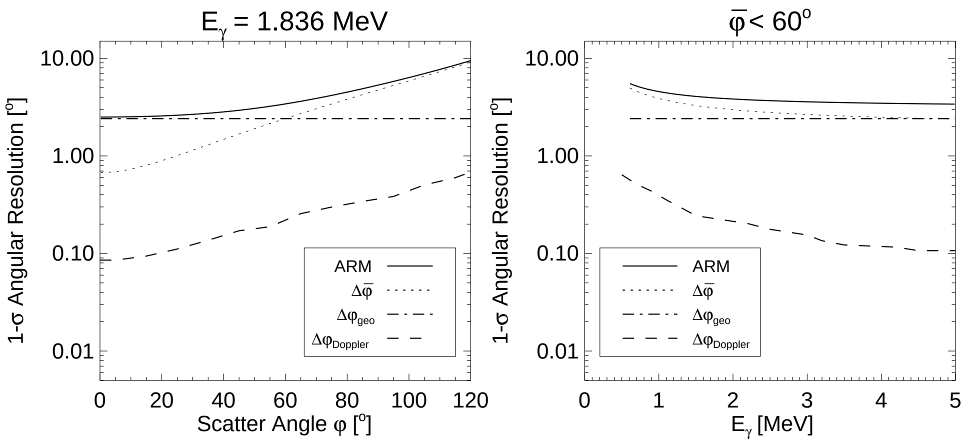

Figure 4.10: Expected angular resolution for LXeGRIT; $\Delta\bar{\varphi}$ and $\Delta\varphi_{\rm geo}$ have been obtained using Eqs. 4.12, 4.14 and combined to give the final ARM according to Eq. 4.16. The angular spread introduced via Doppler broadening is also shown. Being negligible, it has been neglected in the final ARM. *Left:* expected angular resolution vs. $\bar{\varphi}$ for a fixed energy (1.836 MeV). *Right:* expected angular resolution for LXeGRIT vs. energy, selecting $\bar{\varphi}$ <60°, i.e. forward scattering.

The uncertainty on the scatter angle due to the energy resolution is easily obtained from Eq. 4.1:

$$\Delta\bar{\varphi} = \frac{m_e c^2}{\sin\bar{\varphi}}\sqrt{\left(\frac{\Delta E_1}{E_{tot}^2}\right)^2 + \left(\frac{E_1(E_1+2E_2)\Delta E_2}{E_{tot}^2 E_2^2}\right)^2} \tag{4.12}$$

where E_{tot} is the initial energy of the γ-ray, E_1 the energy deposited in the first interaction, $E_2 = E_{tot} - E_1$ and $\bar{\varphi}$ is the scatter angle; Eq. 4.12 is written in a redundant form and there are only two free parameters, e.g. $\bar{\varphi}$ and E_{tot}. Its behavior as a function of $\bar{\varphi}$ and of E_{tot} is shown in Fig. 4.10; the curve for the $\bar{\varphi}$ dependence has been obtained for E_{tot}=1.836 MeV, the one for the E_{tot} dependence has been obtained integrating over $\bar{\varphi} < 60°$ according to the Klein-Nishina cross section. An energy threshold of 150 keV and an energy resolution of 10% / $\sqrt{E\ [\mathrm{MeV}]}$ (FWHM) have been assumed.

The uncertainty on the direction of the scattered γ-ray, $\Delta\varphi_{\rm geo}$, assuming [9] a separation between the first two interaction locations $|\overrightarrow{u}|$ large compared

---

[9] A γ-source far away from the detector or, equivalently, a parallel γ-ray beam is also

to σ_x, σ_y and σ_z, is given by

$$\begin{aligned}\Delta\varphi_{\rm geo} &= \sqrt{(\Delta\varphi_{\rm geo})_x^2+(\Delta\varphi_{\rm geo})_y^2+(\Delta\varphi_{\rm geo})_z^2} \qquad (4.13)\\ \text{with:} & \\ (\Delta\varphi_{\rm geo})_x &= \frac{\sqrt{2}}{|\overrightarrow{u}|}\sigma_x\sqrt{1-\left(\frac{\overrightarrow{u}\cdot\hat{x}}{|\overrightarrow{u}|}\right)^2}\\ (\Delta\varphi_{\rm geo})_y &= \frac{\sqrt{2}}{|\overrightarrow{u}|}\sigma_y\sqrt{1-\left(\frac{\overrightarrow{u}\cdot\hat{y}}{|\overrightarrow{u}|}\right)^2}\\ (\Delta\varphi_{\rm geo})_z &= \frac{\sqrt{2}}{|\overrightarrow{u}|}\sigma_z\sqrt{1-\left(\frac{\overrightarrow{u}\cdot\hat{z}}{|\overrightarrow{u}|}\right)^2}\end{aligned}$$

Under the further assumption of $\sigma_x \simeq \sigma_y \simeq \sigma_z = \sigma_{\vec{x}}$, Eq. 4.13 is eventually reduced to the simplified form

$$\Delta\varphi_{\rm geo} = \frac{2\sigma_{\vec{x}}}{|\overrightarrow{u}|} \qquad (4.14)$$

If $\sigma_x \simeq \sigma_y \gg \sigma_z$ [10], Eq. 4.14 is replaced by

$$\frac{2\sigma_x}{|\overrightarrow{u}|} \geq \Delta\varphi_{\rm geo} \geq \frac{\sqrt{2}\sigma_x}{|\overrightarrow{u}|}\ . \qquad (4.15)$$

For LXeGRIT the 3D-separation between two consecutive interactions is few cm, and considering the lower limit on $\Delta\varphi_{\rm geo}$: $|\overrightarrow{u}| = 10$ mm implies $\Delta\varphi_{\rm geo} = 6.9°$, $|\overrightarrow{u}| = 20$ mm implies $\Delta\varphi_{\rm geo} = 3.4°$, $|\overrightarrow{u}| = 30$ mm implies $\Delta\varphi_{\rm geo} = 2.3°$, $|\overrightarrow{u}| = 40$ mm implies $\Delta\varphi_{\rm geo} = 1.7°$ etc.. In Fig. 4.10 $\Delta\varphi_{\rm geo}$ is shown for $|\overrightarrow{u}| = 30$ mm. This should be taken *cum grano salis*, since $|\overrightarrow{u}|$ is obviously not fixed and its distribution has a rather strong dependence on $\bar{\varphi}$ and E_{tot}, which is usually accounted for properly through a thorough MC simulation.

The angular spread due to Doppler broadening is also shown in Fig. 4.10. It is well known that the Compton formula gives the scattering angle *if* the incident photons were to interact with stationary electrons. For incident photons with energy higher than a few MeV, this is a good approximation

---

tacitly assumed.

[10] As shown in Ch. 2, $\sigma_x = \sigma_y = 0.85$ mm and $\sigma_z = 0.35$ mm for pointlike charge deposition.

since the momentum of atomic electrons is not higher than a few 100 keV/c. For low energy (few 100 keV) photons, the uncertainty in the scatter angle due to Doppler broadening may significantly contribute to the overall ARM. The effect of Doppler broadening is higher for target materials of larger atomic number, such as Ge or Xe, compared to Si or liquid scintillators (see for example Ref. (101)). Doppler broadening clearly constitutes an irreducible limitation to angular resolution in CT's but, on the other side, it should be clear from Fig. 4.10 that Doppler broadening plays essentially no role (2-3% level) in the case of LXeGRIT.

The overall angular resolution $\Delta\varphi$ is defined as

$$\Delta\varphi = \sqrt{\Delta\varphi_{\mathrm{geo}}^2 + \Delta\bar{\varphi}^2} \tag{4.16}$$

As shown in Fig. 4.10, $\Delta\varphi$ is dominated by $\Delta\bar{\varphi}$, unless we restrict ourselves to $\bar{\varphi} < 30°$. For 1.836 MeV the 1 σ angular resolution is about 3° for scatter angles up to 60°, improving for more forward scattering.
The dependence of $\Delta\varphi$ on the interaction separation is shown in Fig. 4.11-*right*, for different position resolution. It is clear that, given the typical separation shown in Fig. 4.11-*left* which is of the order of few cm, a mm position resolution is required for a good imaging performance.

The ARM spectra for real data, 1.836 MeV γ-rays, is shown in Fig. 4.12. For a realistic comparison with expectation, a more detailed analysis has to be based on MC data, which include various detection effects to a high degree of accuracy, is needed.

In this way it is also possible to separate the response for 2- and 3-site events. The result of such an analysis for the energy band 0.5-10 MeVis shown in Fig. 4.13-*left*; in Fig. 4.13-*right* MC data and experimental data are compared for the lines: 0.662 (^{137}Cs), 0.898 (^{88}Y), 1.275 (^{22}Na) and 1.836 (^{88}Y) MeV (2-site events), and 0.898, 1.275 and 1.836 MeV (3-site events). The experimental points have been corrected for the angular spread due to the finite distance between the source and the detector (few meters).

The angular resolution vs. $\bar{\varphi}$ is shown in Fig. 4.14, from the same data (2- and 3-site events combined). The experimental points are compared to the expected angular resolution (as shown in Fig. 4.10-*left*), showing a good agreement. The expectation for a position resolution degraded to 2 mm is also shown and for small $\bar{\varphi}$ the overall performance would be compromised.

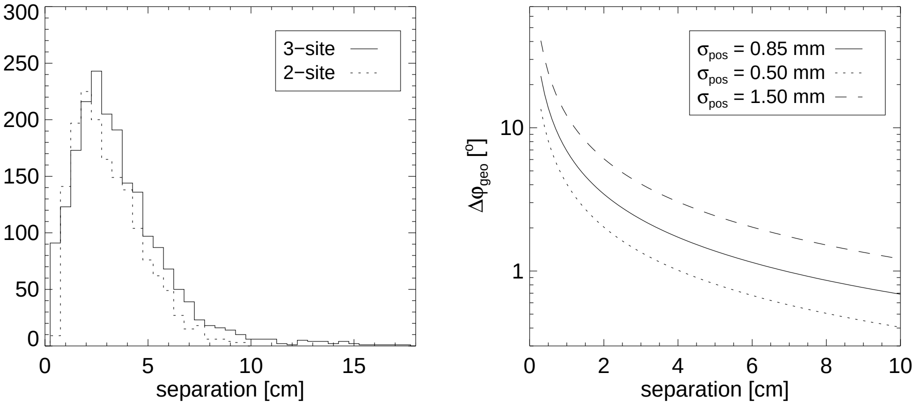

Figure 4.11: *Left:* 3D separation between the first and the second interaction for 1.836 MeV fully contained γ-rays. *Right:* Angular spread $\Delta\varphi_{\rm geo}$ vs. 3D separation (Eq. 4.14) for different values of the position resolution. LXeGRIT achieves a position resolution of 0.85 mm.

4.3.2 Source imaging *

* S. Zhang, private communication.

As already mentioned, any CT measures E_{tot}, E_1, x_1, y_1, z_1 and x_2, y_2, z_2 for each γ-ray photon. Two angles (χ,ψ) on a sphere describing the direction of the scattered γ-ray are obtained from x_1, y_1, z_1 and x_2, y_2, z_2, while the Compton scatter angle $\bar{\varphi}$ is calculated using Eq. 4.1. The direction of the incoming photon is therefore located on a circle projected on the sky. The finite angular resolution turns the ideal circle into an annulus with a width given by the ARM distribution. The scatter direction (χ,ψ) and the scatter angle $\bar{\varphi}$ constitute a 3D data space, in which the object density will be estimated through different kinds of demodulation techniques. Originally (82) the event-circles were directly used to find the source position as the region with maximum density of overlapping event-circles. Maximum entropy (90) and maximum likelihood (38) methods were developed later and successufully applied in analyzing COMPTEL data; different techniques, e.g. direct demodulation (100), had been studied for processing CT data. The most popular and better established technique is the maximum likelihood method, and it has been applied to LXeGRIT data, as described in detail in

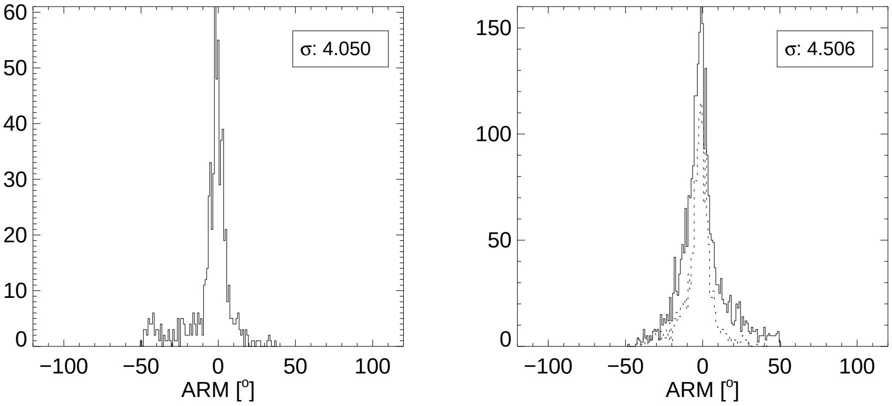

Figure 4.12: ARM spectra for 1.836 MeV γ-rays (^{88}Y source). The source was relatively close to the detector (∼2 m), introducing a non negligible angular spread (∼1.5 °to be combined in quadrature). The standard deviation has been obtained fitting the ARM spectra with a gaussian function. *Left:* 3-site events. *Right:* 2-site events. The dashed line indicates events with $\bar{\varphi}$ restricted to less than 70°. This selection makes the ARM distribution sensibly narrower, getting rid of the extended tails due to large scatter angles. The standard deviation has been derived from this selected sample.

the following.

The imaging problem deals with the derivation of the intensity distribution of the *object region* from the observational data, which can be roughy represented in a 3D binned data space as

$$D_i = \sum_j R_{ij} f_j + N_i \tag{4.17}$$

where D_i is the content of the i^{th} bin in the data space, R_{ij} is the probability to detect a photon from the j^{th} pixel in the object region in the i^{th} bin in the data space, f_j is the intensity of the j^{th} pixel in the object region and N_i is the noise in the i^{th} bin.

The probability of the observed data under a specific model which predicts the number of counts is given by the likelihood function L, defined by

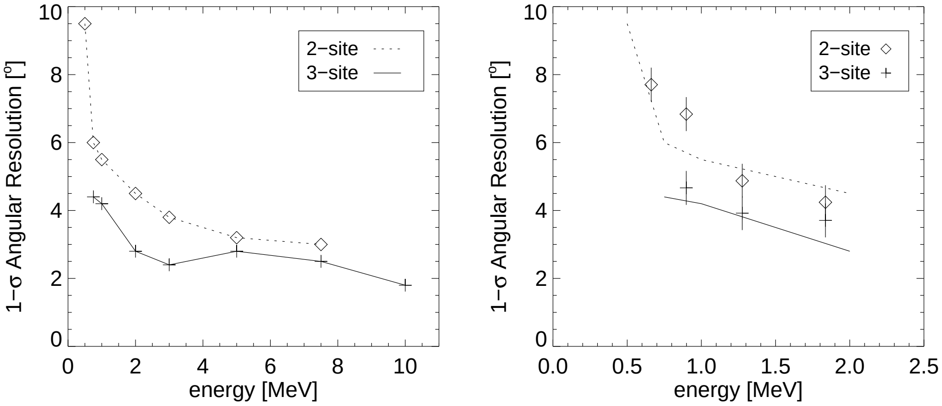

Figure 4.13: ARM spread vs. energy obtained using realistic MC data and experimental data. The 2- and 3-site samples are shown separately. *Left:* MC data; the point at 0.5 MeV in the 3-site data and the one at 10 MeV in the 2-site data have been omitted because of very little statistical significance. Full energy containment has been imposed. *Right:* Experimental data: 0.662 (^{137}Cs), 0.898 (^{88}Y), 1.275 (^{22}Na) and 1.836 (^{88}Y) MeV for 2-site events, 0.898, 1.275 and 1.836 MeV for 3-site events. The corresponding MC curves have been superimposed.

multiplying the probability of each bin

$$L = \prod_i P_i \tag{4.18}$$

For MeV γ-rays, the statistics in each bin is usually given as a Poisson distribution with a special treatment for empty bins (D_i=0)

$$\begin{aligned} P_i &= \frac{\omega_i^{D_i}}{D_i!}\, e^{-\omega_i} && \text{for } D_i > 0 \\ P_i &= 1 && \text{for } D_i = 0,\ \omega_i = 0 \\ P_i &= 0 && \text{for } D_i = 0,\ \omega_i > 0 \end{aligned} \tag{4.19}$$

where $\omega_i = \sum_j R_{ij}^{(3)} f_j + b_i$ is the expected number of counts in the i^{th} bin (b_i is the expected background) and P_i the probability of having D_i counts in the i^{th} bin, given ω_i.

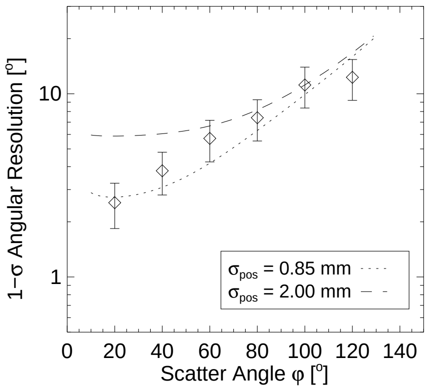

Figure 4.14: Angular resolution vs. scatter angle for a sample of 1.836 MeV γ-rays. Superimposed, the expected angular resolution assuming two different values for the position resolution. 0.85 mm is the *measured* LXeGRIT position resolution and agrees well with the data. A 2 mm position resolution, while still in good agreement with the data for scatter angles larger than 60°, is clearly ruled out by the two points at 20°and 40°, the only ones actually sensitive to $\Delta\varphi_{\rm geo}$.

Taking the logarithm of the likelihood function, one obtains

$$\log L = \sum_i D_i \log \omega_i - \sum_i \omega_i + C \tag{4.20}$$

where $C = -\sum_i \log(D_i!)$ is a constant with respect to the parameters f_j and is therefore model independent and can be neglected. Maximizing now for the intensity f_j results in the following set of equations:

$$\sum_i D_i \frac{\partial \omega_i}{\partial f_j} / \omega_i - \sum_i \frac{\partial \omega_i}{\partial f_j} = 0 \tag{4.21}$$

This is the general expression for maximum likelihood in binned mode.

A different approach, i.e. maximum likelihood in list mode, is possible when, having many parameters attached to each event or reducing the bin size, the number of bins in the data space far exceeds the number of events and we will have 0 or 1 photons for each bin. By getting rid of the bins in which there are no photons, Eq. 4.21 will be dealing with photons rather than bins. The corresponding problem of finding the object intensity will be handled in the so-called list mode, i.e. on a photon-by-photon basis. The probability to detect a photon from the j^{th} pixel of the object region in the i^{th} bin will turn into the probability density for the i^{th} photon in the data space. The list mode maximum likelihood method is very useful in overcoming problems of storage in computer memory and in reducing the CPU time needed for the calculation. A detailed theoretical description of the list mode maximum likelihood technique is given in Ref. (19).

In the specific case of a CT, the equation in list mode can be derived directly from the one in binned mode. Define the source position (χ_0, ψ_0) in a 3D data space ($\bar{\varphi}$, χ, ψ), where χ, ψ is some reference frame, e.g. longitude and latitude or right ascension and declination (Ra, Dec). The instrument response is equivalently given in a 3D data space as $R^{(3)}(\chi, \psi, \bar{\varphi})$ or in a 2D data space as $R^{(2)}(\bar{\varphi}, \varphi_{\text{geo}})$. In the 3D data space $R^{(3)}(\chi, \psi, \bar{\varphi}|\chi_0, \psi_0)$ has a conical shape with a half-opening angle of 45°and the vertex at the source location (χ_0, ψ_0). $R^{(2)}(\bar{\varphi}|\varphi_{\text{geo}})$ is given by the probability of detecting $\bar{\varphi}$ for each φ_{geo}. An example for LXeGRIT is shown in Fig. 4.15. The probability distribution is, as expected, enhanced along the diagonal, i.e. for $\bar{\varphi} = \varphi_{\text{geo}}$, which is equivalent to having the ARM peak at 0°.

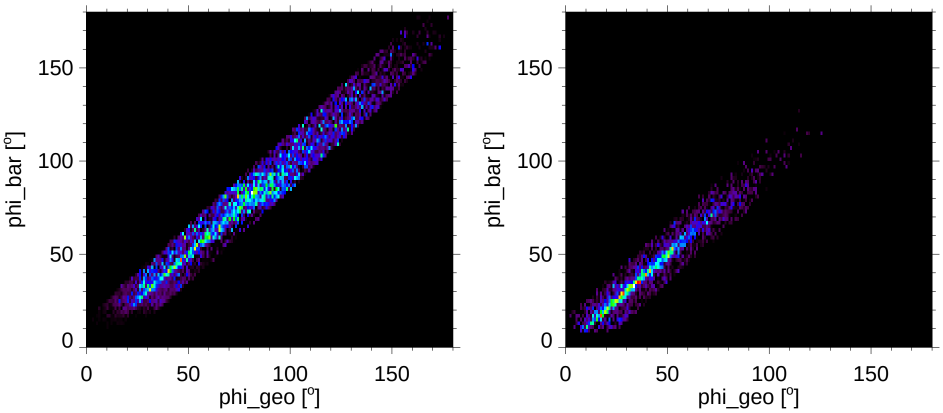

Figure 4.15: $R^{(2)}(\bar{\varphi}|\varphi_{\text{geo}})$ or point-spread function (PSF) for LXeGRIT, as obtained for MC data for a Crab-like source 25°off-axis. The PSF is given by the probability of detecting $\bar{\varphi}$ (phi_bar) for each φ_{geo}(phi_geo). *Left:* 2-site events. *Right:* 3-site events.

$R^{(3)}$ and $R^{(2)}$ are connected through the relation

$$R^{(3)}(\chi, \psi, \bar{\varphi}|\chi_0, \psi_0)\ 2\pi \sin\varphi_{\text{geo}} d\varphi_{\text{geo}} \ = \ R^{(2)}(\bar{\varphi}|\varphi_{\text{geo}})\ \cos\psi d\chi d\psi \tag{4.22}$$

Neglecting the background term, the expected number of counts in the i^{th} bin is now

$$\omega_i = \sum_j R^{(3)}_{ij} f_j \tag{4.23}$$

The logarithm of the likelihood function 4.20 is written as

$$\log L = \sum_i D_i \log(\sum_j R^{(3)}_{ij} f_j) - \sum_{i,j} R^{(3)}_{ij} f_j + C \tag{4.24}$$

If the bin size is reduced until each bin has at most one count, D_i can only be 0 or 1. The first term in Eq. 4.24 is now the sum over events rather than bins. Introducing an index *ie* to indicate events and *id* to indicate bins, Eq. 4.24 can be rewritten as

$$\log L = \sum_{ie} \log(\sum_j R^{(3)}_{ie,j} f_j) - \sum_{id,j} R^{(3)}_{id,j} f_j + C \tag{4.25}$$

Expressing $R^{(2)}(\bar{\varphi}, \varphi_{\text{geo}})$ as a gaussian $G(\bar{\varphi}, V_{\bar{\varphi}})$ for each value of $\bar{\varphi}$

$$R^{(2)}(\bar{\varphi}, \varphi_{\text{geo}}) = I_{\bar{\varphi}} G(\bar{\varphi}, V_{\bar{\varphi}}) \Delta_{\varphi_{\text{geo}}} \tag{4.26}$$

and replacing $R^{(3)}$ in Eq. 4.25 according to Eq. 4.22

$$\log L = \sum_{ie} \log\left(\sum_j \frac{G_{ie,j} f_j}{\sin\varphi_{\text{geo}}}\right) + \sum_{ie} \log \frac{I_{\bar{\varphi}} d\chi d\psi \cos\psi}{2\pi} - \sum_j T_j f_j + C \tag{4.27}$$

where $T_j = \sum_{id} R^{(3)}_{id,j}$ is the sensitivity to the j^{th} pixel in the object region and the second term is a constant since the parameters $I_{\bar{\varphi}}$, χ, ψ do not change for each event. Eq. 4.27 is therefore simplified as

$$\log L = \sum_{ie} \log\left(\sum_j \frac{G_{ie,j} f_j}{\sin\varphi_{\text{geo}}}\right) - \sum_j T_j f_j + C \tag{4.28}$$

which is the likelihood function in list mode.

Two different algorithms have been tried to solve the nonlinear system of equations in 4.21. One is the Expectation Maximization (EM) or Lucy iteration algorithm (63), (61), which iteratively estimates the density of the whole object region until the convergence criterion is satisfied. The resulting source image is often sharp and occupies only few pixels, but the drawback of this algorithm is its slowness. The determination of the uncertainty on the source intensity and the detection significance is also a difficult task using the EM algorithm. Another possible choice to solve the system in Eq. 4.21 is the Newton-Raphson algorithm (76). Instead of simultaneously getting the density distribution of the whole object region, it separately estimates each pixel on the source parameters. The statistical significance is then obtained from $-2\log\lambda$, where λ is the likelihood ratio of the two hypotheses background only and background plus source (38); $-2\log\lambda$ follows a χ^2_3 distribution for an unknown point source and a χ^2_1 distribution for a known source. Using the Newton-Raphson algorithm it takes only several minutes to obtain the source image, but the source image is relatively broad.

4.4 Examples

The Maximum Likelihood imaging techniques in list mode and binned mode have been used [11] to produce images of calibration γ-ray sources (Sec. 4.4.1) and celestial γ-ray sources (Sec. 4.4.2).

4.4.1 Calibration sources

Fig. 4.16 shows the energy spectrum obtained from exposing LXeGRIT to a 2738 kBq ^{88}Y source at a distance of 2 m, on axis, for about 90 minutes once 3-site events have been selected. Details about spectroscopy with LXeGRIT can be found in Ref. (15). Before any selection, the energy spectrum correctly shows the two ^{88}Y lines (0.898 and 1.836 MeV) as main features, together with a continuum which extends up to ∼3.7 MeV due to partially absorbed γ-rays and, especially above 1.836 MeV, to pile-up of independent γ-rays. The energy spectrum after *software collimation* has been superimposed. Here software collimation means the selection of events in the ARM

---

[11] In collaboration with S. Zhang, High Energy Astrophysics Lab, Institute of High Energy Physics, Beijing, China.

peak after the imaging procedure. The continuum is greatly reduced, by a factor of 4 at 1.5 MeVand to a negligible fraction above 2 MeV. The efficiency for the 1.836 MeV line is about 55%, consistent with the results presented in Sec. 4.3. The z and energy distributions for each of the three interactions are shown in Fig. 4.17. Events are selected in the 1836 keV full energy peak and after software collimation. The same distributions as obtained from MC data reproducing the experimental conditions have been superimposed. The capability to measure energy and position for each interaction in a multi-site event is obviously a primary requirement for a CT. The shape of the z-distributions are as expected for a source shining on top of the detector, keeping in mind that the first scatter is most likely in the forward direction. The final image of the source for the 1.836 MeV line is shown in Fig. 4.18, reconstructed with a list mode Newton-Raphson algorithm. The source location is correctly determined with an accuracy of about one pixel, i.e. 1°.

Another example is the resolved image of two calibration sources, ^{60}Co (1.17 and 1.33 MeV) and ^{22}Na (1.28 MeV), shown in Fig. 4.19. The two sources were placed ∼1.7 m above the detector and the angular separation between the two sources was ∼10°. A flat diffuse background and 100% detection efficiency T_j for each pixel in the object region were assumed, together with a variance $V_{\bar{\varphi}}$=3.5°.

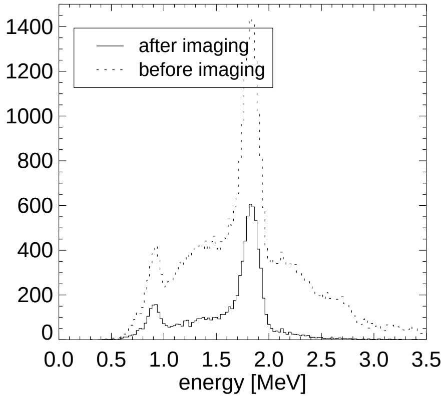

Figure 4.16: ^{88}Y 3-site energy spectrum before and after software collimation.

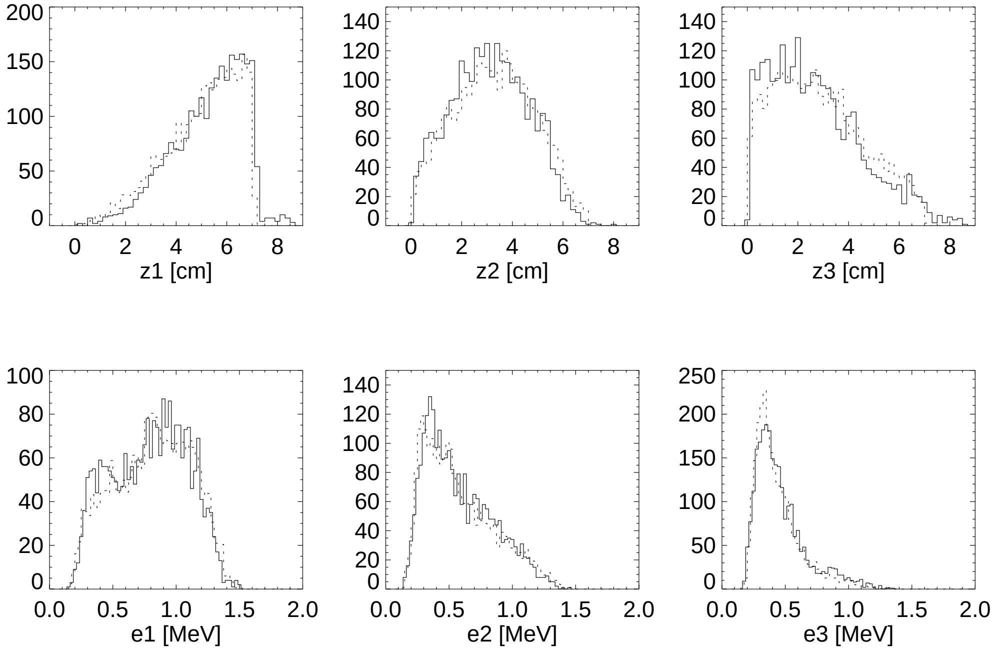

Figure 4.17: From the same ^{88}Y data as in Fig. 4.16, multi-site events selecting the 1836 keV line and applying software collimation. *Top:* z-distribution for the first, second and third interaction. *Bottom:* energy spectra for the first, second and third interaction. Overplotted with a dashed line are Monte Carlo data.

4.4.2 Astrophysical applications

In any realistic astrophysical application, data from a CT will be largely dominated by background events. It has been the case for COMPTEL and it is the case for LXeGRIT, even with an improved signal-to-noise ratio. A large fraction of background events either is produced locally or comes from a wrongly reconstructed time sequence (Sec. 4.2). These events cannot be modeled by the diffuse background from the object region, since they are insensitive to the specific celestial origin. The capability to properly handle the internal background in the framework of a maximum likelihood binned mode algorithm has been achieved by COMPTEL, which produced its standard COMPTEL Processing and Analysis Software System (COMPASS). Since we still do not have a reliable model for the background on an event-by-

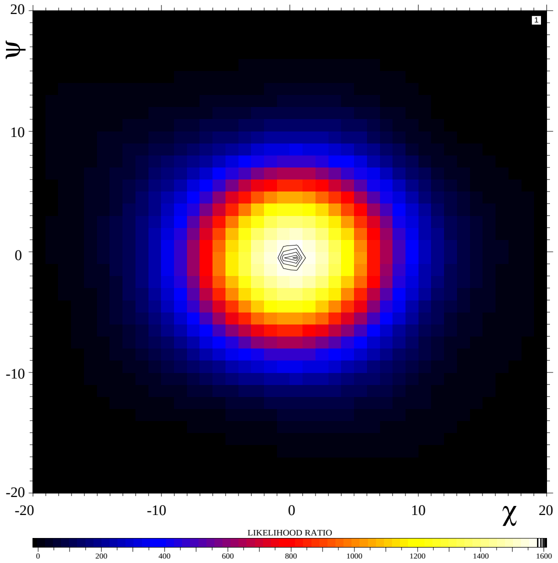

Figure 4.18: Maximum likelihood (list mode) image of a ^{88}Y source 2 m above the LXeGRIT detector.

event basis, which is needed for the list mode maximum likelihood, we used a data filtering technique developed for COMPTEL (22). An example of such an analysis for MC data for a Crab-like source, i.e. with power law spectrum with index 2, combined with the *measured* background level in LXeGRIT at balloon altitude (cfr. Ch. 6) is shown in Fig. 4.20. In COMPASS the background is derived from the observational data themselves by filtering out the source signal along the $\bar{\varphi}$ direction (22). The image in Fig. 4.20 would be obtained by LXeGRIT within a six hour exposure to the Crab nebula assuming the efficiency shown in Fig. 4.4. A six hour exposure is usually achievable during a balloon flight. As discussed in Ch. 3, 6 and 7, the actual efficiency was one order of magnitude lower.

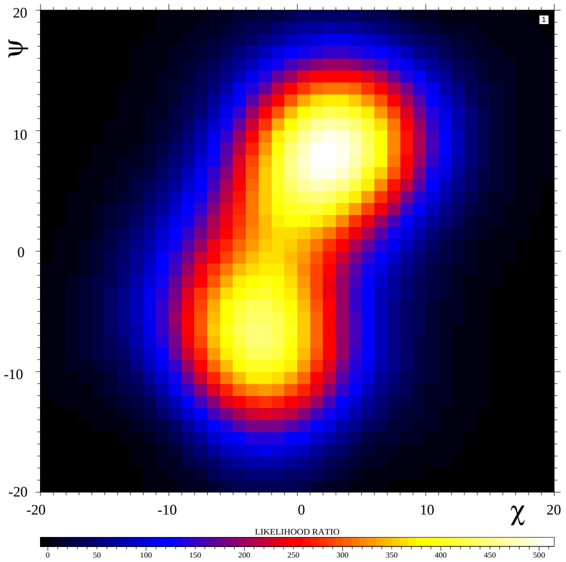

Figure 4.19: Maximum likelihood (list mode) resolved image of two calibration sources, ^{60}Co and ^{22}Na; the angular separation between the two sources was ∼10°.

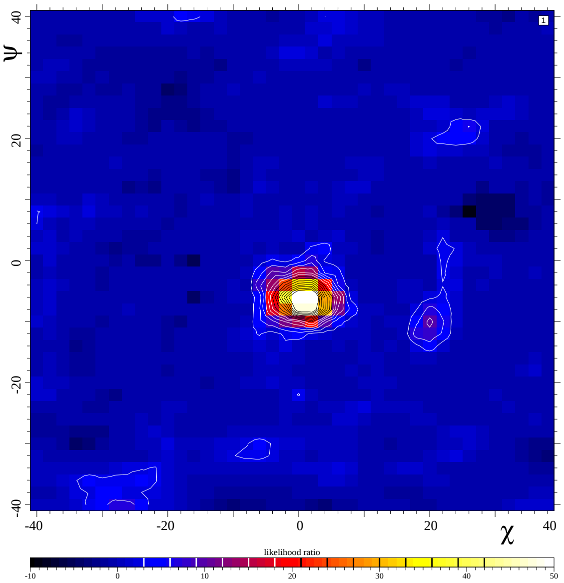

Figure 4.20: COMPASS image of a Crab-like source, assuming a six hour exposure and the efficiency shown in Fig. 4.4, together with the *measured* background level in LXeGRIT at balloon altitude (34).

Chapter 5

Results from the 2000 balloon flight

Introduction

The LXeGRIT instrument in its year 2000 flight configuration has been described in Ch. 2 and Ch. 3. The LXeTPC was built as a laboratory prototype; turning the laboratory prototype into a balloon borne instrument has required new developments mostly in three areas: *i*. a cryogenics flight system, *ii*. a readout electronics and data acquisition flight system and *iii*. an instrumentation and control system. A parallel effort has involved modifications of the gondola and veto shield systems of the University of New Hampshire Directional Gamma-Ray Telescope (DGT) (42), made available for LXeGRIT. The veto shield system was used for the flight in 1999 (see Appendix A) but was eventually removed in preparation of the flight in 2000. The DGT gondola was extensively modified for LXeGRIT and its mass model has been described in Sec. 3.2.1. The LXeGRIT instrument had four balloon flights: two in 1997, one in 1999 and one in 2000. Results from the 1999 flight are given in Appendix A, while results from the 2000 flight are given in this and in the next chapter.

5.1 The 2000 balloon flight

The most recent flight took place on Oct 4–5, 2000, from Ft. Sumner, NM and lasted 27 hours, including ascent. Fig. 5.1 shows the altitude of the

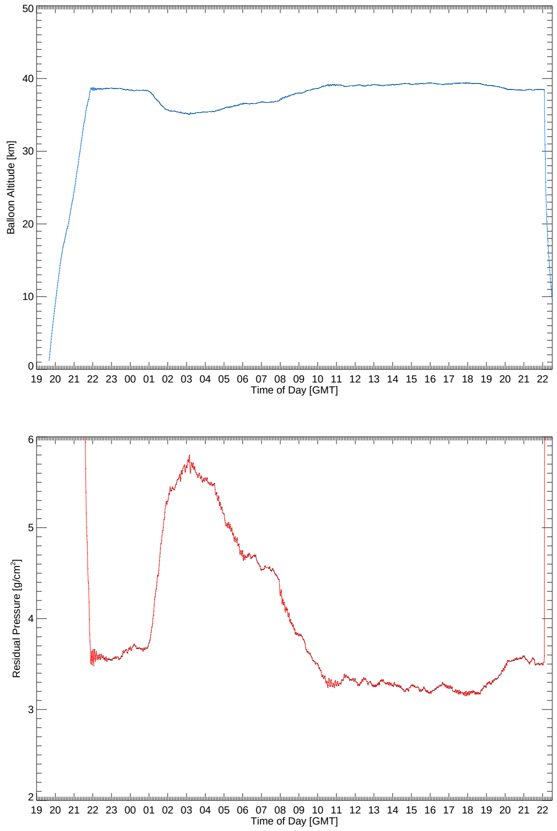

Figure 5.1: *Top:* Altitude of the balloon payload during the 2000 flight. *Bottom:* Atmospheric depth.

balloon payload and the corresponding atmospheric depth, which varies between 5.7 and 3.2 g cm^{-2}. In the 2000 flight configuration, the instrument was sensitive in the energy range from ∼150 keV to 10 MeV. The LXeTPC trigger rate, provided by the primary scintillation light signal (first, level trigger, *FLT*), was ∼600 Hz (Fig. 5.2). The trigger rates for each of the four PMTs are shown separately in Fig. 5.4. This rate was nearly constant throughout the flight, after ascent had been completed. The histograms of the PMT trigger rate are shown in Fig. 5.3; the right panel shows the trigger rates separately for three different periods:

1. ascent (20:00 - 21:30 UTC);
2. at float altitude with a lower threshold (22:30 - 24:15 UTC);

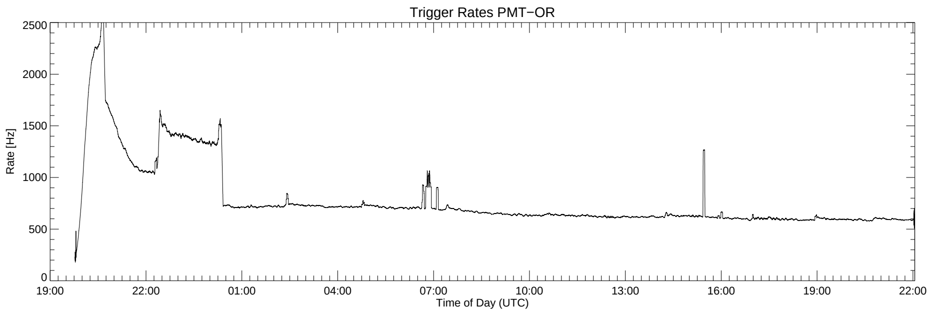

Figure 5.2: PMT-OR rate vs. time.

3. at float altitude with standard settings (24:15 - 22:00 UTC).

During this period, the livetime fraction of the on-board data acquisition system (DAQ) was ∼50% (Fig. 5.5). Since the LXeTPC itself has a deadtime of about 50 μs / event and for a rate of 600 Hz the deadtime fraction amounts to less than 5%, the instrument deadtime is largely determined by the DAQ. The DAQ processor was able to handle ∼300 Hz, the rejection rate at the second level trigger was ∼250 Hz, the rate of selected events ∼50 Hz, all of them transmitted to ground or written to the on-board hard disks (Fig. 5.6). The "gaps" visible in the rate vs. time plots correspond to the TPC cooling periods during which the DAQ is turned off due to the increased noise level on the anodes, while the PMTs remain operational. Three "snapshots" of particle interactions in the LXeTPC during the 2000 balloon flight are shown in Fig. 5.7. LXeGRIT performed flawlessly during the entire flight and collected $\sim 5\ 10^6$ events.

5.2 Instrumentation and control system

Apart from the trigger rates, all the housekeeping and instrument control is handled by a designated processor part of the Instrumentation and Control System (ICS). The control functions include setting the high voltages for the TPC cathode, x-y wire planes and PMTs, and to operate the solenoid valves for cooling of the detector. The corresponding commands are decoded from the signals received by telemetry. The high voltage on the electrodes is raised and lowered at a predetermined rate to avoid an excessive charge build-up due to the voltage change, which could destroy the input of the

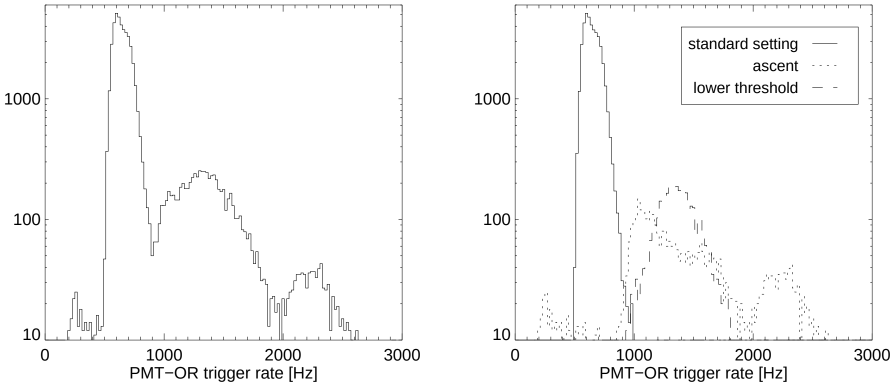

Figure 5.3: Histograms of the first level trigger rate. *Left:* entire flight, as shown in Fig. 5.2. *Right:* the data are subdivided in three sub-samples: ascent (20:00 - 21:30 UTC), lower threshold (22:30 - 24:15 UTC), standard setting (24:15 - 22:00 UTC). While the ascent sub-sample shows a high variability, ranging between ∼200 Hz and ∼2500 Hz, the other two sub-samples are rather stable, at ∼600 Hz and ∼1400 Hz.

charge sensitive amplifiers.

Most of the LXeGRIT electronics is exposed to the environmental conditions during the flight. The ambient pressure at float altitude is around 2 Torr, and the temperature varies typically between -20° C during day time and -40° C during night time, when the payload drops to lower altitudes. During the ascent, the payload passes through even colder regions, below -60° C. The heat produced by the circuits protects them from getting too cold during this half an hour period. Once at float altitude, the low pressure reduces the convection cooling by roughly a factor 20. High-power circuits might overheat, if the produced heat is not efficiently transferred to the aluminum structure of the payload. In addition, white panels shield the gondola and its electronics from solar irradiation. During the flight the temperature of many critical parts is monitored by 16 temperature sensors.

The read-out processor together with its communication module incorporate high-power integrated circuits (IC). Providing an individual heat path for each IC would have been too difficult, therefore the processor box is hermetically sealed and kept under pressure. The CPU and one other circuit are responsible for most of the generated heat. Thereby they are thermally

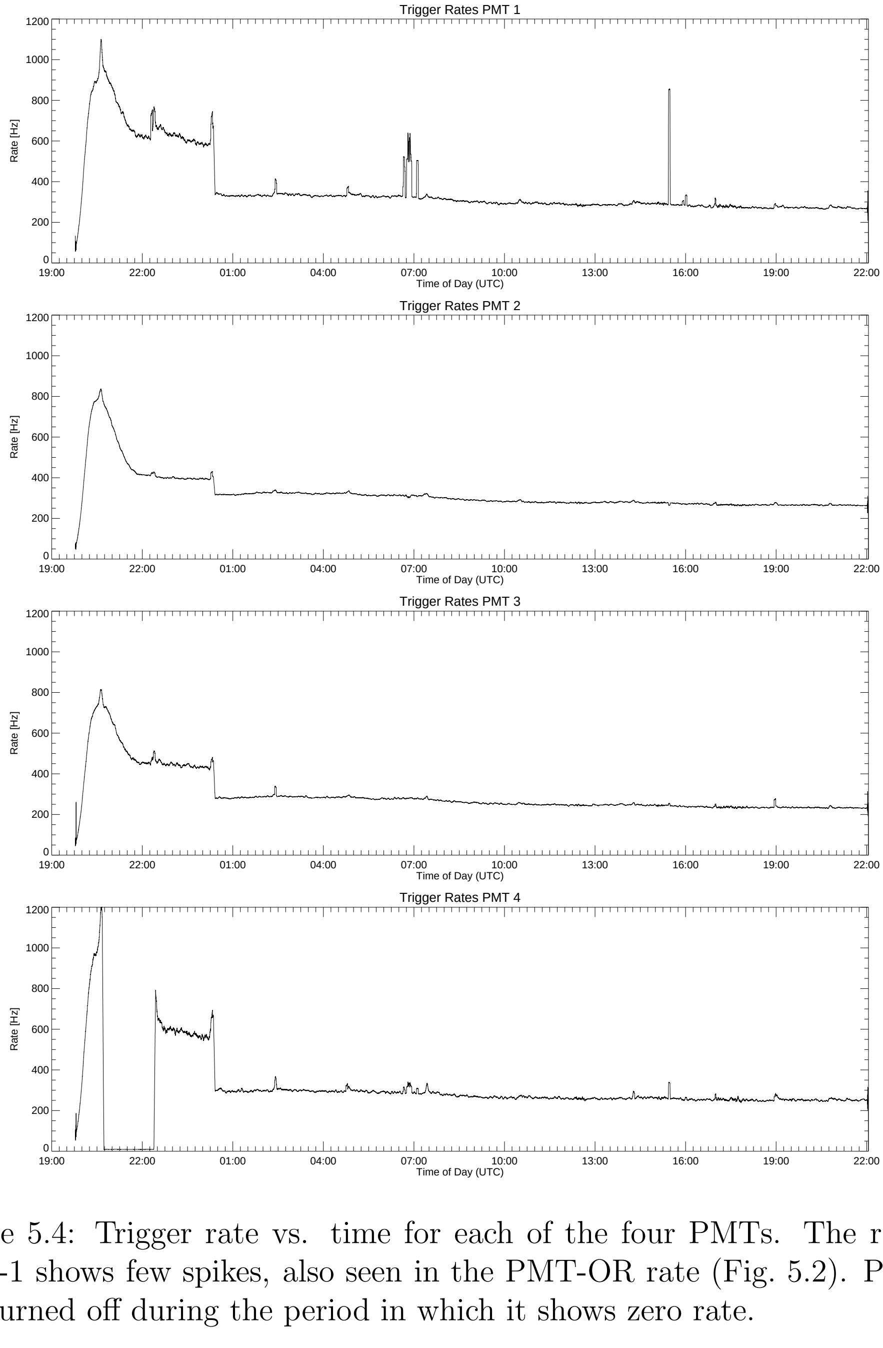

Figure 5.4: Trigger rate vs. time for each of the four PMTs. The rate of PMT-1 shows few spikes, also seen in the PMT-OR rate (Fig. 5.2). PMT-4 was turned off during the period in which it shows zero rate.

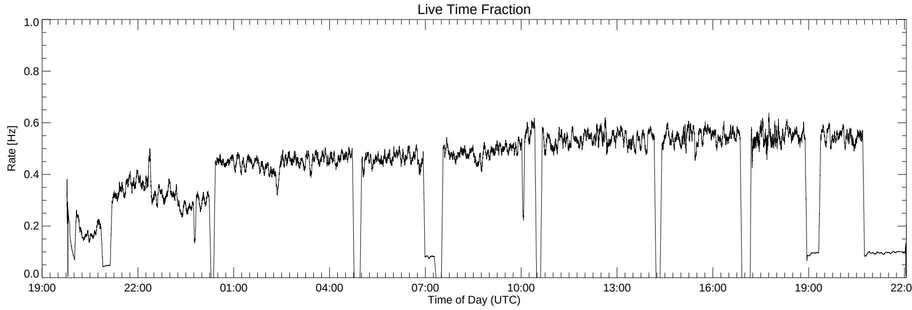

Figure 5.5: DAQ livetime fraction vs. time.

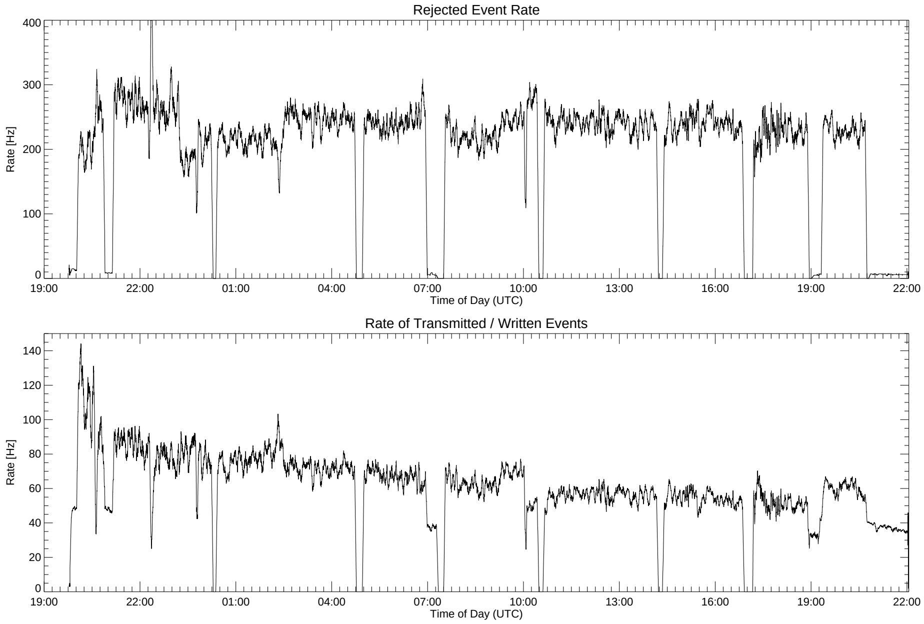

Figure 5.6: Rate vs. time of rejected events (*top*); rate vs. time of events transmitted to ground or written to the on-board hard disks (*bottom*).

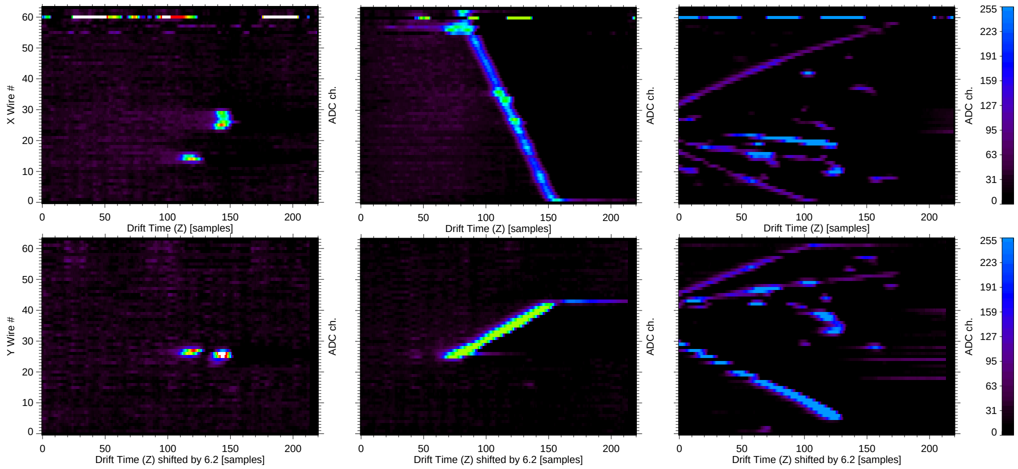

Figure 5.7: "Snapshots" of three different events in the LXeTPC recorded during the balloon flight in year 2000; for each of them the X-Z view and the Y-Z view are shown. *Left:* a 2-site γ-ray interaction. *Center:* a relativistic particle passing through the fiducial volume. Several δ-rays are visible in the X-Z view. *Right:* a more complex interaction with several particles detected in the fiducial volume. The vertex happens below the fiducial volume, i.e. at $Z < 0$.

grounded to the aluminum container. A miniature fan circulates the gas in the closed box, resulting in better heat transfer from the circuits on the board to the outside walls of the container. Hermetic connectors bring all the ports from the processor to the outside. A large aluminum heat sink on the outside of the container serves to increase the convection cooling in the thin atmosphere.

During the first flight of the new processor in 1999, the temperature in the container stabilized at about 75° C. Although the processor was working well under these conditions, it was desirable to lower the operating temperature. For the October 2000 flight of LXeGRIT, the container was therefore filled with one atmosphere of helium. Due to the higher speed of the He molecules, the heat transport to the outside walls is more efficient. This resulted in a reduction of the operating temperature by almost 10 degrees.

The data storage disks also have to be mounted in a hermetic container, filled with air under normal atmospheric pressure. This is not only for thermal considerations, but also because they require an air cushion to separate the writing heads from the magnetic surface during operation. Heat conduction through the mounting of the disks to their container ensured temperature conditions well within specifications.

In addition to the 16 temperature sensors, the temperature of the liquid Xe is also constantly measured. Because of the low temperature and of the precision required for this measurement, a platinum resistor mounted in good heat contact with the bottom flange of the TPC vessel is employed. Given the relation between vapor pressure and temperature, this measurement can be used to manually initiate cooling if the pressure transducer should fail shutting down the automatic system (see Fig. 5.8).

The operation of a HV system is problematic at reduced air pressure. With the reduced density, discharges are frequent at voltages completely safe at normal air pressure. These discharges of course disappear in a good vacuum. The residual pressure at float altitude is about the worst condition for voltage breakdown. The cathode voltage power supply is therefore mounted within the envelope of the TPC cryostat which is evacuated for thermal insulation of the cold detector. The vacuum in the cryostat, provided by the cryo-pump within the LN_2 dewar, is also measured by the ICS.

Whereas the applied voltage is a good measure to determine the field distributions in the TPC, it is the current in the divider chain which tells if all electrodes are supplied with the proper potential. Therefore also the currents in the divider chains for the cathode and field shaping rings, and in the x-y wire planes HV distribution are constantly measured and transfered to ground by the ICS.

In flight, primary low-voltage (28V) electrical power was supplied by a stack of 40 (20 in 1999) lithium batteries, rated at 30Ah each, allowing a flight duration of about 40 hours.

5.3 In-flight coordinates

Looking for celestial sources, one needs to change from the "detector coordinates", as defined by the built-in coordinate system of the TPC, to "sky coordinates", e.g. right ascension and declination. One additional complication is that during the flight the gondola is continuously moving [1], including rotational motion, with respect to the "sky coordinates" and therefore the coordinate transformation has to be defined as a function of time. Here we

---

[1] Even for a stationary telescope, one should account for the movement of the Earth.

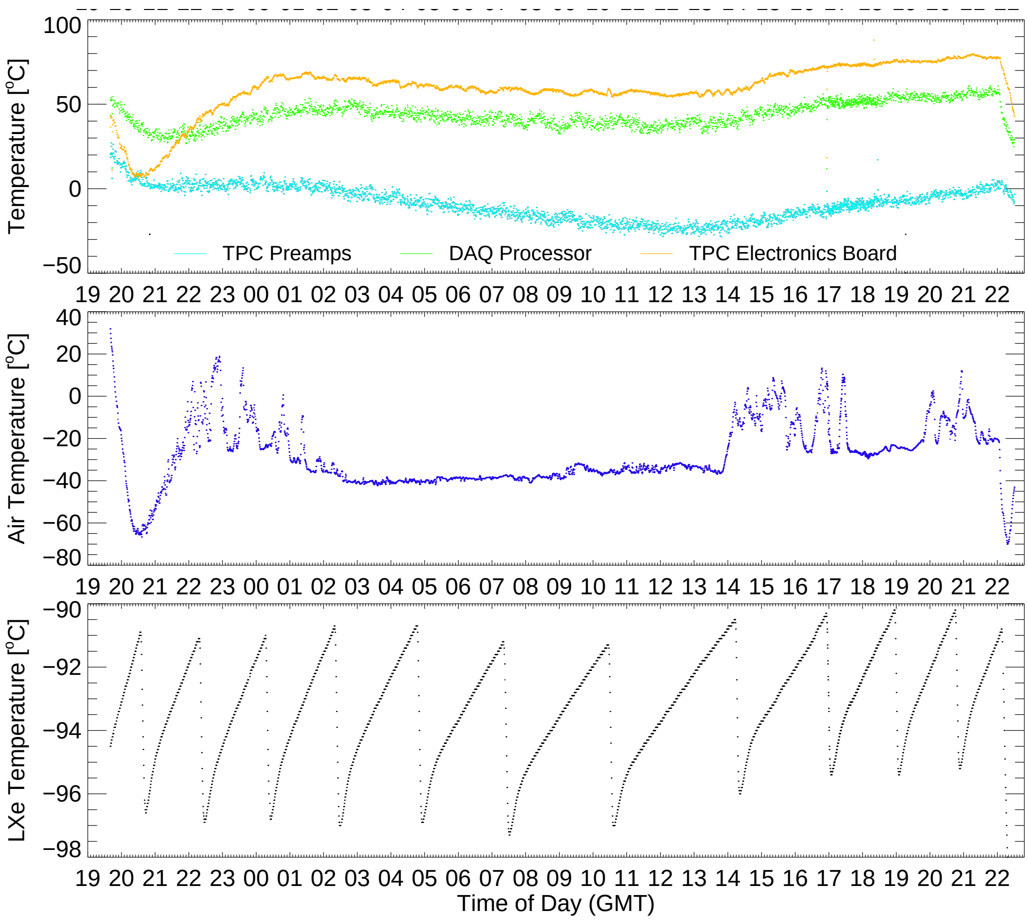

Figure 5.8: *From top to bottom:* 1. temperatures as measured by sensors placed at three different locations (TPC preamplifier boxes, DAQ processor and TPC electronics board); 2. air temperature - some apparently wild variations are due to direct exposure to the Sun as the gondola rotates around its vertical axis; 3. liquid xenon temperature - the "dips" correspond to cooling cycles with liquid nitrogen. (October 2000).

describe the procedure as for the flight 2000 data, but for 1999 data it would be practically identical [2].

5.3.1 Orientation of the gondola

The direction to the geographic North pole is provided by the magnetic North direction as measured by the magnetometer, in combination with the local magnetic declination, defined as the angle between geographic North and the projection of the magnetic field vector on the horizontal plane. By convention, the magnetic declination is positive if magnetic North is East of geographic North, and negative in the other direction:

$$\text{True bearing (geogr. North)} \;=\; \text{Magnetic bearing} \;+\; \text{Magnetic declination}$$

The magnetic declination changes along the flight path by about 3°, and has been computed from the NSBF GPS positions and a public database (71) in 1/2 hour steps; this piece of information is then combined and stored in a binary table. The orientation of the magnetometer with respect to the gondola has been measured before the flight, using a mark indicating the direction of geographic North in Ft. Sumner (the starting point of the 1999 and 2000 flights). The magnetometer was oriented such that the readings were closely aligned with the $\phi_{ds} = 0$ direction pointing to geographic North - where ϕ_{ds} is the azimuth in the detector system - as shown in Fig. 5.9. The magnetic North of the magnetometer should therefore only be corrected for the *difference* of local magnetic declination with respect to the magnetic declination in Ft. Sumner ($b_{geo} = 34.49°, l_{geo} = -104.22°$) of +9.35°, which has been subtracted in the binary table.

The calibration of the gondola scale versus the magnetometer reading shows significant systematics of about ±4°, which could be due to a systematic inaccuracy in the labeling of the angular scale on the gondola. Another possibility to be checked is that the gondola was not hanging straight, and we therefore introduced a parallax effect when orienting the gondola towards the distant source. However, with a distance to the mark of at least ~ 50 m, this effect is expected to be $\lesssim 1°$, assuming that the center of the gondola was displaced < 1 m from the rotation axis. The inaccuracy of the manual alignment with the North direction under windy conditions results in scatter of each datapoint, but should not produce a systematic trend.

---

[2] This section is adapted from U. Oberlack “LXeGRIT Flight Coordinates and Transformations”, 2001, LXeGRIT internal note.

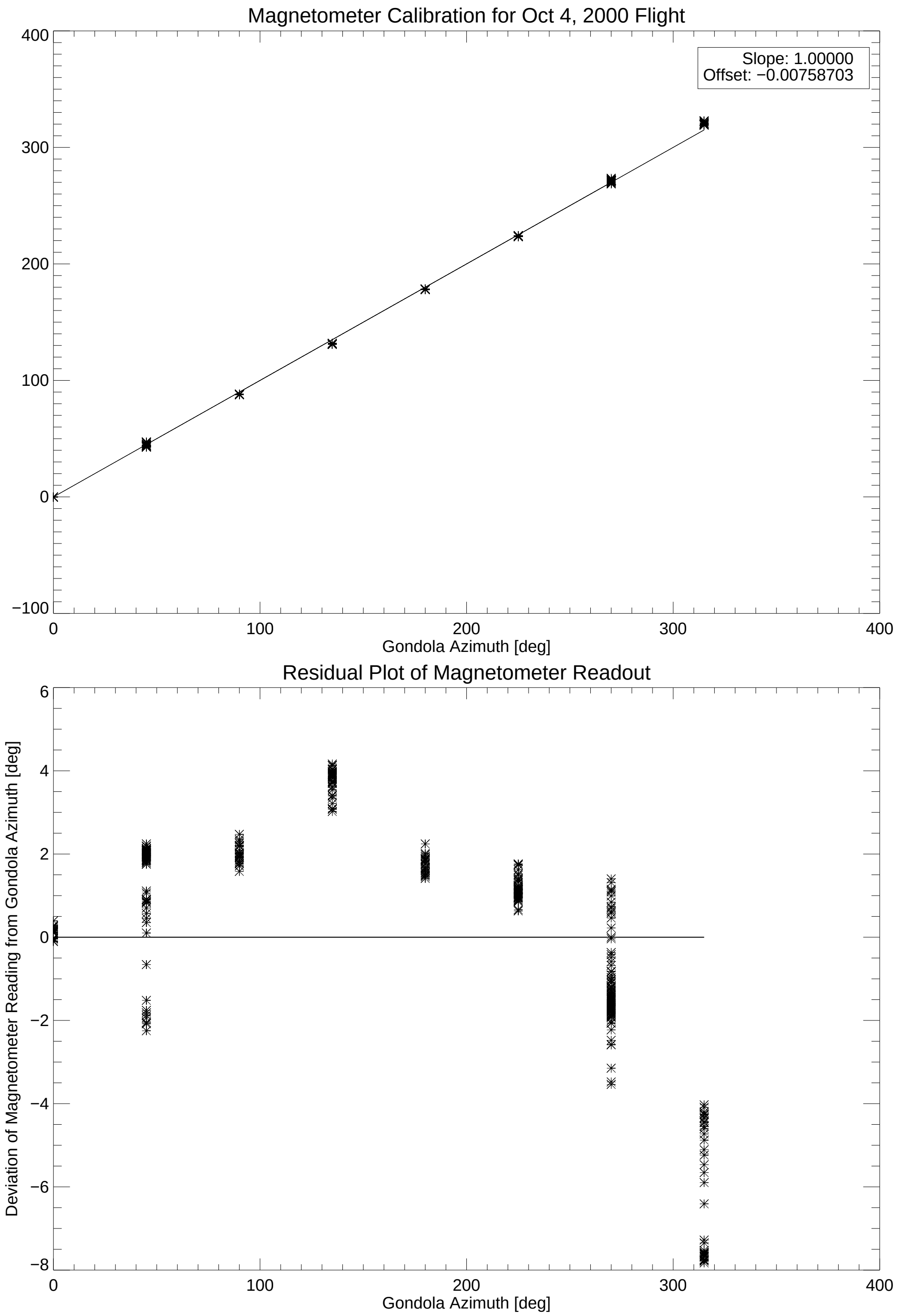

Figure 5.9: Calibration of the relative orientation of magnetometer and gondola.

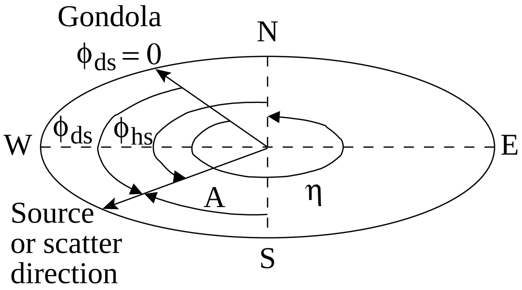

Figure 5.10: Orientation of the detector with respect to the local horizon system.

5.3.2 Coordinate transformations between detector system and sky system

The following steps deal with the coordinate transformations necessary to convert detector coordinates into sky coordinates.

1. Transformation of the detector coordinates (θ_{ds}, ϕ_{ds}) into the local horizon system (θ_{hs}, ϕ_{hs}) : Since the vertical detector orientation in direction of the local zenith is quite stable (within $\pm 1^\circ$) and close to the measurement uncertainty of the magnetometer/inclinometer, we currently neglect this small difference (compared to the angular resolution), and set $\theta_{ds} = \theta_{hs}$. Thus only the azimuth angle ϕ_{hs} needs to be determined, using the knowledge of the direction to the geographic North pole η. Fig. 5.10 shows the relation between detector system and horizon system:

$$\begin{aligned} \phi_{hs} &= 360^\circ - \eta + \phi_{ds} && (5.1) \\ A = 180^\circ - \phi_{hs} &= [\eta - \phi_{ds} + 180^\circ\ (+360^\circ)] \text{ modulo } 360^\circ && (5.2) \end{aligned}$$

   Note that the classical astronomical definition of 'Azimuth' A has its zero-point towards the South direction, and is oriented as a *left-handed* system, i.e., S-W-N-E.[3]

2. Transformation from the horizon system to the fixed equatorial system, using spherical trigonometry. Fig. 5.11 illustrates the equatorial and

---

[3] A can also be found defined with respect to North.

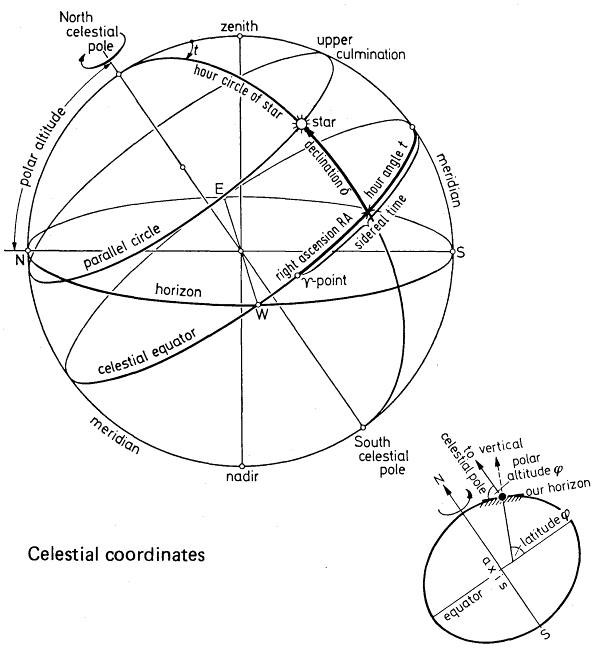

Figure 5.11: Celestial Coordinates (102).

horizon coordinate systems, which can be found in an introductory astronomy textbook, or, briefly summarized, in Zombeck (102).

$$
\begin{aligned}
\cos\delta\ \sin t &= \cos a\ \sin A && (5.3)\\
\cos\delta\ \cos t &= \sin a\ \cos b_{geo} + \cos a\ \cos A\ \sin b_{geo} && (5.4)\\
\sin\delta &= \sin a\ \sin b_{geo} - \cos a\ \cos A\ \cos b_{geo} && (5.5)
\end{aligned}
$$

δ**:** Declination: angle above/below the equator.

t**:** Local Hour Angle, equatorial azimuth angle measured westward (left-handed) from the South.

a**:** Altitude: angle above/below the local horizon. $a = 90° - \theta_{hs}$

A**:** 'Azimuth': measured westward along the horizon from the South.

b_{geo}**:** Geographical latitude of the current location.

Two equations are needed for the unknown t, to cover the four quadrants of the equatorial plane. IDL provides a convenient function ATAN(y, x) with two arguments for the two legs of a right angle x,

y, computing the correct angle in $]-\pi, \pi]$ depending on the signs of x and y:

$t = \mathrm{ATAN}\,(\cos a\ \sin A / \cos\delta,\ (\sin a\ \cos b_{geo} + \cos a\ \cos A\ \sin b_{geo} / \cos\delta)$

3. Transformation from the fixed to the co-rotating equatorial sky system (α, δ):

$$\alpha = \Theta - t \tag{5.6}$$

α: Right Ascension: right-handed azimuth angle in the equatorial system counted with respect to the direction of the vernal equinox.

Θ: Local Mean Sidereal Time: hour angle of the vernal equinox, computed from the local geographical longitude, date, and time during the flight with the program `ct2lst` of NASA's IDL Astrolib program library.

Chapter 6

Background at balloon altitude

Introduction

Since the atmosphere is opaque to MeV photons, observations of celestial objects must be carried out at balloon altitude or in the near space, a particularly harsh radiation environment. Given the low flux from astronomical sources in the MeV region, [1] a measurement of the background level at balloon altitude is a much needed *experimentum crucis* for any new detector concept. LXeGRIT collected data for studies of the background at balloon altitude twice, in 1999 and 2000; in this chapter we focus on the flight in year 2000, while results from the 1999 balloon flight are streamlined in Appendix A.

The measured background level, together with a description of the experiment, is given in Sec. 6.1. Most of the studies available in the literature refer to scintillator (e.g. NaI) detectors or high resolution Ge spectrometers; two classic works are Refs. (37), (47), to which we will be referring largely throughout the present chapter. LXeGRIT is unusual for several reasons: the active medium is LXe which is a novel material for astrophysical applications, the LXeTPC was unshielded, which is another novelty in the field of γ-ray astrophysics, and, rather than an integrated energy spectrum, the LXeTPC provides a large amount of useful information (a three dimensional picture of each interaction with a mm granularity etc.) for each event.

As a consequence, the relative weight of the background components will

---

[1] The Crab nebula, by far the brightest source and standard candle in the MeV sky, gives a flux of $\sim 1.7 \times 10^{-3}\ \gamma\,\mathrm{cm}^{-2}\,\mathrm{s}^{-1}$ integrated in the 1-10 MeV (94) .

be different for LXeGRIT than, for instance, in Ref. (47); a blatant example is offered by the so called "shield leakage and aperture flux" components, which entirely lose their meaning for an unshielded detector as LXeGRIT. To describe the overall background we define three components:

1. the background induced by radiation intrinsic to the detector, i.e. independent of the external radiation environment (Sec. 6.2);
2. the background due to the atmospheric γ-ray flux (Sec. 6.3);
3. the background induced by protons and neutrons, directly or through production of secondary particles (Sec. 6.4).

The in-flight response function is described in Sec. 6.6 (Appendix 1).

6.1 Observations

The performance of LXeGRIT during the 27 hours of the balloon flight in year 2000 has been described in Ch. 5. In the following, we focus on two time stretches where LXeGRIT was operated in consistently stable conditions. The first one (2:30 - 10:00 UTC) suffers from variation in altitude, as shown in Fig. 5.1, due to the customary troubles encountered during night time operations. During the second one (10:00 - 16:50 UTC), the balloon altitude was stable with a residual atmospheric pressure of 3.2 g cm^{-2}. The histograms of the trigger rate is shown in Fig. 6.1, separately for the two different periods. The trigger rate is $\sim$15% higher during the first period, as expected. The rejection rates at the second level trigger are shown in Fig. 6.2 (see Sec. 6.6 (Appendix 1) and Sec. 3.3.3 for explanation).

As shown in Fig. 6.3 and Fig. 6.3, the final rate of selected γ-rays is higher by about 10% during the first period, as expected from available measurements and models of MeV atmospheric γ-rays (e.g. Ref. (31)). The "gaps" visible in the rate vs. time plots correspond to the TPC cooling periods during which the DAQ is turned off due to the increased noise level on the anodes, while the PMTs remain operational.

The measured count rate spectra are shown in Fig. 6.5 and is discussed in detail in the remainder of the chapter.

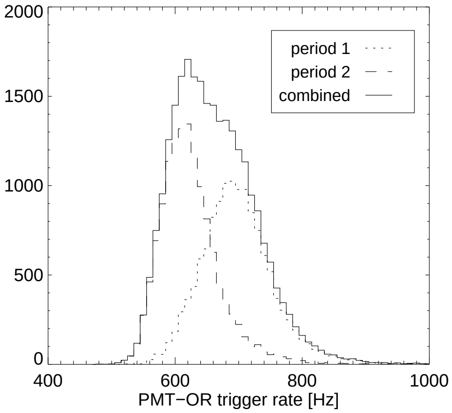

Figure 6.1: Histograms of the first level trigger rate in the time stretch 2:30 - 16:50 UTC; for further analysis it has been split in two periods accordingly to the variation in altitude.

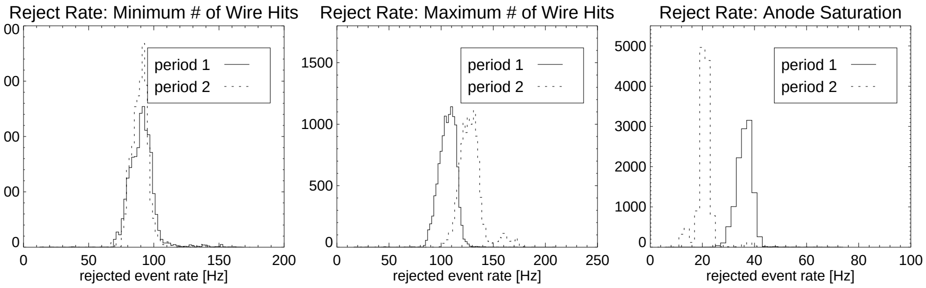

Figure 6.2: Rejection rate after three different selections have been applied as second level trigger (see Sec. 6.6 (Appendix 1) for explanation). *Left:* a minimum number of wire hits, to reject 1-site and low energy events. *Center:* a maximum number of wire hits, to reject charged particles. *Right:* anode saturation, which rejects events with energy deposition larger than ∼10 MeV, mainly charged particles. The combined rejection rate for a maximum number of wire hits and anode saturation is about 140 Hz and is very similar during the two periods.

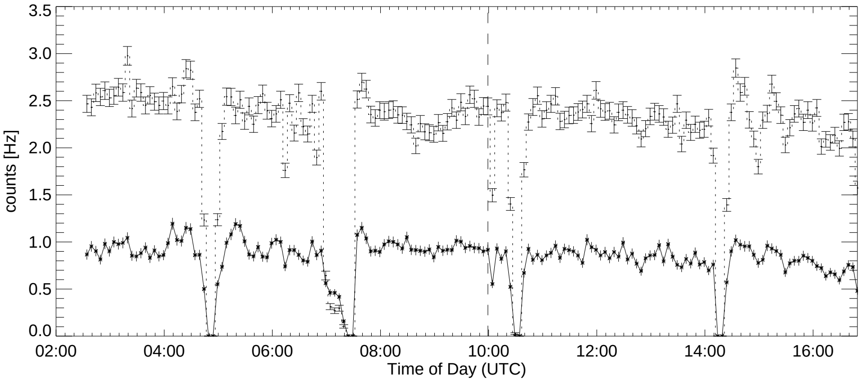

Figure 6.3: Rate vs. time of accepted events, after the entire analysis procedure has been completed; *continuous line:* 1-site events, *dotted line:* multi-site events.

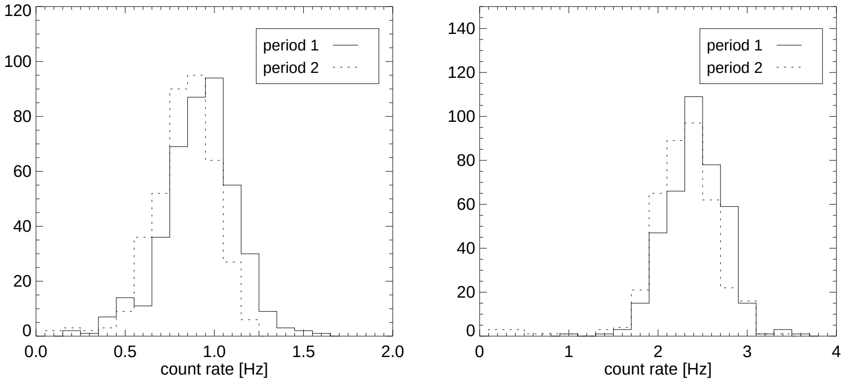

Figure 6.4: Histograms of the rate of accepted events (Fig. 6.3). *left:* 1-site events, *right:* multi-site events.

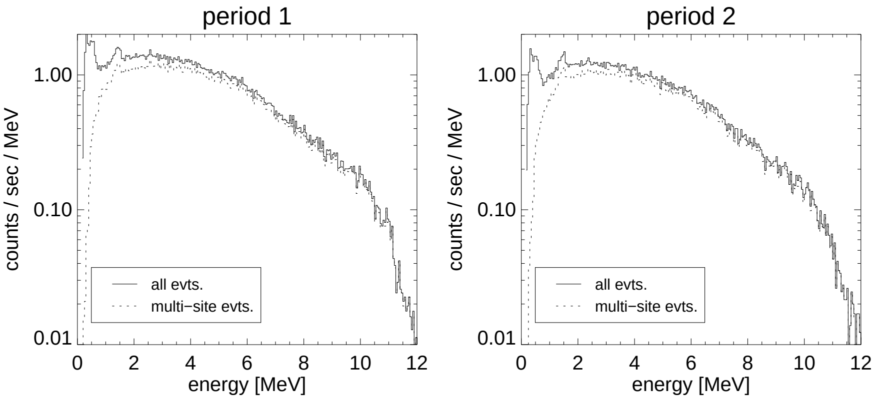

Figure 6.5: Count rate spectra; *left:* 2:30 - 10:00 UTC, *right:* 10:00 - 16:50 UTC.

6.2 Intrinsic radiation

The energy spectrum obtained running the detector in the laboratory without any external source is shown in Fig. 6.6, both for all interaction multiplicities and for multi-site events only. The total rate at the first level trigger is about 250 Hz, and the total built event rate is about 40 Hz, clearly dominated by low energy γ-rays. Two main features have been identified in the spectrum of the internal background: a “strong” ^{40}K line and α-emission, which is narrowly localized in space. We discuss them in detail in the following. Several more spectral features have been identified with a much lower intensity; because of the very limited number of counts, even after an exposure of several hours, these features appear like smooth “bumps” in the energy spectrum rather than sharp peaks. They are: 0.511 MeV from positron annihilation; 1.78 MeV from ^{27}Al(n$_{therm}$,γ)^{28}Al; 2.22 MeV from ^{1}H(n$_{therm}$,γ)^{2}D; 2.6 MeV tentatively identified as the 2.61 MeV line from ^{208}Tl (from ^{232}Th). Because of their low intensity, these features play no role in the in-flight energy spectrum. The *ambient activity* most likely contributes in a significant way to the continuum on the ground, but will be modified at balloon altitude. Therefore we neglect the laboratory ambient activity here.

For the energy spectra in Fig. 6.6 the response function was the same as described in Ch. 3 ; compared to the one in flight (see Sec. 6.6), it generally gives a higher efficiency at energies below ~1.5 MeV. When compared to the flight results, the count spectra have been rescaled accordingly.

6.2.1 ^{40}K

The very apparent ^{40}K line (1.46 MeV) has been proved to be mainly due to the potassium contained in the MACOR (machinable glass-ceramic), used for the wire structure and anode holders and spacers. The amount of potassium in the quartz windows and in the PMT windows and glass housing is comparatively small, and its importance is further reduced by the smaller solid angle. The total MACOR volume inside the TPC is about 236 cm^3, 10% of which (fraction by volume) is K_2O, about 55 g in weight. Given a molar weight of 94.2 g, this amounts to 0.6 mol of K_2O or 7.2×10^{23} potassium atoms. Being 0.0118% the natural abundance of ^{40}K, we expect to have 0.85×10^{20} ^{40}K atoms in the fiducial volume. Considering now decay time (1.42×10^9 y) and branching ratio for γ-emission (10%) of ^{40}K, we have about 200 decays s^{-1} yielding a 1.46 MeV γ-ray. The interaction rate in the fiducial volume is then further reduced by solid angle to about 50 Hz. Given an efficiency of about 1% (cfr. Sec. 3.3.3), the expected rate of detected γ-rays in the full energy peak (FEP) is less than 1 Hz. A more quantitative prediction requires a detailed Monte Carlo (MC) simulation, especially because of the extended geometry of the source.

The ^{40}K source has been distributed following the geometry of the wire structure holder and the MC code described in Ref. (35) and in Ch. 3 has been used and the rate has been normalized according to the numbers given above. The expected FEP rate is $\sim$0.6 Hz, assuming 100% livetime fraction. The uncertainty on such an estimate is 20%, accounting for the uncertainty in ^{40}K total mass and distribution and the accuracy of the MC response. The *measured* FEP rate is $\sim$0.5 Hz after correction for the livetime fraction, well compatible with expectations. Results are shown in Fig. 6.7 for 1-site events ($\sim$50% of the total rate); not only is the rate correctly reproduced, but the z distribution suggests that the ^{40}K background is fully accounted for.

The z distribution, and more generally the spatial distribution of interactions in the active volume, is a useful diagnostic of the source location. Barring any anisotropy in the detection efficiency within the fiducial volume, the density of interactions will decrease exponentially with distance from the source, with a mean free path in LXe for MeV photons of $\sim$5 cm (the actual value being energy dependent). The actual situation is much more complicated because the light trigger efficiency is strongly anisotropic (cfr. Sec. 3.3.3) and needs to be accounted for in a MC calculation. The result of such a calculation is shown in Fig. 6.7, compared to the actual data; the (experimental) z distribution for 1.836 MeV photons (^{88}Y) coming from above the TPC is also shown, to illustrate the "top-bottom" discrimination capability of this technique.

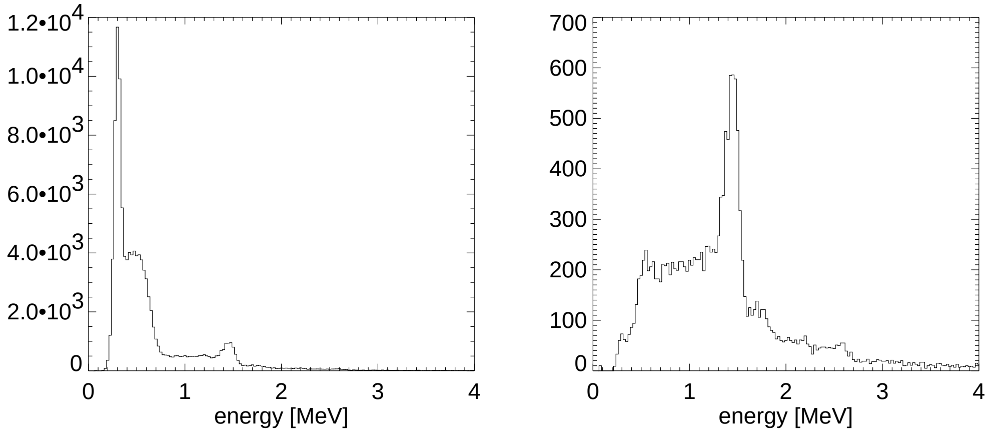

Figure 6.6: Energy spectrum of background events in LXeTPC. *Left:* All multiplicities. The energy spectrum is dominated by low energy, single-site events. The ^{40}K line at 1.46 MeV is clearly identified. *Right:* 2- and 3-site event energy spectrum for the same dataset. The ^{40}K line is now the dominant feature. Also visible hints of 0.511 MeV from positron annihilation; 1.78 MeV from ^{27}Al(n$_{therm}$,γ)^{28}Al; 2.22 MeV from ^{1}H(n$_{therm}$,γ)^{2}D; 2.6 MeV tentatively identified as the 2.61 MeV line from ^{208}Tl (from ^{232}Th).

6.2.2 α-emission

A significant component of the intrinsic/internal background appears narrowly localized (less than 3 mm spread) in the cathode region (see Fig. 6.8-$left$). It has been identified as α-emission, based on:

1. its sharp localization
2. the detected rate
3. the narrowness of the line.

The narrow peak in the z distribution of single-site events by itself rules out γ-rays, which would rather result in a spatial distribution dominated by

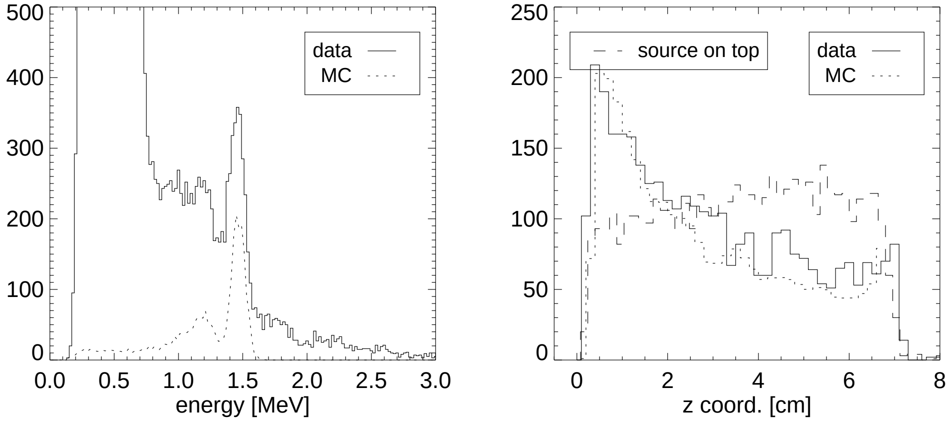

Figure 6.7: MC simulation of the ^{40}K background line, 1-site events, compared to the actual data. *Left:* energy spectrum. *Right:* z distribution of events in the ^{40}K FEP; for the actual data, the z distribution has been corrected for events in the continuum beneath the line by subtracting the z-distribution obtained for events outside the FEP. The z distribution offers an important diagnostic of the distribution of ^{40}K in the TPC, in this case in its lower part. The z distribution for 1.836 MeV coming from above has superimposed for comparison (*dashed line*).

their attenuation length (∼4 cm for 0.5 MeV photons). Selecting a 3 mm thick z-slice around the cathode region, it is possible to study the spectral characteristics of this localized component with ∼15% contamination coming from γ-rays. Doing so, a narrow line is clearly identified; it corresponds to an *equivalent* energy of 400 keV, where *equivalent* energy means as obtained applying the calibration from γ-sources. If the line comes from β-emission the energy scale is appropriate, if it comes from α-emission the true energy would be few MeV. In fact, the charge yield in LXe is different for electron (and therefore γ-rays) and α interactions; for a drift field of 1 kV/cm as in LXeGRIT, less than 5% of the charge from an α particle ionizing interaction is eventually collected, while for electrons about 80% of the charge is collected. The reader is referred to Ref. (4) for a detailed discussion .

We now argue that the background is most likely due to α-emission rather than β-emission. In fact, for electrons, the light trigger efficiency would be extremely low (about 1%) for such a low charge yield combined with a small

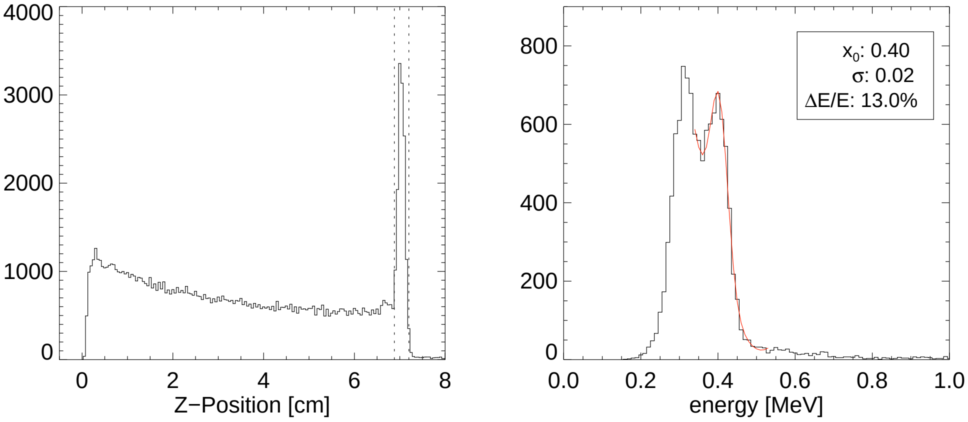

Figure 6.8: *Left:* z-position for background single-events in the LXeTPC. A peak at $z = 7$ cm, cathode location, is very prominent. *Right:* energy spectrum after selecting events at the cathode location (dashed lines). A line (otherwise invisible) is now clearly detected at 0.4 MeV (energy scale for γ-rays). As shown in Sec. 6.2.2 this feature is due to α-emission from the cathode.

solid angle, due to the high z. It would require a large decay rate to build up a detectable line. On the other hand, it is well known that, for the same energy, the light yield is much larger for α-particles, and 0.4 MeV equivalent energy means E_α larger than 5 MeV, which easily saturates the light trigger efficiency and gives an acceptable decay rate. The *detected* rate is $\sim$2 Hz; assuming a factor of two reduction due to the emission direction of the α-particle from the cathode, 100% efficiency for the light trigger and 10% efficiency of the second level trigger, the decay rate would be a reasonable $\sim$40 Hz, to be compared to $\sim$4000 Hz required for a β-source.

Another signature of α-emission is the energy resolution; the line would be too narrow for 0.4 MeV γ-rays (electrons), but it is consistent with the one expected for α-particles, of $\sim$ 5% at 0.40 MeV equivalent energy once the electronic noise has been properly subtracted. In this case the line width is dominated by the electronic noise. A hint of the possible nature of the source of α-emission is the feature at 2.6 MeV in the energy spectrum in Fig. 6.8-*right*. If its identification as the 2.61 MeV line from ^{208}Tl is correct, it would point to the presence of ^{232}Th as the source of α-emission.

In the flight data, this component of the internal background is easily identified and rejected through a fiducial volume cut.

6.2.3 In-flight ^{40}K rate

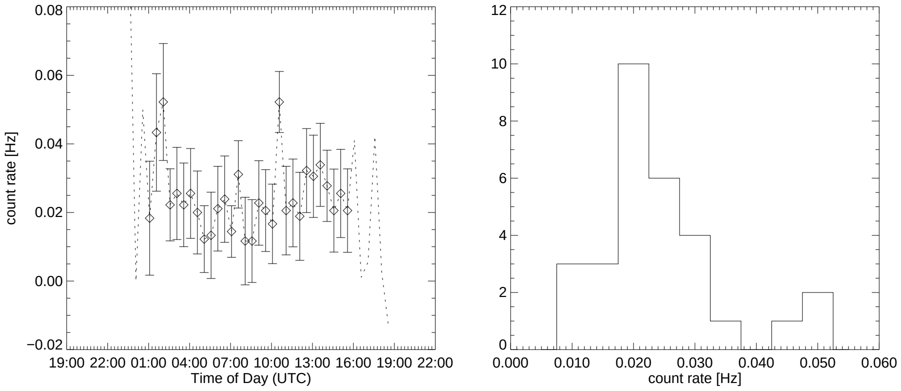

Figure 6.9: *Left:* detected ^{40}K rate vs. time for multi-site events (flight data). *Right:* corresponding histogram.

The reduction in the in-flight ^{40}K rate can be derived comparing the in-flight response function and the one in Ch. 3. At the first level trigger (FLT), the reduction is a factor ~2.5; at the second level trigger (SLT), ~2.2; the livetime fraction was ~50%. The expected rate $R_{^{40}\mathrm{K}}$ would thus be

$$R_{^{40}\mathrm{K}} = 0.4 \cdot 0.45 \cdot 0.5 \cdot (0.5 \text{ Hz}) = 0.045 \text{ Hz}$$

The measured rate for multi-site events is shown in Fig. 6.9; selecting multi-site events reduces the rate by approximately a factor of 2, i.e. the measured rate is expected to be 0.023 ± 0.005 Hz, perfectly consistent with the laboratory experimental result and strengthening our confidence in the correctness of the detector response described in Sec. 6.6 (Appendix 1).

6.3 Atmospheric γ-rays

For the atmospheric γ-ray flux, we follow the model given in Ref. (31), for an atmospheric depth 3 g cm^{-2}. The fluxes, in units of cm^{-2}sec^{-1}MeV^{-1}, are extrapolated in the energy range 100 keV - 15 MeV with four angular bins for the following zenith angles:

- $0.03\ \mathrm{E}^{-1.61}$ (0° - 45°)
- $0.20\ \mathrm{E}^{-1.48}$ (45° - 90°)
- $0.43\ \mathrm{E}^{-1.34}$ (90° - 135°)
- $0.23\ \mathrm{E}^{-1.51}$ (135° - 180°)

It is worthwhile stressing that the atmospheric γ-ray flux is poorly known and suffers from large uncertainties; as large as a factor of two on the overall normalization. An isotropic flux over the zenith angles from 0° to 90° following the power law $0.011\ \mathrm{E}^{-2.3}$ cm^{-2}sec^{-1}sterad^{-1}MeV^{-1} has also been included; it was introduced in Ref. (81) as "cosmic diffuse γ-ray" background, but the cosmic origin has been ruled out by a more recent COMPTEL measurement (57), which has eventually established the genuine cosmic diffuse γ-ray background to be ~10 times lower. The decision to keep it in our model of atmospheric emission has been taken since such a component was *measured* at balloon altitude, together with the atmospheric flux. It is questionable whether such a component should be included, since it may be due to some spurious effect. In practice this component introduces a rather negligible effect, less than 10%, compared to the atmospheric flux. It points one more time to the poor accuracy in our knowledge of the input fluxes. Each photon is propagated through the payload mass and, if the requirement of at least one interaction in the TPC fiducial volume is satisfied, then energy deposit, location and interaction mechanism are recorded for each photon interaction. Photoabsorption is dominant at energies below 250 keV, while Compton scattering dominates up to $\sim$ 6 MeV, so that in this energy band γ-rays are mainly detected through multiple interactions. Above 6 MeV, pair production becomes increasingly important, together with secondary bremsstrahlung photons. From visual inspection of selected events, we expect the model to break down above $\sim$8 MeV because of various effects not included in the MC simulation, of particular importance *i.* the interaction is no more point-like and *ii.* saturation of the dynamic range of the wires may occur. The comparison with the experimental data is eventually shown in Fig. 6.12, where we have chosen to unfold the response function [2] in the measured spectrum rather than to apply the response function to the MC simulated data; this is, in part, just a matter of taste. On the other side, it simplifies the comparison with other components (e.g. spallation background) which are not treated through a full-fledged MC simulation and it is more interesting for future applications to show the rate which should be expected having a fully efficient detector of the same size.

6.4 Other components

Background induced by atmospheric neutrons and protons (other components are much less relevant, due to their negligible initial fluxes) is usually of great concern for balloon borne γ-ray detectors (e.g. Ref. (37)); this is not the case for LXeGRIT, as we will show in the present section and as confirmed by the discussion of the experimental results in Sec. 6.5. The estimates presented here are based on some simplified analytical calculations, combined with previous laboratory measurement available in the literature. The option of a detailed MC simulation has been discarded on the ground that it does not guarantee a better accuracy, given the large uncertainties on the input fluxes and the incomplete knowledge of some of the relevant cross

---

[2] Here the response function is defined as the combination of the light trigger efficiency and the efficiency of the on-line selections, or second level trigger.

sections. Moreover, the effort required seemed disproportionate to the size of the effect we had to explain.

Following the scheme introduced in Ref. (37) the sources of background are classified as: *i.* elastic neutron scattering (Sec. 6.4.2); *ii.* inelastic neutron scattering (Sec. 6.4.3); *iii. spallation*, i.e. the asymptotic level of background after a prolonged exposure to the flux of primary and secondary cosmic rays (Sec. 6.4.4). We neglect *activation*, which in Ref. (37) is defined as the radioactivity derived from interactions involving trapped protons, for LXeGRIT did not pass through any radiation belt. The presence of γ-ray lines in the in-flight energy spectrum is discussed in Sec. 6.4.5.

But before tackling this problem, we consider the background due to charged particles directly interacting with the active LXe.

6.4.1 Charged particles

Here we consider the background due to charged particles directly entering the fiducial volume. These particles are mainly protons [3], which are detected in LXeGRIT through their interactions directly ionizing LXe.

For a detector the size of LXeGRIT, the expected rate due to charged particles, both primary and secondary cosmic rays, is a few hundred Hz. A more precise estimate of the expected charged particle rate is beyond the scope of this work and requires a model of primary and secondary cosmic ray fluxes to be propagated through the LXeGRIT mass model. Passive materials surrounding the TPC attenuate charged particles up to hundred MeV [4], and cosmic rays may pass the sensitive volume only peripherally, depositing correspondingly low amounts of energy. Moreover, since the LXeTPC is 7 cm thick, the angular dependence of the proton flux is in principle important. In any case, we reject a large fraction of this component at the second level trigger, because high energy particles would produce extended tracks in the LXeTPC thus exceeding the upper threshold to the number of wire hits; events resulting in an energy deposition larger than $\sim$10 MeV would also saturate the dynamic range of the anodes and therefore would be rejected on-line. From a visual scan of data recorded without any selections at the second level trigger, we can infer that charged particles make about 2/3 of the total in-flight rate or about 400 Hz. Events not rejected on-line are rejected

---

[3] See for example the recent measurement reported in Ref. (2).

[4] The range of a 100 MeV proton is about 5 cm in LXe, 3 cm in Al and 1.5 cm in Fe.

with an efficiency very close to one by applying off-line selections on the anode waveform and on the fiducial volume. To conclude, when measuring the γ-ray background, the contamination due to charged particles is reduced to a *truly negligible level.* We can use this measurement to constrain the proton and, as we will see in Sec. 6.4.2, neutron fluxes in LXeGRIT, which is a necessary input in order to estimate the contribution to the γ-ray background due to elastic neutron scattering (Sec. 6.4.2)and spallation (Sec. 6.4.4). Under the reasonable assumption that all the protons which deposit more than 10 MeV in LXe trigger the TPC (light trigger), the measured trigger rate of ∼400 Hz immediately gives a fair estimate of the integrated [5] flux in the fiducial volume. To obtain an order of magnitude estimate, we can consider the area through which protons can enter the active volume - including the collection region which is relevant at the light trigger level - to be

$$A_{top} + A_{bottom} + A_{sides} = (400 + 400 + 4 \cdot 200)\ \text{cm}^2 = 1600\ \text{cm}^2$$

Assuming an isotropic proton flux, the energy integrated flux will be ∼0.25 protons cm^{-2} s^{-1}, rather compatible with the one in Ref. (47) . This is a sheer coincidence, since there is reason to expect the two fluxes to be identical *a priori.* In fact, following Ref. (64) the proton flux in the detector is equivalent to the proton flux measured in the atmosphere at a depth equal to the depth of the atmosphere above the instrument plus the equivalent depth of the passive materials. For LXeGRIT, the passive materials surround the LXeTPC in a fashion which is anything but homogeneous and the LXeTPC itself is thick; the measured rate of charged particles suggests the total effective atmospheric depth, once averaged over the entire detector, to be ∼35 g cm^{-2}, as in Ref. (47). This is quite reasonable, since it would correspond to about 12 cm of Al or 5 cm of stainless steel or 17 cm of LXe or some combination of the three.

The flux relevant to the final γ-ray rate due to spallation will be larger, since it has to include atmospheric neutrons. Also the area over which the flux has to be integrated will be larger, including some of the passive materials.

---

[5] Integrated above some broad lower energy threshold: between 10 and 100 MeV, a proton would easily be stopped in the passive materials sorrounding the LXeTPC. The actual energy threshold will depend on the amount of passive materials each single proton has to pass through, which in turn depends on the angular dependence in the proton flux. Therefore, the lower energy threshold will be described by some rather broad distribution. Luckily enough the proton flux is expected to be quite negligible below 10 MeV and even considering zero efficiency below 50 MeV has no major impact on the final numbers.

On the other side, spallation induced γ-rays which originate far outside the fiducial volume will have a lesser impact, because of the reduced solid angle to hit the LXeTPC and absorption in the passive materials which shield the TPC.

6.4.2 Elastic Neutron Scattering

The background induced by elastic neutron scattering (n, n') is negligible in the energy range from 0.5 to 10 MeV, and it becomes sizeable only below 150 keV, which is the LXeTPC lower energy threshold. In clarifying this point we follow Refs. (37), (47).The fraction of energy lost in an elastic scattering on a nucleus of atomic weight A is:

$$\frac{E_n - E_{n'}}{E_n} = \frac{2A(1-\cos\theta)}{(1+A)^2} \tag{6.1}$$

where E_n and $E_{n'}$ are the energies of the neutron before and after the interaction in the reference frame where the nucleus is at rest and θ is the scatter angle in the center-of-mass frame. The fraction of energy lost is maximum for $\theta = 180°$ and, for LXe ($A_{Xe} = 131.3$)

$$\left(\frac{E_n}{E_{n'}}\right)_{max} = 0.03$$

In LXe only a small fraction of the ionization charge produced by α particles or heavier ions or, as in this case, the recoiling Xe atom, is finally collected (see e.g. Ref. (4)). Assuming that only 5% of initial charge contributes to the ionization signal, the maximum detected [6] energy will be

$$(E_{detected})_{max} = 1.5 \times 10^{-3}\ E_n$$

Therefore, in order to be detected above the 150 keV energy threshold, the minimum energy of the incoming neutron has to ~100 MeV.
Following the suggestion in Ref. (47) we adopt the description of the shape of the neutron spectrum as in Rossi (79), i.e.

$$j^{(n)}(E_n, x) = \frac{Ax}{(50+E_n)^2} e^{-x/L}$$

---

[6] According to the energy calibration obtained for γ-rays; here the same charge yield as for α-particles is assumed, but a large uncertainty of at least a factor of 2 should be included.

in units of neutrons cm^{-2} s^{-1} MeV^{-1}, where E_n is the energy of the neutron (MeV), x the interaction depth in the atmosphere (g cm^{-2}), A is a constant to be determined and L the collision mean free path in atmosphere (the nuclear collision length is 60.2 g cm^{-2}). In the present case, x has to account for the residual atmosphere as well as for the passive materials surrounding the LXeTPC. A detailed calculation carefully describing the actual mass model has not be performed. It can be avoided since the neutron flux can be normalized starting from the proton flux (see again Rossi (79)); it is shown in Ref. (47) that the proton and neutron fluxes are very similar above 100 MeV for x$\sim$35 g cm^{-2}.

We now introduce the rate of charged particles measured in LXeGRIT (400 Hz over an area of 1600 cm^2, see Sec. 6.4.1) as an estimate of the rate of neutrons integrated over the LXeTPC sensitive volume for E_n larger than 100 MeV i.e.

$$1600 \times j^{(n)}(E_n \geq 100 \text{ MeV}) = \int_{100}^{E_{max}} \frac{C}{(50+E_n)^2} dE_n = 400 \text{ s}^{-1} \text{ cm}^{-2}$$

and use it to estimate the normalization of the neutron flux: $C = 37.5$ cm^{-2} s^{-1} MeV. Therefore, the resulting flux is

$$j^{(n)}(E_n) = \frac{37.5}{(50+E_n)^2} \text{ s}^{-1} \text{ cm}^{-2} \text{ MeV}^{-1}$$

Since we are interested in giving an upper limit to the background from neutron elastic interactions, we assume that all the neutrons scatter at θ=180° (maximum energy loss) with a cross section of σ_{el}=0.5 barns [7]. The rate per unit of (detected) energy per cm^3 of LXe is

$$\begin{aligned} R(E = E_n \cdot 1.5 \times 10^{-3}) &= \frac{\rho N_A}{A_{Xe}} \sigma_{el}[j^{(n)}(E_n)] \qquad (6.2) \\ &= \frac{3.06 \times 6.02 \times 10^{23}}{131.3} 0.5 \times 10^{-24} \cdot \frac{37.5}{(50+E_n)^2} \\ &= \frac{0.26}{(50+E_n)^2} \text{ counts s}^{-1} \text{ MeV}^{-1} \end{aligned}$$

It is shown in Fig. 6.10 as function of detected energy and integrated over 2.4 l active volume; integrated over energy it gives a total rate of $\sim$4 Hz, which

---

[7] It was impossible to find in the literature σ_{el} for Xe for E_n above 50 MeV; extrapolating from lower energies, σ_{el}=0.5 barns looks conservatively large.

constitutes an upper limit and does not include any detection inefficiency. Since it is negligible, it is not considered in the following.

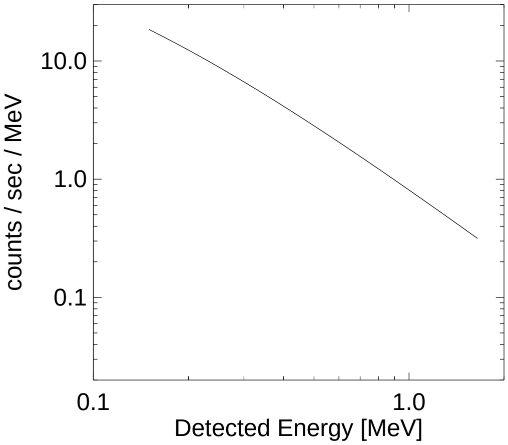

Figure 6.10: Rate of elastic neutron scattering in the LXeTPC as a function of detected energy.

6.4.3 Inelastic neutron scattering

A nucleus may be put into an excited state through an inelastic interaction with a fast neutron, and return to the ground state through γ emission $(n, n'\gamma)$. The critical energy E_c is related to the difference between the two nuclear levels ΔE as

$$E_c = \frac{m_n + M}{M} \Delta E \tag{6.3}$$

A calculation of the resulting γ emission would require a detailed knowledge of the cross sections and energy levels for the relevant Xe isotopes and the passive materials in proximity of the TPC, which is not readily available.

Xe is generally seen as a material with a good *radiation hardness*, even if few experimental works to study the inelastic neutron scattering on Xe are reported in the literature without providing a great deal of information (e.g. Ref. (58)). Of interest to us is the experimental attempt to determine the influence of an intense neutron flux on a high pressure (HP) Xe spectrometer, reported in Ref. (93); this work compares the behavior of HPXe and NaI(Tl) spectrometers under the same experimental conditions, bolstering the credibility of the measurement and allowing an easy comparison to NaI detectors operated at balloon altitude. The relative increase in count rate in the HPXe spectrometer is lower than the one in the NaI spectrometer at every time after irradiation, especially above 0.5 MeV. The two most prominent features detected in the HPXe spectrometer after irradiation were two γ-ray lines: 164 keV from ^{131m}Xe with an half life of 11.9 days and 236 keV ^{129m}Xe with an half life of 8.9 days. Due to their low energy and long half life, these two lines are not expected to produce a sizeable background fraction in LXeGRIT during a 27 hrs balloon flight and are neglected in the following.

6.4.4 Spallation

Differently from Ref. (37) and following Ref. (47) we consider protons and neutrons together as sources of spallation. In Sec. 6.4.1 the proton flux, integrated over proton energies larger than 100 MeV, was estimated to be 0.25 protons s^{-1} cm^{-2}. The neutron flux above 100 MeV should be comparable (see Sec. 6.4.2). At lower energy, the neutron flux can be calculated as a continuation of the flux at 100 MeV. From Refs. (47), (16) the neutron flux in the 1-100 MeV range can be described by two separate power laws, 0.26 E$^{-1.3}$ neutrons s^{-1} cm^{-2} MeV^{-1} in the 1-10 MeV and 0.06 E$^{-0.65}$ neutrons s^{-1} cm^{-2} MeV^{-1} in the 10-100 MeV. Integrated, they give 3.9 10^{-2} neutrons s^{-1} cm^{-2} in the 1-10 MeV and 5.8 10^{-2} neutrons s^{-1} cm^{-2} in the 10-100 MeV, which combined give $\sim$0.1 neutrons s^{-1} cm^{-2}. In the following we will consider a nucleon flux F_n of 0.6 nucleons s^{-1} cm^{-2}. In order to estimate the resulting γ-ray spectrum, we follow the approach described in Ref. (37); the spallation spectrum measured for CsI following irradiation at accelerator facilities is scaled with density and atomic mass of liquid xenon and passive materials. CsI was irradiated with 155 MeV protons; comparisons with similar measurements have shown that the energy of the incident protons appears to introduce only a second order effect. The extension of the approach described in Ref. (37) to energies below 100 MeV, while more uncertain, should have a minor impact due to energy spectrum of the input fluxes.

The spectrum due to spallation in CsI one hour after cessation of the irradiation is

$$g(E)_{CsI} = 8.79 \times 10^{-7} e^{-(E/0.620)} - 9.68 \times 10^{-7} e^{-(E/0.338)} \tag{6.4}$$

in units of counts $\mathrm{s}^{-1}\mathrm{MeV}^{-1}\mathrm{cm}^{-3}$ per nucleon. To convert $g(E)_{CsI}$ to that of liquid xenon one can use a simple formula where $g(E)_{LXe} = Kg(E)_{CsI}$, with

$$K_{Xe} = \frac{A_{CsI}}{A_{Xe}} \frac{\rho_{LXe}}{\rho_{CsI}} = \frac{132.9}{131.3} \frac{3.06}{4.53} = 0.69$$

We also consider the stainless steel used for the vacuum vessel, the cryostat and the spacers as a source of background from spallation; the conversion factor for stainless steel will be

$$K_{SS} = \frac{132.9}{55.4} \frac{7.8}{4.53} = 4.31$$

In the present situation, the background comes from bombardment due to a constant flux F_n of nucleons, apart for crossing the Pfotzer maximum during ascent. Under constant bombardment, the spallation background is supposed to build up until it reaches its asymptotic level, on a time scale $>10^5$ s ((37)), much longer than the duration of the balloon flight. On the other side, after passing through the Pfotzer maximum, part of the spallation spectrum is expected to die away. The rate *detected* in LXeGRIT is stable, and variations can be explained correcting for the known dependence on altitude of the atmospheric γ-ray flux. To follow the time behavior of the spallation background is basically impossible and rather useless for it does not appear in the detected rate. We therefore assume that we can apply Eq. 6.4 as if the spallation background had reached a steady state situation; in steady state conditions under constant bombardment we can use an asymptotic formula derived again in Ref. (37)

$$S(E, asymp) = 3.03 \times 10^4 \; F_n \; (K_{Xe} g(E)_{CsI} + K_{SS} g(E)_{CsI})$$

in units of counts cm^{-3} s^{-1} MeV^{-1}, where F_n is in cm^{-2} s^{-1}.
After having introduced the known flux F_n, it now needs to be integrated over the volume, i.e.

$$S_V(E, asymp) \; = 1.82 \times 10^4 \cdot g(E)_{CsI} \cdot (K_{Xe} \cdot V_{Xe} + K_{SS} \cdot V_{SS})$$

in units of counts s^{-1} MeV^{-1}. The active volume and the passive materials have to be considered separately, since the flux of γ-rays generated within the passive materials is reduced by solid angle and more passive materials between the interaction site and the detector. The active volume is 2,400 cm^3; passive Xe fills about 5,500 cm^3, and we estimate that about 1/3 of the γ-rays reaches the active volume; for the stainless steel, we have about 20,000 cm^3, and we estimate that less than 1/20, on average, of the γ-rays reaches the active volume. Therefore,

$$\begin{aligned} S_V(E, asymp) &= 1.82 \times 10^4 g(E)_{CsI}[0.69 \times (2400 + 1800) + 4.31 \times 10^3] \\ &= 1.3 \times 10^8 g(E)_{CsI} \;\; \text{counts s}^{-1} \text{ MeV}^{-1} \end{aligned}$$

and eventually

$$S_V(E, asymp) = 1.1 \times 10^2 e^{-(E/0.620)} - 1.3 \times 10^2 e^{-(E/0.338)} \;\; \text{counts s}^{-1} \text{ MeV}^{-1}$$

$S_V(E, asymp)$ is shown in Fig. 6.12-$left$. The integrated rate is ~23 counts s^{-1}, i.e. 5 times larger than the upper limit on the interaction rate due to elastic neutron scattering (Sec. 7.4.2).

A signature for an excess of localized β-decays, which account for a sizeable fraction of the spallation background (e.g. Ref. (47)), should be an excess in the 1-site event rate spectrum compared to the multi-site one. This is not the case in LXeGRIT, where the total rate and the rate in multi-site events (Fig. 6.5) is compatible with 100% γ-ray interactions and no β-decay, at least above 0.5 MeV; below that energy, too few multi-site events are expected to make this argument meaningful.

6.4.5 γ-ray lines

γ-ray lines in the in-flight energy spectrum are better looked for in the data sample taken with a lower PMT threshold, for the efficiency below ~1 MeV would be much larger. Above ~ 0.6 MeV the detection efficiency is further enhanced by selecting multi-site events; this effect is even more pronounced due to selections at the second level trigger (see Sec. 6.6). Lines are usually detected as by-products of hadronic interactions both in the active and passive materials. The energy spectrum is shown in Fig. 6.11. Apart for the 0.511 MeV positron annihilation line, which is visible in Fig. 6.5, two more lines are clearly detected: the ^{40}K line at 1.46 MeV clearly detected in laboratory experiments and fully accounted for in Sec. 6.2, and a second line at ~0.84 MeV. We interpret the line as due to γ-rays from ^{56}Mn, which emits at 0.847 MeV with an half-life of 2.5 hrs. ^{56}Mn comes from ^{56}Fe through the reaction

$$^{56}\mathrm{Fe} + \mathrm{n} \rightarrow ^{56}\mathrm{Mn} + \mathrm{p}$$

^{56}Fe is abundant (70%) in the stainless steel which surrounds the LXeTPC; especially the stainless steel spacers inside the vacuum vessel are likely sources of this line because of their proximity to the active volume. Even a rough estimate of the expected rate is problematic, because the period we are considering comes less than 2 hrs after passing through the Pfotzer maximum and the rate is not expected to be stable. We can venture an order of magnitude estimate: the cross section is ∼0.1 barns [8] and we assume a flux of 1 neutrons cm^{-2} s^{-1}, which should be an average between the flux at stable altitude and the one during ascent. The production rate for ^{56}Mn would therefore be ∼8 10^{-3} Hz per cm^3 of ^{56}Fe. Assuming now that the relevant ^{56}Fe is distributed in a layer 1.8 cm [9] thick surrounding the LXeTPC, we would have 1.8×1600 cm^3 of ^{56}Fe. Given a 10^4 s irradiation, we would have 2.3 10^5 ^{56}Mn nuclei; we also assume that 50% of them will decay over the ∼6 10^3 s of our measurement, which would give ∼18 Hz. The number of γ-rays eventually hitting the fiducial volume would be lower by at least a factor of 2, because they need to be emitted toward the fiducial volume; our order of magnitude estimate is therefore ∼10 Hz, which is an intensity ∼25% of the ^{40}K line. In Sec. 6.2.1 we estimated the rate of ^{40}K γ-rays in the active LXe to be ∼70 Hz, which implies the ^{56}Mn line rate to be ∼20 Hz. This rate is too high compared to our previous estimate, but within reason.

The clear detection of this line helps setting an upper limit to the lines lost in the continuum. Depending on the line energy, a reasonable upper limit on undetected lines is ∼10 Hz, before including any detection inefficiency. Given a geometrical area of ∼400 cm^2, a γ-ray line from a celestial object would give a similar rate for a flux of 0.025 cm^{-2} s^{-1}; excluding the 0.511 MeV line, the strongest nuclear line of interest is 1.809 MeV form ^{26}Al, which gives a flux of few 10^{-4} photons cm^{-2} s^{-1}, i.e. ∼1% of our upper limit on background lines. The signal-to-noise ratio can be greatly [10] enhanced exploiting the Compton imaging capability of LXeGRIT rather than using it as a mere spectrometer. For sake of comparison, typical event rates in COMPTEL from individual

---

[8] http://www.nndc.bnl.gov/

[9] 1.8 cm is approximately the radiation length in ^{56}Fe.

[10] For example, the procedure of software collimation applied to the ^{88}Y 1.8 MeV line, as shown in Fig. 4.16, improves the signal-to-noise ratio by a factor of ∼5.

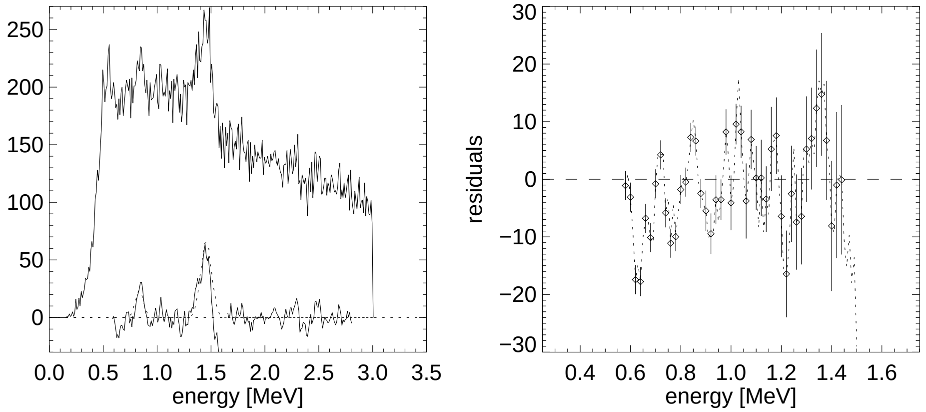

Figure 6.11: Energy spectrum (0-3 MeV) for multi-site events in the time period 22:30 - 24:15 UTC, with a lower energy threshold for the PMT trigger. *Left:* The energy spectrum and its residuals after subtraction of the continuum in the 0.55-2.8 MeV energy range. Two lines are clearly identified: the ^{40}K line at 1.46 MeV (see Sec. 6.2), and a second line at ∼0.84 MeV, interpreted as due to γ-rays from ^{56}Mn. *Right:* residuals in the 0.55-1.5 MeV energy range, after subtraction of the continuum and of the two lines.

background isotopes are ∼0.1 Hz *after* standard imaging selections, with a signal-to-noise ratio of ∼1% for astrophysical γ-ray lines (see Ref. (96)).

Table 6.1 summarizes the cross section for capture of thermal neutrons on the nine stable isotopes in natural Xe. Only two isotopes (^{129}Xe, ^{131}Xe) have significant cross sections for neutron capture. The non detection of a 0.668 MeV from capture of thermal neutrons on ^{131}Xe provides a limit on the flux of thermal neutrons in the LXeTPC. Assuming again that detectability for a line requires 50% of the counts under the ^{56}Mn peak, an upper limit of 10 Hz of 0.668 MeV photons in LXe can be set. Therefore we can set an upper limit on the flux of thermal neutrons $F_{th.n}$

$$\frac{10\ \text{Hz}}{2400\ \text{cm}^3} \ = \ \frac{\rho N_A}{A_{Xe}}\, \sigma_{capture}\, F_{th.n}\ 0.21232 \ = \ 0.357\ F_{th.n}$$

and $F_{th.n} \ < \ 0.01$ neutrons cm^{-2} s^{-1}.

isotope	atomic mass	% nat. abundance	n capture σ [barns]	γ-ray energy [MeV]
^{124}Xe	123.9061	0.095	–	–
^{126}Xe	125.9042	0.089	–	–
^{128}Xe	127.9035	1.910	–	–
^{129}Xe	128.9048	26.40	20	0.536
^{130}Xe	129.9035	4.071	–	–
^{131}Xe	130.9051	21.232	120	0.668
^{132}Xe	131.9042	26.909	–	–
^{134}Xe	133.9054	10.436	–	–
^{136}Xe	135.9072	8.857	–	–

Table 6.1: Stable isotopes in natural Xe (adapted from http://www.nndc.bnl.gov/).

6.5 Discussion

Fig. 6.12 graphically summarizes the outcome of this work: the measured in-flight background is well explained combining *i.* the atmospheric γ-ray flux which is by far the most important component, *ii.* the spallation background discussed in Sec. 6.4.4 and *iii.* the internal background independently measured in the laboratory. Fig. 6.12-*right* shows a discrepancy always within a factor of two in the 0.4-8 MeV band, i.e. within the estimated uncertainty on the model which is essentially reflecting the uncertainty on the input fluxes [11]. It has been proved that a LXe detector at balloon altitude does not suffer any major problem due to activation. The γ-ray lines detected in the energy spectrum (^{40}K and ^{56}Mn) should be removed through a careful choice of the construction materials. We were able to set an upper limit on the undetected lines, which shows a favorable signal-to-noise ratio compared to the COMPTEL satellite mission. The low level of background coming from passive materials surrounding the LXeTPC is most likely due to the compact structure of the detector. Given a detector the size of LXeGRIT with an energy threshold as low as 150 keV and no external shielding, the γ-ray rate at balloon altitude is as high as few kHz. Such a high rate imposes strict requirements on the detector design. In its present configuration, the

---

[11] The intrinsic background, where no external input flux is needed, is accurate to about 10%.

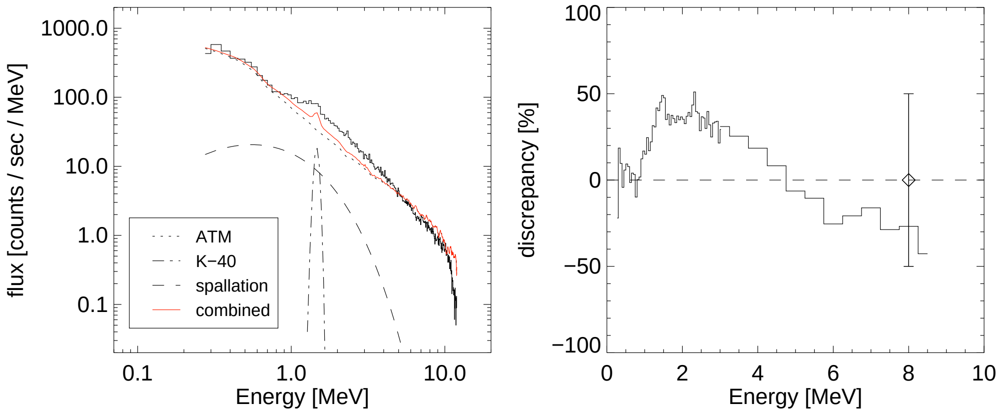

Figure 6.12: *Left:* The measured in-flight energy spectrum after unfolding the detector response function. It is compared to our expectation which includes *i*. the atmospheric γ-ray flux, *ii*. the spallation background (Sec. 6.4.4) and *iii*. a ^{40}K line (Sec. 6.2.1). *Right:* Fractional discrepancy between our expectation, excluding the ^{40}K line, and the measured in-flight energy spectrum. The error bar shows the estimated uncertainty on the model, 50%.

in-flight performance of LXeGRIT is mainly limited by the modest speed of the DAQ system, which in turn imposes a low detection efficiency. The atmospheric γ-ray flux is, in principle, easily shielded. It is anyway a well known problem with external shields that the shields themselves become sources of background when irradiated. For future developments, it looks preferable to keep the LXeTPC "naked" with a largely improved DAQ performance and selectivity at the trigger level.

6.6 Appendix 1: In-flight response function

The "response function" and how it is derived is described in Ch. 3. In the following I discuss the impact of the first level trigger (FLT) and second level trigger (SLT) in the specific flight conditions (year 2000).

FLT

The response function in flight configuration has been assessed through several laboratory measurements, according to the procedure described in Ref. (35) and Ch. 3. It is anyway possible, and advisable, to derive the response function from the flight data themselves. In fact, the impact of the FLT can be studied selecting a tiny sample of events with a *false trigger*. The z distribution of 1-site events is shown in Fig. 6.13-$left$; for each event, the z position is measured as the time elapsed between the fast PMT signal and the detection of the drifting charge on the wires. The physical volume of the LXeTPC is between 0 and 7 cm; events with z >7 cm, which is unphysical, are due to a false trigger which compromises the correct determination of the z position. From the point of view of the light trigger, such events require:

1. a false trigger;
2. the event itself must not cause a trigger, otherwise the event would have been rejected as pile-up.

Since 1-site events have been selected, their definition is complete. Obviously all the events with z >7 cm are due to a false trigger, but a certain fraction of such events will also have z <7 cm, because z is essentially a random number. The energy spectra for events with z >7 cm and z <7 cm are shown in Fig. 6.13-*right*; events due to a false trigger show a softer energy spectrum, as expected. We now define $g(E)$ as the ratio of events with z between 0 and 6.24 cm over events with z between 7 and 7.8 cm, vs. energy. In terms of fraction of false triggers (α_{false}) and efficiency of the FLT (ϵ), it is written as

$$g(E) = N\frac{\epsilon + \alpha_{false} - 2\epsilon\alpha_{false}}{\alpha_{false} \cdot (1 - \epsilon)} \tag{6.5}$$

where N is a normalization factor. The result is shown in Fig. 6.14: on the left, the efficiency as measured in the laboratory (see Ch. 3 for a description of the procedure) up to 2 MeV and extrapolated to 10 MeV; on the right, a comparison between the expected $g(E)$ for such an efficiency and for α_{false} = 1%, and the experimental result. The agreement is fairly good and nicely confirms the laboratory measurement, even if above 3 MeV the significance of the comparison is hampered by the low statistics.

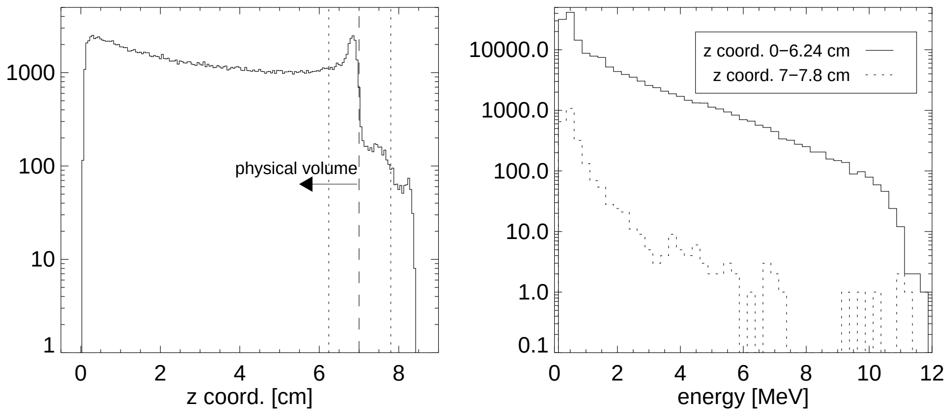

Figure 6.13: *Left:* z distribution for 1-site events. *Right:* energy spectra for events with z <6.24 cm (*continuous line*) and events with z between 7 and 7.8 cm (*dotted line*).

SLT

Here we apply the same procedure as in Ch. 3, i.e., given a sample of events where no *SLT* selections have been applied on-line, the same selections are applied off-line so that their efficiency is immediately known. The final results are shown in Figs. 6.15 and 6.16.

In Fig. 6.2, the rejection rates for both γ and non-γ events are shown, while Figs. 6.15, 6.16 describe the efficiency for γ events, i.e. mainly the requirement of a minimum number of wire hits, while the selections on a maximum number of wire hits and anode saturation essentially reject charged particle events.

6.7 Appendix 2: Angular dependence of the atmospheric γ-ray flux

Only few measurements of the angular distribution of atmospheric γ-rays exist (cfr. Ref. (31) and references therein); within the conceivable experimental accuracy, the flux depends only on the zenith angle and possesses azimuthal symmetry. A new measurement has been obtained using the LXeGRIT 2000

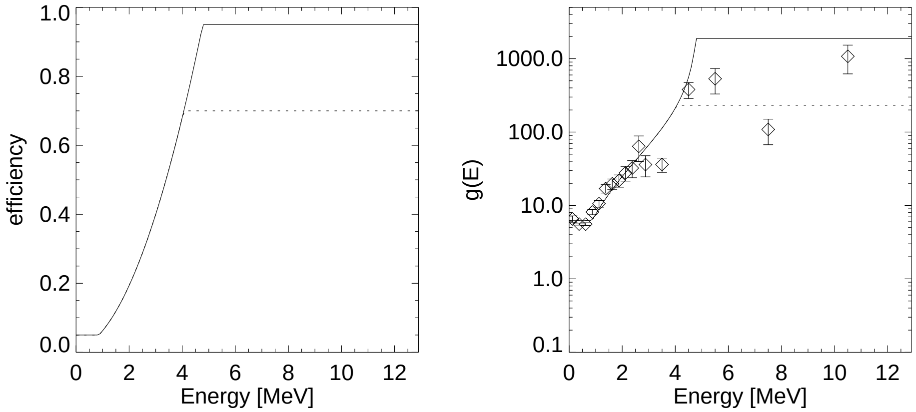

Figure 6.14: *Left:* The FLT efficiency, as derived from laboratory measurements in the 0-2 MeV energy band and extrapolated up to 10 MeV. *Right:* The experimental points are just the ratio of events in the physical volume over events apparently outside the physical volume, within the same energy bin. $g(E)$ (Eq. 6.5) uses the efficiency ϵ as shown on the left; α_{false}, the fraction of false triggers at the FLT, is assumed to be 1%.

data; as it has been shown, most of the detected γ-ray background is explained in terms of atmospheric γ-rays. Therefore, the measurement of the angular distribution of the detected background translates into a measurement of the angular distribution of atmospheric γ-rays.

A sample of 3-site events was selected, applying the following further requirements:

1. forward scattered (less than 30°) γ-rays, as derived from the Compton formula;
2. a 3D separation between the second and third interaction of less than 1 cm;
3. a minimum separation between the first and the second interaction of 1 cm.

A schematic of the measurement is shown in Fig. 6.17-$left$; χ, the angle from the vertical (the z-axis in the LXeTPC), is our estimate of the zenith angle for each γ-ray. Forward scattered γ-rays are needed because the scatter

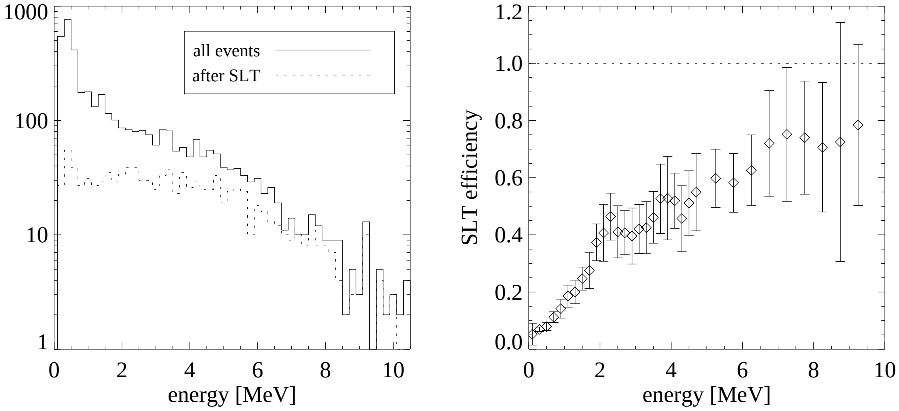

Figure 6.15: Efficiency of the second level trigger (SLT). *Left:* energy spectra combining all multiplicities, before (all events, *solid line*) and after SLT (*dashed line*). *Right:* ratio of the two energy spectra, which gives the SLT efficiency vs. energy.

angle essentially gives the uncertainty on the measured zenith angle. The specific value of 30°was chosen as a good compromise between accuracy and statistics. The distributions of the scatter angle φ for the selected events, and of the uncertainty on the measured zenith angle (its standard deviation for each event, i.e. $2\varphi/\sqrt{12}$) after selecting φ <30°, is shown in Fig. 6.17-*right*. The interactions were sequenced as explained in Sec. 4.2; selection 2 is powerful in obtaining a clean sample of correctly sequenced Compton events. The requirement of a minimum separation was imposed mainly to improve the angular accuracy.

The measured angular distribution is shown in Fig. 6.18, compared to the result in Ref. (80) and the model in Ref. (31); events in the energy band 1.5-10 MeV have been selected. To obtain the angular distribution as in Fig. 6.18, an overall normalization has been applied, so that the flux integrated over zenith angle would give back the flux measured in Sec. 6.5. The main uncertainty comes from the passive materials, since their distribution varies with the zenith angle. The correction to the measured angular distribution has been calculated using the LXeGRIT MC simulation; the uncertainty so introduced is small for χ between 0°and 100°, but becomes the dominant uncertainty for χ >100°, where the gondola itself is in the field of view.

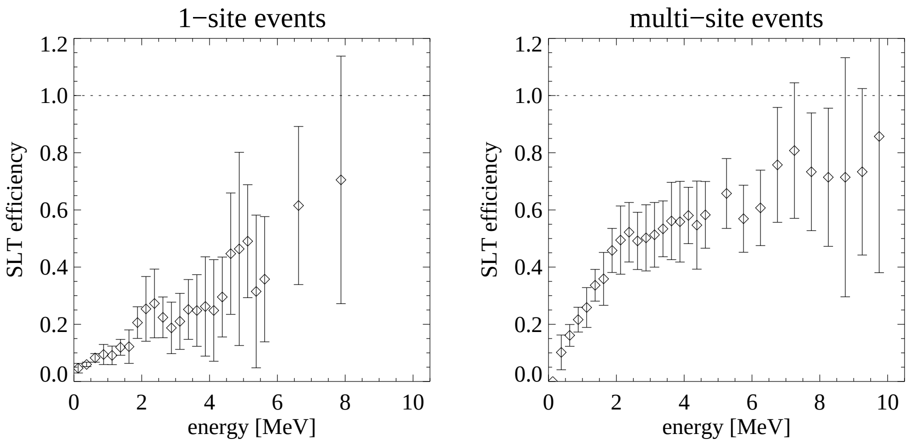

Figure 6.16: Efficiency of the second level trigger for different multiplicities. *Left:* 1-site events; *right:* multi-site events.

The energy spectrum for the selected events is shown in Fig. 6.19, compared to the overall energy spectrum; less than 5% of the total events are eventually selected for this measurement. It is clear that the various selections introduce a significant distortion in the energy distribution; in the 1-10 MeV energy band, energy and zenith angle are expected to be only loosely correlated. The collected statistics is unfortunately too poor to obtain a measurement resolved simultaneously in energy and zenith angle.

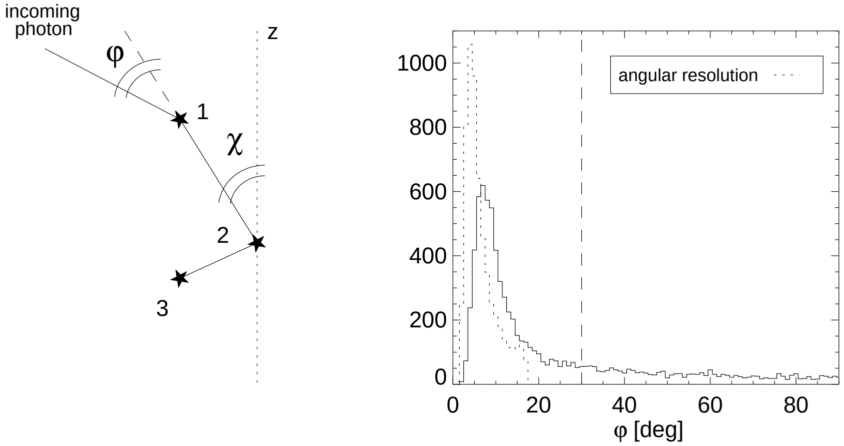

Figure 6.17: *Left:* schematic of the measurement of the zenith angle χ. The scatter angle φ essentially gives the uncertainty on the measured zenith angle. *Right:* histogram of the scatter angle φ for the selected events. The histogram of the uncertainty on the measured zenith angle (its standard deviation for each event, i.e. $2\varphi/\sqrt{12}$) after selecting φ <30°, is also shown (*dotted line*).

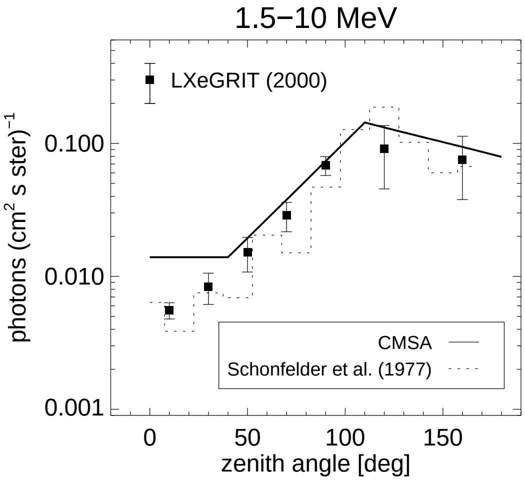

Figure 6.18: Measured angular distribution of the atmospheric γ-ray flux; it is compared the result in Ref. (80) and the model in Ref. (31) events in the energy band 1.5-10 MeV have been selected.

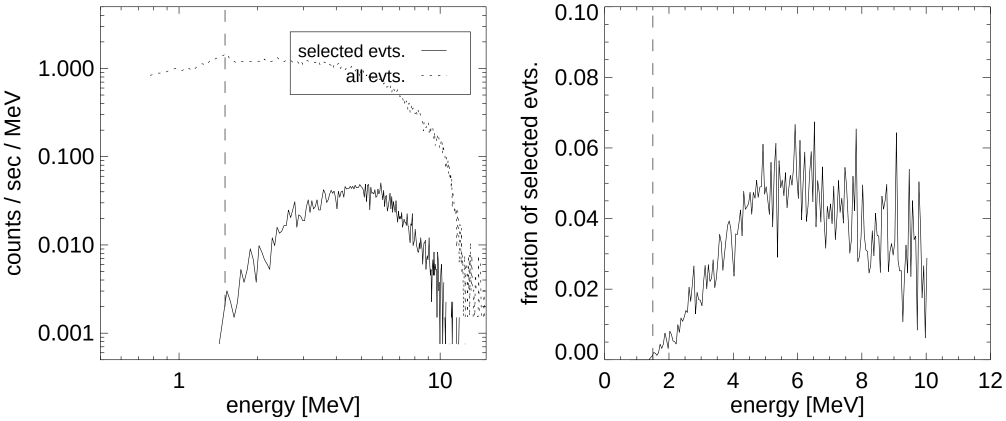

Figure 6.19: Energy spectrum for the selected events, compared to the overall energy spectrum (*left*); less than 5% of the total events are eventually selected for this measurement (*right*).

Chapter 7

Sensitivity to astronomical γ-ray sources

7.1 Sensitivity

The minimum sensitivity, f_n, of an instrument is expressed as the minimum flux which can be detected, and is based on the statistical variation, or number of standard deviations n, of the measured counts, i.e. the combination of signal (S) and background (B) counts. Assuming S and B to obey Poisson statistics, the minimum detectable flux - which may depend on energy (E) and direction (θ, ϕ) - will be

$$f_n(E, \theta, \phi) = \frac{n\ \sqrt{S + B}}{A_{\text{eff}}\ t_{\text{obs}}} \tag{7.1}$$

where A_{eff} is the effective area, which depends E and (θ, ϕ), and t_{obs} is the effective observation time. For a source detected with a significance of n standard deviations, $S = f_n\ A_{\text{eff}}\ t_{\text{obs}}$, which gives

$$f_n = \frac{n^2}{2X}\ \left[1 + \sqrt{1 + \frac{4 f_b X}{n^2}}\right] \tag{7.2}$$

where $X = A_{\text{eff}}\ t_{\text{obs}}$ is the effective exposure and $f_b = B/X$ defines an "equivalent background flux". In the usual case [1] of dominating background, Eq. 7.2 reduces to

$$f_n \approx n\sqrt{\frac{f_b}{X}} \tag{7.4}$$

If the signal is searched for in a given energy window ΔE and angular resolution element $\Delta\Omega$

$$B = t_{\text{obs}} \int_{\Delta E} dE \int_{\Delta\Omega} d\Omega \frac{df_b(E,\theta,\phi)}{dEd\theta d\phi} A_{\text{eff}}(E,\theta,\phi) \tag{7.5}$$

Assuming a smooth variation of $df_b(E,\theta,\phi)/dEd\theta d\phi$ and $A_{\text{eff}}(E,\theta,\phi)$ in the intervals ΔE, $\Delta\Omega$

$$f_n = n\sqrt{\Delta E\ \Delta\Omega\ \frac{df_b(\bar{E},\bar{\theta},\bar{\phi})}{dEd\theta d\phi}\frac{1}{X(\bar{E},\bar{\theta},\bar{\phi})}} \tag{7.6}$$

where $\bar{E}, \bar{\theta}$ and $\bar{\phi}$ are the central values of the intervals ΔE, $\Delta\theta$ and $\Delta\phi$. Energy and angular resolution can reduce ΔE and $\Delta\Omega$ to narrow windows around the signal region, thus improving the instrument sensitivity; a fundamental limit is anyway posed by the intrinsic source properties, i.e. narrow or broad energy lines, or even a continuous energy spectrum, and point sources vs. extended emission. For example, no useful "narrow window" ΔE can be defined for a continuous energy spectrum. Discrete energy lines generated by the instrumental background quite often mask genuine source lines, greatly weakening the effectiveness of background reduction techniques based on high energy resolution alone [2]. For this reason, it is important to minimize the internal background (both lines and continuum) with a careful design of the

---

[1] In the ideal case of negligible background which can be realized only with strong γ-sources in the laboratory, Eq. 7.2 would simply reduce to

$$f_n = \frac{n^2}{X} \tag{7.3}$$

[2] This is not intended to diminish the key role of energy resolution in γ-ray astrophysics; important properties such as line profile can be studied only with a high energy resolution instrument, and energy resolution directly affects angular resolution as discussed in Ch. 4.

instrument and choice of the materials, before relying on other background reduction techniques.

Fig. 7.1 illustrates the dependence of sensitivity on effective exposure X (top panel) for an instrument with an equivalent background flux of 10^{-6} ph cm^{-2} s^{-1}, and equivalent background flux f_b (bottom panel) for an instrument with an effective exposure of 2×10^9 cm^2 s (e.g., 10^6 s observing time with $\sim$ 2000 cm^2 effective area) and indicates the level which have been explored by current instruments. The figure does not include the cosmic diffuse γ-ray background, which contributes at a level of $(5 \times 10^{-3}\,\mathrm{cm}^{-2}\,\mathrm{s}^{-1}\,\mathrm{sr}^{-1}\,\mathrm{MeV}^{-1}) \times \Delta\Omega \times \Delta E$ (at 1 MeV). This is negligible for narrow-line and point sources, but not for diffuse broad-line and continuum emission at energies below 0.5 MeV.

COMPTEL, which is the most sensitive CT to date, achieved a maximum effective exposure of $\sim 7 \times 10^7$ cm^2 s at 1.8 MeV toward the Galactic Center, with an effective observing time of 0.5 yr (out of 5 yr of operation). The corresponding 3σ line sensitivity was $\sim$1.5 10^{-5} γ cm^{-2} s. Using Eq. 7.4, this can be easily translated into an equivalent background flux f_b

$$f_b = X \left(\frac{f_3}{3}\right)^2 = 1.75 \times 10^{-3}\ \mathrm{ph\ cm^{-2}\ s^{-1}}$$

COMPTEL suffered from two main shortcomings: a tiny effective area ($\sim$5 cm^2 after data cuts) and a large internal background. It is therefore clear that the two critical parameters to improve a CT's sensitivity well beyond COMPTEL's achievement will be: *i.* a large *effective area* and *ii.* a low *background level.*

7.2 In-flight performance

7.2.1 Effective area

It has been shown in Ch. 3 and Ch. 4 that the LXeGRIT effective area can be calculated with good precision; in general, a full-fledged MC simulation is needed and MC generated data should be used up to the point of producing source images, i.e. the end point of the data analysis. The effective area for imaging events, as measured in the laboratory (cfr. Table 3.1 and efficiency for the sequencing and imaging process in Ch. 4), is $\sim$1 cm^2 at 1 MeV and $\sim$3 cm^2 at 2 MeV, *including all the actual inefficiencies.* It is not a "hard

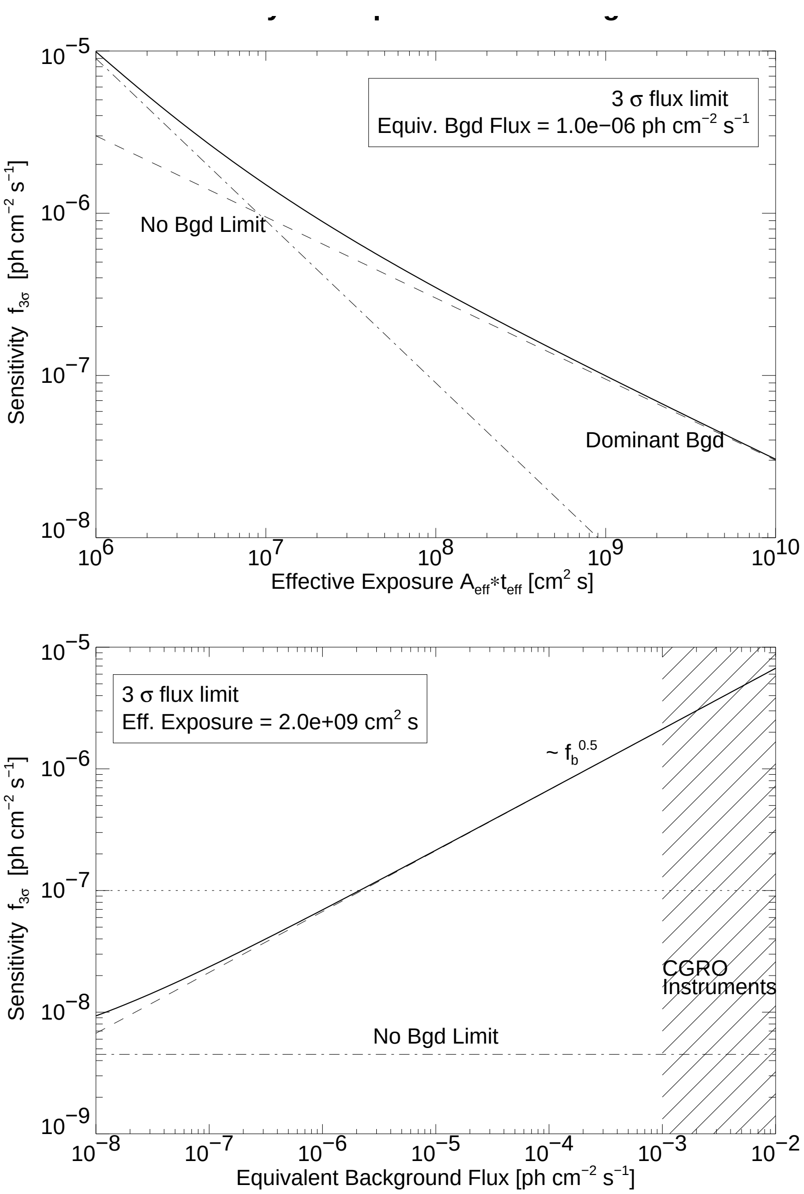

Figure 7.1: Sensitivity as a function of effective exposure (*top*) and background flux (*bottom*). From Ref. (8).

number", for it heavily depends on the source rate which eventually dictates the efficiency at the trigger level [3]. Under flight conditions the detection efficiency was further reduced (Ch. 6 - Appendix 1); given a Crab-like source (see next) the integrated effective area in the 0.5-10 MeV was ∼2 cm^2, with an uncertainty of about 30%. □

7.2.2 Background

The background at balloon altitude in LXeGRIT as an omnidirectional detector has been discussed in great detail in Ch. 6; it is *not* the relevant background for LXeGRIT in CT mode. The background for Compton imaging is derived using the standard COMPTEL Processing and Analysis Software System (COMPASS), where the background is derived from the observational data themselves (Ref. (22)). Assuming an empty field (a fairly good assumption, see next) the fluctuations in the maximum likelihood map give the background level, i.e. $\sqrt{background} = \sigma_{ml}$. Experimentally, $\sigma_{ml} \sim 25$, for an effective area of ∼2 cm^2 and $t_{\mathrm{obs}} \sim 2 \times 10^4$ s, i.e. an exposure $X = A_{\mathrm{eff}}\ t_{\mathrm{obs}} \sim 4 \times 10^4\ \mathrm{cm}^2$ s. Thus,

$$f_b = \frac{B}{X} = \frac{625}{4 \times 10^4\ \mathrm{cm}^2\ \mathrm{s}} = 1.6 \times 10^{-2}\ \mathrm{ph\ cm}^{-2}\ \mathrm{s}^{-1}$$

integrated over energy up to 10 MeV[4]. □

The zenith distance of known celestial γ-ray sources during flight is shown in Fig. 7.2. The brightest persistent source in the MeV sky is the Crab Nebula/Pulsar; during the balloon flight in year 2000, it was in the LXeGRIT field of view - defined within an angular distance of 45° - for about 6 hours, from 7:00 to 15:30 GMT. The Crab flux in the 1-10 MeV energy band is $\sim 1.7 \times 10^{-3}\ \gamma\,\mathrm{cm}^{-2}\,\mathrm{s}^{-1}$ (94). Given an effective exposure $X = 4 \times 10^4\ \mathrm{cm}^2$ s, ∼50 events in our data would be useful for imaging the Crab, which would correspond to a 2σ detection.

Multi-site events recorded during this exposure have been reconstructed and sequenced with the same algorithm tested on calibration data. Preliminary studies based on the COMPASS software package show that a $\sim 2\sigma$

---

[3] Provided a DAQ not deadtime limited at several hundred Hz, the effective area could be as high as ∼15 cm^2 at 1 MeV and ∼20 cm^2 at 2 MeV.

[4] For sake of comparison, COMPTEL's $f_b = 1.75 \times 10^{-3}\ \mathrm{ph\ cm}^{-2}\ \mathrm{s}^{-1}$ is restricted to a 200 keV energy window around 1.8 MeV.

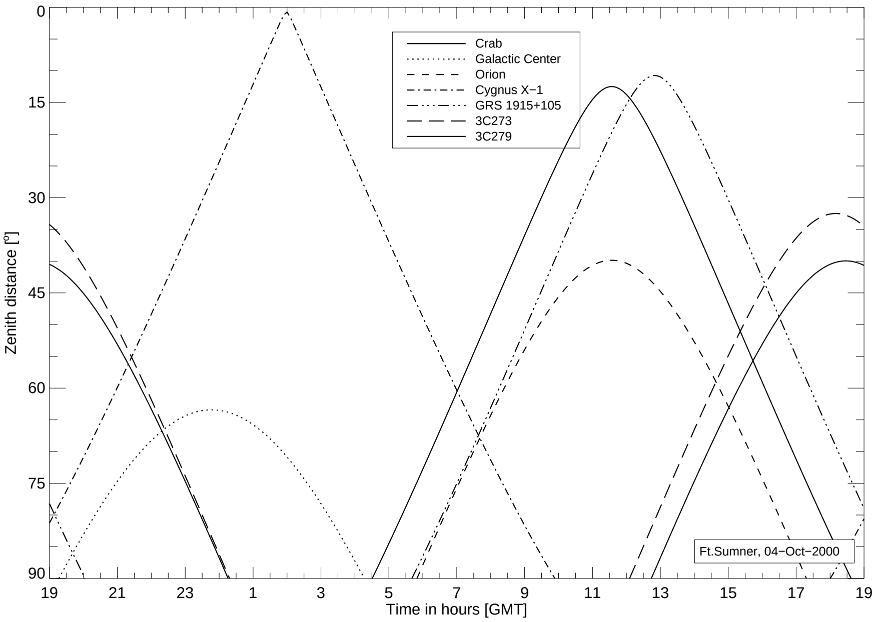

Figure 7.2: Known celestial γ-ray sources in the LXeGRIT field of view during the 2000 flight.

detection is at reach, as shown in the maximum likelihood maps of the Crab region in Fig. 7.3. The visible excess clearly shows an offset of 6°-10°with respect to the nominal Crab position. This offset can be explained with a systematic error in the orientation of the instrument, e.g. in the magnetometer calibration or in its orientation with respect to the gondola. It is unfortunately very difficult to independently test this explanation. For such a low significance detection, the uncertainty on the source localization is also at the level of a few degrees.

A 2σ detection of the Crab translates into a 3 σ sensitivity for a minimum flux of 2.4×10^{-3} $\gamma\,\mathrm{cm}^{-2}\,\mathrm{s}^{-1}$, given an exposure of 2×10^{4} s and an effective area of $\sim$2 cm^2. Such a sensitivity falls well above the sensitivity originally expected for the LXeGRIT prototype and - as explained in Ch. 3 - is decisively limited by the shortcomings of the DAQ system.

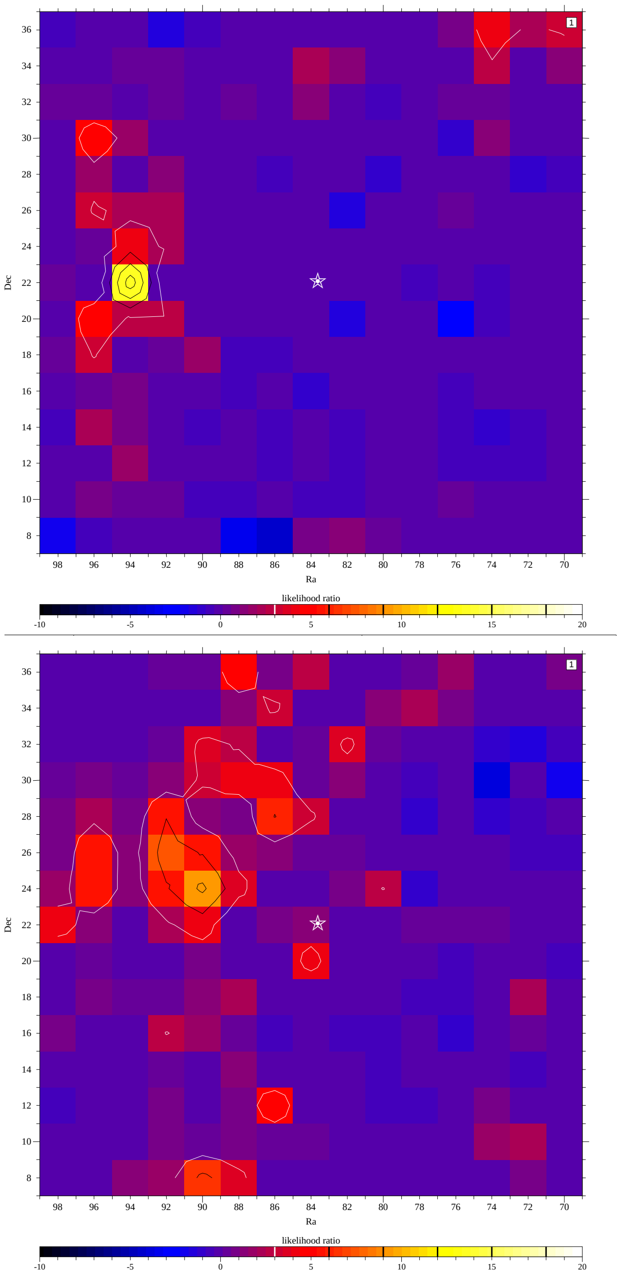

Figure 7.3: Images of the Crab region (LXeGRIT 2000); the nominal Crab position is marked with a star. *Top:* 2-site events. *Bottom:* 3-site events. These images have been obtained in collaboration with S. Zhang, High Energy Astrophysics Lab, Institute of High Energy Physics, Beijing, China.

Chapter 8

Future developments: Compton scattered considerations

Introduction

The Gamma Ray Astronomy Working Group (49) “recommended” a sensitivity of $\sim 10^{-7}$ γ cm^{-2} s to narrow lines and $\sim 10^{-6}$ γ cm^{-2} to broad lines for the next Compton telescope, or Advanced Compton Telescope (ACT). The multi-year sensitivity of COMPTEL is worse by 2-3 orders of magnitude, and COMPTEL is the most sensitive Compton telescope to date. COMPTEL achieved a maximum effective exposure of $\sim 7\times10^{7}$ cm^2 s at 1.8 MeV toward the Galactic Center, with an effective observing time of 0.5 yr (out of 5 yr of operation). The corresponding 3σ line sensitivity was $\sim 1.5\times10^{-5}$ γ cm^{-2} s. Given the two simple definitions

$$\text{sensitivity} \propto \sqrt{\frac{\text{background}}{\text{exposure}}}$$

$$\text{exposure} = t_{obs} \times (\text{geometrical area}) \times (\text{efficiency})$$

together with the large $t_{obs} = 0.5$ yr and the already large geometrical area of COMPTEL ($\sim 4\times10^{3}$ cm^2), it is clear that a future Compton telescope will have to *a*) greatly reduce the background level and *b*) increase the efficiency above the few 10^{-4} of COMPTEL (see Ref. (96) and Sec. 7.1).

In the present chapter I will present some possible steps toward an ACT in the tradition of the LXeGRIT-Columbia: a breakthrough in exploiting the copious scintillation light from liquid xenon, including time-of-flight (ToF) capability, and the renewed proposal of an EXPLORER class mission, with a long duration balloon (LDB) as launch vehicle.

8.1 Scientific objectives for an Advanced Compton Telescope

The scientific objectives of an ACT and the related instrument requirements have been the focus of a recent proposal (25), and are here summarized in Fig. 8.1 and Table 8.1. The three main science topics are: γ-ray line emission from supernovae, γ-ray line emission from galactic and Local Group supernova remnants (from long-lived radionuclides as ^{44}Ti, ^{26}Al and ^{60}Fe), and diffuse line emission from interstellar radionuclides in the Galaxy. Additional objectives include classical novae, black holes and AGN, pulsars, neutron stars, and the extra-galactic diffuse γ-ray background. The study of γ-ray line emission from supernovae - in particular - is expected to lead to breakthroughs in the understanding of the explosion mechanisms and expansion dynamics of supernovae. The goal of detecting 5 Type Ia supernovae per year with a significance of $\sim 15\sigma$ [1] has been set for the proposed ACT. Such a high significance should allow to clearly distinguish among different models. About 50 Type Ia supernovae per year will be detected with less significance. Since γ-ray lines from Type Ia supernovae (^{56}Ni and ^{56}Co) are expected to be Doppler broadened, with typical widths of 3-4%, an excellent sensitivity to broad lines will be needed, as indicated in Table 8.1. A large field-of-view is also needed, in order to be able to observe most of the sky often, and therefore to measure each supernova many times and many supernovae simultaneously.

8.2 The LXeGRIT heritage

Despite relying on a somewhat exotic technology, LXeGRIT has advanced to the point of being the ripest among several detector concepts in the post-COMPTEL era. The LXeGRIT prototype has given definite proof that a monolithic, fine grained detector can be made to work as a Compton telescope. Its energy resolution, spatial resolution, efficiency, time stability and

---

[1] For the 0.847 MeV ^{56}Co line.

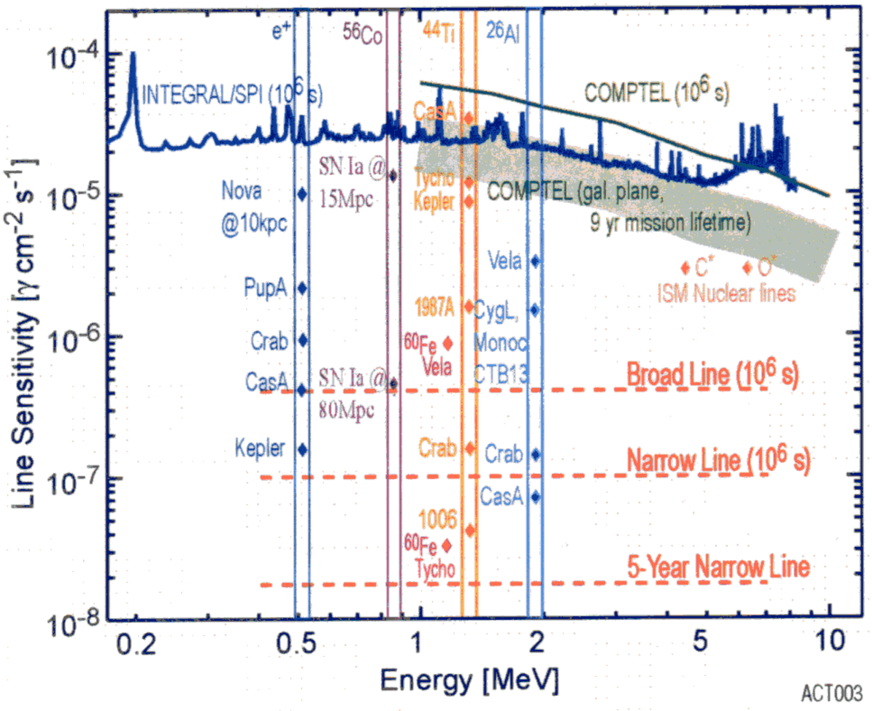

Figure 8.1: ACT science requirements (red lines), from Ref. (25). The ACT is expected to achieve an improvement in γ-ray line sensitivity of two orders of magnitude over COMPTEL and INTEGRAL.

imaging performance have been fully calibrated in the laboratory.
LXeGRIT has been tested at balloon altitude, most recently in Oct. 2000. Important milestones have been reached: measurement of the background at balloon altitude, which turns out to be well described by the atmospheric γ-ray flux, and its zenith dependence; detection, albeit weak, of the Crab in the 1-10 MeV energy band, the first since COMPTEL results (94). The development of the LXeGRIT instrument is now at the same performance level as pre-COMPTEL balloon instruments when they were considered ready to be turned into a major satellite mission (82).

The main limitation, intrinsic to LXe as a detection medium, is the energy resolution which is not going to be better than 5% FWHM at 1 MeV and

Table 8.1: ACT science and instrument requirements. Adapted from Ref. (25).

1. ACT Science Requirements:	
Energy range	0.2 - 30 MeV
Energy resolution	10 keV (FWHM) at 1 MeV
Angular resolution	1°
Field-of-view	4 sr
Source localization	5' bright sources
Line sensitivity	$1\times10^{-7}\ \gamma\,\mathrm{cm}^{-2}\,\mathrm{s}^{-1}$ in 10^6 s (narrow) $5\times10^{-7}\ \gamma\,\mathrm{cm}^{-2}\,\mathrm{s}^{-1}$ (broad)
Continuum sensitivity	$1\times10^{-5}\ \gamma\,\mathrm{cm}^{-2}\,\mathrm{s}^{-1}\mathrm{MeV}^{-1}$ at 0.5 MeV
2. ACT Instrument Requirements:	
Effective area	1000 - 3000 cm^2
Position resolution	1 mm (3D)
Energy Resolution	1% (0.5 - 20 MeV)

cannot compete with a Ge spectrometer [2]. A second limitation, severe for the LXeGRIT prototype but to be overcome in a future development, came from the limited speed of the data acquisition and the trigger system. It reduced the in-flight detection efficiency by about a factor of ten. Efforts to improve the performance of the light trigger system are described in the following. The specifications of the LXeGRIT instrument are gathered in Table 8.2, which should be compared to Table 1.3. Reducing the amount of passive materials in front of the LXeTPC, an effective area as big as ~10% of the geometrical area would be obtainable, and therefore a large area LXeTPC (1×1 m^2, i.e. ~25 modules of the size of the LXeGRIT TPC) could achieve the effective area required for the ACT concept.

---

[2] Very recent developments have shown that the energy resolution in LXe improves significantly combining the charge and light signals. An energy resolution better than 3% FWHM at 1 MeV has been measured and further improvements are still possible (E. Aprile, private communication).

Table 8.2: Specifications of the LXeGRIT instrument. ^{a} assuming the measured background at balloon altitude and the instrument not deadtime limited.

1. Detector:	
a. Detector type:	LXeTPC
b. Geometric arrangement	1 detector module: 7 cm deep total geometric area 350 cm^2
c. Effective area for γ-rays:	10 - 20 cm^2 (if not deadtime limited)
d. Energy range	0.5 - 10 MeV
e. Energy resolution	10% (FWHM) at 1 MeV
f. Angular resolution	3°- 5°(FWHM)
g. Field-of-view	π sr
h. Accuracy on Source Position	better than 1°
2. Experimental Sensitivity^a:	
Telescope Observations of a Point Source	
1) Minimum source detectability (3 σ) Crab-like source 1-10 MeV and 2-week observation	$2\times10^{-4}\ \gamma\,\mathrm{cm}^{-2}\,\mathrm{s}^{-1}$
2) Line sensitivity (3 σ) - 2-week observation	$6\times10^{-5}\ \gamma\,\mathrm{cm}^{-2}\,\mathrm{s}^{-1}$ at 1 MeV
3. Miscellaneous Instrument Specifications:	
a. Weight	190 kg
b. Dimensions	0.48 m × 0.36 m diameter
c. Power	450 W
d. Telemetry Rate	500 kbps
e. Payload Weight - 1999	1100 kg
f. Payload Weight - 2000	960 kg

8.3 Developments in photodetection

The wavelength of LXe scintillation light is in the VUV (174 nm) which makes it difficult to detect it efficiently. Coupling photodetectors to the liquid via UV transmitting windows, as is currently done in LXeGRIT, results in severe light losses due to total internal reflection. When considering a scaled-up detector, the large number of windows needed to effectively cover a large liquid volume will require a much thicker vessel to keep the strength. The only adequate solution seems to be the use of photodetectors placed in the liquid. The design of a compact photo-multiplier tube (PMT) by Hamamatsu Photonics (R6041-06), specifically for the use in LXe, was initiated a few years ago, with development funds provided by our Waseda University collaborators. The metal channel PMT can withstand up to 5 atm overpressure and the low temperature of LXe (∼165 K). It is 2 inch in diameter, with a total length of only 36 mm, equipped with a UV-quartz window. The R6041-06 PMT was successfully used by our group in small test set ups. Its operation in LXe and the impact of the base and cables on the liquid purity were systematically studied with measurements of charge and light response (13). About 600 PMTs of the same type are being used by the MEG collaboration [3]. The PMT characteristics have been improved since the original design. The sensitivity is now maximum at the wavelength of Xe scintillation.

Another recent development is the Hamamatsu R8520 PMT, with a total area of 25.7×25.7 mm^2 and a square shape. This last characteristic allow the PMTs to be easily tiled, giving a very uniform light collection.

Apart for the specific PMT of choice, at least three issues come to mind which will be relevant to a large scale detector where as many as few hundreds PMTs may be immersed in LXe: the high-voltage (HV) to reduce the power consumption, a suitable calibration system and a new design for a trigger/data-acquisition system fully integrating light and charge read-out.

The standard HV divider provided with the PMT uses about 100 mW. This power is mostly dissipated in the resistors of the divider since the current has to be large compared to the current of the last dynode, and this current is used at the maximum voltage on the cathode. The divider should be replaced with a Cockcroft Walton generator, in the same way most HV power supplies are constructed. The intermediate voltages for the dynodes

---

[3] See http://meg.web.psi.ch/

are derived from taps in the Cockcroft Walton multiplier chain. Each current is now consumed at its specific voltage. The total power consumption can be reduced well below 1 mW/PMT, meeting the requirements of a balloon/satellite experiment.

The second issue relates to the gain equalization of a large number of PMTs, which is important for total energy calibration. A dedicated system based on blue light emitting diodes should be developed.

To be read-out, each PMT will be connected to a charge sensitive amplifier which derives a fast logic signal for triggering and an analog signal for energy measurement. The trigger signals have to be passed through a majority coincidence unit requiring at least 2 or 3 simultaneous signals in order to eliminate the remaining thermal noise of the PMTs. The trigger signal will start the charge read-out and serve as a time zero for the event. The system will add the analog signals which will be passed through a single channel analyzer (SCA) with variable thresholds. Similar to a second level trigger, the upper and lower thresholds of the SCA define an energy window of interest, and all events outside the window can be rejected.

8.4 Time of flight

All the photodetectors discussed in the previous section share a good timing capability. In fact, the MEG experiment itself specifically requires it. The time resolution improves with the number of photoelectrons (p.e.), roughly as $1/\sqrt{N_{p.e.}}$ and the MEG collaboration has shown that a time resolution of $\sim$0.3 ns is obtained for $\sim$500 p.e.. It is therefore crucial to maximize the light collection, i.e. to keep the distance between an interaction in the fiducial volume and the closest photodetector as small as possible.

In a Compton telescope fast timing capability is very attractive because of the possibility to apply ToF in sequencing Compton interactions, which would be helpful in - at least - two respects :

2. As shown by COMPTEL, ToF is powerful in rejecting background, once its direction is well separate from the direction of the signal (e.g. upward going signal and downward going background or vice versa).
2. In LXeGRIT the efficiency for Compton imaging steeply declines for γ-ray energies larger than 3 MeV. This happens because the right interaction sequence is searched for based on Compton kinematics; in a com-

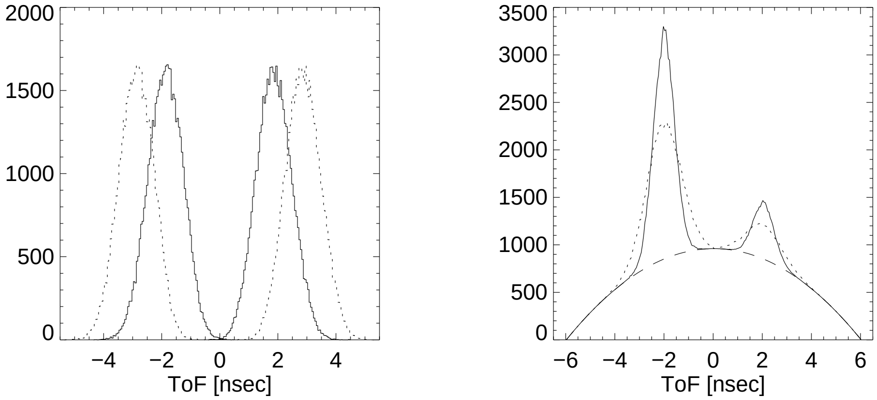

Figure 8.2: *Left:* backward and forward peaks in the ToF distribution assuming 0.3 ns time resolution and 30 cm *(continuous line)* and 60 cm *(dotted line)* separation between the detectors. *Right:* ToF distribution where a "parabolic" continuum has been introduced, assuming a forward-over-backward ratio of 0.25; time resolution of 0.3 ns *(continuous line)* and 0.5 ns *(dotted line)*.

> pact device, based on a high Z, high density material like LXe, above 3 MeV an overwhelming fraction of events will contain pair production interactions and bremsstrahlung photons, which spoil the application of such kinematic methods. Sequencing by ToF would overcome this limitation and recover a good detection efficiency up to 20-30 MeV.

Despite its good historical record, the idea of a ToF measurement in a Compton telescope swims against the tide, since nowadays no other proposed concept foresees such a capability. It should be clear that our proposal does not mean going back to a plain COMPTEL-type instrument. ToF requires two separate modules, like COMPTEL, but the idea is that each module should be a stand-alone LXeGRIT-type Compton telescope.

Given a sub-millimeter position resolution as in LXeGRIT, the two modules do not need to be kept far apart to preserve a good angular resolution, which in the end increases the acceptance for scattered γ-rays and improves the detection efficiency. Fig. 8.2-$left$ shows the backward and forward peaks in the ToF distribution assuming 0.3 ns time resolution, a 50×50 cm^2 area for each of the two modules, 5 cm maximum distance between an interaction

the closest photodetector, 30 cm (continuous line) and 60 cm (dotted line) separation between the two modules. The two peaks have almost no overlap even assuming a separation of 30 cm. The assumption of two identical modules is unrealistic but conservative, since the upper module would be thinner and more easily optimized for light detection.
If the 3D-location is then reconstructed with a sub-millimeter accuracy, as allowed by the TPC readout, the width of the ToF backward and forward peaks can be reduced to the intrinsic time resolution of the photodetectors. This would allow to largely reduce the background due to ToF continuum, i.e. events neither in the backward nor in the forward peak (e.g. the COMPTEL ToF distribution as in Ref. (96)), which requires not only a good up-down separation, but also a good accuracy on the ToF. An example is shown in Fig. 8.2-*right*, where a "parabolic" continuum has been introduced, assuming a forward-over-backward ratio of 0.25, 60 cm separation between the two modules and a time resolution of 0.3 ns (continuous line) and 0.5 ns (dotted line).
Even if still very speculative, this short paragraph shows that the possibility of a ToF measurement in a next generation Compton telescope should be taken seriously.

8.5 LArγE?

Liquid argon (LAr) is a viable alternative to LXe, still in the framework of the TPC approach. A LAr γ-ray experiment (LArγE) would have several advantages over LXeGRIT: the intrinsic energy resolution is better in LAr than in LXe (3), LAr is easier to purify than LXe, a LAr is a "popular" active medium for TPC's and a TPC with a 50 l fiducial volume has been built and successfully operated (17), LAr is orders of magnitude cheaper than LXe. LXe has a large cross-section for photoelectric absorption due to $Z_{Xe} = 54$, exceeding the Compton cross-section below 300 keV. It has a density of ~3 g/cc and an attenuation length well below 1 cm for photon energies of 200 keV or less, so that many interactions are too close to be spatially resolved. On the other side, $Z_{Ar} = 18$ and its density is ~1.4 g/cc; therefore, for the same initial energy, the multiplicity will be on average higher in LAr. This is both an advantage and a disadvantage of LAr vs. LXe. An extremely compact and efficient Compton telescope may be built out of LXe and a compact detector is superior *a priori* when it comes to photodetection, because it makes possible to minimize the distance between the interaction point and the photodetector. At this point only a more detailed comparison, based on fully realistic detector concepts, will settle the dispute between LAr and LXe.

8.6 LDB mission

Given the experience gained with the LXeGRIT prototype and the planned developments, it is our opinion that a full-fledged EXPLORER class mission capable of scientific return would be a very useful intermediate step toward the longed for ACT.

The possibility of such a mission was already studied to a detailed extent and proposed during the last UNEX competition, with the XENA concept (7). It was based on two large area (2500 cm^2) LXeTPCs in coincidence but *without* ToF capability. The instrument characteristics and performance are summarized in Table 1, while the sensitivity and exposure map for such a mission are shown in Figs. 8.3 and 8.4. The in-flight experience with LXeGRIT confirms the soundness of the mission concept. The 3σ sensitivity of LXeGRIT to a Crab-like source has been estimated to be about 1.5 Crab [4] with 6 hr effective observing time. With a geometrical area 6.25 times larger, a foreseen improvement of ∼10 in the efficiency due to a new light-trigger system and ∼84 hr effective observing time, the 3σ sensitivity should reach 0.05 Crab. This is a conservative estimate because the impact of an added ToF capability still needs to be assessed and has not been included. At that level of sensitivity interesting scientific results are expected. Furthermore, recent RHESSI results (e.g. (30) and (89)) also show that MeV γ-ray astronomy may offer exciting results well before reaching the ACT "recommended" sensitivity.

Together with its expected scientific return, a mission like the one proposed here would also be useful for testing diverse experimental ideas, getting rid of the bad ones and helping the good ones to coalesce.

---

[4] The integrated 1-10 MeV flux from the Crab is 1.38×10^{-3} cm^{-2} s^{-1} (94).

Table 8.3: XENA instrument characteristics and performance. From Ref. (7).

Instrument Characteristics	
Energy range (Compton imaging)	0.3 - 10 MeV
Energy resolution (1 σ)	2.5% $(E/1MeV)^{1/2}$
Position resolution (1 σ)	1 mm (3 dimensions)
Angular resolution (1 σ)	0.4° - 2.4°(mode 1 events)
FOV (FWHM)	3 sr
Effective area	185 cm^2 @ 1MeV 220 cm^2 @ 2MeV
Sensitivity (3 σ, $t_{obs} = 4 \times 10^5$ s)	
Narrow line (1.17/1.33/1.81 MeV)	$(9/8/6)\times 10^{-6}$ $\gamma cm^{-2}s^{-1}$
Continuum (1 - 10) MeV	5×10^{-5} $\gamma cm^{-2}s^{-1}$ MeV^{-1}
Compton Telescope Configuration	
Imaging technique	LXeTPC
Upper LXeTPC assembly	4 modules, 25 cm × 25 cm
Lower LXeTPC assembly	4 towers of 4 modules (25 cm × 25 cm / module)
Total geometrical area	2500 cm^2
Separation	10 cm

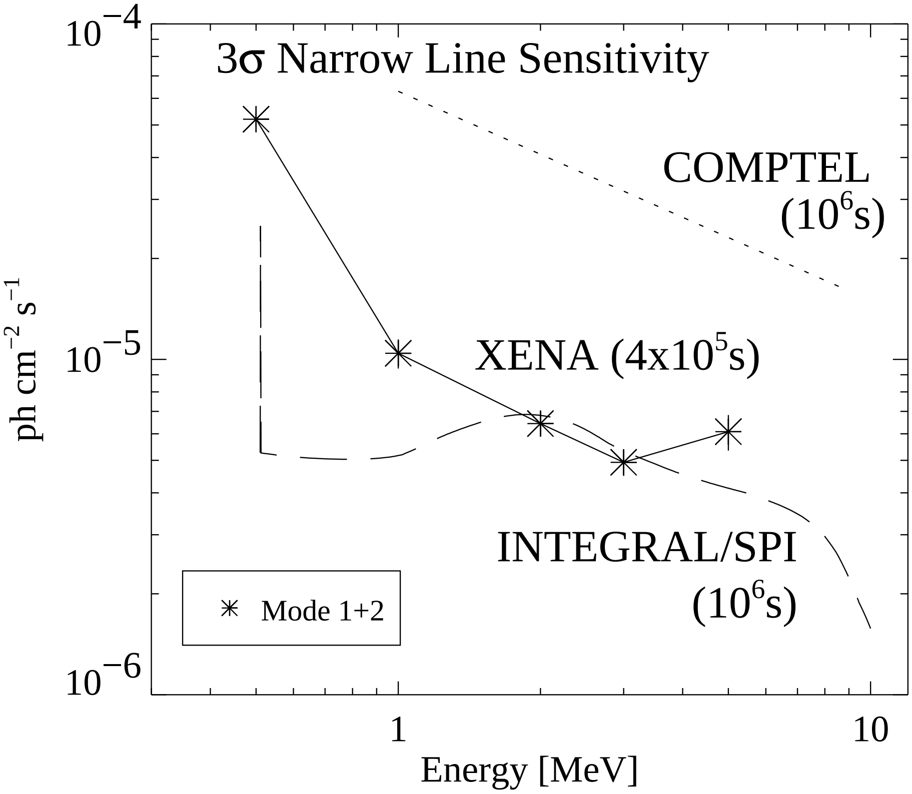

Figure 8.3: XENA narrow line sensitivity for a point source compared to COMPTEL and INTEGRAL/SPI. (From Ref. (7))

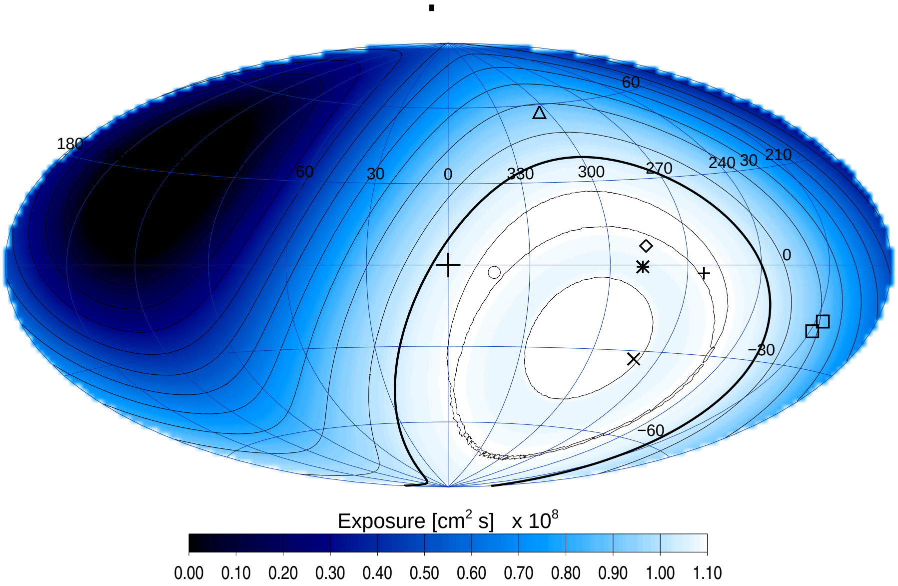

Figure 8.4: Expected exposure for a typical LDB flight of a LXeTPC Compton telescope on the Southern hemisphere. □: positions of Orion clouds A and B, + Vela pulsar, ∗ Carina region, ⋄ PSR B1055-52, △ AGN 3C279, ◯ PSR B1706-44, × LMC. The Galactic Center is marked with a large cross and the thick line indicates the trajectory of the instrument's zenith. (From Aprile et al. (7))

Chapter 9

Conclusions

The LXeTPC approach to an innovative Compton telescope has been pursued for several years at Columbia. When I started working on this project - it was Spring '99 - the LXeGRIT instrument was ready for its 1999 balloon flight. The LXeTPC remained unchanged during the following years, and has been described in Chapter 2. The detailed calibration of the LXeGRIT, both as an imaging calorimeter (Chapter 2) and as a Compton telescope (Chapter 4), was mainly achieved in the years 1999, 2000 and 2001. A large amount of work was devoted to modeling the efficiency of the instrument, as described in Chapter 3.

In the meantime, LXeGRIT had its 2000 balloon flight. The instrument itself was modified building upon the "mixed" 1999 experience (Appendix A): the massive shields surrounding the LXeTPC, which had a troublesome behavior in 1999, were entirely removed; the DAQ was optimized to the point where the main bottleneck, i.e. the read-out of the digital electronics by the DAQ processor, could not be significantly improved any further; the settings of the trigger system were properly tuned to maximize the overall detection efficiency. The 2000 balloon flight provided a wealth of data, which allowed to study the background at balloon altitude (Chapter 6), a "classic" measurement for instruments in MeV γ-ray astrophysics, and to assess the sensitivity to celestial sources (Chapter 7).

In this way, the first, fundamental phase of detector prototyping has been successfully completed. Among several results, I would like to highlight that: *i.* it has been experimentally proved that an effective area of $\sim$0.1$\times$(*geometrical area*) for a Compton telescope is not just reverie and *ii.* a favorably low background level at balloon altitude has been measured, establishing the LXe technology as a main competitor for the still-to-come advanced Compton telescope (ACT).

This process has been fertile soil for new ideas (Chapter 8), among them to combine, in the same detector, a time of flight measurement and fine granularity, but the LXeGRIT prototyping phase has also taught us that the devil often lurks in the details. A new mission on a long duration balloon has been proposed as a bridge to the final ACT. Such a mission promises a valuable scientific return and would be invaluable in facing the still many open technical questions.

Appendix A

Results from the 1999 balloon flight

A.1 LXeGRIT gondola and veto shield system

A simplified block diagram of the LXeGRIT flight system in the 1999 balloon flight is shown in Fig. A.1; a schematic of the LXeGRIT instrument assembled on the balloon gondola is shown in Fig. A.2, again in its 1999 configuration. The instrument in its 2000 configuration has been described in great detail in Ch. 2 and Ch. 3, the main difference, compared to the 1999 configuration, being the removal of the side and bottom shields. The LXeGRIT balloon gondola was assembled starting from the existing gondola of the University of New Hampshire Directional Gamma-Ray Telescope (DGT) (42), which was extensively modified. To reduce the charged particle and γ-ray background rate at balloon altitude, it was first decided to use the available veto shield systems of the DGT to cover the LXeTPC as much as possible. The detector intrinsic 3D event imaging capability allows an effective identification and rejection of single interaction events and charged particles in the off line analysis. However, the decision to use an active shield was motivated by the desire to reduce the overall data rate to be transmitted via telemetry to ground. The shield configuration used for the LXeGRIT balloon flights is shown in Fig. A.3. The back shield consists of six $10\times10\times41$ cm^3 bars of NaI(Tl) with PMTs at one end, covering an area of about 2730 cm^2. The side shield consists of six units, each composed of small chunks of NaI(Tl),

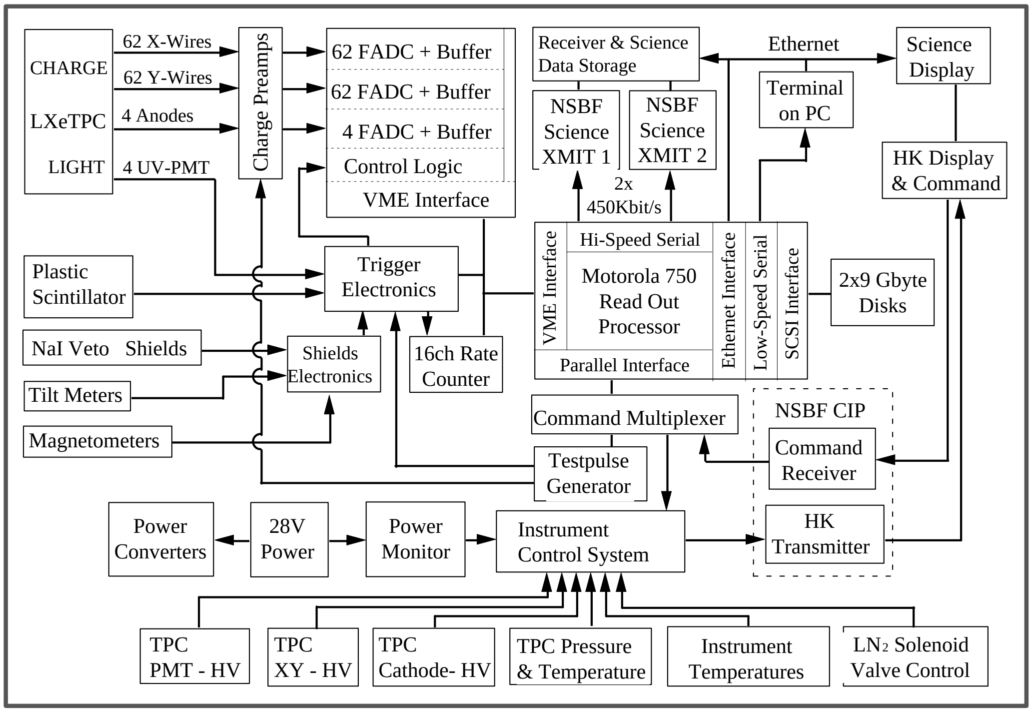

Figure A.1: Block diagram of the LXeGRIT system in the 1999 balloon flight. Also indicated are additional interfaces such as terminal and Ethernet connection of the DAQ processor for laboratory testing and calibration and the basic control units on the ground. See Fig. 2.10 for the LXeGRIT system in the 2000 balloon flight. From Ref. (9).

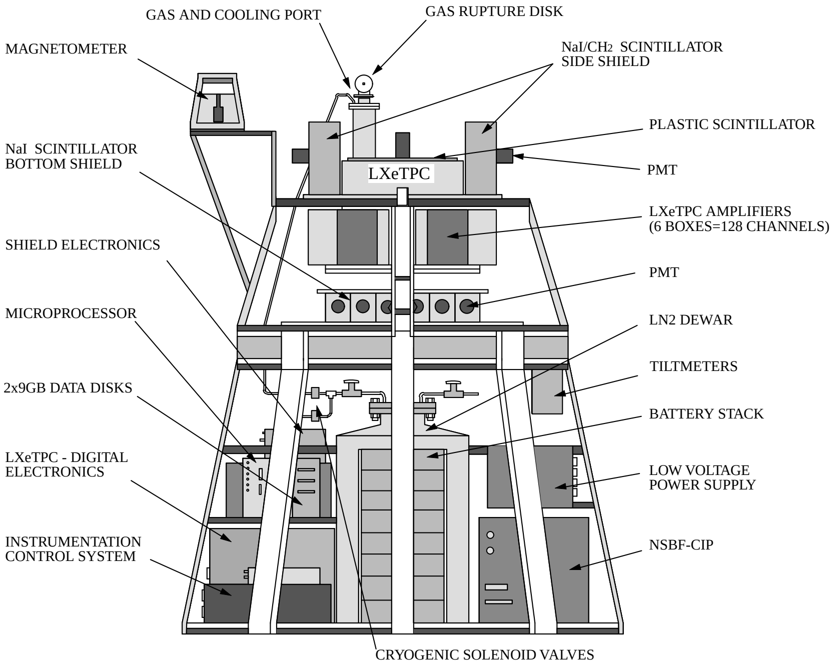

Figure A.2: Schematic of LXeGRIT payload in 1999 flight configuration. From Ref. (9).

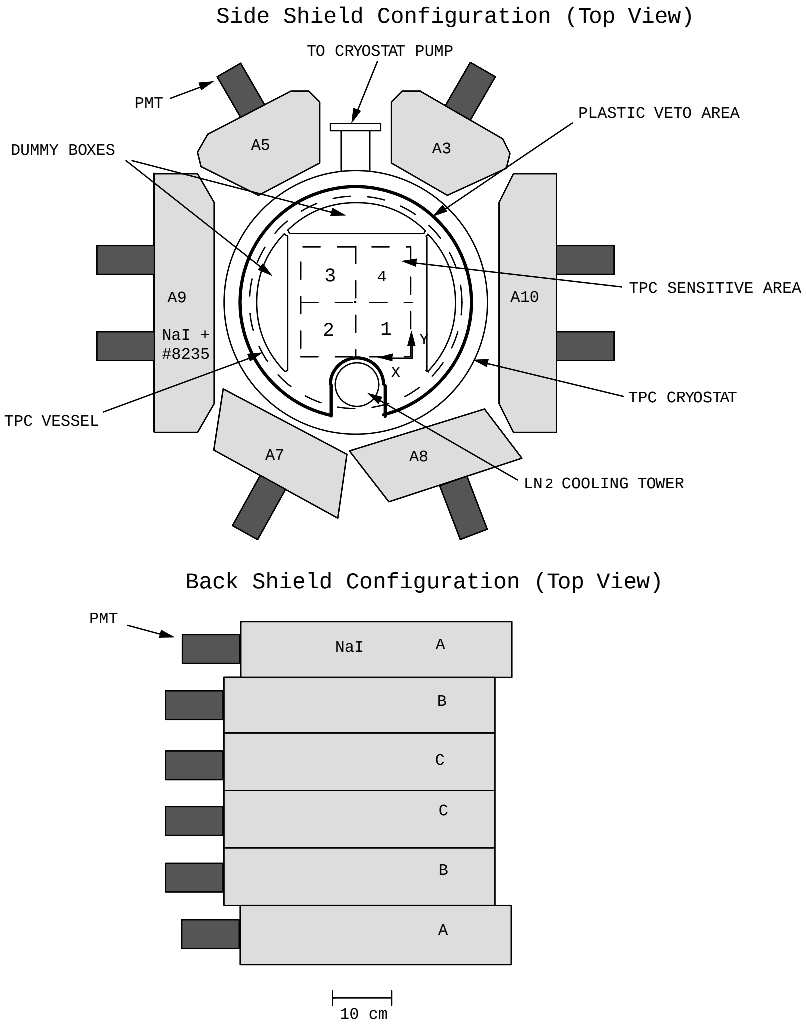

Side Shield Configuration (Top View)

Back Shield Configuration (Top View)

Figure A.3: Schematic of the shield configuration. From Ref. (9).

immersed in liquid scintillator (NE235), sealed in an aluminum container. Each unit is viewed by two PMTs coupled directly to the NE235 mineral oil. The units are of three different shapes, but they all have a thickness of about 10 cm and a height of 25 cm, limiting the TPC field-of-view (FoV) to about 45°. The packing fraction of NaI in the side shields is about 75%. The total mass of the shield system, including the support structures electronics and cables, is about 270 kg. The energy threshold of the side shields, which have poor energy resolution, was adjusted to match the rate in the NaI back shields with a threshold around 0.3 MeV. The original DGT shield electronics and control logic was used. The individual shield rates together with the attitude information from the magnetometers and inclinometers were down-linked to ground through a separate telemetry channel. A plastic scintillator counter of 1.2 cm thickness and an area of 1600 cm^2 was added to veto the charged particles entering the TPC from the top. It is mounted directly on top of the TPC cryostat and is viewed by one PMT in the center. Its signal is measured by one channel of the DGT shields electronics. The logical OR of the signals from all the shield sections, including the plastic, is fed into the LXeGRIT Trigger Electronics System, to veto the LXeTPC light trigger signal.

The count rate in the veto shield system during the 1999 flight is presented in the next session; the overall impact of the veto counters was difficult to evaluate *a posteriori*, and it was questionable whether they helped in reducing the background rate or they were themselves an important source of background, as it is often the case in MeV γ-ray astronomy. As already written, the veto shield system was entirely removed for the 2000 flight.

A.2 Instrument performance during the 1999 flight

LXeGRIT was launched from the National Scientific Balloon Facility (NSBF) in Ft. Sumner, NM, on May 7, 1999 at 7:26:54 local time (13:26:54 UT), using a 28 million cubic feet balloon (Fig. A.4). It reached float altitude after about 2.5 hours, and remained there for 7 hours, before flight termination due to wind conditions. During the entire flight including ascent, a total of $\sim 3\times10^5$ events were collected. The main goal of the flight was a measurement of the background rate in LXeGRIT and to verify the background discrimination capability of the LXeTPC.

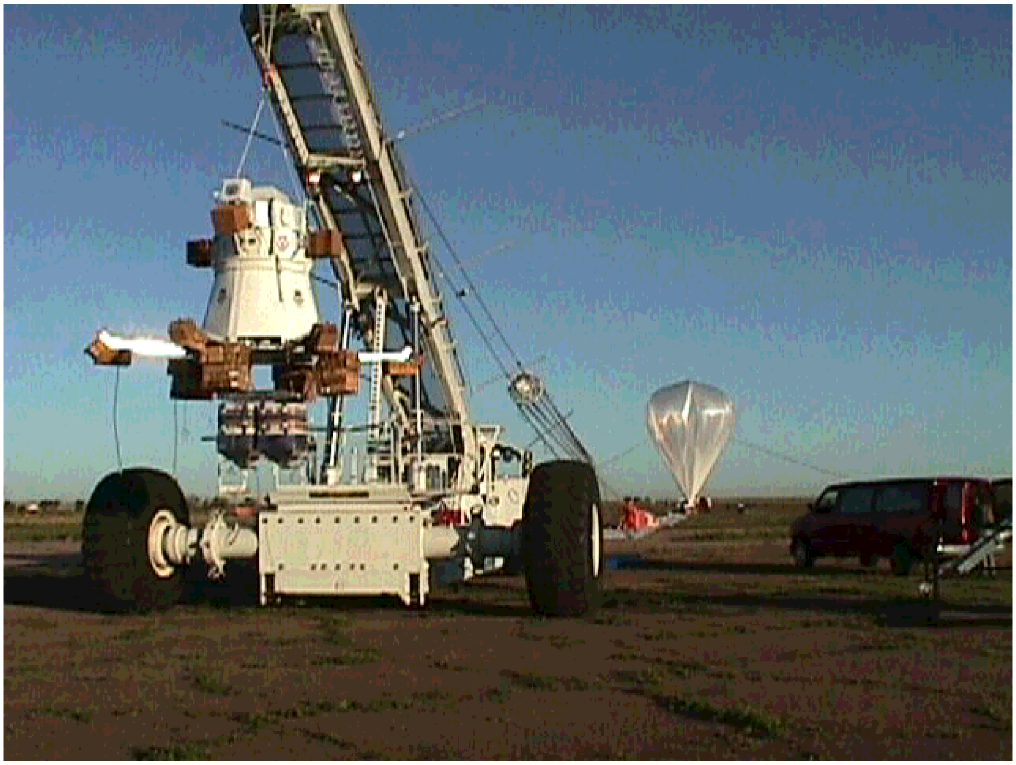

Figure A.4: The LXeGRIT gondola on the launch pad at the National Scientific Balloon Facility (NSBF) in Ft. Sumner, NM, on May 7, 1999 at 7:26:54 local time (13:26:54 UT).

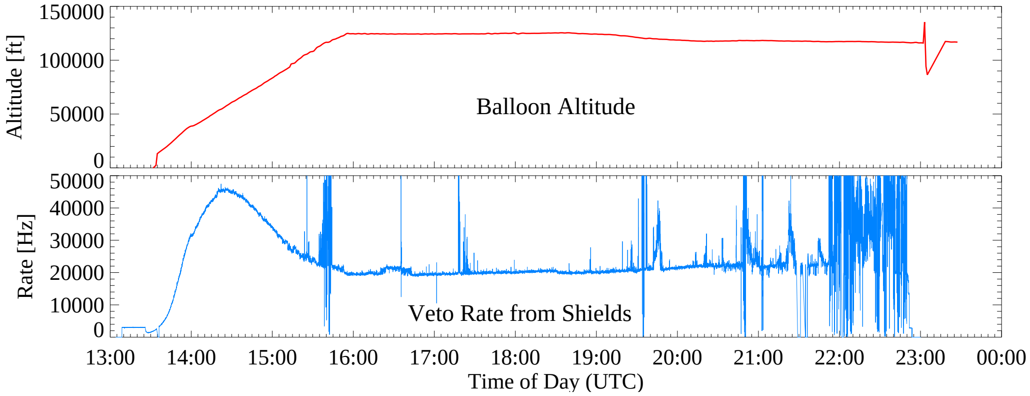

Figure A.5: *Top:* altitude of the balloon payload during the May 1999 flight. *Bottom:* veto rate from all the shields combined (logical OR). The maximum rate is reached at 14:20 UTC, when the payload passes through the Pfotzer maximum. The data are clearly noisy, due to the malfunctioning of some of the veto counters (see Fig. A.6). The rate gradually increases with time; it may be an indicator of activation of NaI.

Fig. A.5 shows the altitude of the payload during the flight and the veto rate from all the shields combined (logical OR). The atmospheric depth varied between 3.7 and 5.2 g/cm^2. LXeGRIT performed well during the flight: the LXeTPC and its high voltage and cryogenics systems, the electronics and data acquisition systems worked in the near space environment as they did in the laboratory. A few problems were encountered with some of the side shield units. The loss of telemetry contact with the ICS for a major part of the flight did not impact the science data. The payload was recovered in good conditions, with mechanical damages to the magnetometers and three side shield units.

The rate on all the shield units, shown in Fig. A.6, gradually increases with time. This effect is apparently consistent with activation of NaI, and with the build-up of radioactive nuclei such as ^{24}Na with a half-life of 15 h. In addition, three sections of the side shields showed excessive rates at float altitude, which required to raise their thresholds. This rendered a large part of the side shield essentially passive below several 100 keV, such that a significant number of low-energy γ-rays may have leaked into the LXeTPC without veto. Also shown in the same Fig. A.6, is the rate measured in the plastic scintillation counter above the LXeTPC.

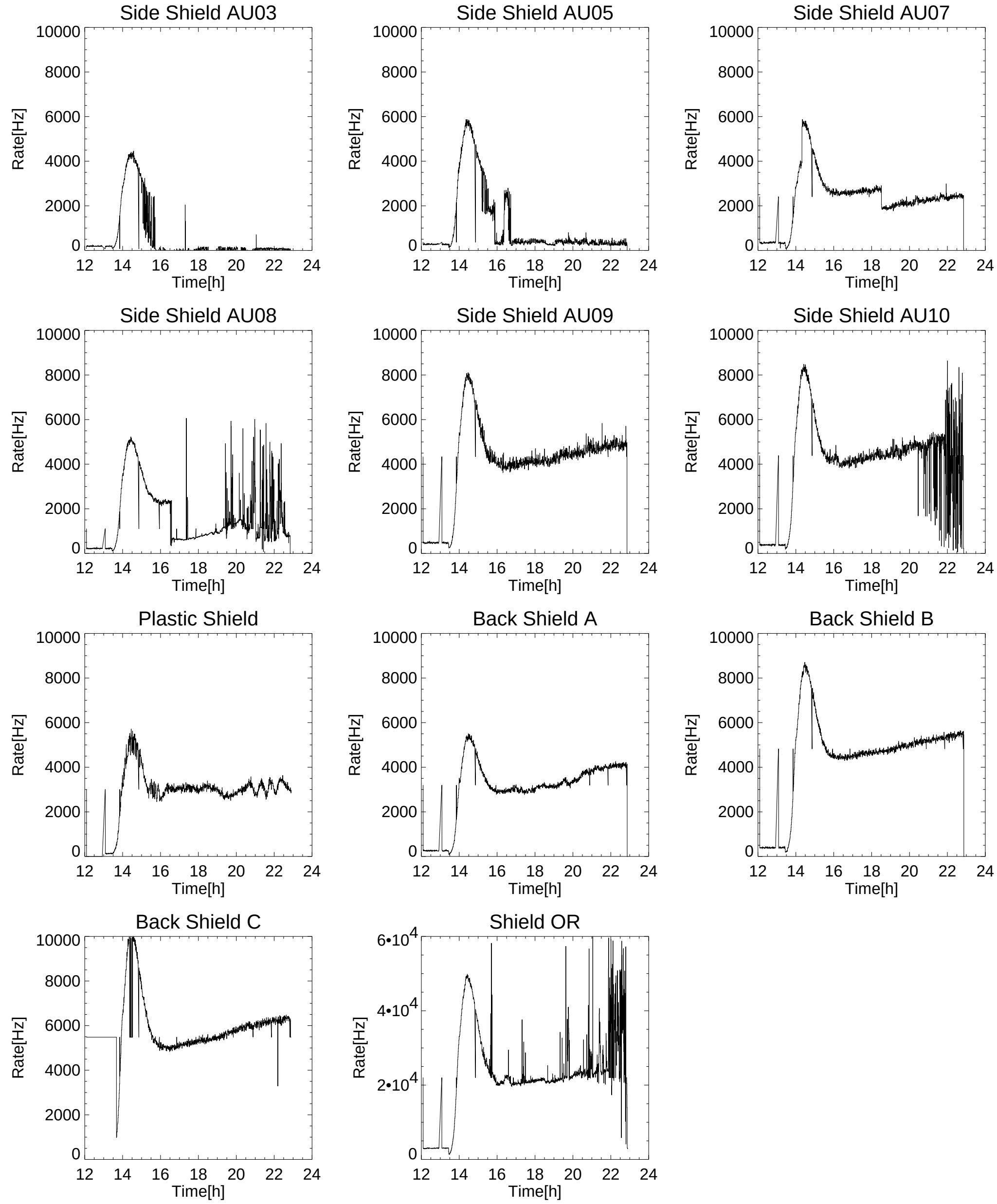

Figure A.6: Veto rates from the six side shield units and the three back units. The lower two plots refer to the plastic shield rate and the logical OR of all the units. From Ref. (9).

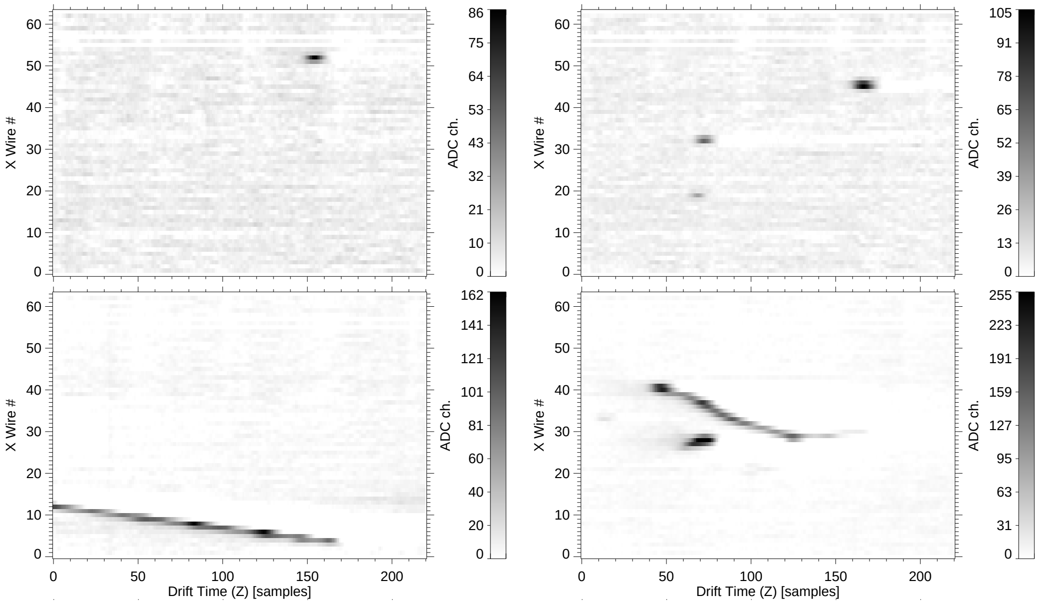

Figure A.7: Different event types are easily recognized by their signature on the sensing wires, as shown in these images projected in the x, z-plane. Single- (top left panel) and 3-site (top right panel) γ-events, a track due to a high-energy cosmic ray crossing the TPC from top to bottom (bottom left), and a more complex event topology involving inelastic scattering (bottom right). From Ref. (9).

The 2D display of four different events recorded during the flight is shown in Fig. A.7, which confirms that the LXeTPC worked very well at balloon altitude maintaining its excellent imaging capability.

A.3 Results

The PMT trigger (logical OR of the four PMTs) rate is shown in Fig. A.8-*top*. The rate was extremely high, ∼20 kHz (during the year 2000 flight the rate was less than 1 kHz); the ABORT rate (*center*) was high as well, and the trigger rate after ABORT rate was ∼4 kHz (*bottom*). As explained in Sec. 3.4, such a high rate greatly reduces the livetime of the detector. Due to an error in the DAQ software, the livetime fraction was not automatically measured at the level of the DAQ processor and it is not precisely known; this makes a quantitative analysis of the flight data extremely difficult. The trigger rate as shown in Fig. A.8 has to be taken *cum grano salis*; the trigger counts are often correlated in time, as it would be the case for a train of noise pulses. Therefore it is believed that the high trigger rate is in part due to spurious triggers. The impact of the shields is hard to quantify, because their lower energy threshold is not known with any acceptable precision; most likely, the shields led to an *increase* in the final rate, rather than reducing it.

In 1999 the lower threshold at the first trigger level was set such to have a large efficiency (∼50%) down to few hundreds keV, which also contributed to produce a high trigger rate.

The final rate of selected γ-rays is shown in Fig. A.9, which should be compared to Fig. 6.3. The most striking difference is the much higher - a factor of about ten - rate for multi-site (i.e. Compton imaging) events obtained in 2000 (see Ch. 6). The rate of selected events is also rather unstable, due to frequent changes in the settings of the first and second level trigger.

The count rate spectra for 1-site and multi-site events are shown separately in Fig. A.10, and are directly comparable to the ones in Fig. 6.5 for the 2000 experiment.

To proceed toward a more refined analysis, similar to the one performed for the 2000 balloon flight data and described in the next chapter, is extremely difficult if not downright impossible. The main obstacles are: *i.* the livetime fraction is not well determined; *ii.* the lower energy threshold of the shields, and more generally the shields' response (e.g. spatial inhomogeneities), is also not well determined; *iii*. the response of the LXeTPC is not well modeled as for the configuration in the 2000 experiment; *iv*. the many different settings of the first and second level trigger are difficult to follow.

It is anyway fair to say that the performance of LXeGRIT instrument greatly improved in year 2000, compared to 1999.

The feature at ∼1.5 MeV in the multi-site energy spectrum (Fig. A.10-*right*) is due to internal background (^{40}K), as explained in Sec. 7.2.

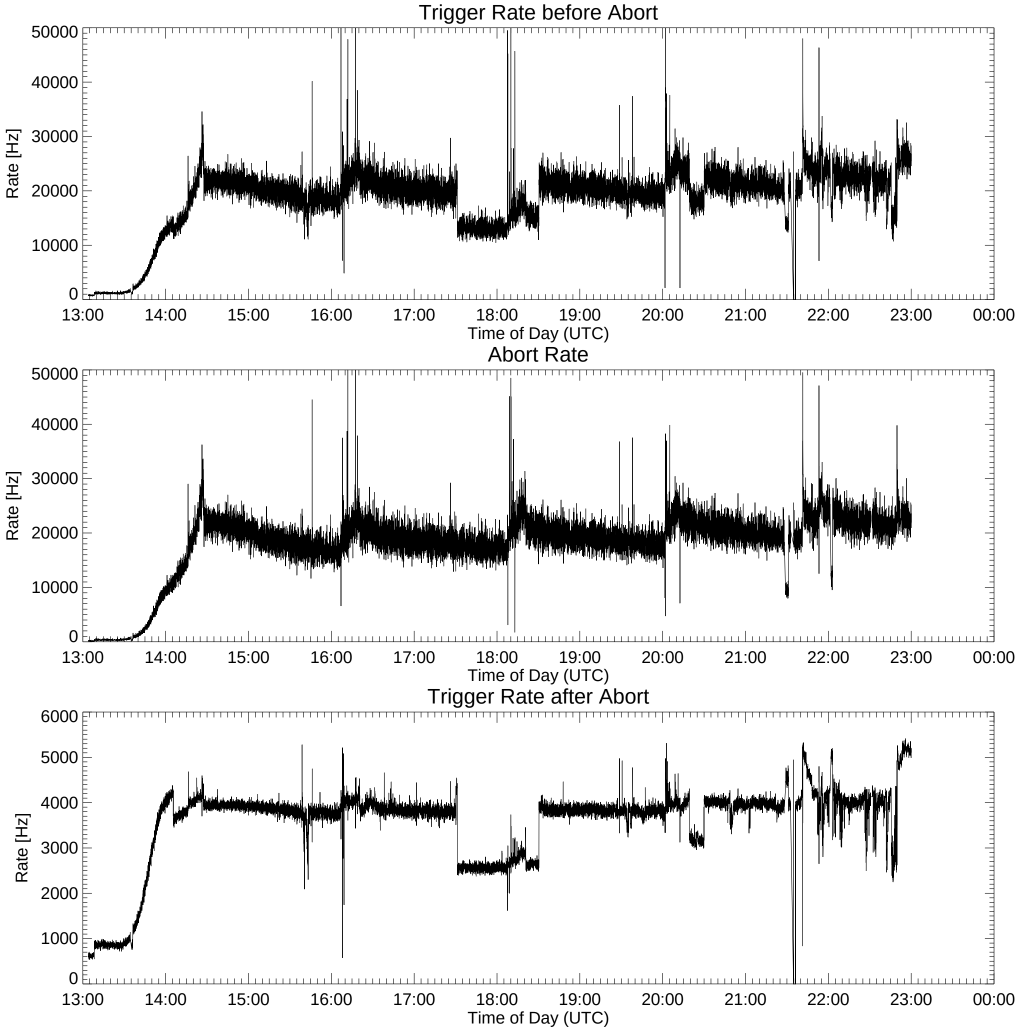

Figure A.8: *Top:* PMT trigger rate. Sudden changes in the trigger rate are due to different settings of the first level trigger. *Center:* ABORT rate. *Bottom:* trigger rate after ABORT (~4 kHz).

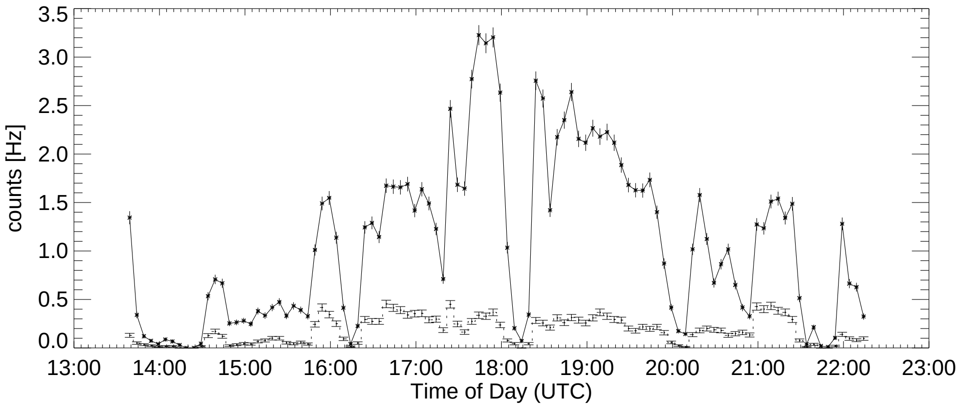

Figure A.9: Rate vs. time of accepted events, after the entire analysis procedure has been completed; *continuous line:* 1-site events, *dotted line:* multi-site events.

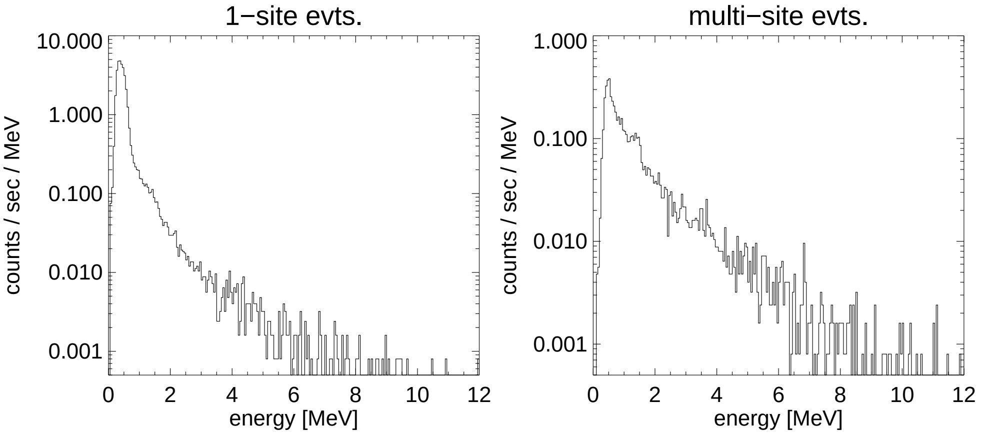

Figure A.10: Count rate spectra; 1-site events (*left*) and multi-site events (*right*).

Bibliography

[1] Abachi, S., et al. 1994 Nucl. Instr. and Meth. A, 338, 185

[2] Ansen, P., et al. 2003 Phys. Rev. D, accepted
hep-ph/0307199

[3] Aprile, E., et al. 1987 Nucl. Instr. and Meth. A, 261, 519

[4] Aprile, E., et al. 1991 Nucl. Instr. and Meth. A, 307, 119

[5] Aprile, E., et al. 1993 Nucl. Phys. B, proc. suppl. 32, 279

[6] Aprile, E., et al. 1998 Nucl. Instr. and Meth. A, 412, 425

[7] Aprile, E., et al. 1998 Vol. 3446 of Proc. of SPIE, 88 eds: R. Diehl & D. H. Hartmann, MPE Report 274 (ISSN 0178-0719), 281

[8] Aprile E., Curioni A., Oberlack U. G. 1999 in: Astronomy with Radioactivities, Proc. 'Astronomy with Radioactivities', eds: R. Diehl & D. H. Hartmann, MPE Report 274 (ISSN 0178-0719), 281

[9] Aprile, E. et al. 2000 Vol. 4140 of Proc. of SPIE, 333,
astro-ph/0012398

[10] Aprile, E. et al. 2001 IEEE Trans. Nucl. Sci, Vol. 48 NO 4, 1299,
astro-ph/0012276

[11] Aprile, E., Baltz, E. A., Curioni, A. et al. 2002 in: Technique and Application of Xenon Detectors, eds. Y. Suzuki et al., World Scientific, 165
astro-ph/0207670

[12] Aprile, E., et al. 2002 Nucl. Instr. and Meth. A, 480, 636

[13] Aprile, E., et al. 2002, IEEE Trans. Nucl. Sci., Vol. 50 NO 5, 1303

[14] Aprile, E., et al. in preparation

[15] Aprile, E., et al. in preparation

[16] Armstrong, T. W., et al. 1973 J. Geophys. Res., 78, 2715

[17] Arneodo, F., et al. 1998 in "Erice 1997, New detectors", hep-ex/9812006

[18] ATLAS liquid argon calorimeter Technical Design Report, 1996, CERN/LHCC/96-41, ATLAS TDR 2, CERN

[19] Barrett, H. H., Parra, L. & White, T. J. 1997 J. Optical Soc. Amer. A, vol. 14, no. 11

[20] Bernabei, R., Belli, P., Cappella, F. et al. 2002 in: Technique and Application of Xenon Detectors, eds. Y. Suzuki et al., World Scientific, 50

[21] Bildsten, L., Salpeter, E. E. & Wasserman, I. 1993, ApJ, 408, 615

[22] Bloemen, H. et al. 1994 ApJS, 92, 419

[23] Bloemen, H. et al. 1999 ApJ, 521, L137

[24] Boggs, S. E. & Jean, P. 2001 A&A, 376, 1126

[25] Boggs, S. E. et al. 2003 proposal submitted in response to NRA 03-0SS-01-VM Call for Mission Concepts: Space Science Vision Missions

[26] Bressi, G. et al. 1990 Nucl. Instr. and Meth. A, 292, 585

[27] Carugno, G. et al. 1993 Nucl. Instr. and Meth. A, 335, 338

[28] Cline D., Curioni, A., Lamarina, A. et al. 2000 Astropart. Phys., 12, 373

[29] Conti, E. et al. 1995 Nucl. Instr. and Meth. A, 356, 286

[30] Coburn, W. & Boggs, S.E., 2003, Nature, 423, 415, astro-ph/0305377

[31] Costa, E., et al. 1984 ApSS, 100, 165

[32] Cottam, J., Paerels, F. & Mendez, M. 2002 Nature 420, 51

[33] Curioni, A. 1998 Tesi di laurea, Università degli studi di Milano

[34] Curioni, A. et al. 2002 Vol. 4851 of Proc. of SPIE, 151, astro-ph/0211584

[35] Curioni A., et al. in preparation

[36] Danilov, M., DeVoe, R., Dolgolenko, A. 2000 Phys. Lett. B, 480, 12 hep-ex/0002003

[37] Dean, A. J. et al. 1991 Space Sci. Rev., 57, 109

[38] de Boer, H. et al. 1992 in *Data Analysis in Astronomy IV*, eds. V. Di Gesù, et al. , Plenum Press, New York, 241

[39] Dermer, C. D. & Skibo, J. G. 1997 ApJ, 487, L57

[40] Dupraz, C., Bloemen, H., Bennett, K. et al. 1997 A&A, 324, 683

[41] Diehl, R., Knödlseder, J., Lichti, G. G. et al. 2003 A&A special INTEGRAL volume
astro-ph/0309097

[42] Dunphy, P. P. et al. 1989 Nucl. Instr. and Meth. A 274, 362

[43] Erber, T. 1966, Rev. Mod. Phys, 38, 626

[44] Fanti, V., et al. 1994 Nucl. Instr. and Meth. A, 344, 507

[45] Veenhof, R. 1997 Garfield, a drift-chamber simulation program, CERN, Geneva

[46] GEANT, Detector Description and Simulation Tools, CERN Program Library, Long Writeup W5013

[47] Gehrels, N. 1985 Nucl. Instr. and Meth. A, 239, 324

[48] Gold, T. 1968 Nature, 218, 731

[49] GRAPWG 1999, Recommended priorities for NASA's gamma ray astronomy program 1999-2013, Tech. Rep. NP-1999-04-072-GSFC, NASA

[50] Hagiwara, K., et al. 2002 Phys. Rev. D, 66, 010001

[51] Herzo, D. et al. 1975 Nucl. Instr. and Meth. A, 123, 583

[52] Hewish, A., Bell, S. J., Pilkington, J. D. et al. 1968 Nature, 217, 709

[53] Research Systems, Inc., 4990 Pearl East Circle, Boulder, CO

[54] Iyudin, A.F., Diehl, R., Bloemen, H. et al. 1994, A&A, 248, L1

[55] Iyudin, A., Schönfelder, V., Bennett, K. et al. 1998 Nature, 396, 142

[56] Jean, P., Knödlseder, J., Lonjou, V. et al. 2003 A&A, 407, L55 astro-ph/0309484

[57] Kappadath, S. C., et al. 1996 A&AS, 120, 619

[58] Kirsanov, M. A., et al. 1993 Nucl. Instr. and Meth. A, 326, 48

[59] Knoll, G. F. Radiation detection and measurements, 2nd ed. (Wiley, 1989)

[60] Kubota, S. et al. 1979 Phys. Rev. B, 20, 3486

[61] Lange, K. & Carson, R. 1984 J. Comput. Assist. Tomogr., vol. 8, no. 2, 306

[62] Leising, M. D. & Share, G. H. 1994 ApJ 424, 200

[63] Lucy, L. B. 1974 ApJ, 79, 745

[64] Mahoney, W. A., et al. 1978 in: Gamma Ray Spectroscopy in Astrophysics, eds., T.L. Cline and R. Ramaty, NASA TM-79619 p. 462

[65] Mahoney, W. A. et al. 1982 ApJ, 262, 742

[66] Mészáros, P. 2002 Ann. Rev. Astron. Astrophys. 40

[67] Miyijima, M. et al. 1974 Phys. Rev. A, 9, 1438

[68] Morris, D. J., Bennet , K., Bloemen, H. et al. 1995 17th Texas Symposium, N.Y. Acad. Sci., 759, 397

[69] Naya, J.E., Barthelmy, S. D., Bartlett, L. M. et al. 1996 Nature, 384, 44 astro-ph/0111170

[70] Naya, J.E., Barthelmy, S. D., Bartlett, L. M. et al. 1998 ApJ, 499, L169

[71] NGDC, National Geophysical Data Center, Boulder, Colorado, USA. http://www.ngdc.noaa.gov/

[72] Oberlack, U. G., 1997 Ph.D. Dissertation Thesis, Technische Universität München, Germany

[73] Oberlack, U. G. et al. 2001 IEEE Trans. Nucl. Sci, Vol. 48 NO 4, 1041, astro-ph/0012395

[74] Oberlack, U. G., et al. in preparation

[75] Pacini, F. 1968 Nature, 219, 145

[76] Press, W. H. et al. 1992 "Numerical Recipes in Fortran", Cambridge University Press (1992)

[77] Purcell, W. R. et al. 1997 ApJ 491, 725

[78] Ramaty, R., Kozlovsky, B. & Lingenfelter, R. E. 1979 ApJS, 40, 487

[79] Rossi, B., High-Energy Particles, (Prentice-Hall, Englewood Cliffs, NJ, 1952), p.486

[80] Schönfelder, V., Graser, U., Daugherty, J. 1977 ApJ 217, 306

[81] Schönfelder, V., et al. 1980 ApJ 240, 350

[82] Schönfelder, V., Graser, U. & Diehl, R. 1982 A&A, 110, 138

[83] Schönfelder, V. et al. 1993 ApJS, 86, 657

[84] Schönfelder, V. et al. 2000 A&AS, 143, 145

[85] Schönfelder, V., Bloemen, H., Collmar, W. et al. 2000 AIP Conf. Proc., 510, 54

[86] Schönfelder, V. (ed.), "The Universe in Gamma Ray", Spinger-Verlag (2001)

[87] Shibamura, E. et al. 1979 Phys. Rev. A, 20, 2547

[88] Shvartsman, V. F. 1972 Astrophysics, 6, 56

[89] Smith, D. A. 2003 ApJ, 589, 55, astro-ph/0304508

[90] Strong, A. & Diehl, R. 1988 in *Data Analysis in Astronomy III*, eds. V. Di Gesù, et al. , Plenum Press, New York, 55

[91] Timmes, F. X. et al. 1995 ApJ, 449, 204

[92] Timmes, F. X., Woosley, S. E., Hoffman, R. D. & Hartmann, D. H. 1996 ApJ, 464, 332

[93] Ulin, S. E., et al. 1997 Vol. 3114 of Proc. of SPIE, 499

[94] van der Meulen, R.D., et al. 1998 A&A, 330, 321

[95] Vogel, P., Devoe, R., Conti, E. et al. 2002 in: Technique and Application of Xenon Detectors, eds. Y. Suzuki et al., World Scientific, 179

[96] Weidenspointner, G., et al. 2001 A&A, 368, 347

[97] Woosley, S. E. & Weaver, T. A. 1995 ApJS, 101, 181

[98] Xu, F. 1998 Ph.D. Dissertation Thesis, Columbia University

[99] Yashino, Y. et al. 1976 Phys. Rev. A, 14, 438

[100] Zhang, S., Li, T. P. & Wu, M. 1998 A&A, 340, 62

[101] Zoglauer, A. & Kanbach, G. 2003 Vol. 4851 of Proc. of SPIE, 1302

[102] Zombeck, M. V. Handbook of Space Astronomy and Astrophysics, 2nd ed. (Cambridge University Press, Cambridge, UK, 1990)